Stony Brook University

DEFECTS STRUCTURES IN SILICON CARBIDE BULK CRYSTALS, EPILAYERS AND DEVICES

A Dissertation Presented

by

Yi Chen

to

The Graduate School

in Partial Fulfillment of the

Requirements

for the Degree of

Doctor of Philosophy

in

Materials Science and Engineering

Stony Brook University

May 2008

Stony Brook University

The Graduate School

Yi Chen

We, the dissertation committee for the above candidate for the

Doctor of Philosophy degree, hereby recommend

acceptance of this dissertation.

Michael Dudley – Dissertation Advisor
Professor, Department of Materials Science and Engineering

Richard J. Gambino - Chairperson of Defense
Professor, Department of Materials Science and Engineering

Xianrong Huang
Associate Physicist, National Synchrotron Light Source II
Brookhaven National Laboratory

Shaoping Wang
Ph.D., Vice President & Chief Technology Officer
Fairfield Crystal Technology, LLC.

This dissertation is accepted by the Graduate School

Lawrence Martin
Dean of the Graduate School

Abstract of the Dissertation

Defect Structures in Silicon Carbide Bulk Crystals, Epilayers and Devices

by

Yi Chen

Doctor of Philosophy

in

Materials Science and Engineering

Stony Brook University

2008

Silicon carbide possesses oustanding properties such as a wide band-gap, high thermal conductivity, good chemical stability and high saturated electron drift velocity that constitute such a significant improvement over conventional semiconductor materials that many potential applications are envisaged. However, while some applications have already been realized, issues relating to crystalline defects remain a barrier to the successful realization of several others. The central focus of this thesis is to study defect structures in SiC bulk crystals, epilayers and devices using synchrotron x-ray topography as well as other characterization techniques. The goals of the studies are to understand the behavior and nucleation mechanisms of various defects and their mutual interactions in SiC bulk crystals, epilayers and devices so as to design strategies to mitigate their negative effects by either reducing their densities or completely eliminating them. The following in-depth studies have been carried out:

I) Chemical vapor deposition growth and characterization of silicon carbide homo-epitaxial layers. Homo-epitaxial silicon carbide layers were grown by low pressure chemical vapor deposition using halide precursors. Growth processes were carried out using different growth parameters, e.g., temperatures and gas flow rates. Thermodynamic process was studied using a simple equilibrium model. The surface morphology and defect structures in the grown epilayers were investigated using scanning electron microscopy, optical microscopy, high-resolution x-ray diffraction and x-ray topography.

II) Investigation of the interactions between basal plane dislocations and threading dislocations and the formation mechanisms of low angle grain boundaries. The interactions between basal plane dislocations and threading dislocations as well as the formation mechanisms of low angle grain boundaries were studied using synchrotron white beam x-ray topography. The threading screw dislocations act as effective pinning points for the basal plane dislocations, while the threading edge dislocations do not. Threading edge dislocation walls act as obstacles for the glide of basal plane dislocations

and aggregation of basal plane dislocations is observed. Interactions between the distributions of basal plane dislocations can induce the formation of low angle grain boundaries. Two cases were observed: (1) where edge type basal plane dislocations of opposite sign are observed to aggregate together to form basal plane tilt boundaries and (2) where similar aggregation occurs against pre-existing prismatic tilt boundaries thereby contributing some basal plane tilt to the boundaries.

III) Investigation of the interaction between advancing Shockley partial dislocations and threading dislocations in silicon carbide bipolar devices. The interaction between the advancing Shockley partial dislocations and threading dislocations in silicon carbide bipolar devices was studied and a novel interaction mechanism was proposed. The advancing Shockley partial dislocations are able to cut through threading edge dislocations without generating any trailing dislocation segments. However, when the advancing Shockley partial dislocation encounters a threading screw dislocation, a prismatic stacking fault is nucleated via the cross-slip and annihilation of partial dislocation dipole. This configuration is sessile and precludes the further formation of double stacking faults which would be even more detrimental to device performance than the single stacking faults.

IV) Determination of the dislocation sense of micropipes. The dislocation sense of micropipes has been studied. The ray-tracing method has been carried out to simulate the (11-28) grazing-incidence synchrotron white beam x-ray topographic images of micropipes. The white elliptical features are canted to one or the other side of the reflection vector, depending on the handedness of the micropipes, which provides a simple, non-destructive and reliable way to reveal their senses.

V) Determination of the dislocation sense of closed-core threading screw dislocations. The handedness of closed-core threading screw dislocations was studied. Ray-tracing simulation indicates that the sense of the threading screw dislocations can be revealed based on the position of the thickened dark contrast in their x-ray topographic images. “Small Bragg angle” back-reflection x-ray topography has been carried out to validate our argument. Complete agreement between the results from grazing-incidence x-ray topography and “small Bragg angle” back-reflection x-ray topography proves that either method provides a simple, non-destructive and unambiguous way to reveal the sense of closed-core threading screw dislocations.

VI) Determination of the character of threading edge dislocations in silicon carbide. X-ray topographic images of threading edge dislocations were studied. Six types of threading edge dislocations were first observed in x-ray topography and their Burgers vectors can be determined from a single (11-28) grazing-incidence x-ray topograph, based on the simulation using ray-tracing method. Their Burgers vectors can be further verified by an additional equivalent (-12-18) reflection and a dislocation half loop containing two threading edge dislocation segments. The threading edge dislocation arrays are tending to orient along <1-100> directions and the Burgers vectors of the individual threading edge dislocations are perpendicular to the arrays, which is expected to minimize the total strain energy.

VII) Determination of the core-structure of Shockley partial dislocations. The core-structure of Shockley partial dislocations was studied. The contrast variation between mobile and immobile partial dislocations in x-ray topography has been ascribed to the focusing or defocusing of diffracted x-ray beams, due to the concave or convex shaped basal planes caused by the displacement field associated with the edge component of the partial dislocation. The core structure can be subsequently revealed by the contrast difference between C-core and Si-core partial dislocations and it is consistent with previous report that mobile partial is Si-core while immobile partial is C-core.

VIII) Assessment of the susceptibility of basal plane dislocations to recombination enhanced dislocation glide. The susceptibility of basal plane dislocations to the recombination enhanced dislocation glide process was studied. The susceptibility of the basal plane dislocations to recombination enhanced dislocation glide process is determined by the angle θ between the dislocation line direction with respect to its Burgers vector. The basal plane dislocations with $30^o<\theta<150^o$ are most detrimental, as both partials are mobile and can advance under forward bias. If $-30^o<\theta<30^o$ or $150^o<\theta<210^o$, only one partial advances. Both partials are immobile if $210^o<\theta<330^o$. Experimental observations are consistent with our argument.

IX) Investigation of the conversion of threading screw dislocation into Frank-type stacking faults in chemical vapor deposition grown epilayers. The conversion of threading screw dislocations into Frank-type stacking fault in chemical vapor deposition grown epilayers was studied. They are bounded by two Frank partial dislocations with Burgers vectors ½[0001] and the fault vectors are the same as the Burgers vectors of the bounding partials. They can be nucleated via the overgrowth of vicinal steps on top of threading screw dislocation spirals.

X) Development of SMART (Strain/Stress Mapping Analysis via Ray-Tracing): a technique for the mapping of stresses in single crystals. A new technique (Strain/Stress Mapping Analysis via Ray-Tracing, "SMART") based on ray-tracing principle, has been invented to map the strain/stress tensor in any single crystals. The theoretical background and examples have been discussed.

Table of Contents

List of Acronyms

AFM	atomic force microscope
BPD	basal plane dislocation
CVD	chemical vapor deposition
FWHM	full width at half maximum
HRXRD	high-resolution x-ray diffraction
LAGB	low angle grain boundary
MP	micropipe
PD	partial dislocation
PVT	physical vapor transport
REDG	recombination enhanced dislocation glide
SEM	scanning electron microscope
SF	stacking fault
SWBXT	synchrotron white beam x-ray topography
TED	threading edge dislocation
TEM	transmission electron microscope
TSD	threading screw dislocation
XRT	x-ray topography

List of Symbols

μ	shear modulus (J/m^2)
γ	surface energy, or stacking fault energy (J/m^2)
ν	Poisson's ratio
χ_h	electrical susceptibility
ξ_h	extinction length
σ	stress (N/m^2)
ε	strain
$\boldsymbol{b}$	Burgers vector (m)
$\boldsymbol{u}$	displacement vector (m)
$\boldsymbol{s}$	wave vector (m^{-1})
$\boldsymbol{n}$	plane normal
$\boldsymbol{l}$	line direction of the dislocation
$\boldsymbol{g}$	reflection vector
$\boldsymbol{R}$	stacking fault vector (m)
(uvw)	factional coordinates of atom in the unit cell
(hkl)	miller indices
F_{hkl}	structure factor of (hkl) reflection
f	atomic scattering factor
Φ_0	incident angle (angle between incidence beam and sample surface)
Φ_h	exit angle (angle between exit beam and sample surface)
r_e	classical electron radius (m)
λ	wavelength (m)
V	unit cell volume (m^3)
K	equilibrium coefficient

**Bold italic symbols are vectors*.

List of Figures

List of Tables

Acknowledgments

First I would like to give my deep and sincere gratitude to Prof. Michael Dudley, my Ph.D. advisor, for providing me this opportunity to work in the crystal growth and characterization field. His wide knowledge and helpful guidance have been of great value for me. His understanding, encouragement and personal guidance have provided an excellent basis for my Ph.D. research. Without a doubt his contributions have helped me earn my recent President's Award to Distinguished Doctoral Students.

Second, I would like to thank my wife, Mrs. Yan Lu, for her great assistance during my Ph.D. study. Without her, I would not have been able to spend so much time on my research and attain so many results.

I also owe Dr. Xianrong Huang for his instructive discussions regarding both experiment and theory. I also thank him for his help in doing the monochromatic topography at the Advanced Photon Source.

I would like to thank Prof. Richard J. Gambino and Dr. Shaoping Wang for being my dissertation committee members and their valuable advice.

Thanks are also given to Dr. Hidekazu Tsuchida and Dr. Isaho Kamata from Central Research Institute of Electrical Power Industry in Japan, for the helpful discussion, especially for the topic covered in Chapter 12. I also thank Dr. Robert Stahlbush for supplying very useful samples, electroluminescence images and instructive discussion regarding the results.

I would also like to thank my colleagues: Ms. Hui Chen, Mr. Ning Zhang, Dr. Balaji Raghothamachar, Dr. Govindhan Dhanaraj, Dr. Guan Wang and Dr. Jie Bai for their help during my research.

This work is supported in part by ONR grants N0001140010348, N000140110302 and N000140211014 (contract monitor Dr. Colin Wood) and by Dow Corning Corporation under contract numbers N0001405C0324 and DAAD1701C0081. Topography experiments were carried out at the Stony Brook Synchrotron Topography Facility, Beamline X-19C, at the NSLS (Contract no. DE-AC02-76CH00016) and Beamline XOR-33BM/UNI-CAT, Advanced Photon Source, Argonne National Laboratory. The XOR/UNI-CAT facility is supported by the U.S. Department of Energy under Award No. DEFG02-91ER45439. The APS is supported by the U.S. Department of Energy, Office of Science, Office of Basic Energy Sciences, under Contract No. DE-AC02-06CH11357.

Publications

1. **Y. Chen**, N. Zhang, X. R. Huang, D. R. Black, and M. Dudley, "Studies of the Distribution of Elementary Threading Screw Dislocations In 4H Silicon Carbide Wafer", **Mater. Sci. Forum** 2008 (in press)
2. **Y. Chen,** M. Dudley, E. K. Sanchez, and M. F. MacMillan, "Sense Determination of Micropipes via Grazing-incidence Synchrotron White Beam X-ray Topographyin *4H*-Silicon Carbide", **Mater. Sci. Forum** 2008 (in press)
3. **Y. Chen,** R. Balaji, M. Dudley, M. Murthy, J. A. Freitas Jr., and S. Maximenko, "Mapping of Defects in Large-Area Silicon Carbide Wafers via Photoluminescence and its Correlation with Synchrotron White Beam X-ray Topography", **Mater. Sci. Forum** 2008 (in press)
4. **Y. Chen,** M. Dudley, K. X. Liu, J. D. Caldwell, and R. E. Stahlbush, "Synchrotron X-ray Topographic Studies of Recombination Activated Shockley Partial Dislocations in *4H*-SiC Epitaxial Layers", **Mater. Sci. Forum** 2008 (in press)
5. M. F. MacMillan, E. K. Sanchez, M. Dudley, **Y. Chen,** and M. J. Loboda, "Micropipe Dissociation Through Thick n+ Buffer Layer Growth", **Mater. Sci. Forum** 2008 (in press)
6. M. Dudley, **Y. Chen**, and X. R. Huang, "Aspects of Dislocation Behavior in SiC", **Mater. Sci. Forum** 2008 (in press)
7. P. Wu, M. Yoganathan, I. Zwieback, **Y. Chen**, and M. Dudley, "Characterization of Dislocations and Micropipes in *4H* n+ SiC Substrates", **Mater. Sci. Forum** 2008 (in press)
8. I. Kamata, M. Nagano, H. Tsuchida, **Y. Chen** and M. Dudley, "High Resolution Topography Analysis on Threading Edge Dislocations in *4H*-SiC Epilayers", **Mater. Sci. Forum** 2008 (in press)
9. R. Wang, R. Ma, G. Dhanaraj, **Y. Chen** and M. Dudley, "Computational Study of SiC Halid Chemical Vapor Deposition System", Proceedings of ASME 2007 International Mechanical Engineering Congress and Exposition
10. **Y. Chen,** N. Zhang, M. Dudley, J. D. Caldwell, K. X. Liu, and R. E. Stahlbush "Investigation of Electron-hole Recombination Activated Partial Dislocations and Their Behaviors in *4H*-SiC Bipolar Devices", **J. of Electronic Materials** (in press)
11. **Y. Chen**, M. Dudley, E. K. Sanchez, and M. F. MacMillan, "Simulation of Grazing-Incidence Synchrotron White Beam X-ray Topographic Images of Micropipes in *4H*-

SiC and Determination of Their Dislocation Senses", **J. of Electronic Materials** (in press)

12. **Y. Chen**, and M. Dudley, "Direct Determination of Dislocation Sense of Closed-core Threading Screw Dislocations Using Synchrotron White Beam X-ray Topography in *4H* Silicon Carbide", **Appl. Phys. Lett. 91,** 141918 (2007)
13. **Y. Chen**, G. Dhanaraj, M. Dudley, E. K. Sanchez, and M. F. MacMillan, "Sense Determination of Micropipes via Grazing-incidence Synchrotron White Beam X-ray Topography in *4H* Silicon Carbide", **Appl. Phys. Lett. 91**, 071917 (2007)
14. X. R. Huang, D. R. Black, A. T. Macrander, J. Maj, **Y. Chen,** and M. Dudley, "High-geometrical-resolution Imaging of Dislocations in SiC Using Monochromatic Synchrotron Topography", **Appl. Phys. Lett. 91**, 231903 (2007)
15. **Y. Chen**, M. Dudley, K. X. Liu, and R. E. Stahlbush, "Interaction between Basal Stacking Faults and Threading Dislocations in *4H*-Silicon Carbide PiN Diode", **Mater. Res. Soc. Symp. Proc., 0994,** 0994-F12-03 (2007)
16. **Y. Chen**, M. Dudley, K. X. Liu, and R. E. Stahlbush, "Observations of the Influence of Threading Dislocations on the Recombination Enhanced Partial Dislocation Glide in *4H*-Silicon Carbide Epitaxial Layers", **Appl. Phys. Lett., 90**, 171930 (2007)
17. **Y. Chen**, H. Chen, N. Zhang, M. Dudley, and R. Ma, "Investigation and Properties of Grain Boundaries in Silicon Carbide", **Mater. Res. Soc. Symp. Proc., 955E,** 0955-I07-50 (2007)
18. G. Dhanaraj, **Y. Chen**, M. Dudley, and H. Zhang, "Chemical Vapor Deposition of Silicon Carbide Epitaxial Films and their Characterization", **J. Electron. Mater. 35,** 1513-1517 (2007)
19. **Y. Chen**, G. Dhanaraj, W. Vetter, R. Ma, and M. Dudley, "Behavior of Basal Plane Dislocations and Low Angle Grain Boundary Formation in Hexagonal Silicon Carbide", **Mater. Sci. Forum 556-557,** 231 (2007)
20. H. Chen, G. Wang, **Y. Chen,** and M. Dudley, "The Formation Mechanism of Carrot Defect in Silicon Carbide", **Mater. Res. Soc. Symp. Proc. 911,** 0911-B05-24, 163-168 (2006)
21. G. Dhanaraj, **Y. Chen**, M. Dudley et al., "Growth Mechanisms and Dislocation Characterization of SiC Epitaxial Films", in "Silicon Carbide – Materials, Processing, and Devices", M. A. Capano, M. Dudley, T. Kimoto, and A. R. Powell (Eds.), **Mater. Res. Soc. Symp. Proc. 911,** 0911-B05-27, 157-162 (2006)

22. **Y. Chen**, G. Dhanaraj, M. Dudley et al., "Multiplication of Basal Plane Dislocations via Interaction with c-axis Threading Dislocations in *4H*-SiC", in "Silicon Carbide – Materials, Processing, and Devices", M. A. Capano, M. Dudley, T. Kimoto, and A. R. Powell (Eds.), **Mater. Res. Soc. Symp. Proc. 911,** 0911-B09-04, 151-156 (2006)
23. R. Wang, R. Ma, G. Dhanaraj, **Y. Chen** and M. Dudley, "Modeling of Halide Chemical Vapor Deposition of SiC", Proceedings of ASME 2006 International Mechanical Engineering Congress and Exposition
24. **Y. Chen**, G. Dhanaraj, and M. Dudley, "Thermodynamic Studies of Carbon in Liquid Silicon Using Central Atoms Model", **J. Am. Ceram. Soc. 89**, 2922-2925 (2006)
25. **Y. Chen,** G. Dhanaraj, H. Chen, M. Dudley and H. Zhang, "Chemical Vapor Deposition and Defect Characterization of SiC Epitaxial Films", in "Progress in Semiconductor Materials V – Novel Materials and Electronic and Optoelectronic Applications, L. J. Olafsen, A. Saxler, M. C. Wanke, and R. M. Biefield (Eds.), **Mater. Res. Soc. Symp. Proc. 891,** 0891-EE12-11.1-11.6 (2006)
26. G. Dhanaraj, **Y. Chen**, M. Dudley, B. Wu, and H. Zhang, "Growth and Surface Morphology of *6H*-SiC Bulk and Epitaxial Crystals", **Mater. Sci. Forum 527-529**, 67-70 (2006)
27. G. Dhanaraj, M. Dudley, **Y. Chen**, B. Raghothamachar, B. Wu and H. Zhang, "Epitaxial Growth and Characterization of Silicon Carbide Films", **J. of Crystal Growth 287,** 344 (2006)

Fields of Study

This section summarizes my major research accomplishments. Many aspects of the defect structures in silicon carbide bulk crystals, epilayers and devices have been studied in depth. Based on the numerous results obtained during my research, the most significant accomplishments which are expected to have the biggest impact on the crystal growth process and the quest for defect density reduction as well as those constituting major contributions to techniques for characterization are summarized below.

1) Detailed quantitative studies were carried out of Frank-type stacking faults. This enabled the proposal of a new method which can be used to significantly reduce the density of threading screw dislocations in silicon carbide crystals. A threading screw dislocation can be converted into Frank faults plus Frank partial dislocations during chemical vapor deposition on vicinal substrates. This conversion process has a major compact on the improvement of crystal quality. It potentially provides a way to significantly reduce the density of threading screw dislocations, or even eliminate them in silicon carbide crystals.

2) A technique was developed which can be used to reveal the dislocation sense of closed-core threading screw dislocations in physical vapor transport grown silicon carbide crystals unambiguously and non-destructively. This technique can be used to map the dislocation sense of threading screw dislocations in commercial silicon carbide wafers easily and unambiguously. The dislocation sense of threading screw dislocations provides crucial information regarding their formation mechanism.

3) A new technique was invented, Strain/Stress Mapping Analysis via Ray Tracing (SMART), together with my colleagues. Residual strain/stress in silicon carbide crystals contains crucial information regarding the growth process and SMART can be used to map the full strain/stress tensor in commercial silicon carbide wafers in a simple and non-destructive way. This technique can also be used for any single crystal materials.

4) The ray-tracing simulation technique for interpreting dislocation images x-ray diffraction topography was significantly expanded. Ray-tracing simulation provides an extremely simple and effective way to qualitatively and quantitatively interpret topographic images of defects. The application of ray-tracing principle has been largely expanded by compiling the simulation process using Mathematica® and used in revealing the character of various defects in silicon carbide. This study will eventually facilitate clarifying the fundamental scientific principles governing contrast formation mechanisms for defect images in x-ray diffraction topography.

1. Introduction

Silicon carbide (SiC) is steadily replacing conventional semiconductor materials, e.g., silicon (Si) and gallium arsenide (GaAs), under certain extreme applications due to its outstanding properties such as high thermal conductivity, high breakdown voltage and high saturated electron drift velocity. The thermal conductivity of SiC is ~2 times higher than Si, the breakdown field is ~18.5 times the one of Si and the saturated electron drift velocity is twice that of the Si. The comparison of some properties between Si and *6H*-SiC is listed in Table 1.

Table 1. Comparison of the properties between Si and *6H*-SiC.

	E_g(eV)	T_w(K)	k (W/cm·K)	μ_e (cm^2/V·s)	μ_h (cm^2/V·s)	E_b (10^5V/cm)	V_s (10^7cm/s)
Si	1.12	410	1.5	1400	600	2	1
6H-SiC	3.0	1200	5	370	90	37	2

E_g: band gap; T_w: working temperature; k: thermal conductivity; μ_e: electron mobility; μ_h: hole mobility; E_b: breakdown field; V_s: saturated carrier velocity.

SiC is noted for its large number of polytypes. Up to now, more than 200 types of phases of SiC have been found. The first SiC structure found is *15R*: the same Si-C bilayer repeats every 15 layers with rhombohedral structure, which was labeled arbitrarily as type I; the second one is the hexagonal structure with six-layer repetition labeled as type II; the third one found is 4-layer hexagonal structure labeled as type III. The cubic structure was the fourth one to be discovered, which was naturally labeled as type IV. When more and more structures of SiC were found, it was impractical to keep using this labelling method. L. S. Ramsdell found that the basic unit that SiC is composed of (close-packed Si-C bilayer) is the same for the structures already found and possibly the same for the future structures. The polytypes come from different stacking sequences of the Si-C bilayers. Therefore, Ramsdell created a labelling principle to define the structures already discovered and even for potential structures to be discovered in the future.[1] The label is composed of a number which indicates the number of bilayers in the repeat unit followed by a letter C, H or R corresponding to cubic, hexagonal or rhombohedral. This is currently the most commonly used nomenclature for polytypes. The polytypes we are interested in are *4H* and *6H*-SiC. Although *3C*-SiC is a commonly observed polytype, we are not going to discuss in detail here because no large-size and high-quality *3C*-SiC can currently be grown. Figure 1 shows the projection of the structures of *4H* and *6H*-SiC onto (11-20) plane. We can see that the stacking sequence is "ABCBABCB…" for *4H*-SiC and "ABCACBABCACB…" for *6H*-SiC.

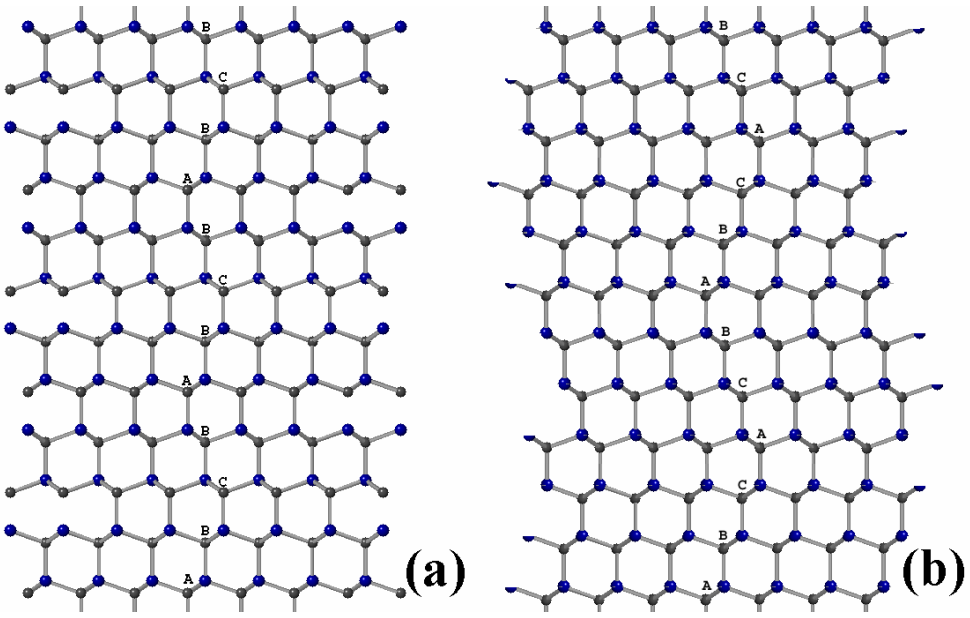

Figure 1. Projection of *4H*-SiC (a) and *6H*-SiC (b) structure into (11-20) plane. Small and large balls indicate C and Si atoms, respectively. The stacking sequences are "ABCB…" and "ABCACB…" for *4H* and *6H*-SiC, respectively.

The different stacking sequences of Si-C pairs are also related to the different densities of state of electrons and hence different properties. Knippenberg has demonstrated that, for short period structures such as *4H*, *6H*, *8H* and *15R*, they are controlled by the growth temperature, which means the short period structures can be explained by energy difference.[2] For long period structures, there is no evidence showing that they are thermodynamically stable. Frank[3] and Jagodzinski[4] presented two possible explanations from screw-dislocation and vibration entropy theory which are supported by experiments more than others, but experimental results that contradict these theories still exist. The influence of polarity of the substrates on the polytype is also reported: usually *6H* SiC crystals are grown on the (0001) Si face of *6H* SiC seed, whereas G. Augustine et al. found *4H* crystals were grown on the (0001) C face of *6H* crystal.[5]

SiC has extremely high melting point but it sublimes before it melts (see Figure 2 for the phase diagram of C-Si system). Therefore, it is not feasible to grow SiC single crystals from the melt (e.g., Czochralski or Bridgman method). The commonly used technique for growing commercial SiC wafers is physical vapor transport (PVT, also called seeded modified Lely growth) and it was first carried out by Tairov and Tsvetkov in 1978.[6] In PVT growth, a growth temperature as high as 2300^{o}C is used and a temperature gradient is applied between the source (high-purity SiC powder) and seed. The high-purity SiC powder decomposes at the higher temperature end in the form of gaseous species and deposits as single crystals at the lower temperature end. The detailed growth process is not going to be discussed here and further information can be referred to a review by Chaussende *et al*.[7]

.

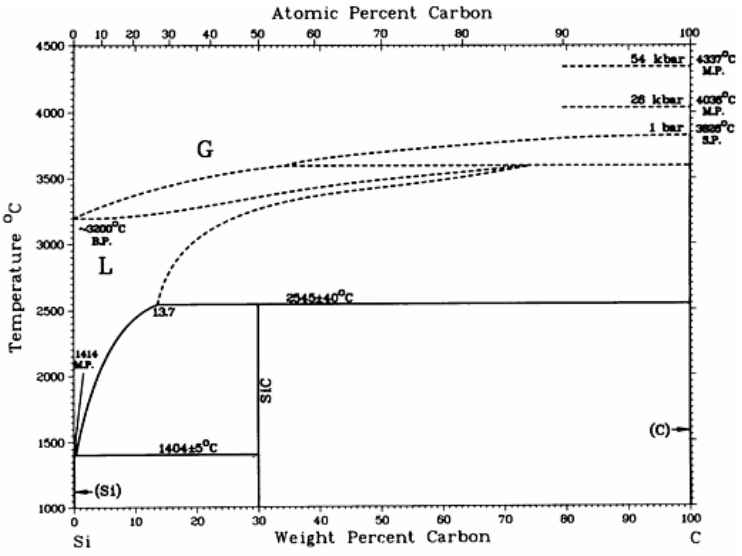

Figure 2. Phase diagram of C-Si.[8] Peritectic point indicates that it is unfeasible to grow SiC from melt.

1.1. Current understanding of defect structures in SiC

3-inch SiC wafers have been commercially available from several vendors (e.g., Dow Corning Compound Semiconductor Solutions, Cree Inc., II-VI Wide Band-Gap and SiCrystal AG) since 2001 while 4-inch wafers recently came on the market. However, the defect density in SiC is still high compared with conventional semiconductor materials. Currently, the defect density in SiC ranges from $10^4/cm^2$ to $10^6/cm^2$. Defects in SiC wafers can be grouped into two categories: growth-induced defects and stress-induced defects. We are going to briefly introduce the current understanding of the two types of defects in the following session.

1.1.1. Growth dislocations

Growth dislocations are observed in crystals grown from vapor, melt, solution and flux.[9] They are formed during growth via the replication of dislocations which thread the moving crystal growth front or interface. The dislocations threading the growth interface can originate from processes such as (a) the continuation of dislocations already present in the seed; (b) the relaxation of stresses arising from handling damage on the surface of the seed; and (c) the relaxation of stresses arising from the incorporation of inclusions of solvent or impurity which can occur on the seed surface or later during growth which can equivalently be viewed as imperfect lattice closure around such inclusions; (d) the relaxation of stresses arising from coalescence between two or more mis-oriented growth centers (for example, spiral hillocks associated with screw dislocations). A further mechanism involving imperfect lattice closure occurring during overgrowth of surface regions exhibiting step-bunching will also be briefly mentioned.

The prime example of the growth dislocation in PVT-grown SiC is the screw dislocation aligned along or close to the *c*-axis, which can have a hollow core (micropipe, MP) or closed core (threading screw dislocation, TSD) depending on the magnitude of the Burgers vector.[10] The hollow core is nucleated to minimize the energy between the

strain energy and surface energy inside the hollow core according to Frank's law.[3] These dislocations have been routinely observed to replicate from the seed. In addition they can be generated in opposite-sign pairs at inclusions.[11] Synchrotron white beam x-ray topography (SWBXT), in conjunction with simulations based on the ray-tracing principle has been used extensively to image MPs and TSDs revealing the magnitude and sign of their Burgers vectors.[12-15]

One possible mechanism for the nucleation of MPs and TSDs involves the imperfect lattice closure experienced during overgrowth of inclusions.[11] Conservation of Burgers vector dictates that this mechanism must ordinarily produce the dislocations in opposite sign pairs. An example where single MPs rather than opposite-sign pairs can be produced involves the nucleation of screws at polytype inclusions. An example is shown in Figure 3 which shows a *15R* inclusion in a *6H*-SiC wafer that was cut parallel to the [0001] growth direction. The *15R* nature of the inclusion was confirmed by detailed synchrotron Laue pattern analysis [Figure 3(b)]. It can be seen that the inclusion causes the termination of many TSDs on its lower side. However, since Burgers vector must again be conserved, the net Burgers vector terminated on the lower side must be continued on the upper side as the *6H*-SiC overgrows the inclusion. This has a tendency to concentrate the net Burgers vector into a few large Burgers vector screw dislocations as observed on Figure 3. Effects similar to this were previously observed in the overgrowth of hexagonal voids.[16] It seems also likely that step bunching effects occurring on the curved extremities of the approximately lens shaped inclusions may lead to further generation of screw dislocations with accompanying Frank partials and faults.[17]

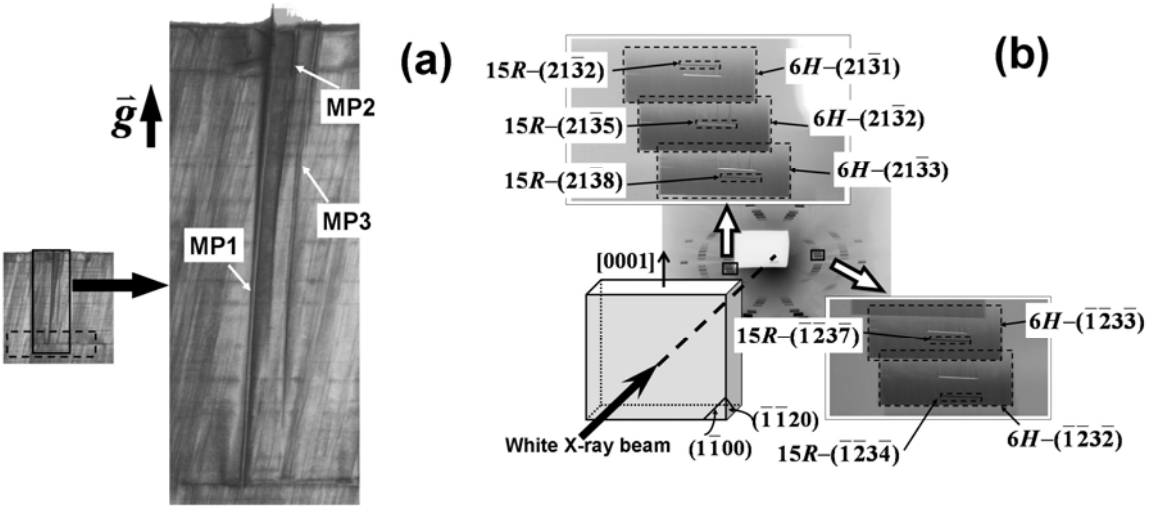

Figure 3. (a) XRT showing nucleation of MP in *6H*-SiC at the *15R* polytype inclusion. (b) Identification of *15R* type inclusion by transmission Laue pattern. Pseudo-hexagonal indices are used for *15R*-SiC.

Another possible mechanism for the nucleation of *c*-axis screw growth dislocations is based on considerations of the differences in local flow rates of the two kinds of advancing demi-steps (exposing either single or double dangling bonds) which exist in vicinal regions of the often dome-shaped growth front.[18] Consideration of such inhomogeneous step flow rates in addition to potential local variations in supersaturation

can lead to significant, inhomogeneous step bunching which when overgrown can lead to lattice closure failure parallel to the *c*-axis which and the nucleation of a screw dislocation. Since Burgers vector must be conserved this requires that the dislocation be nucleated in a form of quarter loop with the screw dislocation running along the *c*-axis and a Frank fault separating two Frank partials being created on the basal plane and emerging on the advancing vicinal step. This is similar to the simultaneous nucleation of screw dislocation/Frank partial pairs at particular demi-step configurations close to the cores of pre-existing threading screw dislocations.[19]

Also included in the category of growth defects generated at the moving growth front are threading edge dislocations (TEDs, the Burgers vectors of which has been analyzed[20] and the details can be seen in Chapter 9) aligned along the *c*-axis which often aggregate into low angle grain boundaries (LAGBs) oriented parallel to {11-20}. These we argue are formed to relax stresses arising from coalescence between two or more growth centers (for example, spiral hillocks associated with screw dislocations) which are mutually mis-oriented about the *c*-axis [see Figure 4(a)]. This mis-orientation can arise from stresses resulting from thermal gradients in either the radial or circumferential directions. Radial gradients can lead to mutual tilt between spiral hillocks located at adjacent positions on the same circumference leading to the formation of circumferential LAGBs. In a similar way, circumferential gradients can generate tilt between hillocks located adjacent to each other on the same radius leading to the formation of radial LAGBs. Typical calculations indicate that the thermal stresses can generate tilts between the growth centers of the order of a few arc seconds. When the spiral hillocks broaden and impinge on each other, they can either elastically deform to accommodate the lattice tilts or a LAGB can be nucleated. It is proposed here that a LAGB is preferentially formed due to the higher energy associated with the elastic deformation. We also propose that the dislocations associated with the LAGB are formed in a sequential manner as the coalescing faces of the two growth centers merge. In order to enable conservation of Burgers vector, we propose that the dislocations nucleate in the form of quarter loops, as shown in Figure 4(b). These quarter loops comprise the TED segment which exits the top face of the coalescing front and a BPD segment which exits the front face. This quarter loop nucleation is then repeated as the islands coalesce further. The TED segments replicate with growth and their aggregates form the frequently observed LAGBs. Since their line directions are perpendicular to the easy glide system in SiC they are expected to be immobile. The BPD segments also replicate with lateral growth. However, since these segments belong to the primary slip system of SiC, they are expected to become mobile under the thermal stresses existing immediately following growth or during post-growth cooling. An example showing some curved BPDs anchored at one end to a TED wall is shown in Figure 5.

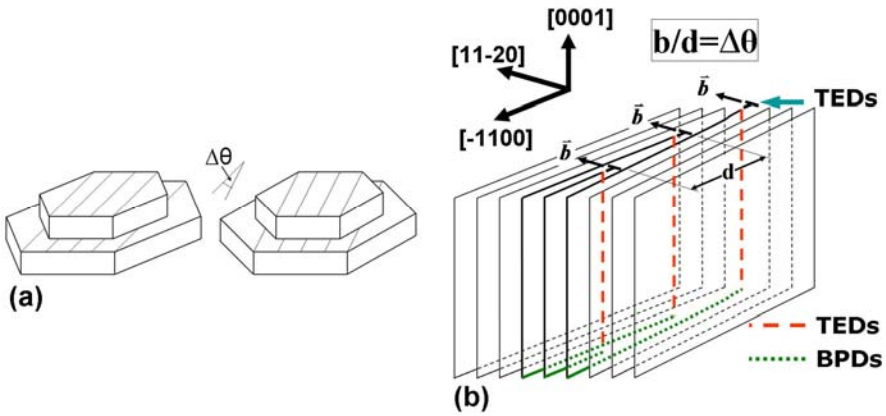

Figure 4. (a) Two growth centers are misoriented. (b) Quarter loops are nucleated when the growth centers impinge.

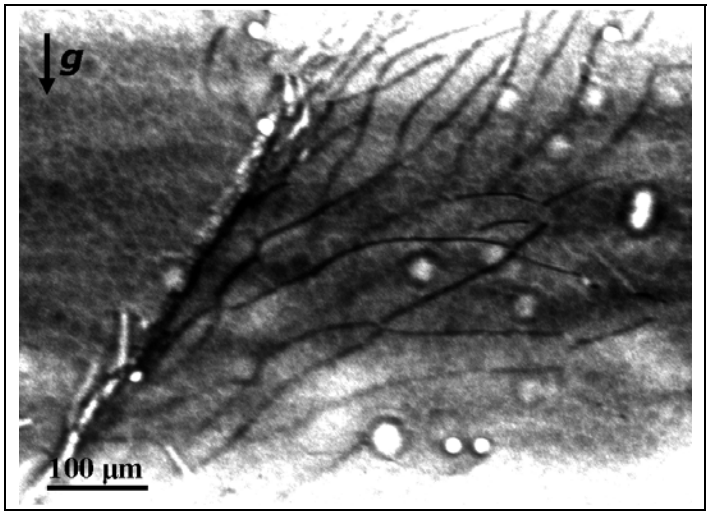

Figure 5. An example of some BPDs anchored at one end to a TED wall.

As in the case of bulk growth, in CVD growth all dislocations which thread the seed interface are expected to be replicated in the epilayer. Observations indicate that the vast majority of the TSDs in the seed are replicated in the epilayer. However, since the substrates are vicinal in nature, the step flow disturbances which can arise due to the interaction between the flowing vicinal demisteps and the spiral demisteps associated with screw dislocations can lead to other possibilities. For example, TSDs can be redirected [21] or deflected onto to the basal plane in the form of a Frank fault bounded by two Frank partials with the same Burgers vector as the original screw.[19] If hydrogen etching exposes the intersection of a faulted BPD with the TSD, similar to the model previously presented for carrot defect formation[22], then an in-plane component will be added to the Frank fault and Frank partials. This is to be discussed in detail in Chapter 12.

The off-cut nature of the seeds (by either 8^{o} or 3.5^{o} for *4H*-SiC) means that BPDs also intersect the growth interface and can be replicated during CVD growth. If the BPDs are in screw orientation, with Burgers vector parallel to the offcut direction, they can propagate in the same orientation into the epilayer. It is also possible for the BPDs to be redirected closer to the overall growth direction such that they are converted into TEDs.[23]

1.1.2. Stress induced dislocations

Plastic deformation induced dislocations are widely observed in PVT grown boules of SiC. The primary slip system in SiC comprises slip on the basal plane in the close packed 1/3<11-20> directions although slip dislocations are often observed to be dissociated into Shockley partials separated by a Shockley fault. Pirouz *et al* have shown that these slip systems persist even when attempts were made to deliberately induce slip on alternate systems.[24] Our observations indicate that these dislocations nucleate primarily in the highly strained outer regions of the boule and become mobile and expand toward the interior of the boule under the action of shear stresses on the basal plane. These shear stresses arise from nonlinearities in the axial thermal gradient.[25] The dislocation nucleation in the outer regions most probably arises from differential thermal expansion effects between polycrystalline and polytype inclusions leading to the generation of further shear stress concentrations. Many dislocations will naturally exist at the interfaces between the polycrystalline grains and those which have segments favorably oriented will expand under stress. Some of these will propagate towards the polycrystalline exterior where they will run into other grain boundaries but others will penetrate in the form of half loops into the crystal interior. Some evidence in support of this can be found from transmission topographs recorded from the outer regions of a thinned down wafer as shown in Figure 6 which shows half loops expanding from a small polycrystalline inclusion. Note that, as is usually the case, the dislocations appear undissociated on these topographs. They are, in fact, most probably dissociated but the width of the stacking fault, which is typically around 33 nm for *4H*-SiC, is beyond the resolution of our technique. On the topographs, these narrowly spaced Shockley partials appear as a single undissociated BPD exhibiting the sum of the Shockley partial Burgers vectors, i.e. 1/3<11-20>. Figure 7 shows a back-reflection topograph recorded with monochromatic synchrotron radiation. Analysis of the white contrast associated with all of the approximately concentric half-loops expanding towards the interior of the wafer (based on the ray-tracing principle) demonstrates that they are all of the same sign[29], consistent with the prediction of our model.

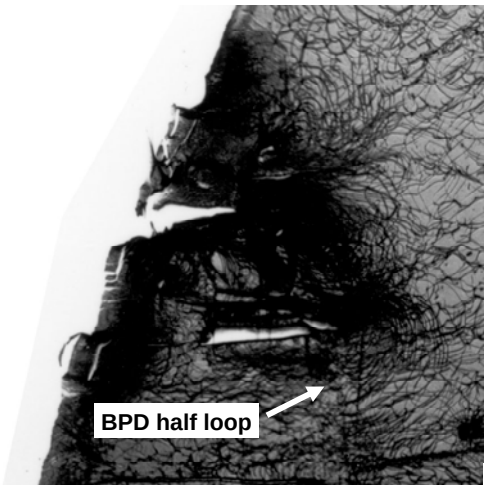

Figure 6. Transmission topograph showing the half loops expanding from a small polycrystalline inclusion.

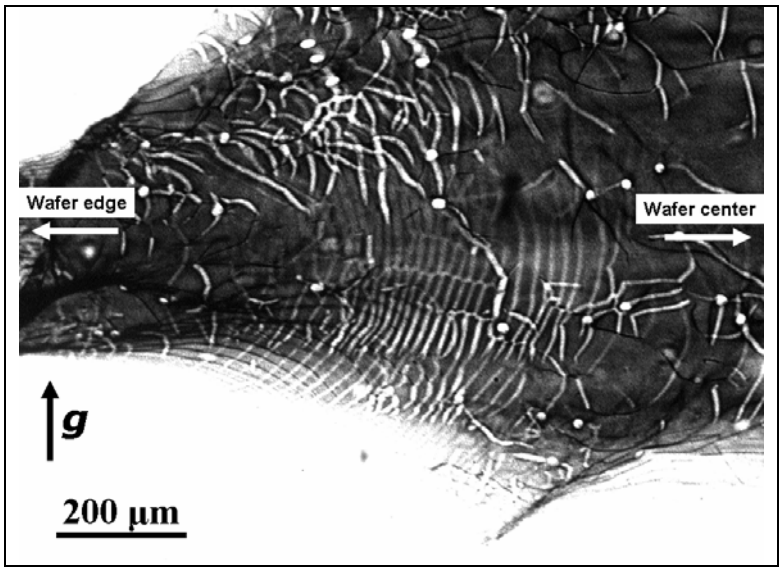

Figure 7. A monochromatic back-reflection topograph demonstrating that the concentric same-sign half-loops are expanding towards the interior of the wafer.

Dislocations in SiC-based devices can be active under electrical stressing due to the energy from electron-hole recombination. Mobility of BPDs under mechanical stress is generally not observed in CVD grown epilayers. This can probably be attributed to the lower growth temperature (compared to PVT) and the attendant increase in critical resolved shear stress. However, in *p-i-n* devices, recombination enhanced dislocation glide (REDG) has been well documented in *4H*-SiC.[26,27] Only those BPDs which are replicated on the basal plane from the substrate become susceptible to REDG while those which have been converted to TEDs are inactive. Synchrotron topography has been applied to the study of the interaction between the mobile partial and the forest of threading dislocations comprising screw and edge types.[28] This will be discussed in Chapter 6. In addition, synchrotron topography can be applied to the determination of the detailed character and sign of the BPDs replicated into the epilayer.[29] The sign and character of the original BPD determines the core structure of the Shockley partials into which it dissociates which in turn determines the susceptibility of the original BPD to REDG[30,31] as will be discussed in Chapter 11.

1.1.3. Extended defects in SiC

In addition to dislocations, other extended defects are widely observed in SiC bulk crystals, epilayers and devices. In bulk crystals, the major extended defects are Shockley-type SFs, Frank-type SFs and LAGBs. BPDs are normally dissociated into Shockley-type SFs, bounded by two Shockley PDs. The equilibrium separation of the two partials is decided by the balance between the stacking fault energy and the repulsive force between the two partials and it is ~33 nm for *4H*-SiC and ~170 nm for *6H*-SiC. While Frank-type PDs have not attracted much attention, the author believes that they are closely related to the nucleation of TSDs, which still needs to be clarified. LAGBs comprise a mixture of dislocations, including BPDs, TEDs and even TSDs/MPs. The strain energy is minimized by particular configurations within this aggregation. Further details are to be discussed in Chapter 5.

Step-controlled growth is often used in SiC epilayer growth due to its advantage in polytype control. Subsequent interactions between the vicinal steps and threading dislocations lead to more complicated extended defects, such as carrot defects[22] and TSD converted Frank-type SFs[19]. In addition, the electrical stressing applied during device operation activates the Shockley partial dislocations and the Shockley-type SFs expand as the Shockley partial advances.

1.2. Motivation

As we discussed earlier, SiC material has been facing serious issues related to various defects existing in the substrates and epilayers, such as MPs, TSDs, TEDs, BPDs, LAGBs consisting of a mixture of defects and SFs.[32-34] MPs are device-killing defects due to the hollow-core associated with them.[35] TSDs play a critical role in maintaining the desired polytype promoting spiral step-flow growth. However, they have been found to degrade device performance, reducing the breakdown voltage by 5-35%.[36] In addition, the forest of TSDs in the as-grown crystal poses a significant barrier which creates a pinning effect on the glide of the BPDs either during growth or post-growth cooling, leading to localized higher densities of BPDs.[37] Furthermore, TSDs have been found to interact with SFs in SiC epitaxial films expanding under forward bias, creating prismatic SFs.[28,38] TEDs play critical roles in the formation of LAGBs and they are also often observed to be converted from BPDs during CVD growth. Being aware of their nature facilitates the understanding of the character of the original BPDs (see Chapter 9). Unconverted BPDs have been observed to be dissociated into partial dislocations and degrade the device performance. The interactions between the advancing PDs and threading dislocations can lead to complex web of dislocations in SiC bipolar devices (see Chapter 6). Various extended defects (carrot defects, triangular defects) have also been observed to pose negative effects on the device performance. Therefore, if one is to be able to exert some control over the defect configurations encountered, this urgently requires a detailed understanding of the observed defect structures and their behavior and origins in SiC bulk crystals, epilayers and devices. Thus the primary motivation for our research in this area is to facilitate the development of strategies to either reduce the densities of the defects or completely eliminate them so as to mitigate their deleterious effects on device performance.

2. Theoretical background

2.1. Fundamentals of x-ray diffraction

X-ray topography is a technique based on the kinematical and dynamical diffraction of x-ray beams while interacting with crystal lattices. When x-ray interacts with very small crystals, kinematical theory provides a good approximation. In kinematical theory, x-ray is assumed to be scattered by atoms only once and the loss of intensity due to re-scattering is negligible. It is commonly used in powder or imperfect crystals and it is also a good approximation for thin perfect crystals where multiple scattering can be ignored. Kinematical diffraction is also a key point in interpreting the topography contrast. In a perfect crystal, the x-ray is diffracted dynamically where multiple scattering occurs. Bloch waves are generated inside the crystals as the x-ray interacts with the periodic crystal lattice and the wave field inside the crystal is the sum of a series of plane waves.[39]

According to the kinematical theory, the diffracted intensity of the x-ray beam is given by[40]:

$$I = F_{hkl}^2 \frac{\sin^2(\pi n_1 q_1)}{\sin^2(\pi q_1)} \cdot \frac{\sin^2(\pi n_2 q_2)}{\sin^2(\pi q_2)} \cdot \frac{\sin^2(\pi n_3 q_3)}{\sin^2(\pi q_3)}, \quad (1)$$

where F_{hkl} is the structure factor, n_i (i = 1,2 or 3) is the number of unit cells along $\boldsymbol{a_i}$ direction ($\boldsymbol{a_1}$, $\boldsymbol{a_2}$, and $\boldsymbol{a_3}$ are unit vectors defining the unit cell) and q_i is the deviation component (in radians) along $\boldsymbol{a_i}$. This equation gives a very good approximation for thin crystals. However, this equation fails for thick crystals. First, it indicates that the diffracted intensity is proportional to the volume of the crystal and it approaches infinity as the crystal becomes thicker and thicker. This clearly disobeys the conservation of energy. However, this equation helps understand the dislocation images arisen from extinction contrast in x-ray topography and this is to be discussed in Section 2.2. Second, the width of the diffraction peak varies inversely with the number of the unit cells according to this equation. Thus, extremely narrow peak is expected for thick crystals. This is contradictory with the experimental observation. For example, assuming a 1 mm-thick defect-free Si wafer, the number of unit cells is 1 mm/ 5.43 Å $\approx 1.84 \times 10^6$, the full width at half maximum should be approximately $1/1.84 \times 10^6$ (radians)=0.11 (arcsec), which is two orders narrower than the actual rocking curve width. Therefore, dynamical diffraction has to be carried out for nearly perfect crystals. In the diffraction theory, a few concepts which are important in interpreting x-ray diffraction topography are briefly introduced below: rocking curve width, the diffracted intensity and penetration depth. We will explain the contrast mechanism of defects in XRT of SiC according to the diffraction theory in the following section.

2.1.1. Rocking curve width

The rocking curve width (FWHM) for perfect crystals is given by[41]:

$$2\delta_{hs} = \frac{2r_e\lambda^2}{\pi V \sin 2\theta_B}\frac{1}{\sqrt{|\gamma|}}|C|\sqrt{F_{hkl}F_{\bar{h}\bar{k}\bar{l}}} \quad \text{(Bragg case)} \tag{2}$$

and

$$2\delta_{os} = \frac{2r_e\lambda^2}{\pi V \sin 2\theta_B}\sqrt{|\gamma|}|C|\sqrt{F_{hkl}F_{\bar{h}\bar{k}\bar{l}}} \quad \text{(Laue case),} \tag{3}$$

where r_e is the classical electron radius, λ is the x-ray wavelength, V is the volume of the unit cell, θ_B is the Bragg angle, γ is the asymmetric ratio, C is the polarization factor (C=1 for σ polarization and C=cos2θ_B for π polarization) and F_{hkl} is the structure factor.

The rocking curve width is critical in studying single crystal materials and it is a key parameter to appraise crystalline quality. The narrower the rocking curve, the higher the crystalline quality. The broadening of the rocking curve can be due to various reasons, such as dislocations, mis-orientation or residual strain. In addition, the extinction contrast, one of the most commonly accepted contrast mechanisms in XRT, is intimately related to the rocking curve width. This is because the rocking curve width determines the volume of the kinematically diffracted region near the dislocation core (the highly deformed region where the normal of crystal lattice falls outside the full width at half maximum of the rocking curve) which subsequently determines the width of the dislocation image. The different intensity from kinematically and dynamically diffracted regions leads to the dislocation images (darkened contrast). Such contrast mechanism of dislocation image is called “extinction contrast” and to be discussed later in this section.

2.1.2. Diffracted beam intensity

The intensity of the diffracted beam determines the intensity of the topographic images and it is a key parameter for us to select the appropriate diffractions for imaging the defects. The diffracted intensity is proportional to the square of the magnitude of the structure factor if no absorption is considered. The rocking curve width is also intimately related to the magnitude of the structure factor, as we can see from Equations (2)and

(3). Therefore, the structure factor is most critical parameter in our studies. The larger the structure factor, the wider the rocking curve and the narrower the dislocatioin image. The structure factor F_{hkl} is defined as[42]:

$$F_{hkl} = \sum_i f_i \exp\{-2\pi \mathrm{i}(\mathrm{hu}+\mathrm{kv}+\mathrm{lw})\}, \tag{4}$$

where f_i is the atomic scattering factor, (hkl) are the miller indices of the reflection plane and (uvw) are the fractional coordinates of the atoms in the unit cell (see Table 2).

Table 2. Fractional coordinates of the Si and C atoms in the unit cell for *4H*- and *6H*-SiC.

	4H-SiC	*6H*-SiC
Si	(0,0,0), (0,0,1/2), (1/3,2/3,3/4),(2/3,1/3,1/4)	(0,0,0), (0,0,1/2), (1/3,2/3,1/3), (1/3,2/3,2/3), (2/3,1/3,1/6), (2/3,1/3,5/6)
C	(0,0,11/16), (0,0,3/16), (1/3,2/3,15/16), (2/3,1/3,7/16)	(0,0,1/8), (0,0,5/8), (1/3,2/3,11/24), (1/3,2/3,19/24), (2/3,1/3,23/24), (2/3,1/3,7/24)

Therefore, the structure factors of *4H*- and *6H*-SiC are given as following:

4H-SiC:

$$F_{hkl}=\sum_i f_i e^{-i2\pi(hu+kv+lw)}$$

$$=f_c(e^{-i2\pi\frac{11}{16}l}+e^{-i2\pi\frac{3}{16}l}+e^{-i2\pi(\frac{1}{3}h+\frac{2}{3}k+\frac{15}{16}l)}+e^{-i2\pi(\frac{2}{3}h+\frac{1}{3}k+\frac{7}{16}l)})+f_{Si}(e^{-i2\pi 0}+e^{-i2\pi\frac{1}{2}l}+e^{-i2\pi(\frac{1}{3}h+\frac{2}{3}k+\frac{3}{4}l)}+e^{-i2\pi(\frac{2}{3}h+\frac{1}{3}k+\frac{1}{4}l)}) \tag{5}$$

and *6H*-SiC:

$$F_{hkl}=\sum_i f_i e^{-i2\pi(hu+kv+lw)}$$

$$=f_c(e^{-i2\pi\frac{1}{8}l}+e^{-i2\pi\frac{5}{8}l}+e^{-i2\pi(\frac{1}{3}h+\frac{2}{3}k+\frac{11}{24}l)}+e^{-i2\pi(\frac{1}{3}h+\frac{2}{3}k+\frac{19}{24}l)}+e^{-i2\pi(\frac{2}{3}h+\frac{1}{3}k+\frac{23}{24}l)}+e^{-i2\pi(\frac{2}{3}h+\frac{1}{3}k+\frac{7}{24}l)})$$

$$+f_{Si}(e^{-i2\pi 0}+e^{-i2\pi\frac{1}{2}l}+e^{-i2\pi(\frac{1}{3}h+\frac{2}{3}k+\frac{1}{3}l)}+e^{-i2\pi(\frac{1}{3}h+\frac{2}{3}k+\frac{2}{3}l)}+e^{-i2\pi(\frac{2}{3}h+\frac{1}{3}k+\frac{1}{6}l)}++e^{-i2\pi(\frac{2}{3}h+\frac{1}{3}k+\frac{5}{6}l)}) \tag{6}$$

The diffracted beam intensity of the commonly used (000*l*) (back-reflection geometry, for both *4H*- and *6H*-SiC), (11-28) (grazing-incidence geometry for *4H*-SiC) is proportional to the square of the magnitude of the structure factor.

4H-SiC (000*l*):

$$F_{000l}=(f_C e^{-i\frac{3}{8}\pi l}+f_{Si})(e^{-i\pi l}+1+e^{-i\frac{3}{2}\pi l}+e^{-i\frac{1}{2}\pi l}) \tag{7}$$

$$\Rightarrow \left|F_{000l}\right|^2=16\left[f_{Si}^2+f_C^2+2f_{Si}f_C\cos\frac{3\pi l}{8}\right]. \tag{8}$$

4H-SiC (11-28):

$$F_{11\bar{2}8}=4(f_{Si}-f_c). \tag{9}$$

$$\Rightarrow \left|F_{11\bar{2}8}\right|^2=16(f_{Si}-f_c)^2. \tag{10}$$

6H-SiC (000*l*):

$$F_{hkl}=\sum_i f_i e^{-i2\pi(hu+kv+lw)}$$

$$= f_c(e^{-i2\pi\frac{1}{8}l} + e^{-i2\pi\frac{5}{8}l} + e^{-i2\pi\frac{11}{24}l} + e^{-i2\pi\frac{19}{24}l} + e^{-i2\pi\frac{23}{24}l} + e^{-i2\pi\frac{7}{24}l}) + f_{Si}(e^{-i2\pi 0} + e^{-i2\pi\frac{1}{2}l} + e^{-i2\pi\frac{1}{3}l} + e^{-i2\pi\frac{2}{3}l} + e^{-i2\pi\frac{1}{6}l} + + e^{-i2\pi\frac{5}{6}l})$$

$$\Rightarrow \left|F_{000l}\right|^2 = 36\left[f_{Si}^2 + f_C^2 + 2f_{Si}f_C\cos\frac{\pi l}{4}\right]. \tag{11}$$

Off-oriented *4H*-SiC substrates are usually used in epilayer growth because of the advantage of step-controlled growth and we are giving the detailed values of the structure factors for 8° off-cut *4H*-SiC samples in the commonly used geometries. The schematics showing the geometries used in most of our studies are given in Figure 8.

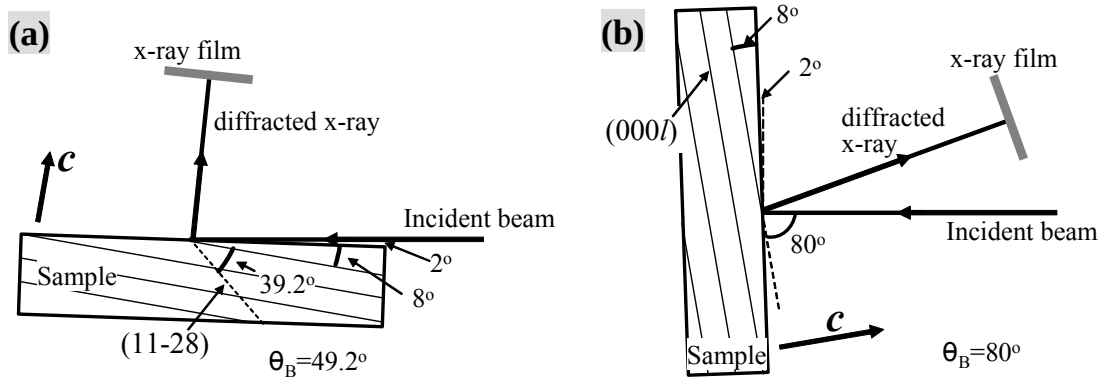

Figure 8. Schematics showing the geometries used in (11-28) grazing-incidence XRT (a) and back-reflection XRT (b) of an 8° off-cut SiC sample.

It has been established that structure factor is independent of the shape and size of the unit cell. In monochromatic synchrotron XRT, we set the appropriate wavelength to satisfy the Bragg condition by rotating the monochromator. In grazing-incidence geometry, the wavelength of the incident beam is usually set to be 1.48Å (8.36 keV) so that in the geometry used in Figure 8(a) the incident angle (the angle between the incident beam and crystal surface) is 2°. In the back-reflection geometry, the Bragg angle is set to be 80° and the corresponding wavelength of the incident beam is 1.65 Å (7.52 keV). The value of $\sin\theta_B/\lambda$ is 0.596 $Å^{-1}$ and the corresponding atomic scattering factors of C and Si atoms are estimated to be 1.6 and 5.1, respectively. The magnitude of the structure factor of (000.12) reflection based on Equation (8) is calculated to be 21.38. Similarly, the atomic scattering factors of C and Si corresponding to (11-28) reflection are 1.69 and 6.0, respectively, and the subsequent magnitude of the structure factor based on Equation (10) is 17.24. The structure factors of (11-28) and (000.12) are comparable. Note here that in the white beam XRT, the topograph is composed of harmonic reflections (especially in back-reflection where unusually large Bragg angles are used) and detailed analysis can be referred to Ref.43.

2.1.3. Penetration depth

Obtaining penetration depth of x-ray beam is very helpful for interpreting the topographic images. It gives information about the crystal volume imaged and thus helps in the understanding of the defect configurations, especially in epilayers. It can be applied to defective crystals and the photoelectric absorption based penetration depth t is given by

$$t = \frac{1}{\mu\left(\frac{1}{\sin\phi_0} + \frac{1}{\sin\phi_h}\right)}, \tag{12}$$

where μ is the absorption coefficient (cm^{-1}), Φ_0 is the incident angle and Φ_h is the exit angle. In (11-28) reflection of *4H*-SiC [λ=1.48 Å, see Figure 8(a)], the penetration depth based on photoelectric absorption is calculated to be 2.69 μm, while for (000.12) reflection [λ=1.65Å, see Figure 8(b)], the penetration depth is 20.9 μm.

However for nearly defect-free crystals, the penetration depth in Bragg geometry is governed by extinction distance. According to the dynamical theory, the extinction distance Λ is given by[44]

$$\Lambda = \frac{\lambda\sqrt{|\gamma_h\gamma_0|}}{C\sqrt{\chi_h\chi_{\bar{h}}}}, \tag{13}$$

where λ is the wavelength, $\gamma_h = cos\psi_h$ (ψ_h is the angle between the diffracted beams with the inward-going surface normal), $\gamma_0 = cos\psi_0$ (ψ_0 is the angle between the incident beams with the inward-going surface normal), C is the polarization factor (C=1 for σ polarization and $cos2\theta_B$ for π polarization) χ_h and $\chi_{\bar{h}}$ are the electric susceptibilities for (*hkl*) and (-*h*-*k*-*l*) reflections, respectively and χ_h is defined by equation

$$\chi_h = -\frac{r_e\lambda^2}{\pi V}F_h, \tag{14}$$

where r_e is the classical radius of electrons, V is the volume of the unit cell. The penetration depth is thus given by:

$$z_e = \frac{\Lambda}{2\pi\sqrt{1-\eta^2}}, \tag{15}$$

where η is the deviation parameter (the deviation from the rocking curve peak). The minimum penetration depth corresponds to the situation when the incident beam is exactly at the rocking curve center and the penetration depth is $\Lambda/2\pi$.

The minimum penetration depths so obtained (at rocking curve peak) for (11-28) (λ=1.48Å) and (000.12) reflections (λ=1.65Å) are calculated to be (σ polarization, C=1)

$$z_e(11\bar{2}8) = \frac{\lambda\sqrt{|\gamma_h\gamma_0|}}{2\pi C\sqrt{\chi_h\chi_{\bar{h}}}} = \frac{\lambda\sqrt{|\gamma_h\gamma_0|}}{\frac{2\pi r_e\lambda^2}{\pi V}\sqrt{F_hF_{\bar{h}}}} = 1.07\ (\mu m);$$

(16)

$$z_e(000.12) = \frac{\lambda\sqrt{|\gamma_h\gamma_0|}}{2\pi C\sqrt{\chi_h\chi_{\bar{h}}}} = \frac{\lambda\sqrt{|\gamma_h\gamma_0|}}{\frac{2\pi r_e\lambda^2}{\pi V}\sqrt{F_hF_{\bar{h}}}} = 4.04\ (\mu m).$$

(17)

By comparing the results from Equations (12) and (15), we can see that the dynamical penetration depth is much smaller than the photoelectric absorption penetration depth. This is because when the incident wave vector falls within the rocking curve width (dynamical diffraction dominates), the scattering from each atomic layer is in phase and the intensity of the forward diffracted beam drops down drastically. Whereas, if the incident wave vector falls outside of the rocking curve, the attenuation of the forward beam is only related to the photoelectric absorption $I=I_0e^{-\mu t}$. In our studies, the photoelectric penetration depth is used because of the relatively high dislocation density.

2.2. Synchrotron x-ray diffraction topography

X-ray diffraction topography has been a powerful way to image defects in low defect density single crystals ($<10^6/cm^2$) for more than 50 years. Synchrotron radiation is especially suitable for x-ray topography because of the high brightness and low divergence of the x-ray beam. Due to the small source dimensions, low divergence angle as well as long source-specimen distance, extremely high resolution can be achieved using synchrotron radiation compared to that achieved in in-house topography (e.g., Lang topography). The vertical divergence angle of synchrotron radiation is given approximately by m_0c^2/E, where m_0 is the electron rest mass, c is the velocity of light and E is the electron energy. This value is typically 10^{-4} rad. The topographic resolution (R_x) is decided by the source size in the incidence plane (S_x), source-specimen distance (D) and the specimen-film distance (d) and it can be given by[45]

$R_x=d\ S_x/D.$

(18)

The theoretical resolution so obtained is ~0.4 μm for Beamline X19C at National Synchrotron Light Source and ~0.06 μm for Beamline XOR-33BM /UNI-CAT at Advanced Photon Source if D=10 cm is used (vertical reflection geometry).

Interpreting topographic contrast of defects is complicated and varies from defect to defect. Topographic contrast arises from the complex interaction between the x-rays and the crystal lattice. Basically the topographic contrast arises due to changes in the of x-ray wavefields in the crystals and may or may not be associated with strain in the crystals. Generally speaking, there are two mechanisms accounting for the topographic contrast of defects: orientation contrast and extinction contrast. According to Bowen and Tanner, orientation contrast arises when a region of the crystal is misoriented by an

amount larger than the beam divergence.[46] It appears as undarkened patch. The orientation contrast mechanism is often associated with crystals containing twins, grain boundaries, electric and magnetic domains i.e., which exhibit domains (separate volumes of crystal) that have different orientation separated by domain walls (twin boundaries, grain boundaries, domain boundaries) where the orientation change is sudden. Orientation contrast can also be observed from with the continuous misorientation of lattice planes surrounding defects such as dislocations or precipitates (this is also possible for some grain boundaries). In the white beam XRT, the misoriented regions can automatically select the appropriate wavelengths satisfying the Bragg condition and the orientation contrast appears as either undarkened patch due to the divergence of diffracted x-ray beams, or darkened patch due to the convergence of x-ray beams. Such orientation contrast is not restricted to White Beam topography but can also be observed in monochromatic XRT due to a combination of the finite x-ray spectrum width ($\Delta\lambda/\lambda=10^{-4}$) and the divergence of the x-ray beam. The orientation contrast from continuously misoriented lattice planes will be further discussed in the computer simulation of dislocation via "ray-tracing" principle.

Another type of contrast is extinction contrast. Due to the strain field associated with the dislocation, the dynamical diffraction breaks down and the crystal lattice surrounding the dislocation core diffracts kinematically. This is because this region falls out side of the full width at half maximum of the rocking curve so that the rescattering is negligible. This is similar to the case of small crystal diffraction, which is dominated by kinematical diffraction. The diffracted intensity from near the dislocation core is higher than the one from the surrounding matrix under low absorption condition and its intensity is proportional to the length of the path in kinematical diffracted region. Under low absorption case, for instance, $\mu t<1$ (μ is the absorption coefficient and t is the thickness of the crystal), the diffracted intensity from the dislocation core is higher than that from the matrix, resulting in dark dislocation lines (kinematical diffraction) in a grey background (due to primary extinction from dynamical diffraction). This is usually what we observe in transmission topographs of SiC. If under high absorption condition ($\mu t>10$), the dislocations appear as white lines due to anomalous absorption (Borrmann effect). In the Laue geometry, the diffracted beam is supposed to be extremely weak if μt is more than 10 ($I=I_0e^{-\mu t}=4.68\times10^{-5}I_0$). However, fairly strong diffracted beam has been observed for nearly perfect crystals and this was first discovered in 1941 by Borrmann and it is thus called Borrmann effect (or anomalous absorption). In Borrmann effect, two standing waves are generated in the crystal and they have the same periodicity as the reflection planes. The wave field activated by one of the two tiepoints on the dispersion surface has much less photoelectric absorption than the other because its nodes lie on the atomic positions (thus much higher photoelectric absorption).[47] Therefore, the dislocation images under anomalous absorption condition appear as white lines since the dislocation breaks the periodicity of the crystal lattice. As for the case of SiC, the typical wavelength used in Laue geometry is ~0.8 Å and the corresponding μt is ~0.85 for a wafer of normally 400 μm thick. Anomolous absorption does not occur in our studies.

In recently years Huang developed a modeling process based on ray-tracing principle to simulate the x-ray topographic images of dislocations in SiC.[48] This model

has successfully clarified the dislocation character of the MPs and it has been successfully used in interpreting the topographic images of TSDs, TEDs and BPDs in various geometries.[13,14,29, 49] Large amount of observation indicates that orientation contrast is dominent over the extinction contrast in the x-ray topography of SiC in most cases.

Fringe contrast is sometimes observed in crystals as well. They are usually associated with stacking faults in crystals. Although there is no strain field associated with the stacking fault, different wave fields are generated due to the different boundary conditions and the interference between different wave fields contributes to the fringe contrast of the stacking faults. Sometimes the fringes can be observed at the crystal edge, which is due to the wedge shaped edge, resulting in the Pendellösung fringes.[50]

2.3. Fundamental aspects of dislocation theory

SiC is an excellent crystal for studying basic dislocation theory. There are various dislocations in SiC crystals, including edge type, screw type (including MPs with gigantic Burgers vector), and various partial dislocations, including even stair-rod dislocations. There is only one primary slip plane {0001} in SiC and the primary slip system is (0001)<11-20>. The BPDs are glissile dislocations with both line directions and Burgers vectors in the basal plane {0001}. TSDs/MPs are growth dislocations in screw orientation with line directions along [0001] and Burgers vector n<0001> (n is an integer). They are usually sessile. Note that TSDs can be tilted slightly away from *c*-axis, which imparts mixed character upon them, while MPs are usually parallel to *c*-axis due to their much larger strain energy. TEDs are dislocations with line directions roughly parallel to *c*-axis and Burgers vectors in *c*-plane. Shockley partials are in *c*-plane with Burgers vectors 1/3<1-100> type and Frank partials have Burgers vector component out of *c*-plane and its dislocation line is usually in *c*-plane. The characters of those dislocations are summarized in Table 3.

Table 3. Characters of various dislocations in *4H*-SiC

	Dislocation line (***u***)	Burgers vector (***b***) (magnitude)
BPD	Parallel to *c*-plane	1/3<11-20> (3.08 Å)
TED	Roughly parallel to [0001]	1/3<11-20> (3.08 Å)
TSD	Roughly parallel to [0001]	n<0001> (10.05n Å)*
MP	Parallel to [0001]	n<0001> (10.05n Å)*
Shockley PD	Parallel to *c*-plane	1/3<1-100> (1.778 Å)
Frank PD**	Parallel to *c*-plane	1/4<0001> (2.51 Å)

* n is an integer. ** This is only one special type of Frank PD.

In order to further understand characters of the dislocations and their images in XRT, the displacement field of each type of dislocation is discussed in detail. Understanding the displacement field of the dislocations is the basis for interpreting their images in XRT. In addition, it is the most critical part in the ray-tracing simulation of their XRT images. Furthermore, as a dislocation is close to a surface, its strain field has to be modified to satisfy the free surface condition (the strain components perpendicular

to the surface is zero). This is called surface relaxation effect and it is also to be discussed for certain types of dislocations.

2.3.1. Basal plane dislocations

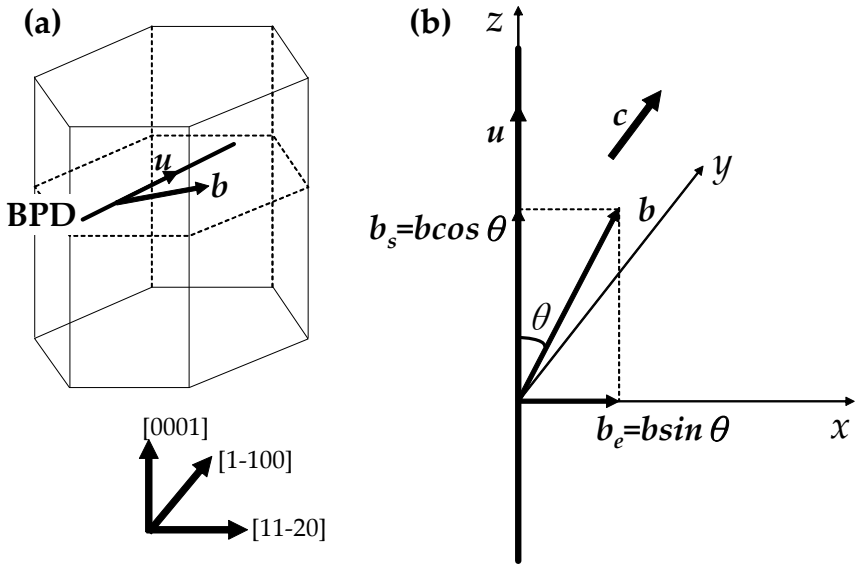

Figure 9. (a) A straight BPD on (0001) basal plane. (b) Geometry used in obtaining the displacement field of a BPD with Burgers vector at angle θ to the line direction.

Assume a BPD in *c*-plane with line direction along *z*-axis. The *y*-axis is parallel to *c*-axis and *xz* plane is parallel to the basal plane. The Burgers vector direction is at angle θ to its line direction (see Figure 9). Since it is a mixed dislocation with both edge and screw components, we can break the Burgers vector into two components: one is along *x*-axis ($\boldsymbol{b}_e=|\boldsymbol{b}|sin\theta\ \boldsymbol{i}$) and the other one is along *z*-axis ($|\boldsymbol{b}_s|=|\boldsymbol{b}|cos\theta\ \boldsymbol{k}$). The displacement field can thus be obtained by combining the components associated with the edge character ($\boldsymbol{b}_e$) and screw character ($\boldsymbol{b}_s$). The displacement field associated with the screw component is along *z*-axis and given by[51]:

$$u_z = \frac{b\cos\theta}{2\pi}\tan^{-1}\left(\frac{y}{x}\right). \tag{19}$$

The displacement field associated with the edge component has both *x*- and *y*- component [52]:

$$u_x = \frac{b\sin\theta}{2\pi}\left[\tan^{-1}\frac{y}{x} + \frac{xy}{2(1-\nu)(x^2+y^2)}\right], \tag{20}$$

$$u_y = -\frac{b\sin\theta}{2\pi}\left[\frac{1-2\nu}{4(1-\nu)}\ln(x^2+y^2) + \frac{x^2-y^2}{4(1-\nu)(x^2+y^2)}\right], \tag{21}$$

where ν is the Poisson's ratio. The total displacement can be obtained by combining Equations (19)-(21).

2.3.2. Threading screw dislocations (TSDs) and micropipes (MPs)

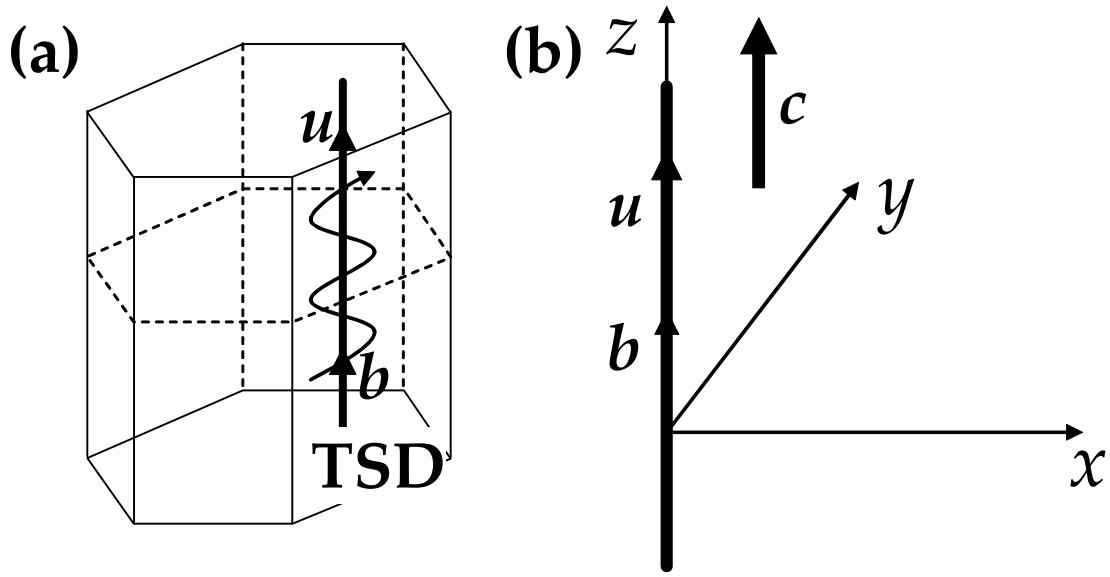

Figure 10. (a) A TSD in SiC. (b) Geometry used in obtaining the displacement field of a TSD or MP.

TSDs and MPs are both screw dislocation, with different magnitude of Burgers vectors. Their dislocation lines are approximately along *c*-axis and their Burgers vectors are parallel to *c*-axis. According to the fundamental dislocation theory, the displacement field has only *c*-component[51]:

$$u_z = (b/2\pi)\arctan(y/x), \tag{22}$$

where *b* is the Burgers vector of the MP.

If a TSD/MP is close to the surface, the strain components perpendicular to the crystal surface has to be zero in order to satisfy the free surface condition. An additional in-plane (*c*-plane) displacement is thus resulted due to such surface relaxation effect. According to Eshelby and Stroh [53], the additional displacement field of a screw dislocation in an infinite plate/disc with surfaces $z=\pm t$:

$$u_x = u_\theta(x,y,z)\frac{-y}{\sqrt{x^2+y^2}};$$
$$u_y = u_\theta(x,y,z)\frac{x}{\sqrt{x^2+y^2}}, \tag{23}$$

where

$$u_\theta(x,y,z) = -\frac{b}{2\pi}\sum_{n=0}^{\infty}(-1)^n\left\{\frac{x^2+y^2}{(2n+1)t-z+\sqrt{\left[(2n+1)t-z\right]^2+\left(x^2+y^2\right)}}-\frac{x^2+y^2}{(2n+1)t+z+\sqrt{\left[(2n+1)t+z\right]+\left(x^2+y^2\right)}}\right\}. \quad (24)$$

The additional displacement field associated with the surface relaxation effect [Equation (23)] does not influence the images of TSDs in back-reflection XRT since it is in the basal plane which is the reflection plane used in this geometry. However, it plays a critical role in the topographic images of TSDs in grazing-incidence geometry and it results in the asymmetric contrast in the images. Such asymmetrical contrast provides an unambiguous way to distinguish the TSD sense. We will see this in Chapter 8.

2.3.3. Threading edge dislocations (TEDs)

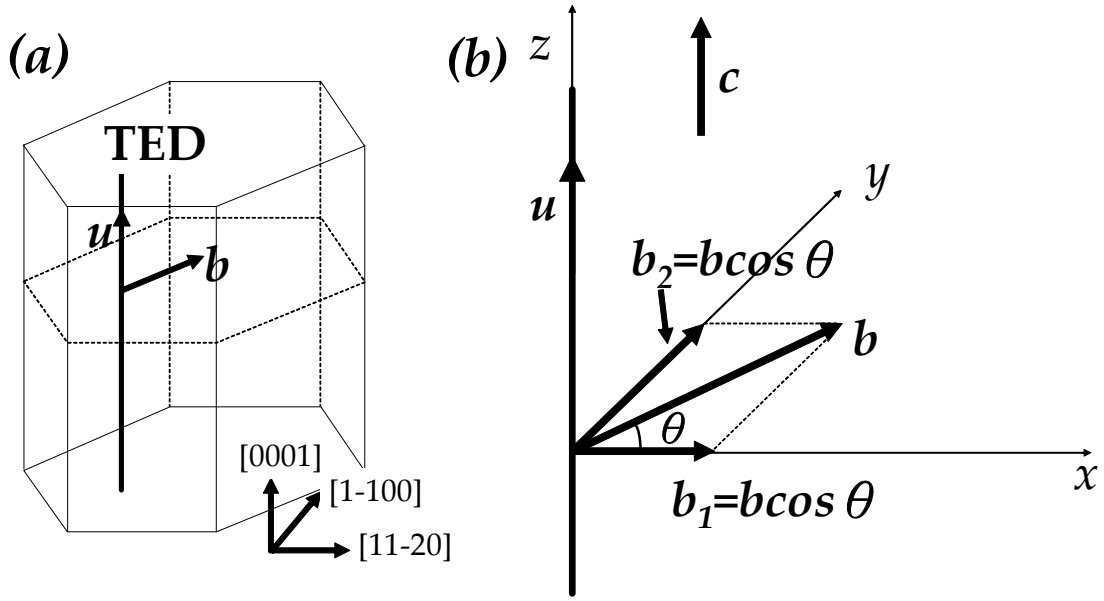

Figure 11. (a) A TED in SiC. (b) Geometry used in obtaining the displacement field of a TED.

Assume a TED along *c*-axis, the Burgers vector is at angle θ to the *x*-axis (see Figure 11). The *x*-axis is set not parallel to the Burgers vector in order to give a more general condition, which is going to be used in simulating the TED images in grazing-incidence geometry (to be discussed in Chapter 9). It is set parallel to the projection of the reflection vector on the basal plane. Thus, the displacement field is a combination of two edge components, $\boldsymbol{b_1}$ and $\boldsymbol{b_2}$. The displacement associated with the edge component $\boldsymbol{b_1}$ is given by[52]:

$$u_x = \frac{b\sin\theta}{2\pi}\left[\tan^{-1}\frac{y}{x}+\frac{xy}{2(1-\nu)\left(x^2+y^2\right)}\right], \quad (25)$$

$$u_y = -\frac{b\sin\theta}{2\pi}\left[\frac{1-2\nu}{4(1-\nu)}\ln\left(x^2+y^2\right)+\frac{x^2-y^2}{4(1-\nu)\left(x^2+y^2\right)}\right]. \quad (26)$$

Similarly, the displacement associated with component $\boldsymbol{b_2}$ is:

$$u_x = \frac{b\cos\theta}{2\pi}\left[\tan^{-1}\frac{-x}{y} + \frac{-xy}{2(1-\nu)(x^2+y^2)}\right], \tag{27}$$

$$u_y = -\frac{b\cos\theta}{2\pi}\left[\frac{1-2\nu}{4(1-\nu)}\ln(x^2+y^2) + \frac{y^2-x^2}{4(1-\nu)(x^2+y^2)}\right]. \tag{28}$$

The displacement field can thus be obtained by combing Equations (25)-(28).

2.3.4. Shockley partial dislocations

Shockley partial dislocations have line direction in *c*-plane and Burgers vectors of 1/3<1-100> type. The geometry used in obtaining its displacement field is the exactly same as the case of BPDs illustrated in Figure 9, except that the Burgers vector ***b*** is 1/3<1-100>. The detailed equation can be easily obtained by using appropriate Burgers vector in Equations (19)-(21).

2.3.5. Frank partial dislocations

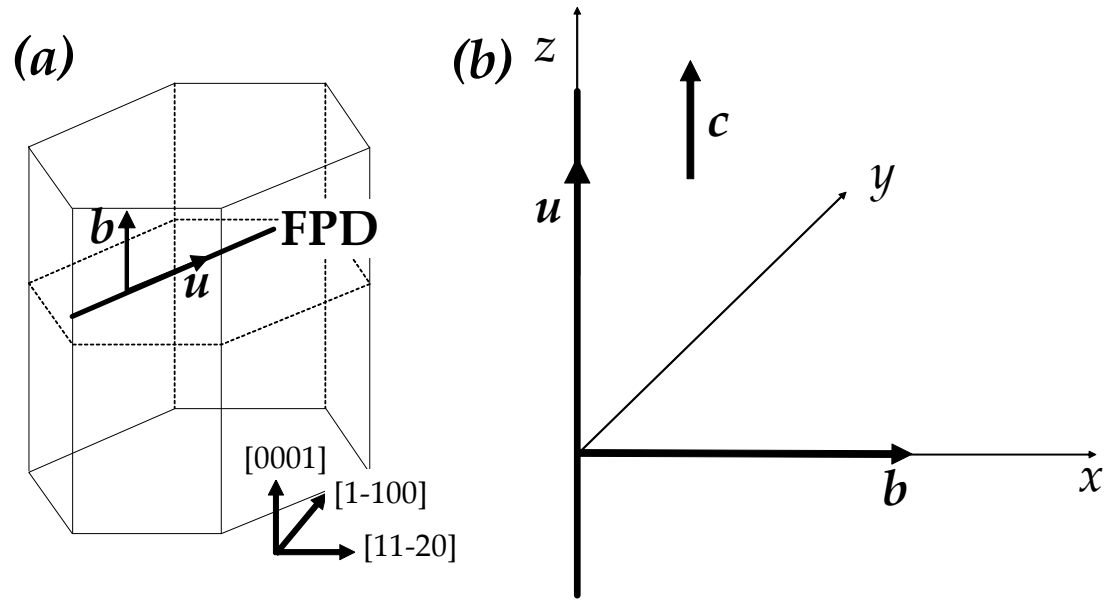

Figure 12. (a) A Frank PD in SiC. (b) Geometry used in obtaining the displacement field of a Frank PD.

Any partial dislocation in the basal plane with out-of-plane Burgers vector component can be considered as a Frank partial dislocation. We are here only discussing one type of them, whose Burgers vector is ¼<0001> and line direction is in *c*-plane (see Figure 12). They are associated with an extrinsic stacking fault in (0001) plane which can possibly be nucleated simultaneously with the TSDs, or converted from a TSD during CVD growth.[54]

Coordinate system is set so that line direction is along *z*-axis and Burgers vector is along *x*-axis (see Figure 12). The displacement field associated with the Frank partial is thus given by:

$$u_x = \frac{b}{2\pi}\left[\tan^{-1}\frac{y}{x} + \frac{xy}{2(1-\nu)(x^2+y^2)}\right], \tag{29}$$

$$u_y = -\frac{b}{2\pi}\left[\frac{1-2\nu}{4(1-\nu)}\ln(x^2+y^2) + \frac{x^2-y^2}{4(1-\nu)(x^2+y^2)}\right]. \tag{30}$$

2.3.6. Surface relaxation effect

When a dislocation is close to a free surface of the crystal, the strain and displacement fields need to be modified, since the strain components perpendicular to the crystal surface have to be zero in order to satisfy the free surface condition. Yoffe has calculated the stress and displacement fields for a straight dislocation intersecting a free surface of a semi-infinite, isotropic elastic body at an arbitrary angle (see Figure 13).[55] The results are given below.

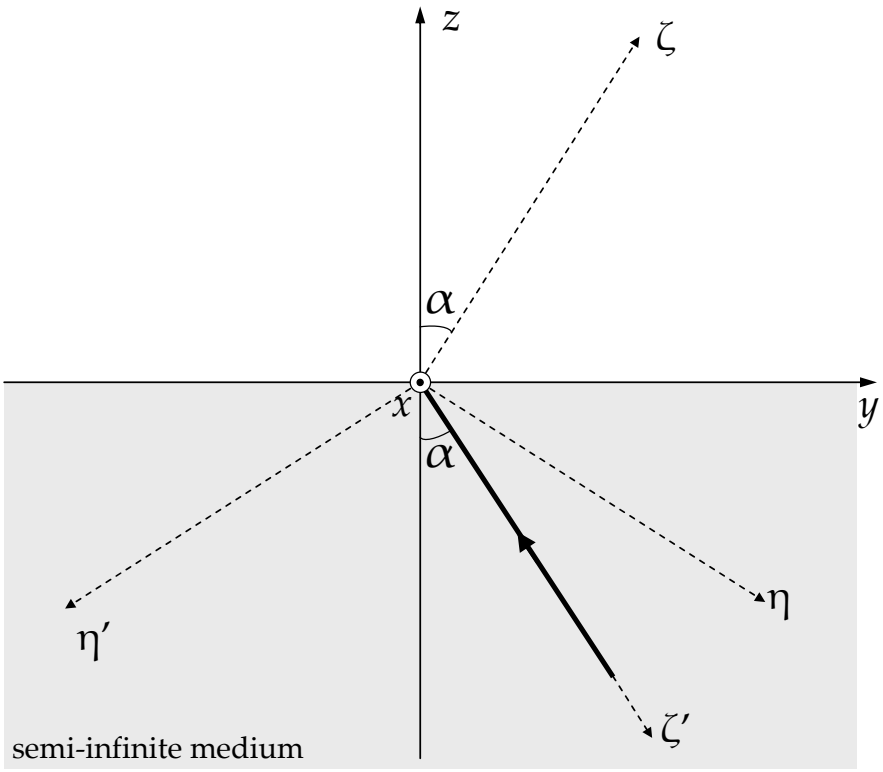

Figure 13. Coordinate system used in obtaining the displacement field of a dislocation in a semi-infinite isotropic medium at arbitrary angle α to the inward surface normal.

Assume that the dislocation has Burgers vector ***b*** and it can break up into x, y and z components b_x, b_y and b_z. The displacement field associated with component is given b_x by

$$
\begin{aligned}
2\mu u_x &= z\frac{\partial^2\varphi}{\partial x\partial z}+(1-2\nu)\frac{\partial\varphi}{\partial x},\\
2\mu u_y &= z\frac{\partial^2\varphi}{\partial y\partial z}+(1-2\nu)\frac{\partial\varphi}{\partial y},\\
2\mu u_z &= z\frac{\partial^2\varphi}{\partial z^2}-2(1-\nu)\frac{\partial\varphi}{\partial z}.
\end{aligned}
\tag{31}
$$

where

$$
\varphi=\frac{\mu b_x\cot\alpha}{2\pi(1-\nu)}\{\zeta\lg(r-\zeta)+2(1-\nu)r+(1-2\nu)z\lg(r-z)
$$

$$
+2(1-\nu)\cot\alpha\left[\eta\lg(r-\zeta)-y\lg(r-z)-x\left(\tan^{-1}\frac{y}{x}-\tan^{-1}\frac{\eta}{x}+\tan^{-1}\frac{xr\sin\alpha}{x^2\cos\alpha+y\eta}\right)\right]\Bigg\},
$$

$r=\sqrt{x^2+y^2+z^2}$ and

$\eta = y\cos\alpha - z\sin\alpha$,

$\zeta = y\sin\alpha + z\cos\alpha$,

$\eta' = -y\cos\alpha - z\sin\alpha$,

$\zeta' = y\sin\alpha - z\cos\alpha$.

The displacement field associated with the Burgers vector component b_y is:

$$
2\mu u_x=\frac{\mu b_y}{4\pi(1-\nu)}\cos\alpha\left[-\frac{x^2}{r(r-\zeta)}-\frac{x^2}{r(r-\zeta')}+(1-2\nu)\lg(r-\zeta)(r-\zeta')\right]+z\frac{\partial^2\varphi}{\partial x\partial z}+(1-2\nu)\frac{\partial\varphi}{\partial x}
$$

,

$$
2\mu u_y=\frac{\mu b_y}{4\pi}\left(\tan^{-1}\frac{\eta}{x}-\tan^{-1}\frac{\eta'}{x}+\tan^{-1}\frac{xr\sin 2\alpha}{\eta\eta'-x^2\cos 2\alpha}\right)+
$$

$$
\frac{\mu b_y}{4\pi(1-\nu)}\left[\frac{\sin\alpha\cos\alpha}{r-\zeta}+\frac{\sin\alpha\cos\alpha}{r-\zeta'}-\frac{y\cos\alpha}{r(r-\zeta)}-\frac{y\cos\alpha}{r(r-\zeta')}\right]+z\frac{\partial^2\varphi}{\partial y\partial z}+(1-2\nu)\frac{\partial\varphi}{\partial y},
$$

$$
2\mu u_z=\frac{\mu b_y}{4\pi(1-\nu)}\left[\frac{\cos^2\alpha}{r-\zeta}-\frac{\cos^2\alpha}{r-\zeta'}-\frac{z\cos\alpha}{r(r-\zeta)}-\frac{z\cos\alpha}{r(r-\zeta')}\right]+z\frac{\partial^2\varphi}{\partial z^2}-2(1-\nu)\frac{\partial\varphi}{\partial z},
$$

(32)

where

$$
\varphi=\frac{\nu\mu b_y}{2\pi(1-\nu)}\left[\frac{xz}{r-z}x\lg(r-z)\right].
$$

The displacement field associated with the Burgers vector component b_z is:

$$2\mu u_x = \frac{\mu b_z \sin\alpha}{4\pi(1-\nu)}\left[(1-2\nu)\lg(r-\zeta)(r-\zeta') - \frac{x^2}{r(r-\zeta)} - \frac{x^2}{r(r-\zeta')}\right] + \frac{\mu b_z y}{\pi(r-z)} + z\frac{\partial^2\varphi}{\partial x\partial z} + (1-2\nu)\frac{\partial\varphi}{\partial x},$$

$$2\mu u_y = \frac{\mu b_z x \sin\alpha}{4\pi(1-\nu)}\left[\frac{\sin\alpha}{r-\zeta} + \frac{\sin\alpha}{r-\zeta'} - \frac{y}{r(r-\zeta)} - \frac{y}{r(r-\zeta')}\right] - \frac{\mu b_z x}{\pi(r-z)} + z\frac{\partial^2\varphi}{\partial y\partial z} + (1-2\nu)\frac{\partial\varphi}{\partial y},$$

$$2\mu u_z = \frac{\mu b_z}{2\pi}\left(\tan^{-1}\frac{\eta}{x} - \tan^{-1}\frac{\eta'}{x} + \tan^{-1}\frac{xr\sin 2\alpha}{\eta\eta' - x^2\cos 2\alpha}\right)$$

$$+ \frac{\mu b_z x \sin\alpha}{4\pi(1-\nu)}\left[\frac{\cos\alpha}{r-\zeta} - \frac{\cos\alpha}{r-\zeta'} - \frac{z}{r(r-\zeta)} - \frac{z}{r(r-\zeta')}\right] + z\frac{\partial^2\varphi}{\partial z^2} - 2(1-\nu)\frac{\partial\varphi}{\partial z}, \tag{33}$$

where

$$\varphi = \frac{\mu b_z}{2\pi(1-\nu)}\left[-x\sin\alpha\lg(r-\zeta) + z\left(\tan^{-1}\frac{y}{x} - \tan^{-1}\frac{\eta}{x} + \tan^{-1}\frac{xr\sin\alpha}{x^2\cos\alpha + y\eta}\right)\right].$$

Once the displacement fields resulted from the surface relaxation effect can be calculated by Equations (31)-(33), the topographic images of dislocations can be simulated via ray-tracing method. The detailed simulation process is discussed in the next section. In the case of screw dislocation intersecting the crystal surface, the infinite plate/disc type surface relaxation obtained by Eshelby and Stroh is used in the simulation.[53] The displacements discussed in this section are for general case, in which a straight dislocation intersects the crystal surface in a semi-infinite medium.

3. Experimental and simulation

3.1. Synchrotron x-ray topography

Synchrotron XRT in our studies was done at the National Synchrotron Light Source (NSLS), Beamline X19C and at the Advanced Photon Source (APS), Beamline XOR-33BM/UNI-CAT. White beam XRT was carried out at NSLS and monochromatic XRT was carried out at the APS. The direct white beam from the storage ring is used at the NSLS and the maximum beam size at the sample is approximately 7×40 mm^2. The vertical divergence angle is $mc^2/E \approx 0.18$ mrad (m is the mass of the electron, c is the velocity of the light and E is the electron energy). In APS, the white beam is monochromatized by two cooled parallel Si(111) crystals and the x-ray energy is tunable between 2.4 – 40 keV. The schematic experimental setting-ups at NSLS and APS are illustrated in Figure 14.

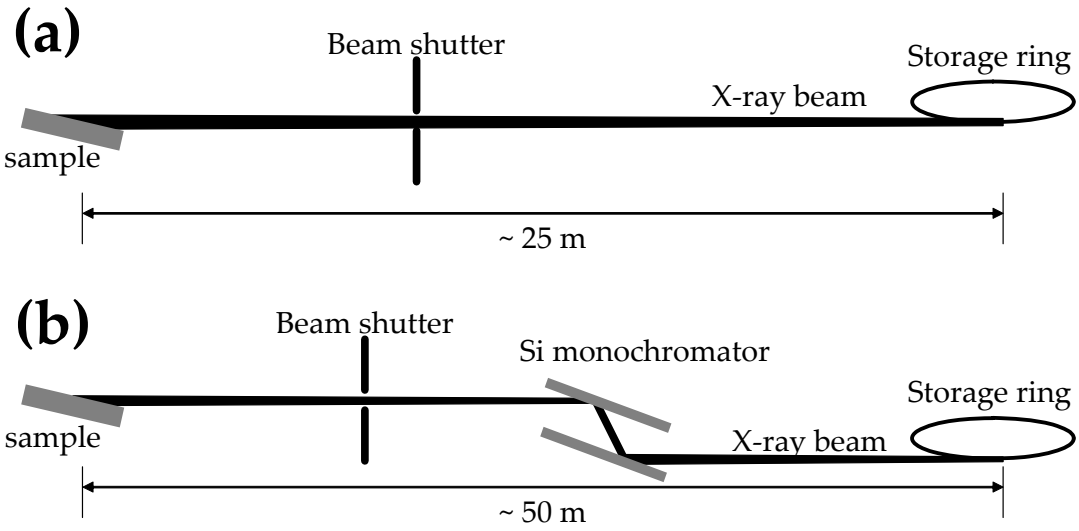

Figure 14. Schematics showing the experimental setting-ups at NSLS (a) and APS (b).

Mainly three geometries are used in our studies. The schematics of the three geometries are illustrated in Figure 15. The first one [Figure 15(a)] is the transmission geometry, also called Laue geometry. In the transmission mode, the x-ray beam passes through the sample and the topographs recorded reveal the bulk defect information. In grazing-incidence reflection [Figure 15(b)], a very small incident angle is used (typically 2^o) and the (11-28) or (11-2.12) reflection is recorded. Grazing-incidence is carried out because of the low penetration depth of x-ray beam in such geometry, which is particularly good for the studies of epilayers. The penetration depth can be tuned by rotating the sample along the reflection vector, or by simply adjusting the incident angle (the wavelength should be accordingly adjusted, of course). In back-reflection geometry, a large Bragg angle is used for basal plane reflection (000l) (typically 80^o). The screw dislocations along c-axis and the basal plane dislocations within the penetration depth of x-rays can be clearly recorded. The wavelength satisfying Bragg condition is

automatically selected in white beam x-ray topography while in monochromatic XRT, the energy of x-ray beam has to be pre-set to satisfy the diffraction condition.

Diffracted images are recorded on Agfa Structurix D3-SC, Ilford L4 nuclear plate, or VRP-M holographic films, depending on the resolution needed. Exposure time depends on the actual geometry and recording media and it varies between a few seconds and two hours. Kodak D19 developer and fixer were used to process the exposed emulsions.

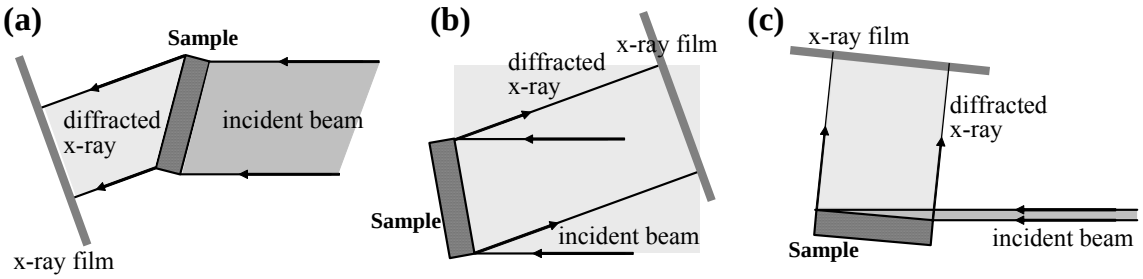

Figure 15. Schematics of transmission (a), back-reflection (b) and grazing-incidence reflection (c) geometries used in our studies.

3.2. Ray-tracing simulation

It is sometimes very difficult to interpret the x-ray topographs due to the complex interaction between the x-ray and crystal lattice. However, ray-tracing simulation has been shown to provide a simple yet powerful tool for interpreting x-ray topographic images of defects in SiC. As we discussed earlier in section 2.2, there are mainly two contrast mechanisms associated with the dislocations in x-ray topography: orientation contrast and extinction contrast. Extensive comparisons between experiment and simulation have indicated that orientation contrast is dominant in topographs of SiC. Therefore, ray-tracing simulation based on orientation contrast mechanism provides an excellent model to qualitatively and quantitatively interpret the topographic observations of dislocations in SiC. It has been successfully used in the back-reflection XRT to clarify the screw character of the MPs.[56] It also has been used to reveal the dislocation sense of TSDs/MPs (see Chapters 7 and 8), the Burgers vectors of TEDs (Chapter 9), core structure of Shockley partial dislocations (Chapter 10) and the sign of Frank partial dislocations (Chapter 12).

The schematic of simulation based on ray-tracing principle is shown in Figure 16.[48] In ray-tracing simulation, the specimen surface is divided into small squares of constant area. The plane normal $\boldsymbol{n}(x,y,z)$ after distortion due to the strain field associated with the dislocation varies from the original plane normal $\boldsymbol{n}^0(x,y,z)$ before distortion and it is calculated for each constant area. The contrast on the simulated image is determined by the superimposition or separation of beams diffracted from the individual small areas on the specimen surface. Modified ray-tracing simulation can also take account of the diffraction from areas beneath the crystal surface allowing for the effects of photoelectric absorption.

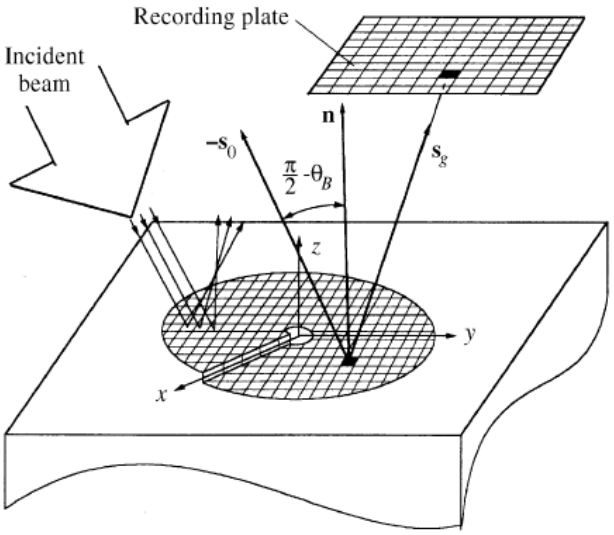

Figure 16. Schematics showing the simulation based on ray-tracing principle (after X. R. Huang**Error! Bookmark not defined.**).

3.2.1. $\vec{n} = \vec{n}^0 - \nabla\left[\vec{n}^0 \cdot \vec{u}\right]$

In ray-tracing simulation, the key point is to obtain the plane normal after distortion due to the strain fields associated with the defects. The plane normal $\boldsymbol{n}$(x,y,z) after distortion is given by[57]

$$\vec{n}(x,y,z) = \vec{n}^0(x,y,z) - \nabla\left[\vec{n}^0(x,y,z) \cdot \vec{u}(x,y,z)\right], \quad (34)$$

where $\boldsymbol{n}^0(x,y,z)$ is the plane normal before distortion and $\boldsymbol{u}(x,y,z)$ is the displacement field of the dislocation. The physical interpretation of this equation is seen in Figure 17. $\boldsymbol{n}^0(x,y,z) \cdot \boldsymbol{u}(x,y,z)$ gives the magnitude of the component of plane normal $\boldsymbol{n}^0(x,y,z)$ along $\boldsymbol{n}^0(x,y,z)$. ∇ [$\boldsymbol{n}^0(x,y,z) \cdot \boldsymbol{u}(x,y,z)$] is the vector pointing to the direction of the greatest rate of increase of $\boldsymbol{n}^0(x,y,z) \cdot \boldsymbol{u}(x,y,z)$ and its magnitude is the greatest rate of change of $\boldsymbol{n}^0(x,y,z) \cdot \boldsymbol{u}(x,y,z)$. $\boldsymbol{n}^0(x,y,z) - \nabla$ [$\boldsymbol{n}^0(x,y,z) \cdot \boldsymbol{u}(x,y,z)$] is the vector perpendicular to the plane after deformation.

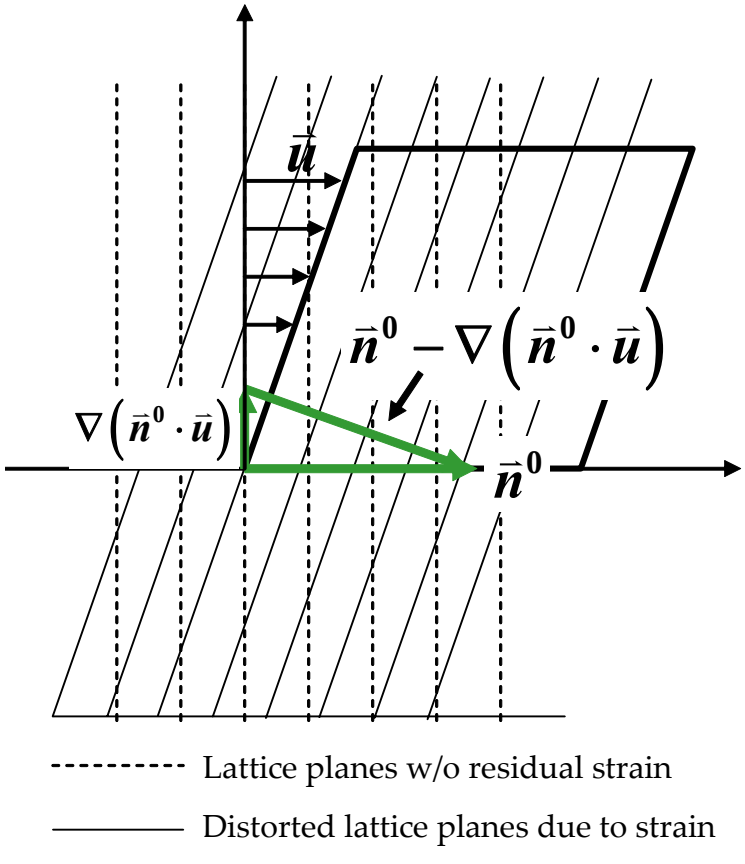

Figure 17. Schematics showing the physical interpretation of the Equation (34).

Equation (34) can also be mathematically proved. Assume a point in a certain flat lattice plane: *(x,y,z)*, which satisfies the equation $F(x,y,z)=0$. The plane normal before distortion (without dislocation) is $\boldsymbol{n}^0=F_x\boldsymbol{i} + F_y\boldsymbol{j} + F_z\boldsymbol{k}$, where F_x, F_y and F_z are partial derivatives of the function $F(x,y,z)$ on x, y and z, respectively ($F_x = \partial F/\partial x$, $F_y = \partial F/\partial y$, $F_z = \partial F/\partial z$). Since it is a flat plane before distortion, F_x, F_y and F_z are constant.

Assume a displacement field $\boldsymbol{u}=u^x(x,y,z)\boldsymbol{i} + u^y(x,y,z)\boldsymbol{j} + u^z(x,y,z)\boldsymbol{k}$, where $u^x(x,y,z)$, $u^y(x,y,z)$ and $u^z(x,y,z)$ are the x, y and z components of the displacement field. Due to the displacement field, (x,y,z) shifts to $(x+ u^x, y+ u^y, z+ u^z)$. Let us define:

$$x' = x + u^x(x,y,z)$$
$$y' = y + u^y(x,y,z)$$
$$z' = z + u^z(x,y,z). \qquad (35)$$

So we have

$$x = x' - u^x(x,y,z),$$
$$y = y' - u^y(x,y,z),$$
$$z = z' - u^z(x,y,z). \qquad (36)$$

We are now introducing an important assumption here. We imagine that the crystal possesses a mosaic structure and each mosaic region is small enough so that the

displacement within it can be considered to be constant.[58] This means that $u^x(x,y,z) = u^x(x',y',z')$. We can now rewrite Equation (36) as:

$x = x' - u^x(x,y,z) \approx x' - u^x(x',y',z')$
$y = y' - u^y(x,y,z) \approx y' - u^y(x',y',z')$
$z = z' - u^z(x,y,z) \approx z' - u^z(x',y',z')$.

(37)

(x,y,z) has to satisfy the equation $F(x,y,z)=0$ so that we have:

$F(x' - u^x(x',y',z'), y' - u^y(x',y',z'), z' - u^z(x',y',z'))=0$.

(38)

Now we can replace x' with x:

$F(x - u^x(x,y,z), y - u^y(x,y,z), z - u^z(x,y,z))=0$.

(39)

This equation gives the lattice plane after distortion due to the strain field associated with the dislocation. The new plane normal is given by $\boldsymbol{n}=F_x\boldsymbol{i} + F_y\boldsymbol{j} + F_z\boldsymbol{k}$. Based on the properties of partial derivatives, we have

$$\frac{\partial F\left[x-u^x, y-u^y, z-u^z\right]}{\partial x} = \frac{\partial F}{\partial\left(x-u^x\right)}\frac{\partial\left(x-u^x\right)}{\partial x} + \frac{\partial F}{\partial\left(y-u^y\right)}\frac{\partial\left(y-u^y\right)}{\partial x} + \frac{\partial F}{\partial\left(z-u^z\right)}\frac{\partial\left(z-u^z\right)}{\partial x}.$$

(40)

Since $F_x = \partial F(x,y,z)/\partial x$ is a constant (since the reflection plane is flat before distortion, as we discussed earlier),

$\partial[F(x - u^x(x,y,z), y - u^y(x,y,z), z - u^z(x,y,z))]/\partial(x - u^x(x,y,z)) = \partial F(x,y,z)/\partial x = F_x$.

Equation (40) is then given by:

$$\frac{\partial F\left[x-u^x, y-u^y, z-u^z\right]}{\partial x} = F_x - F_x u_x^x - F_y u_x^y - F_z u_x^z,$$

where $u_x^x = \partial u^x/\partial x$, $u_x^y = \partial u^y/\partial x$ and $u_x^z = \partial u^z/\partial x$.

In a similar procedrure, we will also have:

$$\frac{\partial F\left[x-u^x, y-u^y, z-u^z\right]}{\partial y} = F_y - F_x u_y^x - F_y u_y^y - F_z u_y^z$$

and

$$\frac{\partial F\left[x-u^x, y-u^y, z-u^z\right]}{\partial z} = F_z - F_x u_z^x - F_y u_z^y - F_z u_z^z.$$

Therefore, the plane normal after distortion is given by

$$\vec{n} = \left(F_x - F_x u_x^x - F_y u_x^y - F_z u_x^z\right)\vec{i} + \left(F_y - F_x u_y^x - F_y u_y^y - F_z u_y^z\right)\vec{j} + \left(F_z - F_x u_z^x - F_y u_z^y - F_z u_z^z\right)\vec{k}.$$

(41)

On the other hand, the plane normal calculated from $\vec{n}^0 - \nabla\left[\vec{n}^0 \cdot \vec{u}\right]$ is given by:

$$\vec{n}^0 - \nabla\left[\vec{n}^0 \cdot \vec{u}\right]$$
$$= F_x\vec{i} + F_y\vec{j} + F_z\vec{k} - \left(\frac{\partial}{\partial x}\vec{i} + \frac{\partial}{\partial y}\vec{j} + \frac{\partial}{\partial z}\vec{k}\right)\left(F_x u^x + F_y u^y + F_z u^z\right)$$
$$= \left(F_x - F_x u_x^x - F_y u_x^y - F_z u\right)\vec{i} + \left(F_y - F_x u_y^x - F_y u_y^y - F_z u\right)\vec{j} + \left(F_z - F_x u_z^x - F_y u_z^y - F_z u\right)\vec{k}.$$

(42)

By comparing Equation (41) and (42), we have $\vec{n} = \vec{n}^0 - \nabla\left[\vec{n}^0 \cdot \vec{u}\right]$. This equation gives us a straightforward way to calculate the plane normal after the distortion associated with the dislocation, by knowing the displacement field of the dislocation. The displacement fields for different dislocations have been referred to Chapter 2.

3.2.2. $\vec{s}_0 \times \vec{n} = -\vec{n} \times \vec{s}$

Once the plane normal ***n*** after distortion is known, the diffracted wave vector ***s*** can be calculated based on equation $\vec{s}_0 \times \vec{n} = -\vec{n} \times \vec{s}$ if the incidence beam wave vector $\boldsymbol{s_0}$ is given. In our simulation, we assume an ideal plane wave and the wave vector of the incidence beam is fixed. The intensity distribution on the x-ray film can be mapped by calculating the wave vector of each diffracted beam from each small area defined on the crystal surface. Therefore, the dislocation image, which is actually a mapping of the diffracted beam intensity, can be simulated.

3.2.3. Simulation process

The simulation process using Mathematica® can be followed according to the steps below:

I. Select appropriate coordinate system. The coordination system should be selected in such a way that the displacement field of the dislocation is easily calculated.

II. Calculate the wavevector of the incident beam, plane normal before distortion and locate the position of the dislocation image on the film.

III. Set up a matrix to store the intensity map of the diffracted beam. The number of elements in this matrix decides the resolution of the simulated image. The resolution is selected in such a way that a) the resolution is not too low and b) there are not too many elements in the matrix so that the simulation takes extremely long. Normally a 500 × 500 matrix is used.

IV. In the mathematica code, a loop is set so that for each time in the loop, the position of diffracted beam from one pre-set surface area is calculated. The position of the diffracted beam is subsequently stored in the matrix. Note that the surface area should not be too fine (too much time needed) or too coarse (the resolution of the simulated image too low).

V. A intensity map of the matrix is plotted (the intensity is the value of each matrix element).

A simulation code for the (11-28) grazing-incidence reflection of a TSD is attached in the Appendix I. Simulation was carried out on a DELL Precision 530 Workstation, using the commercial software Mathematica® v5.1. Grayscale maps were plotted also using Mathematica. Processing takes up to a few days depending on the complexity of the calculation. The angle of view is from behind the X-ray film (antiparallel to the diffracted beam) in all our discussion.

4. Homo-epitaxy of SiC by Chemical Vapor Deposition

Recently, halide CVD has been paid much attention due to the lower decomposition temperature of halide precursors such as silicon tetrachloride ($SiCl_4$) which provides a potential way to grow SiC epitaxial films or even bulk crystals at lower temperature. These precursors are also readily available in high purity form. In this chapter, halide CVD using $SiCl_4$ and C_3H_8 precursors is studied. The carrier gas is ultra high purity H_2, which also acts as a co-reactant. Ar is also used as carrier gas at higher temperature to reduce etching caused by hydrogen.

4.1. Growth system set up

The CVD system for growing SiC epitaxial films was designed and fabricated by modifying a previously constructed PVT system.[59,60] It consists of an induction power-supply, water-cooled reactor chamber, hot-zone, IR pyrometer for non-contact temperature measurement, gas flow controllers and high vacuum system with a control to monitor and maintain the reactor pressure. Figure 18 shows a schematic diagram of our horizontal hot-wall CVD reactor chamber with integrated gas lines. The hot-zone containing the cylindrical graphite susceptor with rigid graphite insulation is heated by a 30 KW induction power supply (Huttinger Electronic, Inc.). The substrate is held horizontally or with a small angle to the gas flow at the bottom of the cylindrical susceptor. The induced eddy currents flowing within the susceptor generates heat in it. The substrate is then heated by radiation from the susceptor. Better heat containment is achieved by using a novel multi-segmented insulation cylinder surrounding the graphite substrate.[59] The temperature at the graphite support holding the substrate is monitored by a two-color IR pyrometer (Ircon Modline 3^{TM}). Using a turbomolecular pumping station the growth chamber can be evacuated down to 10^{-6} Torr, and the reactor pressure can be maintained at any predetermined value using a throttle valve coupled with a mechanical pump. The predetermined flow rates of propane, silicon tetrachloride precursors and hydrogen/argon carrier gases are set using the mass flow controllers (MFCs). The gaseous products coming out from the reactor chamber are completely burned in the pyrolysis furnace at 800°C and then let to the atmosphere through the exhaust. The silicon tetrachloride gas is obtained by controlled hydrogen bubbling into silicon tetrachloride liquid contained in a temperature controlled source bottle. The silicon tetrachloride gas lines and the vacuum line running from the reactor to the pyrolysis furnace are maintained at 60°C to prevent the condensation and subsequent catastrophic corrosion-induced leaking of hazardous gases. Typical growth parameters used are listed in Table 4.

Table 4. Typical growth parameters used in your growth.

H_2(slm)	$SiCl_4$(sccm)	C_3H_8(sccm)	T(^oC)
5~15	15~120	10~20	1400~1850

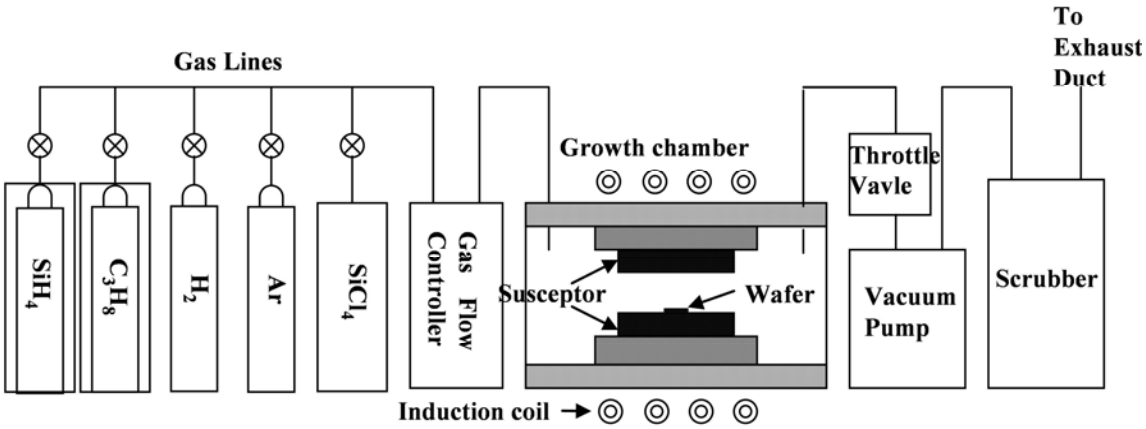

Figure 18. Schematic diagram of CVD system.

Complete information on the 3-dimensional temperature field in the hot-zone of the CVD reactor is essential for better understanding of the SiC growth. It is desirable to have uniform temperature inside the susceptor that can accommodate 2-3 inch wafers. The high temperature and the coupling of the induction heating on the thermocouple make it difficult to carry out detailed temperature measurements inside the susceptor. A numerical algorithm has been developed to predict the temperature distribution, growth rate and shape of the growing crystal as well as the thermo-elastic stress distribution.[61]

4.2. Polytype control

One of the two challenges that impede the growth of large-size and high-quality SiC is the polytypism. The different polytypes possess the same chemical makeup, but the stacking sequence varies along the *c*-axis of the lattice, and hence, they demonstrate different physical properties such as band-gap. Small free energy differences make it possible to grow different polytypes at the same growth condition. The crystals may contain inclusions of other polytypes and these can become the source for the generation of micropipes. Thus, if the growth conditions are not optimized, inclusions of different polytypes occur and thereby deteriorate the growing crystal. Therefore, maintaining growth of one polytype is essential to obtain high quality bulk crystals. *6H* and *4H*–SiC are the polytypes we are interested in.

The primary way of controlling polytype is to use a native substrate. Temperature is also a critical parameter that affects the polytype. Figure 19 gives the summary of the polytypes grown at different temperatures by CVD on graphite, silicon and SiC substrates (*4H/6H*) from 66 papers. The triangles indicate hexagonal polytype growth (*4H/6H*-SiC) and squares denote cubic polytype growth (*3C*-SiC). No hexagonal polytype can be grown on graphite and silicon substrate. At all temperatures (≤1600℃) *3C*-SiC was grown. This means at these temperatures, cubic SiC is the most stable phase. Actually our deposition on graphite substrates showed that at temperatures up to 1700^{o}C, *3C*-SiC is the stable phase. The growth on hexagonal substrates can be divided into three regions. Below 1100^{o}C, there is only cubic SiC and no hexagonal polytype is grown. At temperatures between 1100^{o}C and 1600^{o}C, both cubic and hexagonal polytypes are grown depending on the growth parameters such as the substrate orientation (on-axis or

off-axis) and growth rate. At temperatures beyond 1600°C, only hexagonal polytype is grown. It should be noted that on-axis and off-axis growth are not distinguished here and it may happen that cubic SiC inclusions are present in the film at temperatures beyond 1600 °C. However, it is clearly known that off-axis substrates enable much better control of polytype as is discussed further below.

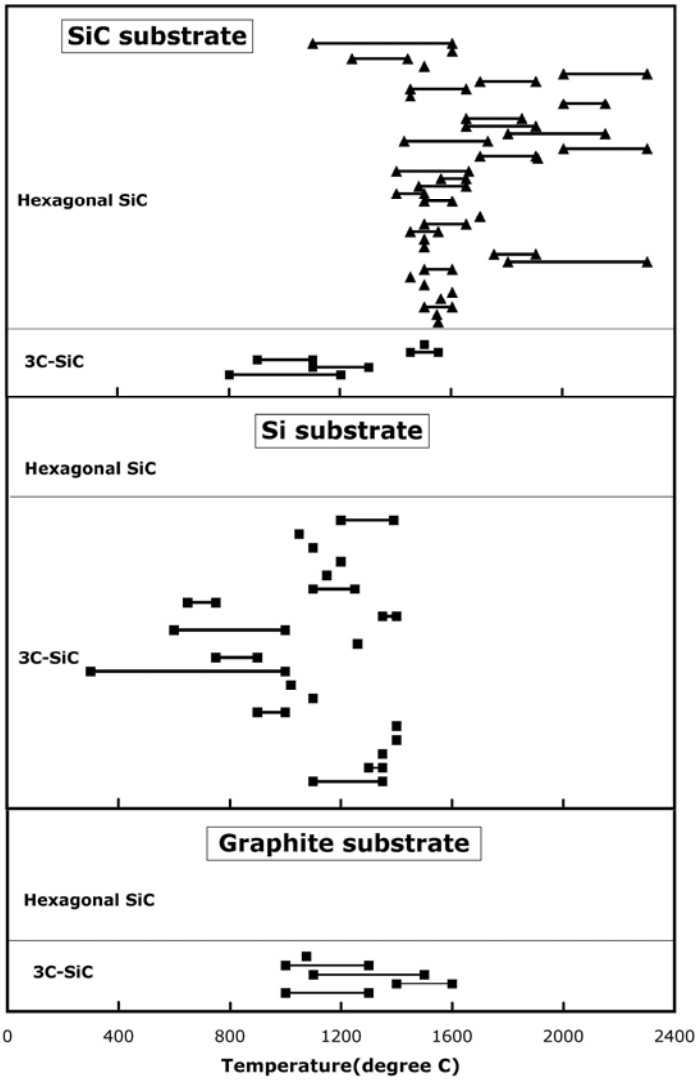

Figure 19. Summary of SiC polytypes grown by CVD using different substrates at different temperatures.[62-142] Bottom: graphite substrates; Middle: silicon substrates; Up: silicon carbide substrates. ▲: *4H*/*6H*; ■: *3C*.

SiC epitaxial films were grown by CVD on off-axis substrates as early as 1987.[143,144] The quality of the films and the performance of devices fabricated upon them were found to be improved significantly by using vicinal growth. While the growth on on-axis substrates is mainly controlled by 2D nucleation, the growth on off-axis is realized by the exact replication of the steps on the seed surface, which is called "step-controlled growth" or "step-flow growth". The comparison of two growth modes is illustrated in Figure 20. 2D island nucleation is realized by the formation of islands followed by the expansion of the islands. This growth mode causes a large amount of polytype inclusions because the islands may not copy the exact stacking sequence of the substrate and cubic SiC is the stable phase at the commonly used temperatures. Islands

expand followed by coalescence and misorientation between separate islands provides sites for dislocation nucleation.

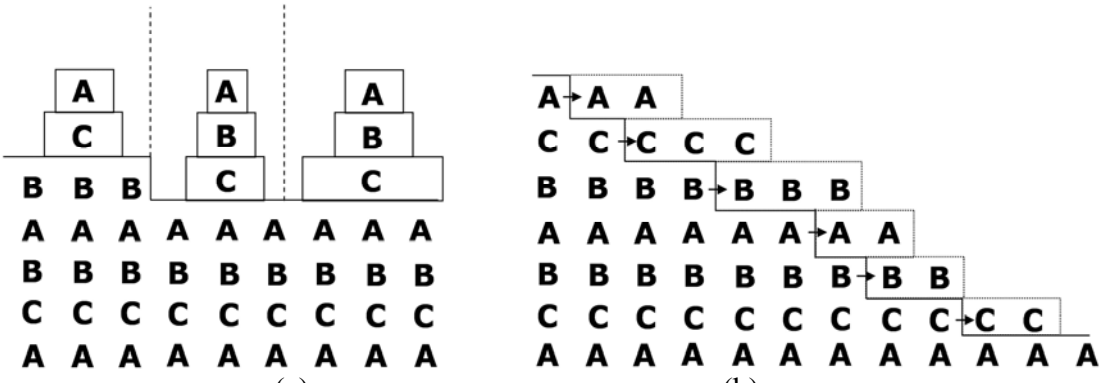

(a) (b)

Figure 20. Two different growth modes of CVD epitaxy on *6H*-SiC. (a) 2D nucleation mode; (b) step-controlled growth.

Figure 21 shows double crystal rocking curves of two SiC samples with epitaxial films on them. One sample was grown on on-axis *6H*-SiC substrate and the other one was grown on 8° off-axis *4H*-SiC substrate. The FWHMs before deposition are similar for both substrates (~30 arcsec). They were loaded in the growth chamber side by side and one hour growth was performed. One can see that the on-axis substrate has much larger FWHM (126 arcsec) compared to off-axis substrate (85 arcsec). The different growth mode causes the FWHM difference: the inclusions, double positioning boundaries and possibly other defects deteriorate the quality of on-axis growth film.

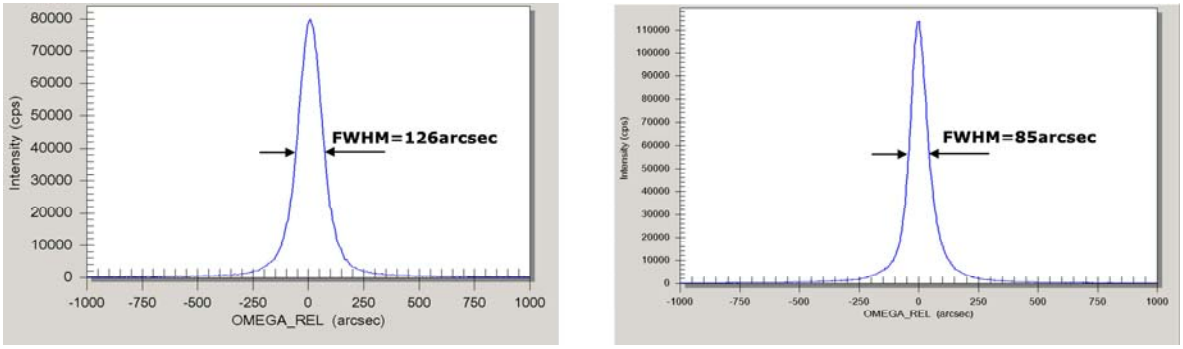

(a) (b)

Figure 21. Double crystal rocking curves of epitaxial film on an on-axis *6H*-SiC substrate (a) and an 8° off-axis *4H*-SiC substrate (b). FWHM: 126 arcsec (a); 85 arcsec (b). The samples were grown in the same run side by side. Both FWHMs before growth are ~30 arcsec.

4.3. Growth mechanism of halide CVD

It is commonly observed growth rate increases when temperature increases in CVD growth of SiC. However, it is not always the case. Figure 22 shows growth rates vs. T curves at two different growth parameters. Left curve shows the increase of growth rate

with temperature while right curve shows the slightly decrease of growth rate as temperature increases.

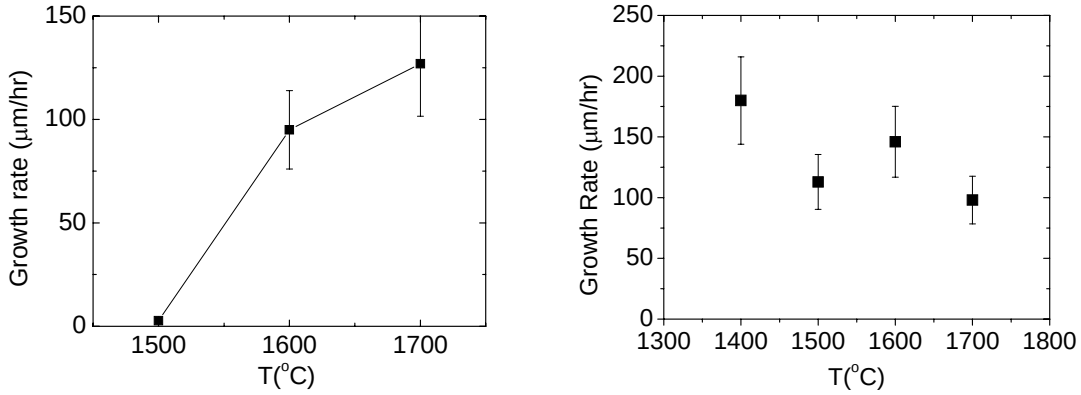

(a) (b)

Figure 22. Growth rate vs. Temperature at two different growth conditions. (a) Growth rate increases with temperature. $SiCl_4$=120 sccm, C_3H_8=10 sccm, H_2=15.2 slm. (b) Growth rate shows a decrease with the increase of temperature. $SiCl_4$=120 sccm, C_3H_8=10 sccm, H_2=5.2 slm.

The thermodynamics during the growth process was studied using a simple equilibrium model at $SiCl_4$, C_3H_8 and H_2 flow rate of 120 sccm, 10 sccm and 5200 sccm, respectively. These are the growth parameters used in Figure 22(b). It is assumed that gases stay in the hot-zone for a sufficient period of time that various species of gases reach equilibrium in the hot-zone. In this process, each gas species that was taken into account (listed in Table 5) possess specific partial pressure after passing through the hot-zone so that thermodynamical equilibrium is reached. The equation

$$\Delta G^0(T) + RT \ln K = 0 \tag{43}$$

must be satisfied for each reaction (listed in Table 5), where $\Delta G^0(T)$ is the standard Gibbs free energy change at temperature T and K is the equilibrium coefficient. According to thermodynamic theory, K is a function of gas species activity and in our calculation the activity is the partial pressure of each gas species assuming ideal condition at this pressure range used in our experiments.

Table 5. Gas species considered in calculation

CH	CH_2	CH_3	CH_4	C_2H	C_2H_2	C_2H_4
C_2H_6	C_3H_6	C_3H_8	CH_3Cl	CH_2Cl_2	$CHCl_3$	CCl_4
CHCl	C_2Cl_2	C_2Cl_4	C_2Cl_6	C_2HCl	CCl	CCl_2
CCl_3	$SiCl_4$	$SiCl_3$	$SiCl_2$	SiCl	SiH_4	SiH_3Cl
SiH_2Cl_2	$SiHCl_3$	SiH	H_2	H	Cl_2	Cl
HCl	Si	Si_2	Si_3	Si_2C	SiC_2	C_2
C_3	C_4	C_5				

Table 6. Reactions considered in the calculation.
(*g*, *l*, *s* indicate gas, liquid and solid, respectively)

$C_2H_2(g)=2CH(g)$	$CCl_2(g)=C(s)+Cl_2(g)$
$C_2H_2(g)= CH_2(g)+C(s)$	$CCl_3(g)=C(s)+3/2Cl_2(g)$
$C_2H_2(g)= 2/3CH_3(g)+4/3C(s)$	$SiCl_4(s)=SiCl_2(g)+Cl_2(g)$
$C_2H_2(g)=1/2\ CH_4(g)+3/2C(s)$	$SiCl_3(s)=SiCl_2(g)+1/2Cl_2(g)$
$C_2H_2(g)+2C(s)=2\ C_2H(g)$	$SiCl_2(s)=SiCl\ (g)+1/2Cl_2(g)$
$2C_2H_2(g)= C_2H_4(g)+2C(s)$	$SiH_4(g)=Si(g)+2H_2(g)$
$3C_2H_2(g)= C_2H_6(g)+4C(s)$	$SiCl_2(g)+3/2H_2(g)=SiH_3Cl(g)+1/2Cl_2(g)$
$4C_2H_2(g)= C_3H_8(g)+5C(s)$	$SiCl_2(g)+ H_2(g)=SiH_2Cl_2(g)$
$C_2H_2(g)=2C(s)+H_2(g)$	$SiCl_2(g)+ 1/2H_2(g)+1/2Cl_2(g)=SiHCl_3(g)$
$SiCl_2(s)=Si(g)+Cl_2(g)$	$SiH(g)=Si(g)+1/2H_2(g)$
$C_2H_2(g)+Cl_2(g)+2H_2(g)=2CH_3Cl(g)$	$H_2(g)=2H(g)$
$C_2H_2(g)+Cl_2(g)=C(s)+CH_2Cl_2(g)$	$Cl_2(g)=2Cl(g)$
$C_2H_2(g)+3Cl_2(g)=2CHCl_3(g)$	$H_2(g)+Cl_2(g)=2HCl(g)$
$CCl_4(g)=C(s)+2Cl_2(g)$	$2Si(g)=Si_2(g)$
$C_2H_2(g)+Cl_2(g)=2CHCl(g)$	$3Si(g)=Si_3(g)$
$C_2Cl_2(g)=2C(s)+Cl_2(g)$	$SiC(s)=1/2Si_2C(g)+1/2C(s)$
$C_2Cl_4(g)=2C(s)+2Cl_2(g)$	$SiC(s)+C(s)= SiC_2(g)$
$C_2Cl_6(g)=2C(s)+3Cl_2(g)$	$2C(s)=C_2(g)$
$C_2H_2(g)+Cl_2(g)+2C(s)=2C_2HCl(g)$	$3C(s)=C_3(g)$
$CCl(g)=C+1/2Cl_2(g)$	$4C(s)=C_4(g)$
	$5C(s)=C_5(g)$

Based on the results of Kingon *et al.*[145] and Fischman *et al.*[146], Si(*l*)/Si(*s*) is the possible condensed phase(*s*) in Si-C-Cl-H system. However, our calculation indicated that the partial pressures of Si(*g*) is always lower than the saturated pressure of Si(*g*) with Si(*l*)/Si(*s*) (Figure 23) at our gas flow rates provided abundant graphite, so that no condensed Si phase was present after reaching equilibrium. This is consistent with our SiC CVD deposition experiments using polished graphite substrate (Figure 24): no peak of Si was detected. Only the thermodynamic data of cubic SiC was used because at temperatures below 1800^{o}C cubic SiC is the most stable phase, and on the other hand, the difference of Gibbs free energy between cubic and hexagonal SiC is very close. Our polycrystalline SiC deposition experiment on graphite substrate also has demonstrated that at temperatures 1400-1700^{o}C the cubic SiC is the most stable phase and no other phase of SiC is present. Hence we are using cubic SiC in our calculation although step flow growth could occur on the off-axis substrate.

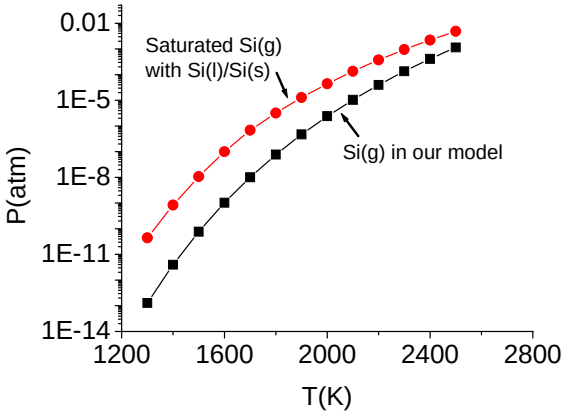

Figure 23. Calculated Si(*g*) pressure and saturated Si(*g*) pressure with Si(*l*)/Si(*s*). The pressure of Si(*g*) in CVD growth is always smaller than the saturated pressure of Si(*g*) with Si(*l*)/Si(*s*). This indicates that condensed Si phases do not exist after reaching equilibrium.

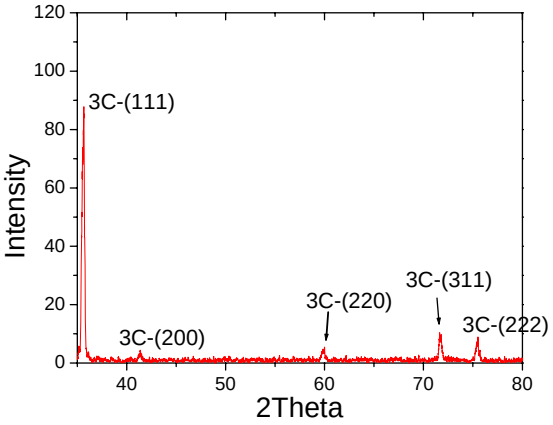

Figure 24. XRD pattern of self-nucleated deposition at 1700°C. No silicon phase was detected and only cubic SiC was present.

Our results (Figure 25) showed that HCl was the most dominant gas species next to H_2 and it constitutes about 10% of the total pressure at all temperatures. This is the main reason for the corrosion in our growth chamber. CH_4 is the dominant carbon source at temperature below 1800K and its pressure decreases while temperature increases. C_2H_2 becomes the dominant carbon source instead of CH_4 at temperatures beyond 1800K and its pressure increases with the increase of temperature. This results from the severer H_2 etching of graphite at higher temperature. $SiCl_2$ is the major silicon carrier at all temperatures and its pressure increases with temperature. H and Cl partial pressures increase while temperature increases because H-H and Cl-Cl bonds are tending to break at higher temperature. Figure 26 shows the percentage of Si source which deposits as SiC at various temperatures. It indicates that after reaching equilibrium, most of Si source deposits as SiC and the amount of SiC deposited at higher temperatures is less than that grown at lower temperatures. This is consistent with our experimental data shown in Figure 22(b) and report by Nigam *et al.*[147] As observed in our experimental data, the growth rate slightly decreases with the increase of temperature. Under such condition, the growth rate is limited by thermodynamics, which can be called "thermodynamically controlled growth". When carrier gas flow rate is high, as in case Figure 22(a), the growth rate is limited by kinetics rather than thermodynamics and growth rate increases

with the increase of temperature.

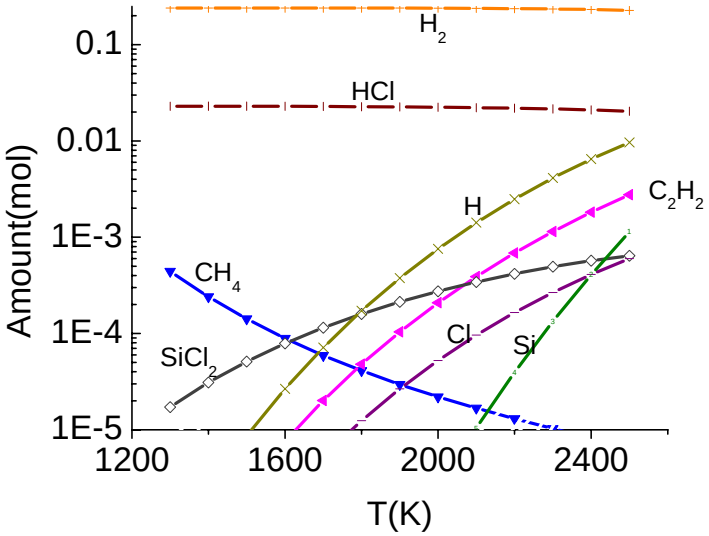

Figure 25. Equilibrium gas species at various growth temperatures. Large amount of HCl exists. CH_4 is the dominant C carrier below 1800K while C_2H_2 dominates beyond 1800K. $SiCl_2$ is the only dominant Si carrier.

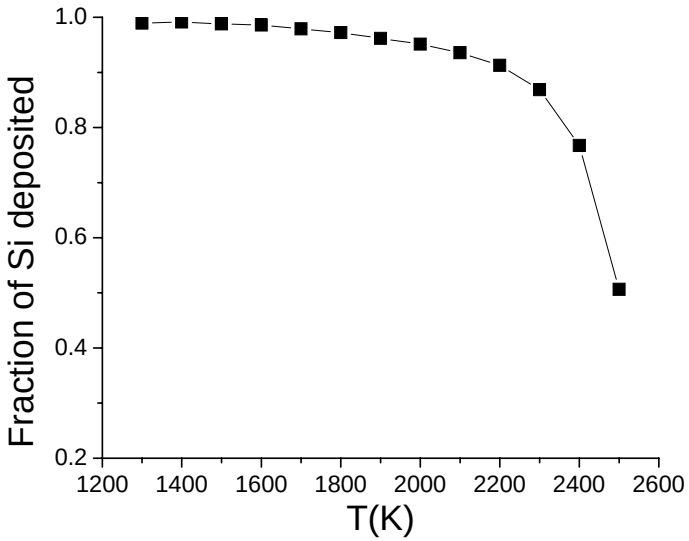

Figure 26. Fraction of Si deposited as SiC at various temperatures. Fraction of Si deposited as SiC decreases as growth temperature increases.

4.4. Characterization of CVD grown SiC epilayers

SiC epitaxial layers grown by CVD were characterized by Nomarski optical microscopy (Nikon Eclipse E600 POL), synchrotron white beam X-ray topography (beamline X19C, Brookhaven National Laboratory) in combination with scanning electron microscopy (LEO Gemini 1550) and molten potassium hydroxide (KOH) etching.

4.4.1. Surface morphology

Epilayers of a few microns thick as well as 100-200 μm thick have been successfully grown. Figure 27 shows a typical optical cross-sectional image of the grown layer (transparent layer is the epilayer, thickness is 126μm). Figure 28 shows the comparison of CVD epilayer on on-axis substrate and off-axis substrate. Macro-steps are clearly seen on on-axis substrate. The 8^{o} off-axis epilayer showed mirror-like surface.

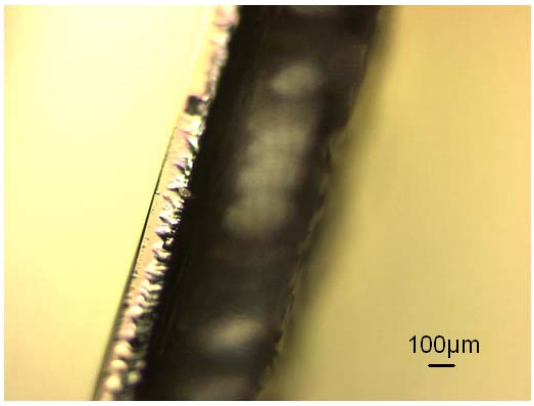

Figure 27. Typical cross-sectional view of grown layer.

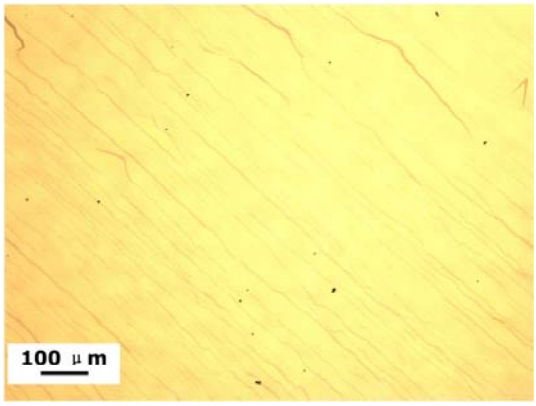

(a)

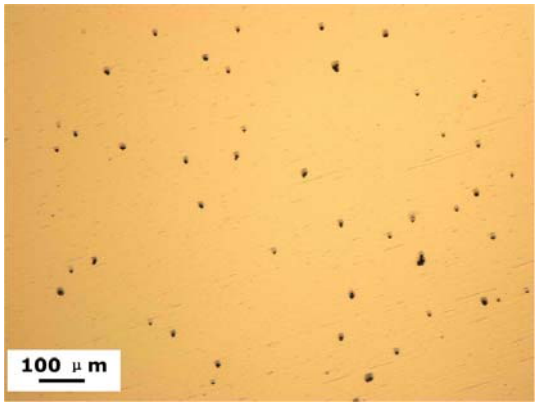

(b)

Figure 28. Surface morphology of epilayers on an on-axis *6H*-SiC substrate (a) and an 8^{o} off-axis *4H*-SiC (b). They were grown in the same experiment by loading two substrates side by side.

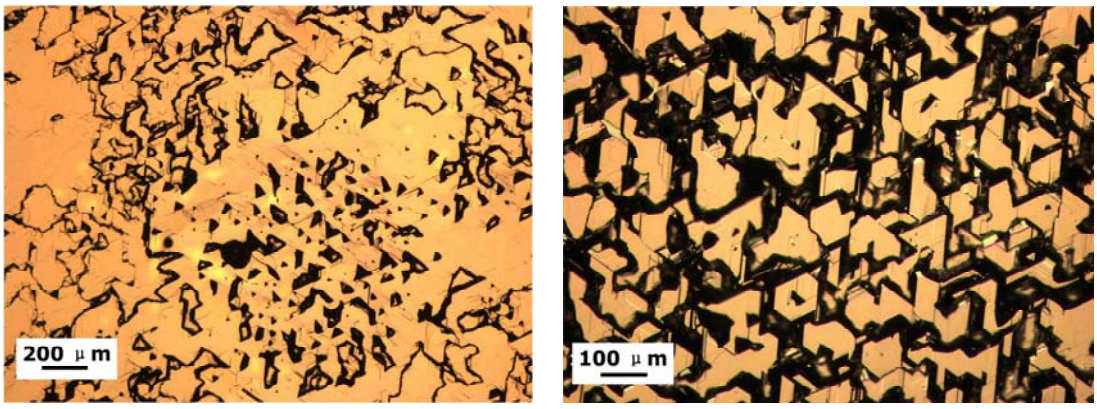

(a) (b)

Figure 29. Optical micrograph of epitaxial layers grown at 1600°C. (a) Epilayer grown on an on-axis *6H*-SiC substrate, 146µm/hr. (b) Epilayer grown on an 8° off-axis *4H*-SiC substrate, 155µm/hr.

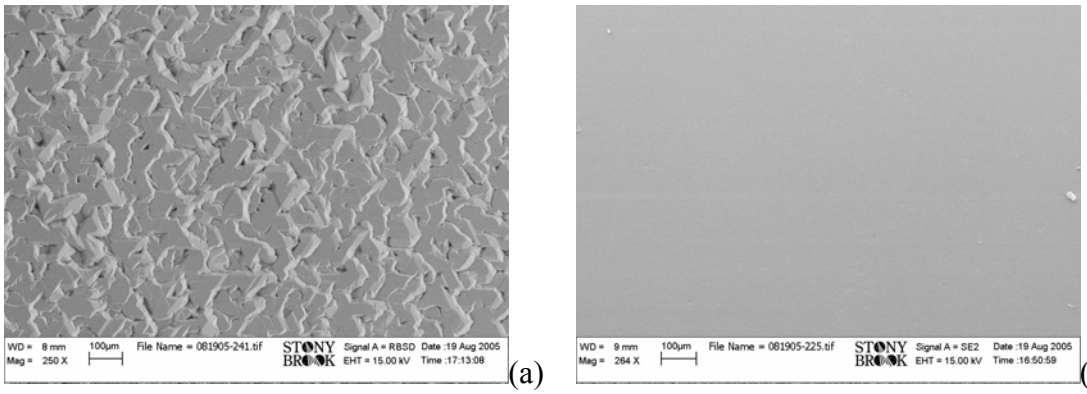

(a) (b)

Figure 30. (a) Epitaxial layers grown on an 8° off-cut (0001) *4H*-SiC at high growth rate (140µm/hr) show very rough surface due to the nucleation of large numbers of islands'; (b) Epitaxial layers grown on an 8° off-cut (0001) *4H*-SiC at low rate (4µm/hr) show smooth surface morphology.

Figure 29 shows the surface morphology of SiC epilayer at very high growth rate on on-axis and off-axis substrates at 1600°C. At very high growth rate, 2D nucleation dominates in both substrates (including off-axis substrate) and optical images show clearly the islands nucleated. This high growth rate caused large amount of polytype inclusions, especially cubic phase and this could be verified by transmission Laue pattern. Growth rate has to be lowered to prevent 2D nucleation. Figure 30 compares the rough surface of the high growth rate epilayer (140 µm/hr) with smooth surface morphology of epilayer at low growth rate (4 µm/hr). No growth islands and associated grain boundaries are seen in the microscope and this film showed narrow rocking curve which proved the high quality of this low growth rate epilayer. Thus, the growth rate and temperature need to be optimized to grow high quality epilayers.

A novel hydrogen defect etching technique was also developed to obtain the location and distribution of the micropipes present in the substrate. This hydrogen assisted etching was performed with $SiCl_4$ at 30 sccm and C_3H_8 at 5~10 sccm. The

etching pressure is 200 Torr and etching temperature is 1700^{o}C. Figure 31 shows a typical optical micrograph of growth assisted surface etching. Hillock-like features containing micropipes at the center are actually etch pits and this fact was confirmed by studying under the Nomarki microscope. Also the X-ray topographic image recorded for the same wafer confirms the one-to-one correspondence between hillock-shaped etch pit and the micropipe out-crop shown in the topograph (Figure 32). During the hydrogen defect etching a small amount precursor gas at C/Si =0.5~1 ratio is passed. A possible mechanism is suggested here: both detachment of units in the crystal lattice due to the etching as well as reassembly of the growth units due to the precursor gases proceed simultaneously to different degrees resulting in stabilized etch pits at micropipe out-crops, while uncontrolled etching shows no clear information (inset in Figure 31). This hydrogen defect etching can be conveniently performed inside the reactor chamber and can reveal the presence of micropipes without ambiguity. Figure 33 shows a magnified image of an etched pit surrounding a micropipe showing beautiful spiral steps.

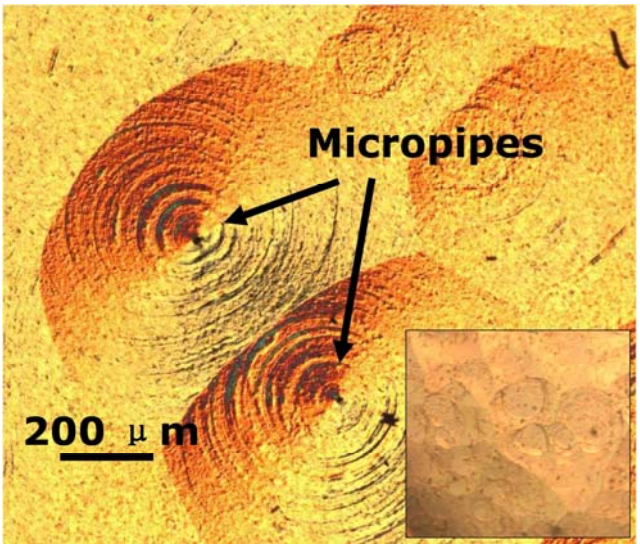

Figure 31. Typical growth assisted etching pattern showing micropipe centered etch pits. Inset shows uncontrolled etching.

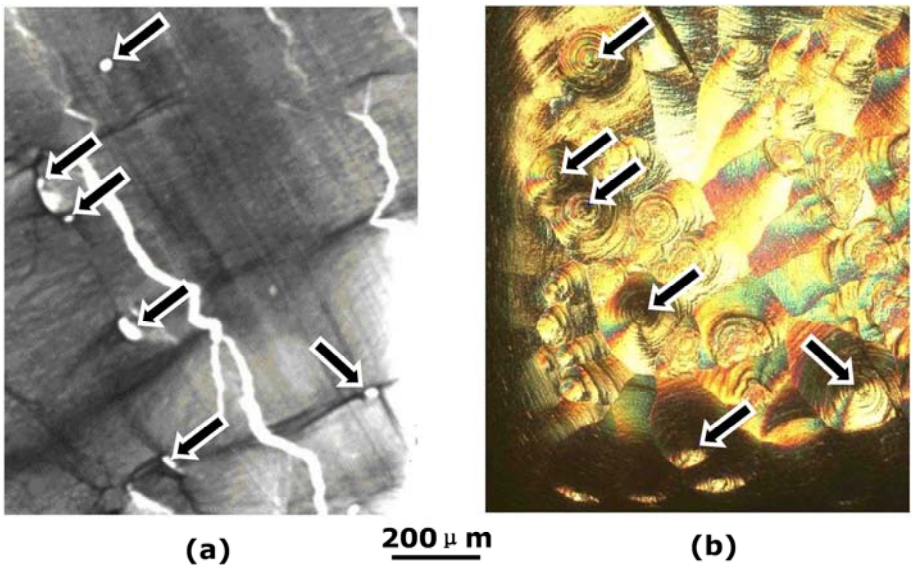

Figure 32. The back reflection synchrotron x-ray topograph (a) and growth assisted etching (b) pictures show the one–to-one correspondence unambiguously. The pointed arrow marks clearly show the presence of six micropipes in both the cases. The hillock-like etch pits in (b) with the pointed tips at the center are due to the micropipes. The flat shaped are probably due to general dissolution.

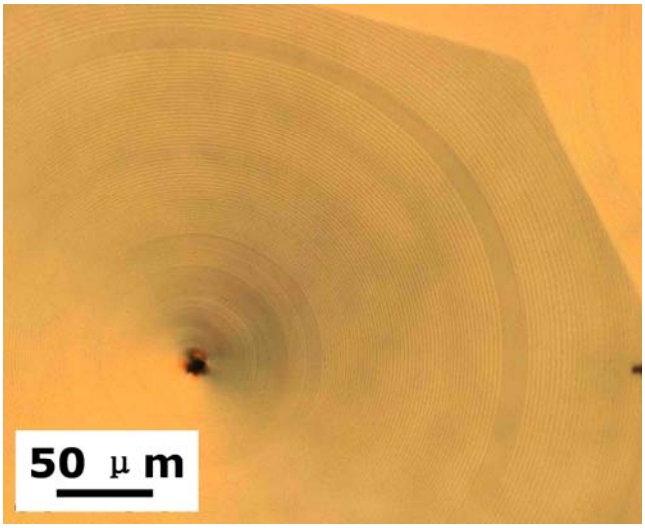

Figure 33. Optical micrograph showing etched steps surrounding a micropipe.

4.4.2. Defect characterization

Growth on on-axis substrates is studied first. On-axis growth is known to be controlled by two-dimensional growth. Growth is realized via either the nucleation of islands followed by expansion of islands or the expansion of screw spirals. The lack of vicinal steps on substrates gives no step template for the epitaxial layer. Thus, there is more chance that the stacking sequence with the lowest free energy is favored. The coalescence of the misoriented growth islands provides the nucleation sites for dislocations, such as threading edge dislocations and threading screw dislocations. Figure

34 gives the rocking curves of a *6H*-SiC substrate before and after deposition and a broadening of rocking curve is clearly seen after deposition.

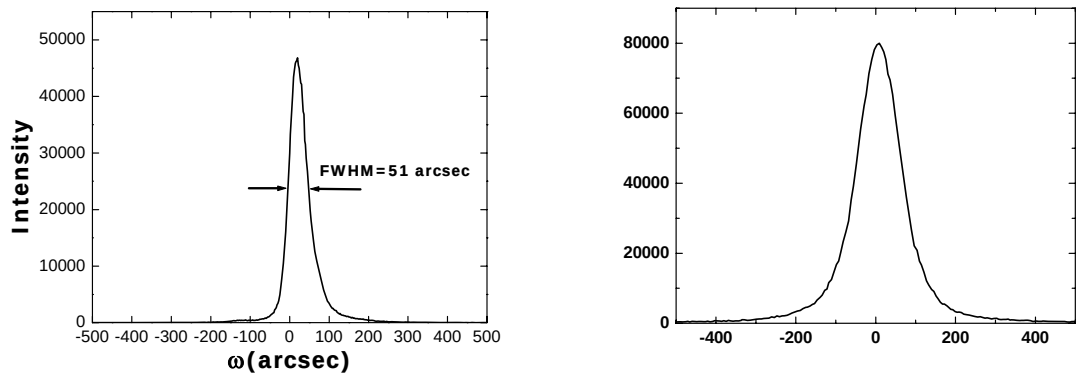

(a) (b)

Figure 34. Rocking curves of before (a) and after epilayer growth (b). Epilayer thickness: 98μm.

Topographs were taken to compare the detailed defect information of the epilayer with that of the substrate for a 6 μm epilayer grown on *6H* on-axis substrate. Figure 35(a) and (b) show the back-reflection topograph and grazing-incidence topograph of epilayer grown on *6H* on-axis SiC substrate. The left region in Figure 35(a), which is the edge of the 2-inch wafer, shows dark contrast. They are grain boundaries resulting from the misorientation between the wafer and the low-quality region surrounding the boule in PVT growth. The BPDs are mostly aligning along one direction <1-210> and this is caused by the thermal stress resulted from thermal gradient in the hot-zone (temperature gradient is along <-1010> direction according to the hot-zone design). No new micropipes form in the epilayer. Figure 35(c) and (d) show the magnified picture of the marked regions in (a) and (b), respectively. The micropipes (MP) propagate into the epilayer. TSDs are distributed all over the wafer and act as pinning points for BPDs. No new TSDs were observed. Most of the BPDs have Burgers vectors 1/3[11-20] or 1/3[-1-120] since they disappear in [1-104] topograph (Figure 36). These BPDs are nucleated due to thermal gradients during growth or cooling (up to ~30˚ per min). These should be reduced through slower cooling rates. In [10-14] grazing incidence topograph (Fig. 31), an alignment of screw dislocations along grain boundary is seen. This may contribute to a twist grain boundary.

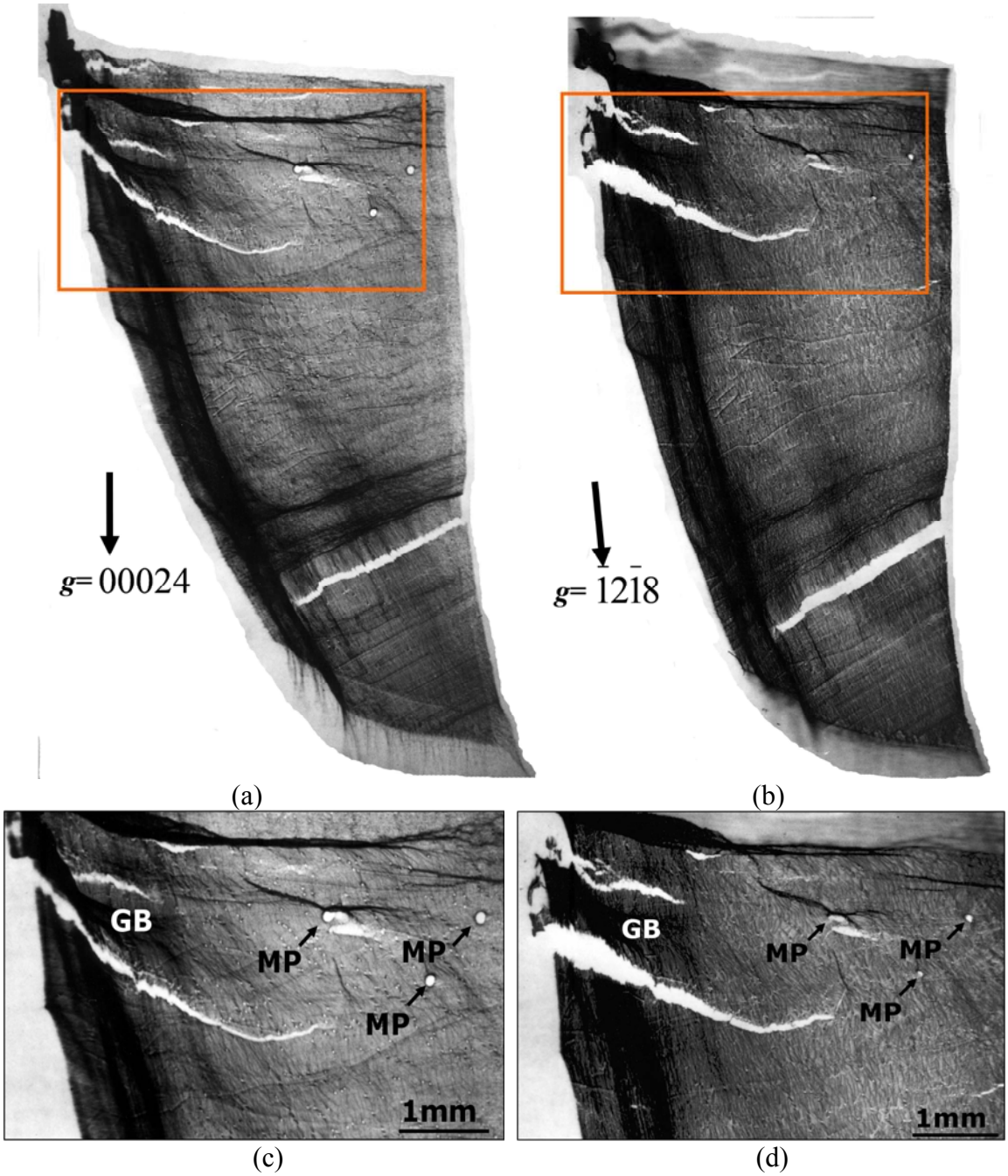

Figure 35. Back reflection (a) and grazing incidence (b) topographs taken from 6μm thick epilayer on *6H* on-axis substrate. (c) and (d) are magnified images from marked regions in (a) and (b), respectively.

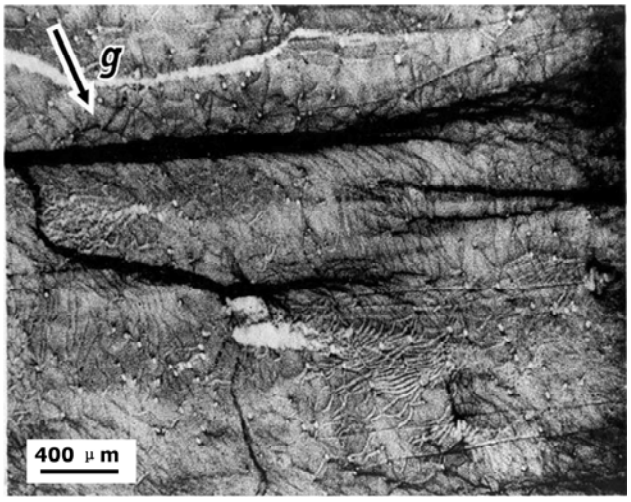

Figure 36. [1-104] topograph of the three-micropipe region in Figure 35. Most of the BPDs are out of contrast. By applying $\boldsymbol{g}\cdot\boldsymbol{b}=0$ rule and knowing that the Burgers vectors of BPDs lie in basal plane, we can know that the Burgers vectors of the BPDs are 1/3[11-20] or 1/3[-1-120].

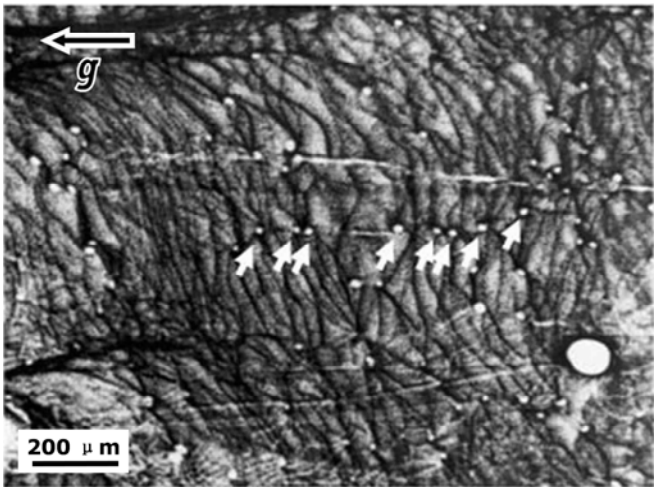

Figure 37. A series of screw dislocations (marked by arrows) align along the grain boundary (can be seen in [10-14] topograph clearly). This may result in the twisted component of the grain boundary.

Some of the white circular dots (corresponding to the TSDs) show different features in the back-reflection topograph and the [-12-18] grazing-incidence topograph. Figure 38 shows the contrast difference of TSDs in two topographs. All TSDs which show contrast difference are marked by a white circle. One possible reason might be the reorientation of the TSDs. The proposed mechanism is explained schematically in Figure 39. Macrosteps form due to layer-by-layer growth near the growth spiral associated with a TSD which then advance towards the dislocation core due to lateral growth, as depicted in Figure 39(a) and (b). At this point the TSD experiences an attractive image force pulling it toward the step surface. The TSD is tilted due to the combination of image forces from both the step surface and the free surface above [Figure 39(d)] or, the TSD is bent completely into the horizontal direction [Figure 39(e)] and an edge segment forms. We are going to discuss the bending of TSDs into basal planes in Chapter 12. Then the image force from above the free surface is tending to pull the TSD up [Figure 39(e)]. Both of the tilted TSDs in (d) and (f) have line component $\boldsymbol{u_E}$, which shows the edge component of the tilted TSD. The contrast of TSD is weakened due to the tilt of TSD. The edge segment in horizontal region and/or edge component of the tilted TSD possibly caused the dark contrast observed in the grazing-incidence topograph.

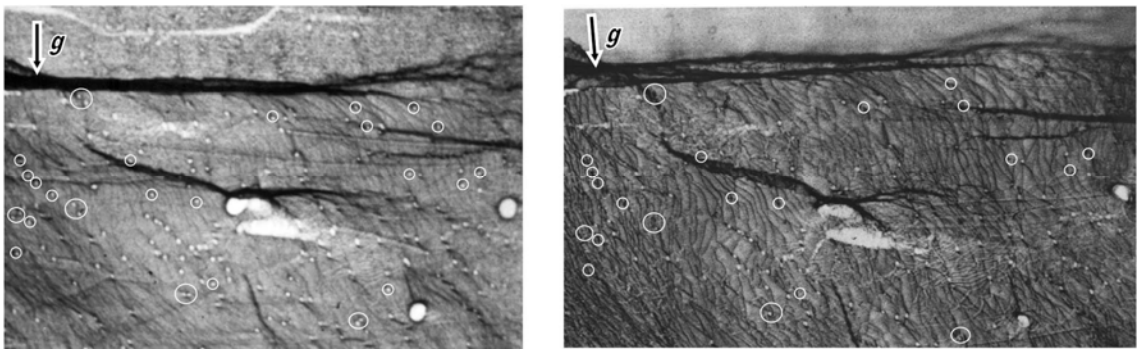

(a) (b)

Figure 38. [000.24] back-reflection topograph (a) and [-12-18] grazing-incidence topograph (b) of 6μm epilayer on an on-axis *6H*-SiC substrate. All TSDs which show contrast difference are marked by a white circle.

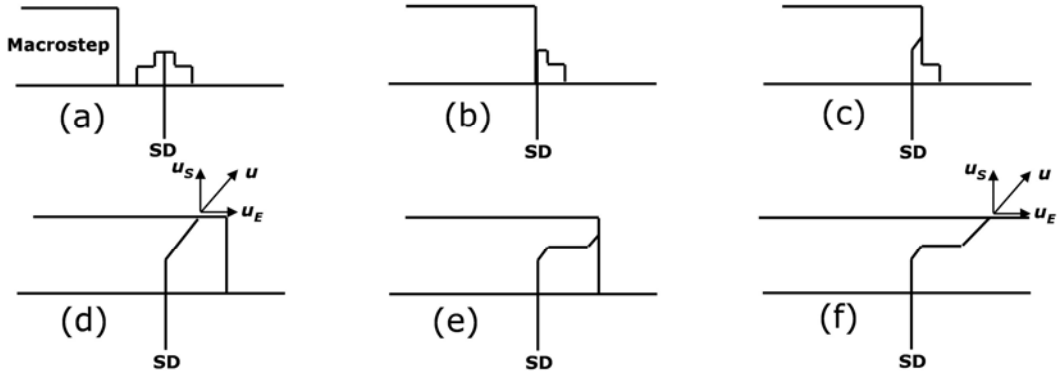

Figure 39. Schematic diagram showing the redirection of screw dislocation. (a) macrostep approaching the spiral associated with a TSD; (b) macrostep reaches the TSD by lateral growth; (c) redirection of TSD caused by the image force from the step surface; (d) tilted dislocation due to the image force from above the free surface and the tilted dislocation shows screw component ($\boldsymbol{u_S}$) and edge component ($\boldsymbol{u_E}$); or (e) complete bending of TSD and image force from above surface causes the redirection of dislocation upward; (f) tilted dislocation showing screw component ($\boldsymbol{u_S}$) and edge component ($\boldsymbol{u_E}$).

Molten potassium hydroxide (KOH) etching was used to map the threading edge dislocations (TEDs). The sample was immersed in molten KOH at 500℃ for 10 mins and cooled down to room temperature then rinsed in water. TED walls were observed to be associated with the low angle grain boundaries [top right corner in Figure 40(a) and the long line in Figure 41]. Other than grain boundaries, TEDs distribute more or less uniformly around the whole sample. Although TEDs can be clearly mapped by KOH etching, BPDs cannot be observed and MP etch pits cannot be distinguished from the ones from TSDs clearly. Figure 40(b) shows the magnified "MP II" region in Figure 40(a). Other than the etch pit from MPs, the other two large etch pits come from the two TSDs. The pit dimensions are similar between the TSDs and MP. Inset is the magnified MP etch pit showing hexagonal shaped hollow core with diameter ~2μm. BPDs lie in the *c*-plane and no etch pits associated with the BPDs can be observed for the on-axis sample. The information of BPDs provided by etching is very limited.

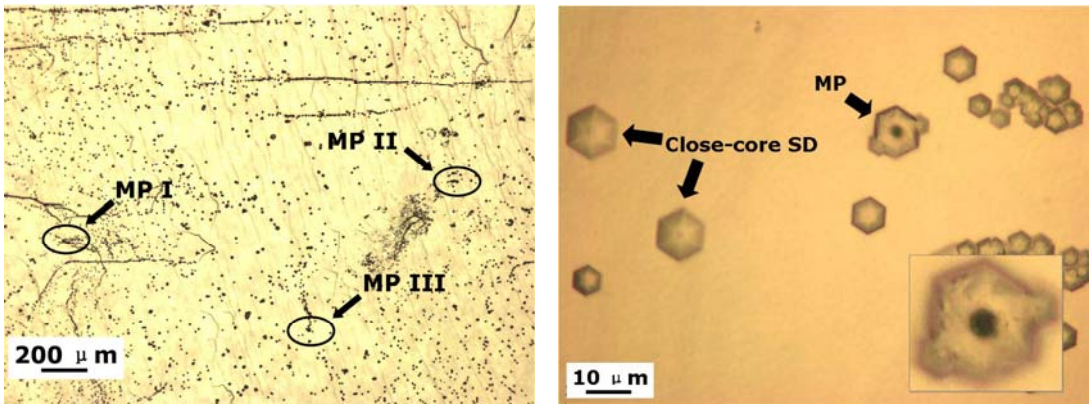

(a) (b)

Figure 40. (a) Optical micrograph of epilayer grown on an on-axis *6H*-SiC substrate after KOH etching; Micropipes are located in the circled regions (etching pits of MPs cannot be differentiated clearly). (b) The magnified picture of "MP-II" region. Although threading edge dislocations can be mapped, BPDs cannot be detected and also micropipes cannot clearly be seen.

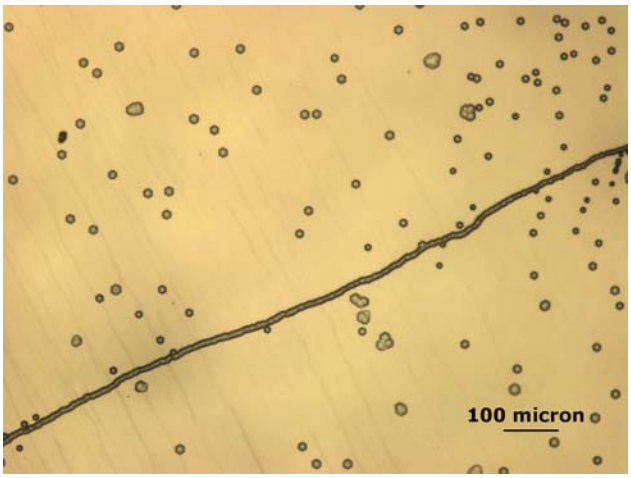

Figure 41. Optical image of etched *6H*-SiC showing a line of TED etch pits.

Epitaxial films with high growth rate on on-axis *6H*-SiC substrates were also studied. Back-reflection was used to study the defect information in epilayer since in this case back-reflection shows mostly the defect information in epilayer due to large thickness (113µm). Figure 42(a) and (b) are the back-reflection topographs before deposition and after deposition, respectively. The topographic image was deformed after deposition, which is due to the residual strain in the film. One could also see the small dark contrasts distributed around the epilayer image, which are low angle grain boundaries resulted from the 2D growth where two growth islands coalesce. The major low angle grain boundaries and micropipes in the substrate were all replicated in the epilayer. Contrast of some micropipes was concealed by the contrast from the highly strained film.

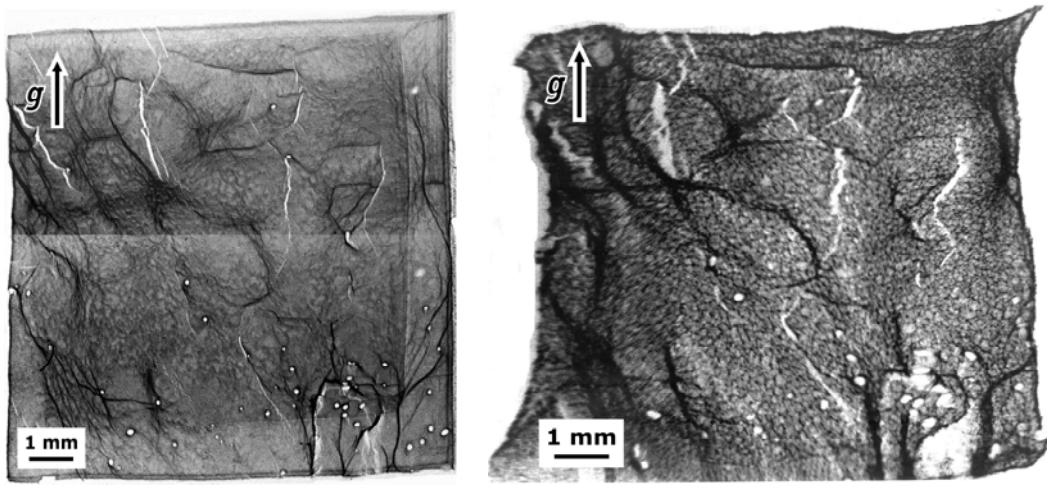

(a) (b)

Figure 42. Back reflection topographs taken before (a) and after (b) deposition. Growth temperature is 1500°C and thickness is 113μm grown in one hour. Substrate is on-axis *6H*-SiC. Highly strained film deformed the diffraction pattern.

SWBXT was used to record the diffraction image of the substrate and epilayer on 8° off-axis *4H*-SiC substrate. Figure 43 and Figure 44 are the topographs recorded from epilayers grown on an 8° off-axis *4H*-SiC substrate at 1500°C and 1600°C, respectively. Unfortunately, due to the high density of dislocations in the substrates and overlapping of their stain fields, not much information can be observed from the topographs. Thus, HRXRD is used to study the *4H* epitaxial sample.

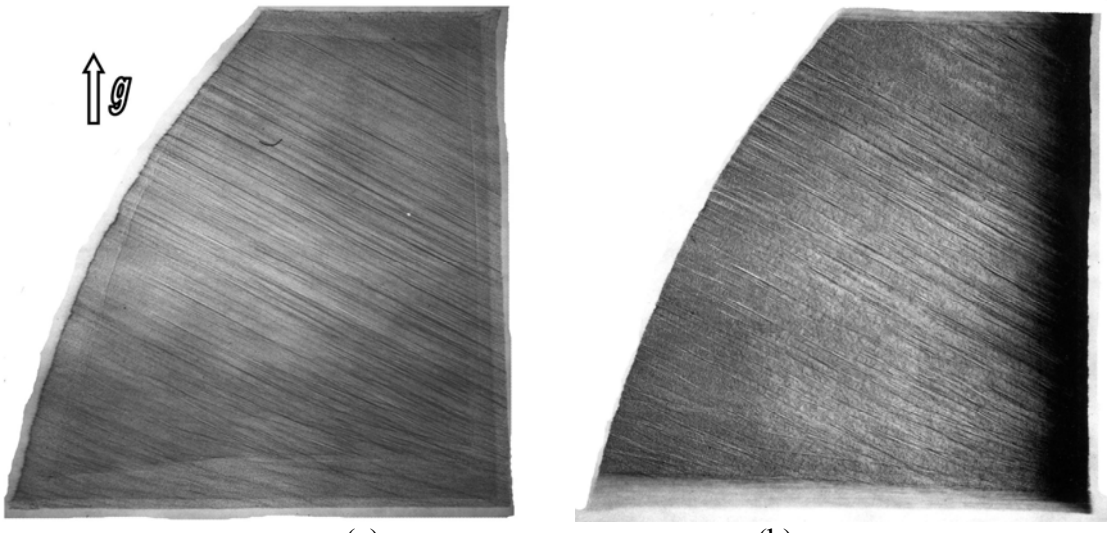

(a) (b)

Figure 43. Back reflection (a) and grazing incidence (b) topographs of epitaxial film on an 8° off-axis *4H*-SiC substrate. Growth temperature is 1500°C and thickness is 2.7μm.

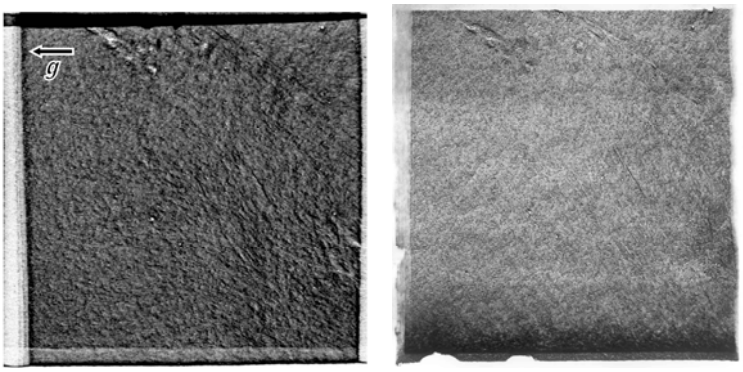

(a) (b)

Figure 44. (a) Back-reflection topograph of substrate. g=(00016). (b) Grazing-incidence topograph of substrate with epilayer. Growth temperature is 1600°C and epilayer thickness is 10.6 μm.

Figure 45 shows two reciprocal maps recorded from sample with (a) and without (b) epilayer. The epilayer was deposited at growth rate of 155 μm/hr on 8° off-cut *4H*-SiC substrate. Substrate mapping in (a) shows a narrower peak in the horizontal direction in comparison to the vertical direction. After deposition the peak in the reciprocal space mapping expanded along horizontal direction. In reciprocal space mapping, the horizontal direction indicates mainly the tilt information and vertical direction indicates the *d*-pacing. The broadening of peak in this sample is caused by the two-dimensional island nucleation (growth rate is so high that 2D nucleation dominates over step-controlled growth) and thus the broadening of the peak along horizontal direction is seen. The coalescence of islands is able to be observed in optical image Figure 29(b) and SEM image Figure 30(a). Figure 40 is the reciprocal space map of the other epilayer on 8° off-axis *4H*-SiC substrate cut from the same wafer. It was grown at much lower growth rate and controlled by step-flow mode where mirror-like surface morphology was achieved and no growth islands could be seen under optical microscope. The layer-by-layer replication realized by advancing of steps experiences much less chance of island formation and the epilayer shows similar a peak to the substrate vertically and horizontally.

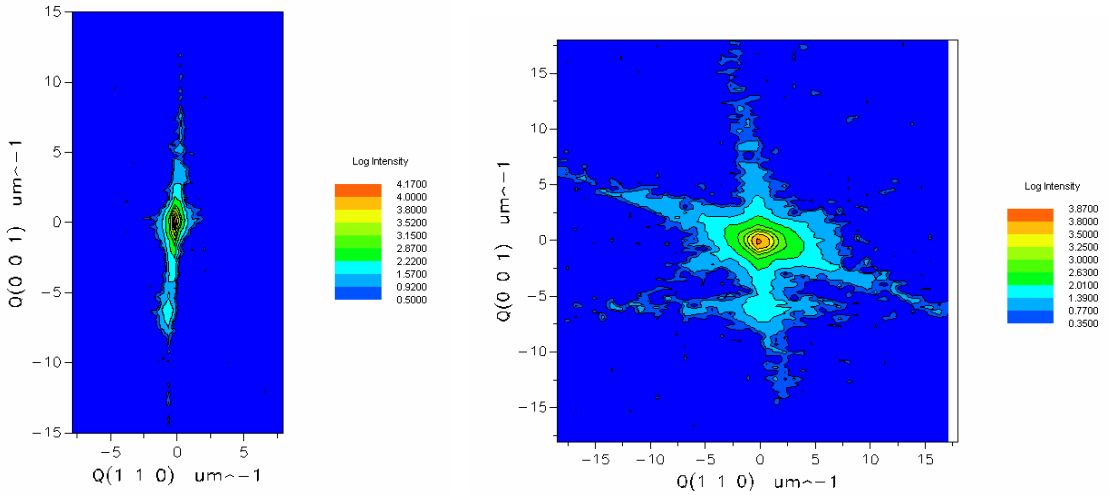

(a) (b)

Figure 45. Reciprocal space maps before (a) and after (b) growth on an 8° off-axis growth sample. T=1700°C, growth rate is 155μm/hr. The peak expanded in the horizontal direction. This is caused by the misorientation between growth islands.

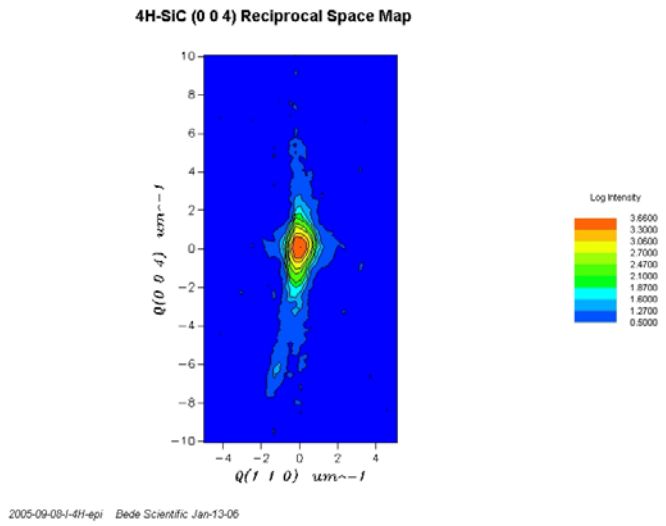

Figure 46. Reciprocal space map of step-controlled growth on an 8° off-axis *4H*-SiC substrate (10.6μm/hr). Peak width in horizontal direction proves a much better control of grain tilting compared to island dominated growth.

Figure 47 shows double crystal HRXRD rocking curves for the 8° off-axis *4H*-SiC substrate before and after deposition. Interestingly, instead of broadening, the rocking curve became narrower after deposition, although the same location was measured before and after growth. As we observed before, epilayer replicates almost all of the grain boundaries, TSDs and MPs from the substrate. In the meanwhile, conversion and even annihilation of dislocations can possibly happen. Although we have observed the change of TSD contrast between substrate and epilayer, this could not account for the narrowing of rocking curve because this happens only for a very small percentage of TSDs. In the growth on off-cut substrate, BPDs intersect the substrate surface and they have to propagate into the epilayer during CVD growth in order to conserve the Burgers vectors. In the meantime, previous studies indicated that most of the BPDs were bent into the growth direction during CVD growth.[148] Image force provides the driving force of such reorientation. Once BPDs are bent into *c*-direction, they do not contribute to the broadening of rocking curve using basal plane reflection because they do not result in basal plane tilt any more.[149] It has been observed that nearly all the BPDs intersecting the substrate surface were converted into TEDs. Figure 48 is a monochromatic XRT image showing the conversion of BPDs in the slip bands into TEDs after CVD growth: each dark line (BPD) is connected with a white dot (TED) in its end. Therefore, bending of BPDs in epilayer growth accounts for the narrowing of FWHM in HRXRD.

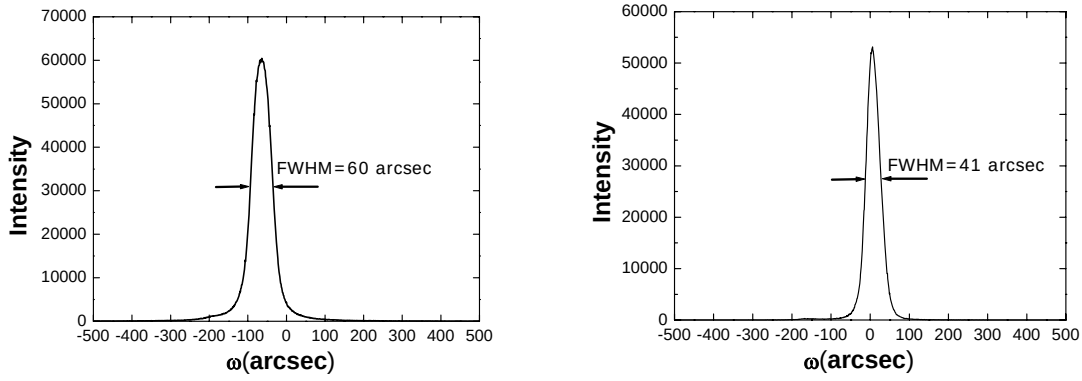

(a) (b)

Figure 47. Double crystal rocking curves of an 8° off-axis *4H*-SiC substrate before (a) and after (b) epitaxial layer growth. The epilayer shows narrower FWHM than the substrate.

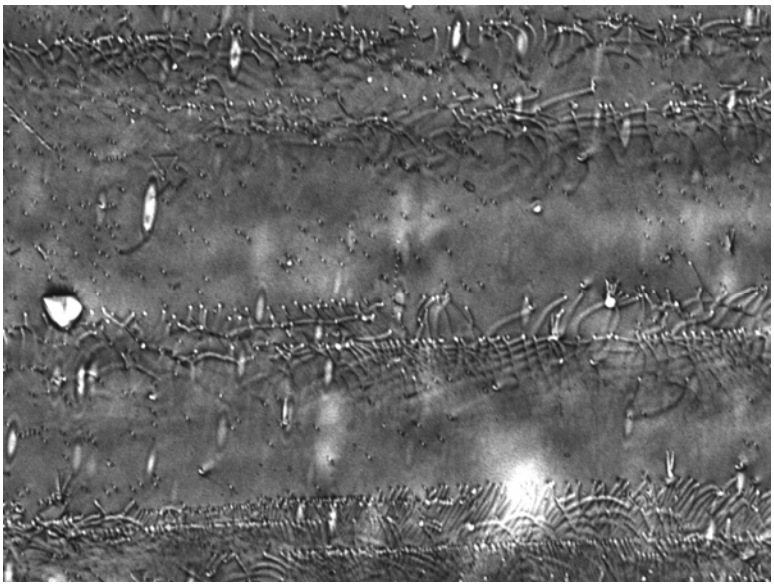

Figure 48. Grazing-incidence XRT showing the conversion of BPDs into TEDs after CVD growth.

5. Investigation of low angle grain boundaries in SiC

5.1. Outline

The interactions between basal plane dislocations (BPDs) and threading screw/edge dislocations (TSDs/TEDs) in hexagonal SiC have been studied using synchrotron white beam x-ray topography (SWBXT). TSDs are shown to strongly interact with advancing BPDs while TEDs do not. A BPD can cut through an individual TED without the formation of jogs or kinks. The BPDs were observed to be pinned by TSDs creating trailing dislocation dipoles. If these dipoles are in screw orientation segments can cross-slip and annihilate also potentially leaving isolated trailing loops. The three-dimensional (3D) distribution of BPDs can lead to aggregation of opposite sign edge segments leading to the creation of low angle grain boundaries (LAGBs) characterized by pure basal plane tilt of magnitude determined by the net difference in densities of the opposite sign dislocations. Similar aggregation can also occur against pre-existing prismatic tilt boundaries made up of TED walls with the net difference in densities of the opposite sign dislocations contributing some basal plane tilt character to the LAGB.

5.2. Introduction

It is believed that the influence of LAGBs on device performance is related to the presence of BPDs which in part comprise them. Although the properties and formation mechanisms of micropipes have been studied by many researchers[11] and much effort has been made to reduce their density, the behavior of the BPDs and the formation mechanisms of LAGBs have not been studied in great detail. In this chapter we will examine interaction processes between the BPDs and threading dislocations in SiC crystals. We will also demonstrate that the understanding of such dislocation interactions provides critical insight not only into the evolution of the 3D BPD distributions in the crystals but also sheds light on their role in the formation mechanisms of various kinds of LAGBs.

5.3. Experimental

The SiC crystals used in this study were commercially available wafers grown by the PVT technique. Wafers were thinned down to 30~90 μm to reduce the dislocation image overlap on transmission topographs. Back-reflection and transmission geometry topographs were recorded following the thinning down process. Back-reflection topographs mainly revealed information on the TSDs while transmission topographs revealed complete information on the distribution and configuration of the BPDs. The imaging was carried out at the Stony Brook Synchrotron Topography Station, Beamline X-19C, at the National Synchrotron Light Source at Brookhaven National Laboratory, using Agfa Structurix D3-SC film at a specimen-to-film distance between 10 and 15 cm. The Si-face side is always the x-ray exit surface.

5.4. Results and Discussion

5.4.1. Interaction between a BPD and a single/well-spaced TD

BPDs are mostly nucleated at the outer region of the as-grown SiC boules which contain polytype inclusions and large angle grain boundaries. Meanwhile, the resolved thermal shear stress near the periphery of the boule or seed-mounting surface has been simulated to be large enough to lead to dislocation glide.[150] The BPDs glide under thermal shear stress toward the center of the boule and encounter a forest of threading dislocations (TDs, including TEDs and TSDs/MPs). TEDs are dislocations aligned along the *c*-axis with Burgers vectors of 1/3<11-20> (tilting of the TED away from the *c*-axis can result in partially mixed character) and TSDs are dislocations with line direction and Burgers vector along [0001]. The Burgers vectors of TSDs can be ***nc***, with larger values of *n* leading to hollow-cores, minimizing strain energy according to Frank's rule.[151] TEDs and TSDs have different influence on the glide of BPDs.

The interactions between the advancing BPDs and the SDs and TEDs can lead to the complicated dislocation tangles often observed in SiC. Our observations indicate that threading SDs act as effective pinning points for the advancing BPDs whereas the well-spaced or individual TEDs do not. This is illustrated in Figure 49 which shows a (-12-10) transmission topograph (a) and a (11-28) grazing incidence topograph from the same region of *4H*-SiC substrate with epilayer. Note the curved BPD segments which appear in (a) but not in (b), which means that they are located in the substrate since the penetration depth in (b) is only half the epilayer thickness (i.e., 10 μm). Detailed analysis shows that almost every junction between BPDs in (a) corresponds to a TSD in (b) (some of these are marked by arrows). While individual or well-spaced TEDs initially pin the advancing BPDs, they do not act as effective barriers to their motion because the BPD can cut through the TEDs without interruption. The interaction of BPDs with TEDs and TSDs are to be discussed separately below.

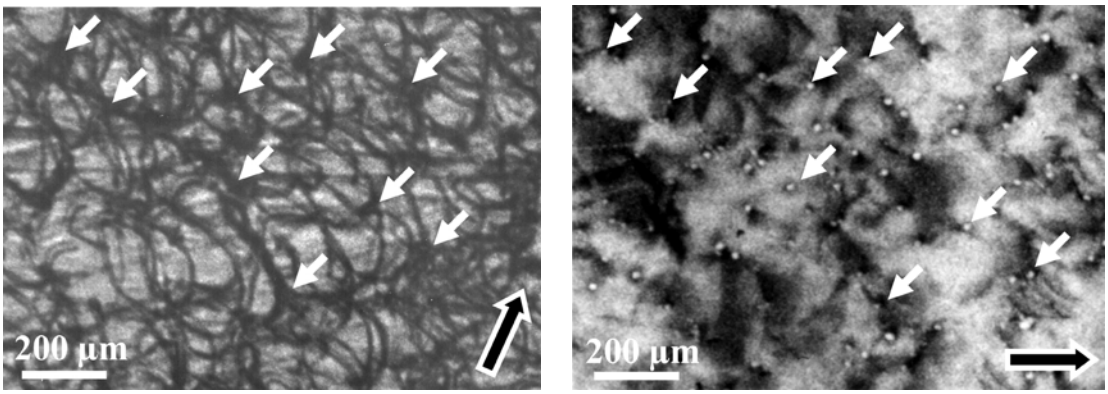

Figure 49. Transmission x-ray topograph [(a), g=[-1-120]] and grazing incidence [(b), g=[11-28]] of 20 μm epilayer on 8^{o} off-cut *4H*-SiC substrate. Circular BPDs anchored by SDs are seen. Some anchor points are marked by arrows. Grazing-incidence topograph in (b) was recorded by Dr. W. M. Vetter.

When a BPD is gliding on its primary slip plane (the basal plane) and encounters a TD, interactions occur in two stages. First, the long range strain fields of the two dislocations will interact. The force exerted on a BPD by a TED has been calculated to have only ***c*** component (as per the Peach-Koehler equation) which does not affect the glide of the BPD on its primary slip plane. In contrast, the force exerted on a BPD by a TSD is always in the *c*-plane and this force is significant close to the TSD core. This force will change the line shape of the BPD near the TSD core before the BPD gets pinned by the TSD. Following this interaction between the strain fields, the BPD can either cut through the forest dislocation creating kinks or jogs on each dislocation (each equal to the Burgers vector of the other), or get pinned, generating a trailing dipole if the formation of kinks or jogs is energetically unfavorable. In the case of a TED, a BPD can cut through the TED creating a kink on the BPD and a kink/jog on the TED if the formation of kink/jog is energetically favorable. If the creation of kinks/jogs is unfavorable, the "cutting through" of a TED by a BPD can be achieved by bowing out and self-annihilation of BPD arms, without leaving dislocation segments behind, since the TED does not change the slip plane of the BPD. The mechanism is schematically illustrated in Figure 50. As the BPD moves towards the TED (a), the two segments I and II [shown in (b)] of BPD swing independently around the TED pinning point. The portion where they meet together [dashed line in (c)] is annihilated since they have the same Burgers vector but opposite sign. Eventually, the BPD effectively passes through the TED without the need for the formation of any jog, kink or additional dislocation. Thus, a BPD can cut through a single TED regardless of the thermal shear stress conditions. In the case of a TSD, the spiral shape of the lattice planes surrounding the TSD core splits the pinned BPD into two segments gliding on two parallel slip planes separated by the TSD Burgers vector. Even if the formation of a [0001] jog is energetically favorable on the BPD, this would likely be sessile because of the difficulty in activating the secondary {1-100}<11-20> slip system.[152] Thus, a single or well-spaced TED does not act as obstacle for the glide of BPDs while a TSD should act as an effective pinning point for BPDs.

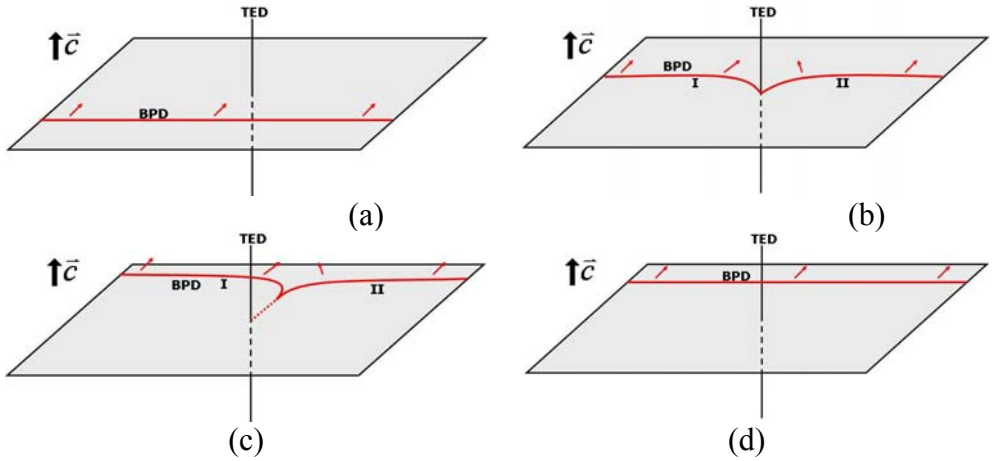

Figure 50. Interaction of BPD with TED. (a) BPD is approaching TED; (b) after BPD meets TED, segments I and II swing around; (c) the portion where segments I and II meet with each other is annihilated (dashed line); (d) BPD passes through TED without generation of jog/kink/additional dislocation.

Most of the TSDs are observed to act as pinning points for the BPDs, because of the much larger energy needed to generate kinks/jogs in these dislocations due to the large Burgers vectors of the TSDs. On the other hand, due to the spiral shaped lattice planes surrounding the TSD core, there will be a mutual shift (equal to the magnitude of the TSD Burgers vector) of the two dilsocation arms when the BPD is pinned by the TSD. The dislocation dipole thus cannot simply annihilate with each other in the same way as in Figure 50. However, while most TSDs are observed, using SWBXT, to act as effective pinning points for BPDs, a few are occasionally observed to behave differently. These latter TSDs are observed to be surrounded by BPDs bowing out in different directions so that they must have been cut through by the BPDs without leaving any trailing segments visible to SWBXT. A possible model is proposed to explain this process as shown schematically in Figure 51. Normally a BPD is dissociated into leading and trailing partials with a stacking fault ribbon in between. When the BPD (edge-oriented in this case) advances and meets a TSD, it is pinned and the two dissociated arms swing around [Figure 51(a)]. The two stacking fault arms are now on different basal planes separated by one TSD Burgers vector magnitude because of the spiral shape of the lattice planes surrounding the TSD core. As the stacking fault arms swing around, the leading and trailing partial segments will re-associate into screw orientation, enabling elimination of the fault via cross-slip, as shown in Figure 51(b). Once in screw orientation, the mutual attraction between the two dipole components is equivalent to the force exerted by an applied shear stress of 9.46 GPa, which is more than the *theoretical critical shear stress* of $\mu/30$ under which crystal planes can be sheared without the need for dislocations. This is more than large enough for the BPD dipole to cross slip on the prismatic plane and self-annihilate, leaving behind a [0001] superjog of length equal to the TSD Burgers vector [Figure 51(c)]. As the BPD continues to advance under stress, this process repeats, effectively advancing the superjog on the prismatic plane, allowing the BPD to overcome the influence of the TSD. Similar processes might be expected not only for edge-oriented dislocations, assuming that the trailing perfect dislocation dipoles are able to orient themselves into screw orientation. Such re-orientation and subsequent annihilation has been observed for Shockley partial dislocation dipoles in *4H*-SiC epilayers during electrical stressing.[28]

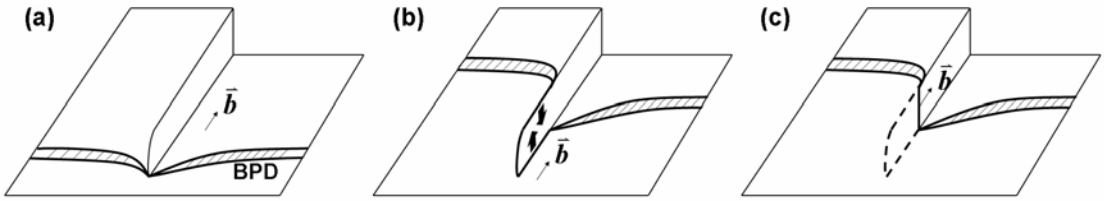

Figure 51. The schematic diagram showing a BPD cuts through a TSD by dragging a superjog behind. (a) Dissociated BPD pinned by a TSD; (b) A screw-oriented dislocation dipole is dragged behind. The force between the two segments in the dipole is more than large enough for them to cross slip. (c) The dipole self-annihilates via cross-slip and a [0001] superjog is created.

5.4.2. Interaction between BPDs and TED wall

TED walls are often observed in SWBXT images or etch patterns. These comprise high densities of TEDs with average spacing ranging from a few tenths to a few microns. The TED walls are observed in most cases to be oriented along <1-100> due to polygonization. As we discussed previously, single or well-spaced TEDs can be cut through by BPDs even at low thermal shear stress. However, the aggregation of BPDs is often observed when a BPDs approach a TED wall as shown schematically in Figure 52(a)-(b) and the SWBXT observation is shown [Figure 52(c)]. As the BPD encounters the TED wall (assuming the TEDs are equally spaced), the BPD is pinned by the TEDs and bow out between them. Dislocation dipoles are created due to the pinning effect of the TEDs [Figure 52(b)]. Figure 52(c) shows an SWBXT image of such interactions. Each segment is on the same slip plane since the TED does not change the slip plane of the BPD. In order for the dislocation dipoles to self-annihilate, a critical resolved thermal shear stress is needed (this critical situation is such that the BPD bows out to a semi-circular shape between two adjacent TEDs under the thermal shear stress). This stress has been proposed to be $\alpha\mu b/d$, where α is a constant, μ is the shear modulus of SiC, b is the magnitude of the BPD Burgers vector and d is the distance between two TEDs.[37] If the resolved thermal shear stress is less than this critical value, the glide of the BPD will be stopped by the TED wall and aggregation of BPDs will be observed. The aggregation of BPDs of various Burgers vectors contributes basal plane tilt character to the LAGB. Similar situations occur if the BPD is dissociated into Shockley partial dislocations bounding a ribbon of stacking fault.

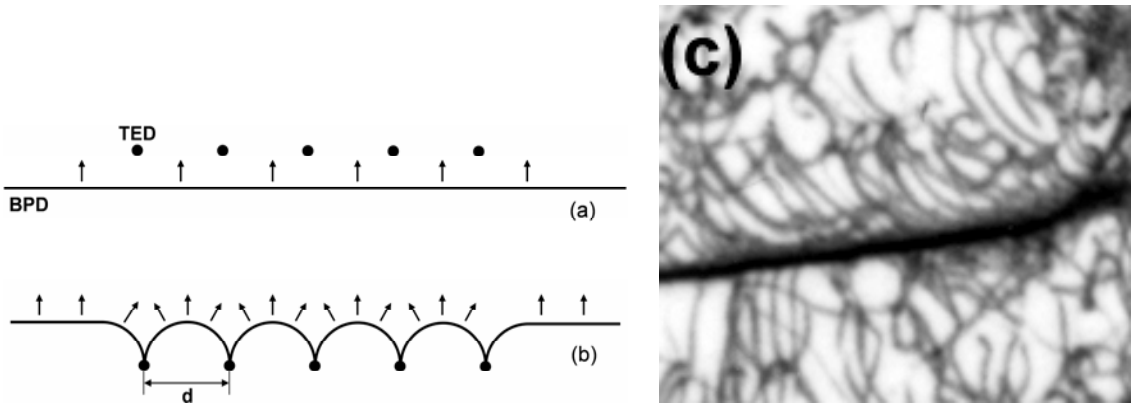

Figure 52. Interaction between a TED wall with a BPD parallel to it. (a) A BPD is approaching toward the TED wall; (b) The BPD is pinned by the TED wall. Dislocation dipoles are created near each TED due to the pinning effect of them. The dislocation dipoles can self-annihilate if a critical resolve shear stress is reached (the BPD segment bows out at a half circle between two adjacent TEDs). (c) SWBXT image showing the aggregation of BPDs at the TED wall.

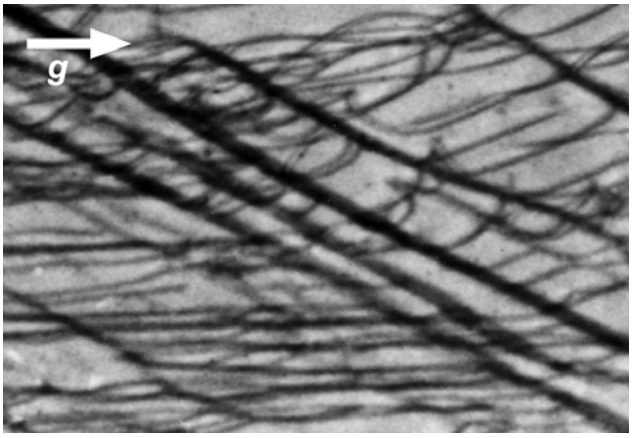

Figure 53. (-1-120) transmission SWBXT image of a PVT grown SiC substrate. Horizontally aligned BPDs interact with LAGBs with TED arrays involved (the LAGBs align at 30^o to the horizontal direction). Uniform contrast along the LAGB indicates that the BPDs do not aggregate at the TED array while they glide.

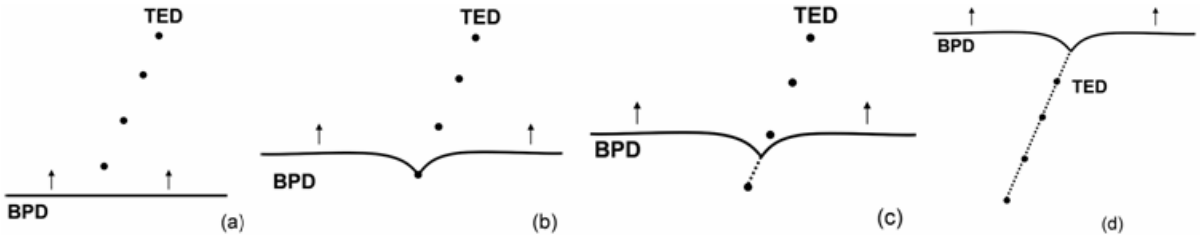

Figure 54. Interaction of a BPD with a TED wall at an angle. (a) A BPD is approaching toward the TED wall. (b) The BPD is pinned by the first TED and two dislocation arms wind around the pinning TED. (c) Dislocation arms annihilate with each other and the BPD cuts through the first TED. (d) Similar process in (b)-(c) occurs as the BPD encounters other TEDs and eventually the BPD overcomes the TED wall even the formation of jog/kink is energetically unfavorable.

If a BPD approaches a TED wall at an oblique angle, a different situation occurs. Figure 54 shows transmission SWBXT images recorded from a PVT grown SiC crystal. Several LAGBs with TED arrays involved are visible (at ~30^o to the horizontal direction). Horizontal BPDs gliding under shear stress are visible and they interact with the TED walls. The uniform contrast along the LAGBs indicates that they do not aggregate against the TED wall (the contrast is from the prismatic tilt caused by the TED arrays). The proposed operating mechanism is shown in Figure 54. When a BPD approaches the TED wall at an oblique angle [Figure 54(a)], it is pinned by the first TED and the two dislocation arms swing around the pinning TED [Figure 54(b)]. The two dislocation arms will eventually meet with each other and self-annihilate because they are opposite-sign dislocations on the same slip plane [Figure 54(c)]. Similar processes repeat [Figure 54(b)-(c)] and the BPD overcomes the TED wall even under very low shear stress [Figure 54(d)].

5.4.3. Low angle grain boundaries in SiC

The temperature gradient during growth or post-growth cooling is one of the main reasons that induce the generation and motion of BPDs. BPDs can be generated on periodically spaced basal planes due to the accumulation of this thermal gradient. The three-dimensional distribution of BPDs in the crystal caused by the thermal gradient will lead to the formation of low angle grain boundaries in SiC. Our observations show that

the LAGBs are mostly composed of edge type BPDs contributing to basal plane tilt and can form with or without the presence of prismatic tilt which is introduced by a TED wall. The observation of an LAGB without a TED wall is shown in Figure 55 where edge segments of BPDs are approaching from opposite sides [all these dislocations disappear on the same (1-100) reflection and are bowing out, under the same thermal shear stress, in opposite directions]. These edge segments are shown to aggregate together to form an LAGB with purely basal plane tilt. This boundary is completely out of contrast on the (1-100) reflection. This proposed process is shown schematically in Figure 56. The LAGB cannot form if there is just one type of BPD because the same sign BPDs will keep advancing under thermal shear stress and polygonization cannot occur. When BPDs of opposite sign meet with each other (b), the pairs of closely spaced BPDs with opposite sign attract each other and most of their strain field is cancelled. Under this scenario, polygonization of BPDs with opposite sign takes place to reduce the total strain energy and the BPDs with opposite sign aggregate vertically near the prismatic (11-20) plane (c). The net difference in accumulated Burgers vector of the opposite sign BPDs determines the magnitude of the basal plane tilt.

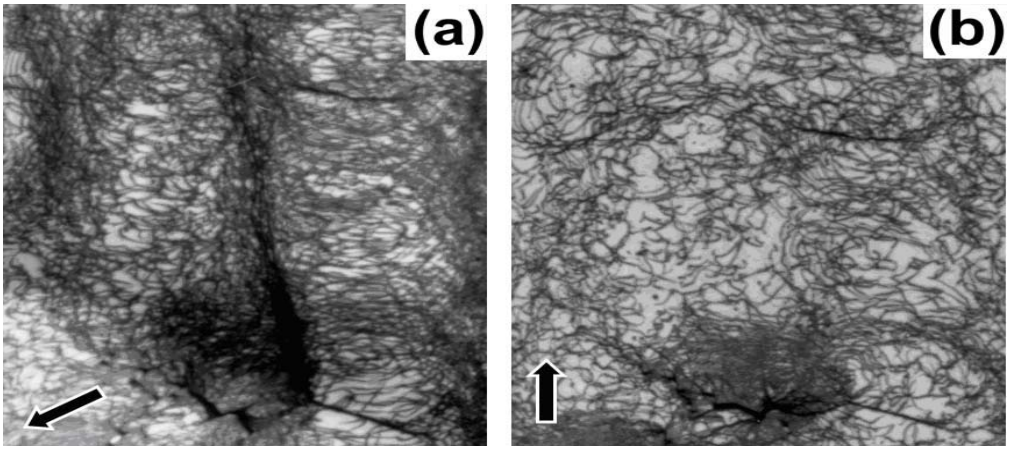

Figure 55. Transmission topographs of LAGB without TED array. (a) g=(01-10); (b) g=(1-100). It has been verified by etching pattern that the TED array does not exist. There is not any clear dislocation along the boundary in (b), which indicates that this LAGB is composed of only edge type BPDs. BPDs which remain in contrast in (b) are from a different slip system.

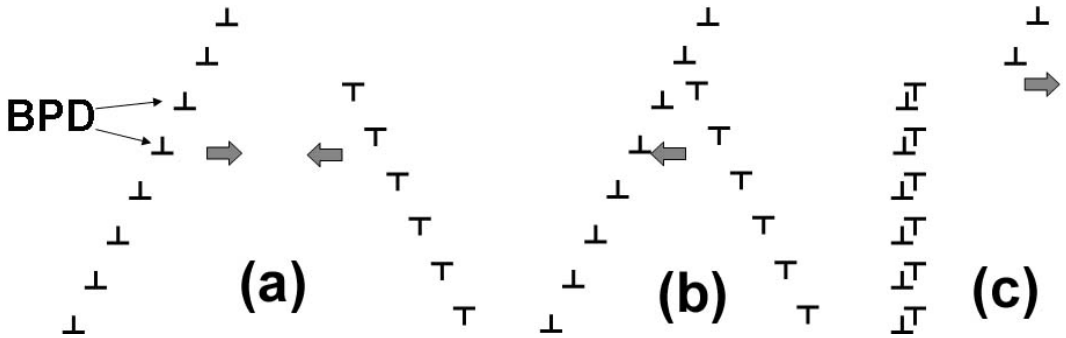

Figure 56. Formation of GB without TED wall. (a) approach of opposite sign BPDs toward each other; (b) BPDs meet with each other and aggregate; (c) polygonization of BPDs near (11-20) plane.

Such aggregation of edge type BPDs can also occur at pre-existing prismatic tilt boundaries comprising TED walls. When opposite sign edge segments of BPDs aggregate against such a prismatic tilt boundary, this modifies the character of the boundary whereby the net difference in accumulated Burgers vector of the opposite sign BPDs contributes some basal plane tilt character to the boundary. Examples of this are shown in Figure 57 and Figure 58 shows a schematic representation of this process. The dislocations that comprise the TED arrays can not glide easily because of the difficulty in activating the secondary slip system (1-100)<11-20> in SiC.[153] When the BPDs from one side arrive at the TED wall (a), they will aggregate there because a high density of TEDs poses a barrier for the advancing BPDs. When more and more BPDs aggregate at the TED wall, the leading BPD can cut through the TED wall because it experiences larger stress due to the pile-up of the BPDs.[154] This is the reason why occasionally we can observe a few BPDs apparently penetrating through the TED walls in Fig.5b. When BPDs with opposite sign also arrive at the TED wall from the opposite side [Figure 57(b)], the two sets of BPDs will polygonize to reduce the total energy [Figure 58(c)] at this time because most of the strain field is cancelled by the interaction between the opposite sign BPDs. The difference in densities of the opposite sign BPDs determines the net basal tilt associated with the LAGB. It should be noted that once the LAGB is formed, further BPDs can aggregate on one side. This is often observed.[155]

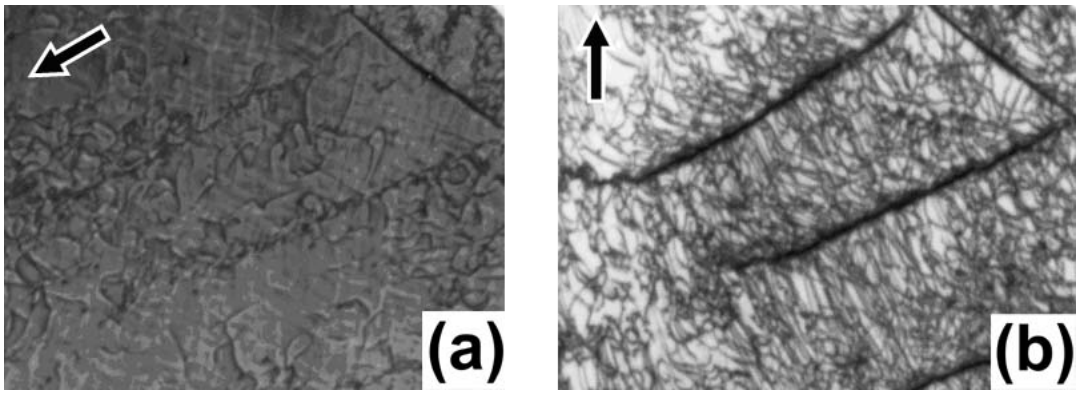

Figure 57. Transmission topographs of LAGB with TED array. (a) g=01-10; (b) g=1-10). It has been verified by etching pattern that the TED array exists. The LAGBs show weak contrast in (a), which indicates that this LAGB is composed of mostly edge type BPDs.

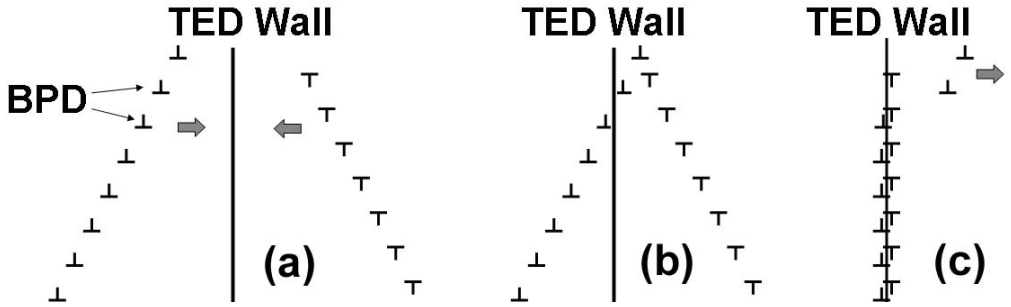

Figure 58. Formation mechanism of LAGB with TED wall. (a) approach of opposite-sign BPDs from both sides; (b) the BPDs from the left side arrive at the TED wall first and some of them can cut through the TED wall; (c) BPDs with opposite sign arrive at the TED wall; (d) polygonization of BPDs at the TED wall.

As we discussed, the LAGBs are composed of different character dislocations and they contribute various types of tilt components. Although LAGBs without TED walls have been observed, TED walls are involved in most cases. BPDs as well as TEDs are major components of the LAGBs although TSDs/MPs are occasionally involved. The various tilt components arise as follows: the TED arrays contribute prismatic plane tilt; edge segments of BPDs lead to the basal plane tilt and TSDs/MPs or screw segments of the BPDs result in the prismatic twist of the LAGB (as illustrated in Figure 59). Here we ignore the segments of kinks/jogs on the TEDs/BPDs. A good summary is given by Ha *et al*.[155]

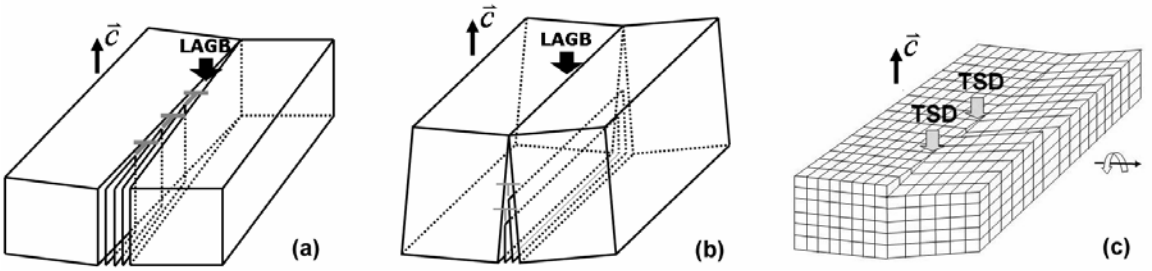

Figure 59. Schematic diagram showing the different tilting components of the LAGB resulting from various dislocations. (a) the prismatic tilt is resulted from the polygonized TED array; (b) edge segments of the BPDs contribute to the basal plane tilt of the LAGB; and (c) the TSDs lead to the prismatic twist of the LAGB. Prismatic twist can also come from the screw segments of the BPDs.

5.5. Conclusion

In conclusion, threading screw dislocations exert strong influence impeding the advancement of basal plane dislocations while threading edge dislocations do not. Basal plane dislocations can cut through the threading screw dislocation by dragging a superjog behind, via successive cross slip of the screw orientation dipole segments which are dragged behind the basal plane dislocations. Interactions between the distributions of basal plane dislocations can induce the formation of low angle grain boundaries. Two cases were observed: (1) where edge type basal plane dislocations of opposite sign are observed to aggregate together to form basal plane tilt boundaries, with the magnitude of the tilt determined by the net difference in Burgers vector between the opposite sign basal plane dislocations; and (2) where similar aggregation occurs against pre-existing prismatic tilt boundaries thereby contributing some basal plane tilt to the boundaries. In both cases, the basal plane dislocations polygonize near the prismatic plane to reduce the total strain energy. Once these low angle grain boundaries are formed, they will propagate as the crystal grows.

6. Interaction between advancing Shockley PDs with TDs

6.1. Outline

Electron-hole recombination enhanced glide of Shockley partial dislocations bounding expanding stacking faults and their interactions with threading dislocations have been studied in *4H* silicon carbide epitaxial layers. The mobile silicon-core Shockley partial dislocations bounding the stacking faults are observed to cut through threading edge dislocations leaving no trailing dislocation segments in their wake. When the Shockley partial dislocations interact with threading screw dislocations, 30^{o} partial dislocation dipoles are initially deposited in their wake. These partial dislocation dipoles quickly and spontaneously snap into screw orientation whereupon they cross slip and annihilate leaving a prismatic stacking fault on the (2-1-10) plane.

6.2. Introduction

The application of devices made from SiC has been hindered by failure issues related to various defects.[33] Recently, the increase in forward voltage drop observed in SiC bipolar devices under forward biasing was attributed to the motion of silicon-core (Si-core) Shockley partial dislocations (PDs) generated by dissociation of perfect BPDs and activated by the electron-hole recombination enhanced dislocation glide (REDG) process occurring along the Peierls valley of the PD.[156] The Si-core PD is found to be mobile while the carbon-core (C-core) PD is stationary.[157] As these expanding stacking faults (SFs) encounter the forest of TDs in these crystals, including TEDs (10^{4}~10^{5}/cm^{2}) and TSDs (10^{3}~10^{4}/cm^{2}), various interactions are expected. These interactions result in a complex web of stacking faults and dislocations that can fill the active region of bipolar devices and degrade their performance. Understanding these interactions can provide insight regarding the mechanisms by which these complex webs of fault are created and may shed light on factors which determine or limit the extent of the deleterious effects of the REDG process. In this chapter, we present studies of the interactions between the advancing Shockley PDs and TSDs/TEDs in *4H*-SiC epitaxial layers that are used in PiN diodes.

6.3. Experimental

The *4H*-SiC substrates used in this study were commercially available wafers grown by physical vapor transport (PVT) technique with an 8° off-cut angle in the [11-20] direction. The epitaxial layer structure is typical for 10 kV PiN diodes. It consists of a 100 μm n^{-} layer capped by a p^{+} layer. The electroluminescence (EL) imaging was carried out *in situ* at 1 A/cm^{2} and electrical stressing was in the range from 1–10 A/cm^{2}. Images were collected in the wavelength range from 600 to 1000 nm using a sensitive setup that is described elsewhere.[158] Grazing-incidence topographs were recorded following the forward bias stressing.

6.4. Results and discussion

Figure 60(a) is a (22-4.12) grazing-incidence SWBXT image of a device cell after forward bias stressing. PDs bounding five SFs, numbered SF1-SF5, are visible on the topograph while the SFs themselves are out of contrast since $\boldsymbol{g}\cdot\boldsymbol{R}$ is equal to an integer for the (22-4.12) reflection, where $\boldsymbol{R}$ is the fault vector of the SF and $\boldsymbol{g}$ is the reflection vector. The x-ray penetration depth on this image is limited to ~17 μm so that only those portions of the PDs that lie within this depth are imaged. As schematically shown in Figure 60(b), SF2-SF4 are in typical rhomboid shaped configuration, while SF1 exhibits a more complicated geometry that is discussed below. The [11-20] off-cut direction is horizontal in Figure 60 so that the intersection of the basal plane with the crystal surface is vertical. SF5 has expanded to the device surface forming a right triangle (the vertical side is the surface intersection). Contrast extinction analysis carried out on the Shockley PDs bounding the expanded SFs has shown that the Burgers vector of the PDs is 1/3[01-10] (consistent with a previous report[159]), which is 30° to the off-cut direction, as marked in the image. Two TSDs [S_1 and S_2 in Figure 60(a)] are found to have interacted with the expanded SFs. One can understand how this final configuration of defects came about by examining the EL images recorded *in situ* during device stressing.

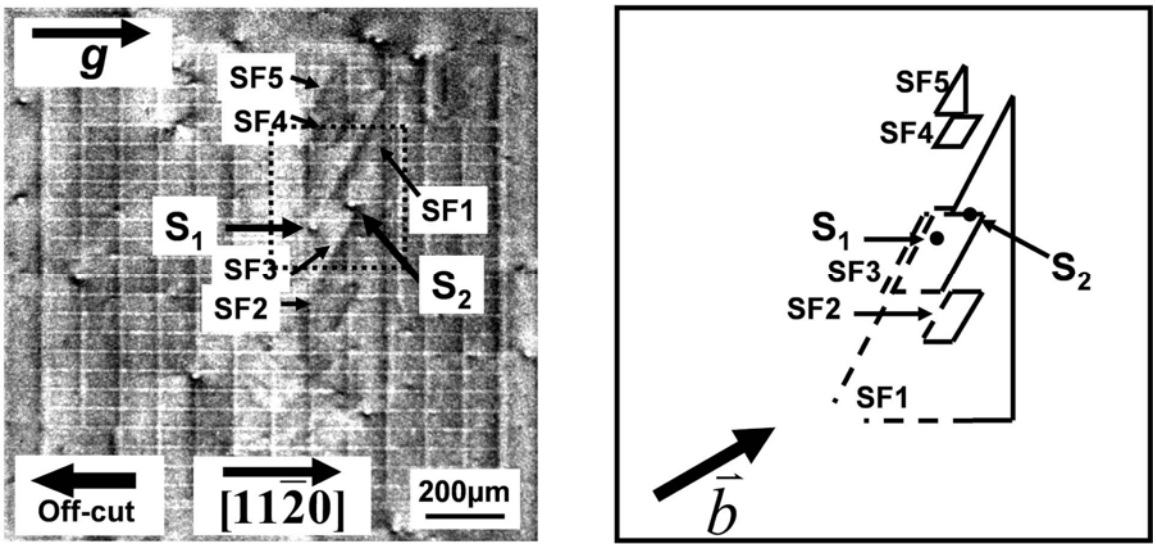

Figure 60. (22-4.12) Grazing incidence SWBXT of a device cell of a *4H*-SiC PiN diode (a) and schematic diagram showing the geometry of the SFs (b). All of the PDs have the same Burgers vector, $\boldsymbol{b}$.

Figure 61(a)-(d) are sequential EL images (excerpted from a larger sequence of images) recorded from the area indicated by the dashed box on Figure 60(a), which contains two TSDs [S_1 and S_2, confirmed by SWBXT in Figure 60(a)] and SF1. In Figure 61(a), the luminescent horizontal Si-core PD, aligned along the [11-20] Peierls valley, which bounds the expanding SF rhomboid (hatched region) is gliding toward upper right corner of the view. As the PD meets S_1, it is observed to split into two segments, AB and CD, at the point of intersection, and these two segments continue to advance, albeit at different velocities. As the PD splits, the separated segments advance on parallel (0001) slip planes, which are displaced by 1$\boldsymbol{c}$ (the magnitude of the Burgers vector of S_1). This is

due to the spiral nature of the lattice planes surrounding the core of a screw dislocation. Segment BC, which trails the initially faster moving segment, CD, is a single C-core PD lying along the [-12-10] Peierls valley direction bounding the SF.[160] By the time segment CD reaches S_2 (a similar splitting occurs creating segment EF), the slower moving AB segment begins to pass S_1, and the advancing segment AB now begins to trail a Si-core partial between S_1 and B. This Si-core PD couples with the preexisting C-core PD forming a PD dipole due to the strong interactive forces. Without the interaction with the C-core PD, the Si-core PD would expand to the right. This dipole initially lies along the [-12-10] Peierls valley. As the SF expansion continues, that part of the trailing dipole closest to the TSD core is observed to "snap" into [01-10] screw orientation. As this occurs, that end of the reoriented screw dislocation dipole that is remote from the screw drags the lower end of the original dipole away from its [-12-10] Peierls valley orientation. The remainder of the original dipole is then observed to adopt a metastable zigzag configuration [YD in Figure 61(c) and a clearer view is also shown in the inset] as it is dragged towards the right and eventually it also snaps into screw orientation. For example, see the dipole YS_2 that has snapped into the [01-10] direction, which is also the direction of the Burgers vectors of the two PDs. This process is shown schematically in Figure 61(e) and (f). A similar process occurs subsequently at S_2. It should be noted that during this process, two TEDs [indicated in Figure 61(a) and (b)] are clearly cut through by the PD without creating any trailing dipole segments. This suggests that either kink/jog formation is favored enabling the dislocations to cut through each other or trailing segments are created which immediately self-annihilate since they are located on the same slip plane.[37]

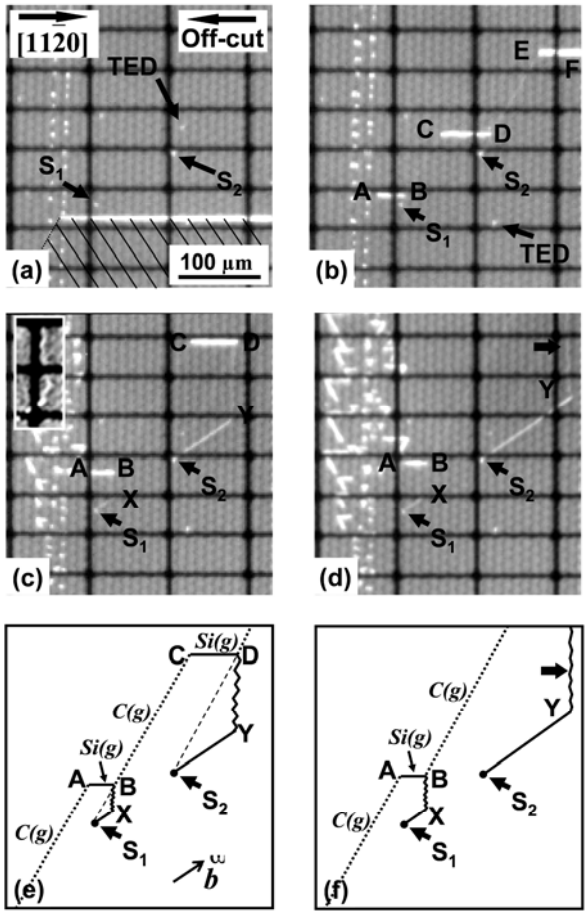

Figure 61. Sequential EL images [(a)-(d)] showing the interaction between advancing Shockley PD with two TSDs and schematic diagrams [(e) and (f)] showing the dislocation geometries in (c) and (d), respectively. EL images were provided by Dr. R. E. Stahlbush at Naval Research Lab.

From these observations, it is clear that while the TEDs do not constitute effective barriers to the motion of the PDs, the PD remains pinned at the TSD creating trailing dipoles when they interact. The reason for this pinning is related to the energy required for the kink and jog formation, with the formation of jog on the PD being most prohibitive. It is also noted that even if such a jog were formed, it would most likely be sessile due to the difficulty for dislocations in SiC to glide on {11-20} at room temperature.[161]

The question arises as to why the trailing dislocation dipoles spontaneously align themselves into screw orientation. Insight into this behavior is afforded by considering the strength of the interaction between the dislocations constituting the dipole, one C-core and one Si-core partial. Initially, the dipole is aligned along the [-12-10] Peierls valley so that the partials are in 30° orientation [as shown in Figure 62(b)]. The equilibrium position of the two partials is such that the Si-core partial sits just behind the projected position of the C-core partial on the (0001) plane. The Si-core partial activated by REDG process continues to advance rightward, although as it moves the strong mutual force causes it to push the C-core partial along with it. The mutual force between Si-core and C-core PDs in the dipole is up to $2.5\times10^{8}\mu b^{2}/2\pi(1-\nu)$, where μ is shear modulus, b is the magnitude of the Burgers vector of the PD and ν is the Poisson's ratio. This is equivalent to the force exerted by a shear stress of 1.67 GPa, the same order as the *theoretical critical shear stress* $\mu/30$ (6.43GPa). Thus, it is safe to say that the force exerted by the

Si-core PD is large enough to force the C-core PD to accompany it as it glides. Individual Si-core PDs normally migrate by the creation and lateral motion of kinks consisting of segments lying in the [-2110] (90° segment) and [11-20] (30° segment) Peierls valley directions[162]-see Figure 62(a). The kinks are connected by segments lying in the original [-12-10] Peierls valley. However, in this case one end of the Si-core PD is anchored by the TSD [Figure 62(b)], and as the dislocation attempts to orient itself into the [11-20] kink orientation (still pushing the C-core partial ahead of it) by swinging around the TSD, it passes through the [01-10] screw orientation.

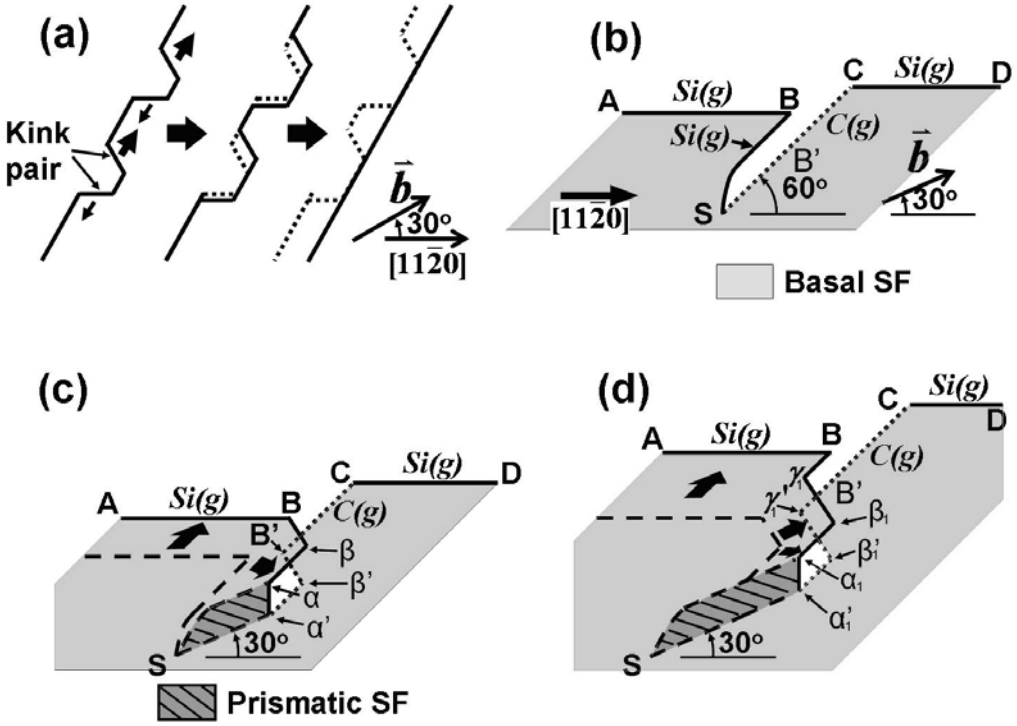

Figure 62. Schematic diagram showing the mechanism of motion of a single PD (a) and the formation of a prismatic SF when an advancing PD interacts with a TSD [(b)-(d)].

Once in screw orientation, the C-core partial will align itself exactly below the Si-core partial, separated by 10.053 Å, and subsequently they cross slip. This cross-slip would seem to be unavoidable due to the extremely large attractive force between the PDs. Simple calculation shows that this force is equivalent to an applied shear stress of 5.46 GPa, which is similar to the *theoretical critical shear stress* of μ/30 (6.43 GPa) under which crystal planes can be sheared without generating any dislocations. This stress is more than large enough to induce cross-slip on the normally inactive {11-20} slip plane. This cross-slip and annihilation process necessarily creates an area of prismatic SF [Sαα' in Figure 62(c)], i.e., on the (-2110) plane, which has the same fault vector as the original basal fault. A [0001] segment of PD, αα' is also created in this process. Cross-slip and annihilation of screw dislocation dipoles have been observed in other systems. For example, Rasmussen simulated that a screw dislocation dipole with a height less than 1 nm annihilates spontaneously in copper.[163] The minimum distance between screw dislocations on different slip planes with opposite signs based on

experiments has been estimated to be 50 nm in copper, and screw dislocation dipoles with heights less than this value will annihilate spontaneously via cross-slip.[164] In this case, it can also be shown that the cross-slip and annihilation of the Shockley PD dipole are favored from the energetic point of view. If cross-slip occurs, the Shockley PD dipole annihilates, leaving a prismatic SF which is one TSD Burgers vector magnitude wide. The energy per unit length of the Shockley screw PD dipole, ignoring end effects, is $\mu b^2 \ln(\alpha r/b)/2\pi$ (μ is the shear modulus, b is the magnitude of the Shockley partial Burgers vector, α is ~1 and r is the height of the PD dipole).[165] This energy is calculated to be $\sim 1.14\times10^{-9}$J/m. The energy per unit length of the prismatic SF in our case (~10 Å width) estimated, based on the basal SF energy, is of the order of 10^{-10}~10^{-11}J/m if the prismatic SF energy γ is assumed to be 1~2 orders bigger than that of the basal SF. Therefore, the formation of the prismatic SF via the cross-slip and annihilation of the screw-oriented Shockley PD dipole reduces the strain energy by 1~2 orders of magnitude.

Once the prismatic SF is created, the original fault can no longer expand as the prismatic fault constitutes a sessile configuration, e.g., at Sαα' in Figure 62(c). If Sα was able to pass over Sα', this would create an area of double SF separated by one TSD Burgers vector. Compared to single SFs, such double SFs would introduce thicker layers of *3C*-SiC into the *4H*-SiC matrix, worsening the effect on device performance (e.g., further lowering Schottky barrier heights in diodes[166]). On the other hand, while regions such as Sαα' are locked, segments αβ and βB continue to advance due to the REDG process, albeit at different velocities, represented by arrows of different sizes in Figure 62(d) (the 90° PD advances faster than the 30° PD[167]), pushing the C-core PDs, α'β' and β 'B' ahead of them. The PDs reach the positions $\alpha_1\beta_1$ and $\beta_1\gamma_1$ and $\alpha_1'\beta_1'$ and $\beta'_1\gamma_1'$ in Figure 62(d) as AB advances. The fresh segments γ_1B and γ_1'B' are created in order to maintain line continuity in the PDs. The PD dipole Bβαα'β'B' in (c) becomes dipole $B\gamma_1\beta_1\alpha_1\alpha_1'\beta_1'\gamma_1'B'$ in (d). At the same time, the prismatic SF extends to $S\alpha_1\alpha_1'$. The same process in Figure 62(c)-(d) repeats as AB advances, leaving a prismatic SF on the (-2110) plane and a PD dipole with zigzag configuration [SF and PD dipole are observed as S_2Y and YD, respectively, in Figure 61(c)]. No contrast is observed from the prismatic SF or PD dipole in the SWBXT image [Figure 60(a)] because $\vec{g}\cdot\vec{R}$ is equal to an integer for the SF and there is no long range strain field associated with the PD dipole.

6.5. Conclusion

In summary, the recombination enhanced dislocation glide process activates advancing Shockley partial dislocations bounding SFs in *4H*-SiC PiN diodes that are able to cut through threading edge dislocations without generating any trailing dislocation segments. However, when the advancing Shockley partial dislocation encounters a threading screw dislocation, it is pinned and is forced to generate a trailing dipole as it advances. This partial dislocation dipole, which initially aligns along the [-12-10] Peierls valley, spontaneously snaps into screw orientation and subsequently self annihilates via cross-slip leaving behind a prismatic stacking fault with the same fault vector as the original expanding stacking fault. This configuration is sessile and precludes the formation of double stacking faults which would be even more detrimental to device performance than the single stacking faults. The replacement of the partial dislocation

dipole by the prismatic stacking fault is energetically favored, reducing the free energy by 1~2 orders compared with the partial dislocation dipole.

7. Sense determination of MPs by grazing-incidence SWBXT

7.1. Outline

Computer modeling using the ray-tracing method has been used to simulate the grazing-incidence x-ray topographic images of micropipes in *4H* silicon carbide recorded using the pyramidal (11-28) reflection. Simulation results indicate that the images of micropipes appear as white features of roughly elliptical shape, canted to one side or other of the **g**-vector depending on the dislocation sense. Observed images compare well with the simulations, demonstrating that the direction of cant provides a simple, non-destructive and reliable way to reveal the senses of micropipes. Sense assignment has been validated using back-reflection reticulography.

7.2. Introduction

Devices made from silicon carbide (SiC) have been facing various issues caused by defects such as elementary[168] and hollow-core axial screw dislocations (micropipes, MPs), [169] triangular defects, stacking faults (SFs) and low angle grain boundaries (LAGBs).[33] MPs are device-killing defects, reducing the breakdown voltage significantly. Various techniques have been used to record the MPs present in bulk crystals and epitaxial layers, e.g., molten potassium hydroxide (KOH) etching and x-ray topography. Synchrotron white beam x-ray topography (SWBXT) in various geometries has been successfully utilized to image elementary threading screw dislocations (TSDs) and MPs in bulk crystals and epilayers. In back-reflection geometry, TSDs and MPs appear as white circles of various dimensions surrounded by narrow dark rings, features which have been shown to be consistent with simulations carried out using the ray-tracing method.[56,29] However, the dislocation sense of the elementary TSDs and MPs cannot be revealed by either molten potassium hydroxide etching, or directly from back-reflection SWBXT images. Revealing the dislocation sense of the elementary TSDs and MPs can provide further insight into their propagation and formation mechanisms (e.g., opposite-sign MP pairs can be nucleated due to inclusions[11]) during bulk and epitaxial growth and may facilitate the formulation of strategies designed to minimize their densities thereby mitigating or eliminating their deleterious effects on the device performance. Although x-ray section topography has been used to determine the senses of TSDs and MPs, difficulty in locating the dislocation core makes it impractical to apply to sense mapping over large crystal areas. Likewise, back-reflection x-ray reticulography can be used to determine the sense of large Burgers vector MPs (>8c, the corresponding image size is ~80 μm at specimen-film distance of 20 cm). However, sense determination for small Burgers vector MPs (<6c) and TSDs is made extraordinarily difficult due to the smaller feature size. Transmission x-ray topography carried out on specially cut cross-sectional specimens can also reveal dislocation sense but this is evidently destructive. Here, we introduce a simple, non-destructive method to reveal MP sense which uses plan-view, grazing-incidence x-ray topography employing pyramidal plane reflections.

In this chapter, we present observed and simulated images of MPs in grazing-incidence x-ray topography using the (11-28) plane reflection. We demonstrate that the

sense of the MP can be determined from simple inspection of the contrast features. The dislocation sense of a MP is able to be revealed directly from the configuration of its image. The results from larger Burgers vector MPs were validated by back-reflection SWBXT reticulography.

7.3. Experimental

SiC crystals used in the study are commercial 3-inch *4H*-SiC wafers, grown by the physical vapor transport (PVT) technique, with 8° off-cut towards [11-20]. Grazing-incidence SWBXT images using the (11-28) plane reflections were recorded from the Si-face side at an x-ray incidence angle of 2°, and (000.16) back-reflection reticulographs (with 8° Bragg angle) were recorded. For the latter, a fine-scale copper grating with periodicity of 50 μm was placed in the incident x-ray beam.[170] The imaging was carried out at the Stony Brook Synchrotron Topography Station, Beamline X-19C, at the National Synchrotron Light Source at Brookhaven National Laboratory, using Agfa Structurix D3-SC film at a specimen-to-film distance of 10~15 cm for back-reflection geometry and 15~20 cm for grazing-incidence geometry, respectively. Simulation and plotting were carried out on a Dell Precision 530 Workstation, using the commercial software Mathematica v5.1. The point of view is from behind the x-ray film. The projection of the reflection vector on the plate is pointing downwards throughout our discussion.

7.4. Results and discussion

The ray-tracing method has been previously used to simulate the back-reflection SWBXT images of MPs and successful correspondence has been obtained between observed and simulated images.[48] In ray-tracing simulation, the specimen surface is divided into small squares of constant area and the plane normal at each area is calculated. The contrast on the simulated image is determined by the overlap of beams diffracted from the individual small areas on the specimen surface. Figure 63 gives the geometry used in the simulation and imaging process. Cartesian coordinates are used. The *z*-axis is chosen such that the ***c***-axis of the specimen is parallel to it, the *x*-axis is chosen along the [11-20] (parallel to the off-cut direction) and the y-axis is oriented along [1-100]. The origin is set at the surface intersection of the MP core. The x-ray beam is incident at a 2° angle to the crystal surface and lies in the *xz* plane and the (11-28) diffracted beam image is recorded. MPs in PVT grown SiC crystals are oriented very close to the ***c*** axis (minimizing their energy), so that fundamental dislocation theory defines the displacement of this screw dislocation along the z-axis as: $u_z=(\boldsymbol{b}/2\pi)\arctan(y/x)$, where ***b*** is the Burgers vector of the MP.[171] Displacements in the ***c***-plane (u_x and u_y) also exist due to surface relaxation effects (assuming that the MP is in an infinite plate/disc with surfaces $z=\pm t$) and these can be defined as:[172]

$$u_x = u_\theta(x,y,z)\frac{-y}{\sqrt{x^2+y^2}};$$
$$u_y = u_\theta(x,y,z)\frac{x}{\sqrt{x^2+y^2}},$$

(44)

where

$$u_\theta(x,y,z) = -\frac{b}{2\pi}\sum_{n=0}^{\infty}(-1)^n\left\{\frac{x^2+y^2}{(2n+1)t - z + \sqrt{\left[(2n+1)t - z\right]^2 + \left(x^2+y^2\right)}} - \frac{x^2+y^2}{(2n+1)t + z + \sqrt{\left[(2n+1)t + z\right] + \left(x^2+y^2\right)}}\right\}. \quad (45)$$

The plane normal $\vec{n}(x,y,z)$ at (x, y, z) due to the displacement field of the MP is given by:

$$\vec{n}(x,y,z) = \vec{n}_0(x,y,z) - \nabla\left[\vec{n}_0(x,y,z)\cdot\vec{u}(x,y,z)\right], \quad (46)$$

where $\vec{u}(x,y,z) = u_x\vec{i} + u_y\vec{j} + u_z\vec{k}$ ($\vec{k}$ is unit vector along positive z), and $\vec{n}_0(x,y,z)$ is the plane normal in the perfect crystal (without distortion from the MP). The unit vector of the diffracted beam $\vec{s}$ can be obtained by solving equation $\vec{s}_0 \times \vec{n} = -\vec{n} \times \vec{s}$, where $\vec{s}_0$ is the unit vector of the incident x-ray beam. Simulation was carried out on a DELL Precision 530 Workstation, using the commercial software Mathematica v5.1. Grayscale maps were plotted also using Mathematica. Processing takes up to 24 hrs depending on the complexity of the calculation. The angle of view is from behind the x-ray film throughout our discussion.

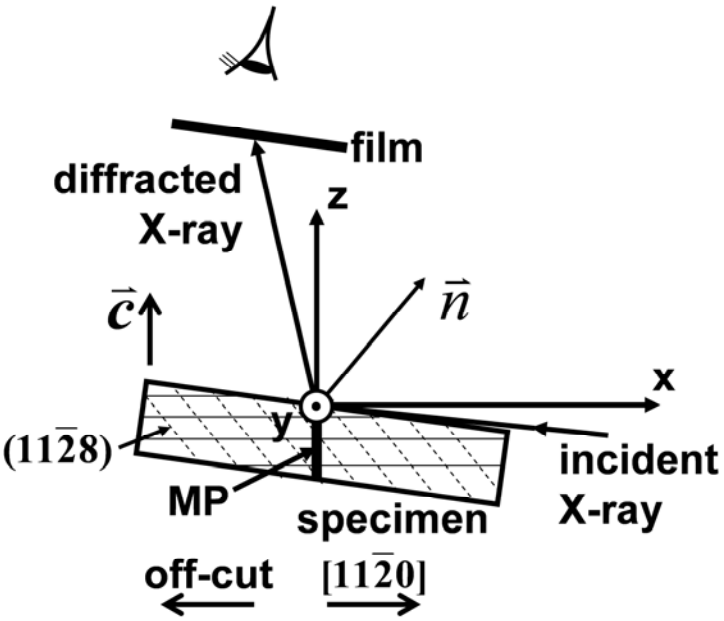

Figure 63. Schematic diagram showing the geometry used in the imaging and simulation. The angle of view is from behind the x-ray film for all the images discussed.

A SWBXT image recorded using grazing-incidence geometry is shown in Figure 64(a). One can notice that the images of MPs appear as white features of various dimensions with roughly elliptical shape, canted to one side or other of the g vector, with perimeters of dark contrast which thicken at both ends. Figure 64(a) shows examples of the features canted clockwise and counterclockwise from the vertical configuration [see Figure 64(b)]. A back-reflection SWBXT image was recorded from the same region and the corresponding images of MPs "L" and "R" are shown in the insets of Figure 64(a) (note these are on a different scale from the grazing-incidence topograph). These images appear circular, indicating that they correspond to isolated MPs (not MP pairs or groups).

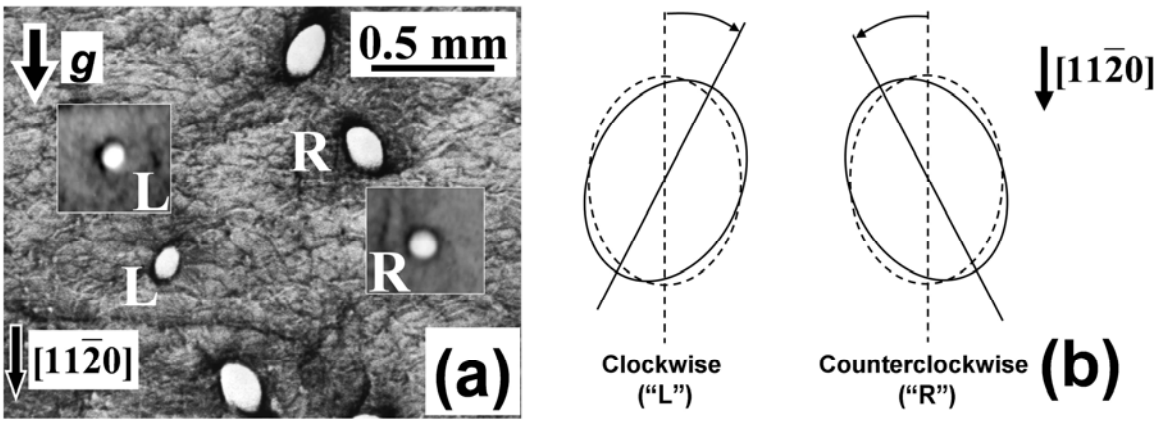

Figure 64. (a) A (11-28) grazing-incidence SWBXT image of *4H*-SiC. MPs appear as roughly oval shape with various orientations and dimensions. The MPs can be divided into two groups according to the orientation of the white elliptical contrast. Examples of each kind are shown (marked by "L" and "R"). Their images in back-reflection geometry appear as complete circular shapes (see insets, on a different scale), indicating that they are isolated MPs (not MP pairs or groups). (b) Schematics showing two orientations of the MP images, canted clockwise ("L") or counterclockwise ("R") from the vertical configuration.

From the observations in Figure 64(a), it appears that the roughly elliptical white contrast feature associated with MP in grazing-incidence topographs are either canted clockwise or counterclockwise from the vertical configuration. Simulations of these images carried out using the ray-tracing method are shown in Figure 65. Figure 65(a) and (b) are images of left-handed and right-handed 8*c* MPs, respectively (viewpoint behind the film, as indicated in Figure 63). They appear as roughly elliptical white features with dark perimeters that thicken along one side and at each end. The observed [Figure 64(a)] and simulated (Figure 65) images correlate very well. Simulation shows that left-handed MPs appear as nearly elliptical features canted clockwise while right-handed MPs are canted counterclockwise [see Figure 64(b)].

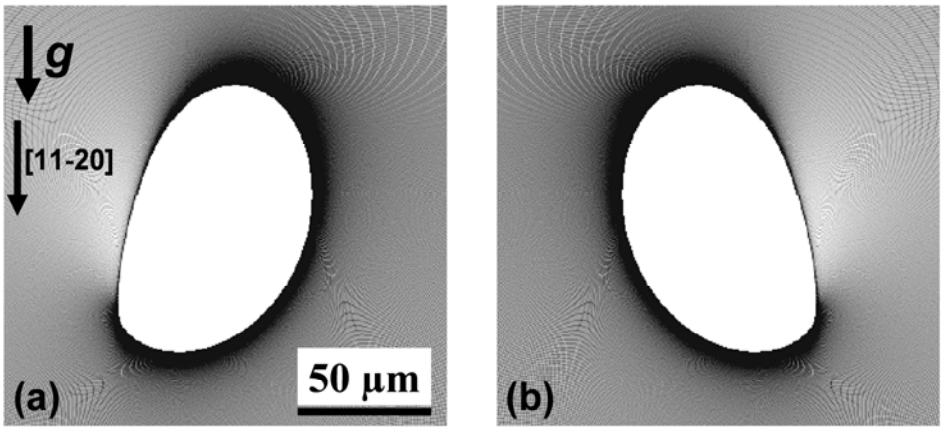

Figure 65. Simulated grazing-incidence x-ray topographic images of left-handed (a) and right-handed (b) 8*c* MPs at a specimen-film distance of 35 cm. (11-28) reflections are simulated. Both images appear as roughly white ellipses canted clockwise (a) or counterclockwise (b) from vertical configuration.

In order to confirm the sense determination, back-reflection reticulographs were recorded from the same region in Figure 64. In reticulography, an x-ray absorption mesh splits the diffracted beam into individually identifiable microbeams and by examining the rotation of the mesh images around the MPs, the dislocation sense can be determined unambiguously.[173] Assuming the point of view is behind the x-ray film, clockwise rotation of the mesh images indicates a right-handed MP while counterclockwise rotation of the mesh images indicates a left-handed MP.[174] Figure 66(a) shows the grazing-incidence topographic images of the crystal region containing MPs "L" and "R" discussed in Figure 64(a) and Figure 66(b) is the corresponding back-reflection reticulograph. On Figure 66(b), mesh features diametrically opposed across the micropipe are indicated by dashed lines. Apparently the mesh arrays are twisted counterclockwise around the MP "1", and clockwise around the MP "2", indicating a left-handed MP "1" and a right-handed MP "2". This result is consistent with our prediction based on grazing-incidence SWBXT images and ray-tracing simulation. Complete agreement has also been obtained by comparing numerous other reticulographic images of MPs with the grazing-incidence topographs (see Figure 66, left-handed MPs are labeled "L" and right-handed ones are labeled "R"). Moreover, further confirmation of the sense determination was obtained from transmission SWBXT images recorded, using the basal plane reflection, from cross-sectional samples [sample surface parallel to (1-100) with the MP is parallel to the surface; see Ref. 48 for details of cross-sectional topography of MPs]. Our observation indicates that the results from transmission topographs of cross-sectional samples are also consistent with those from grazing-incidence images.[175] Similar results were obtained for *6H*-SiC. Simulation results also indicate that other pyramidal planes [e.g., (11-2.12)] can be used to determine the MP sense, although the white contrast in the MP images deviates slightly further from elliptical configuration.

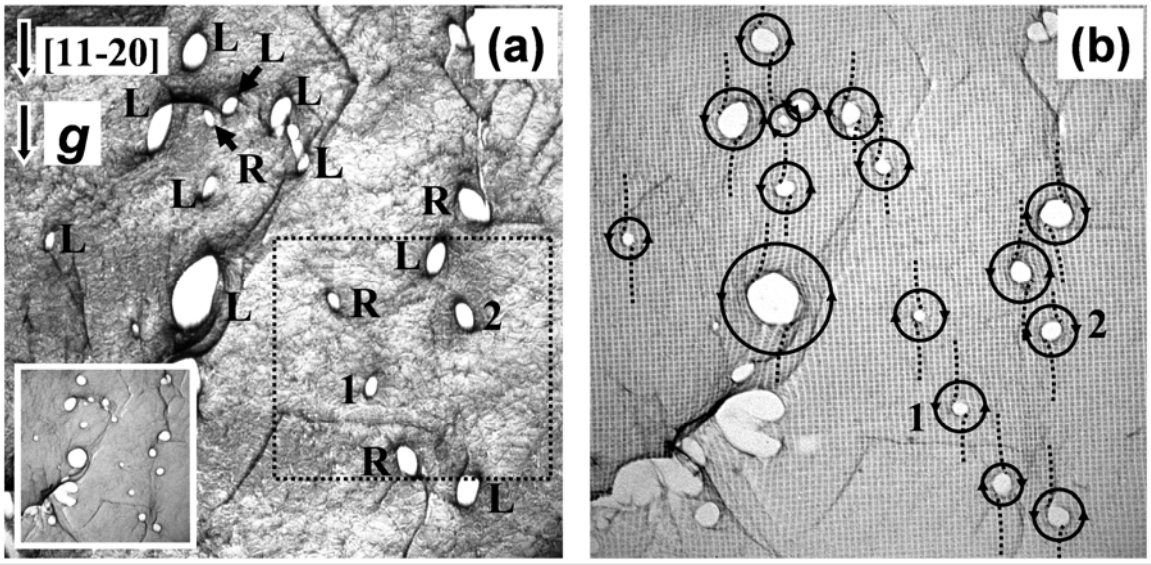

Figure 66. (a) Grazing-incidence SWBXT of the crystal region containing the MPs "L" and "R" discussed in Figure 64. Inset shows the corresponding back-reflection SWBXT image. (b) The corresponding back-reflection reticulograph. The area in the dashed box is the same region as in Figure 64(a) and MPs "1" and "2" correspond to "L" and "R" in Figure 64(a), respectively.

7.5. Conclusion

In summary, the ray-tracing method has been applied into the simulation of grazing-incidence synchrotron white beam x-ray topographic images of micropipes. The images appear as roughly elliptical white features, canted to one side or other of the *g* vector, with perimeters of dark contrast that thicken along one side and at both ends. Good correspondence has been obtained between observed and simulated images of micropipes. The features are canted clockwise and counterclockwise, respectively, for left-handed and right-handed micropipes. The different image orientations of the left-handed and right-handed micropipes provide a simple, non-destructive and reliable way to reveal their senses. Back-reflection reticulography confirms the sense determination.

8. Direct determination of the dislocation sense of closed-core TSDs in *4H*-SiC

8.1. Outline

Grazing-incidence synchrotron white beam x-ray topography images of closed-core threading screw dislocations in 4*H* silicon carbide appear as roughly elliptically shaped white features, with an asymmetric perimeter of dark contrast which is greatly enhanced on one side or other of the **g**-vector. Ray-tracing simulations indicate that the relative position of the enhanced dark contrast feature reveals the sense of the closed-core screw dislocation. Dislocation senses so obtained were validated using back-reflection images recorded with small Bragg angle. Therefore, the sense of the closed-core threading screw dislocations can be unambiguously revealed using either grazing-incidence or "small Bragg angle" back-reflection synchrotron white beam x-ray topography.

8.2. Introduction

MP densities have recently been significantly lowered. However, TSDs remain in densities ranging from 10^3 - 10^4. TSDs in SiC are of great interest from several different points of view. First, it should be noted that TSDs play a critical role in maintaining the desired polytype by promoting spiral step-flow growth. [176,177] Second, they have been found to degrade device performance, reducing the breakdown voltage by 5-35%. [178] Third, the forest of TSDs in the as-grown crystal poses a significant barrier, which creates a pinning effect on the glide of basal plane dislocations (BPDs) during either growth or post-growth cooling, leading to localized higher densities of BPDs.[37] Fourth, TSDs have been found to interact with SFs expanding under forward bias in SiC epitaxial films, creating prismatic SFs.[28,179]

Various techniques have been used to observe TSDs present in bulk SiC crystals and epitaxial layers, e.g., molten potassium hydroxide (KOH) etching and x-ray topography. Synchrotron white beam x-ray topography (SWBXT) in various geometries has been applied to image TSDs in bulk crystals and epilayers. [29,56] However, the sense of the TSDs cannot be revealed by either molten KOH etching, or directly from back-reflection SWBXT images. Whether the TSDs are randomly distributed in terms of sense or they are nucleated in same-sign groups in the grown crystals remains unclear. Knowledge of the sense of the TSDs can provide further insight into their propagation and formation mechanisms during bulk and epitaxial growth; e.g., opposite-sign pairs can be nucleated at inclusions.[11] Moreover, knowledge of the TSD sense provides critical information regarding their interaction with other defects (e.g., BPDs and SFs) and their ultimate influence on device performance. Consequently, revealing the senses of the TSDs can definitely benefit understanding of their roles in affecting device performance and may shed light on strategies designed to mitigate their deleterious effects.

Although x-ray section topography[48] and back-reflection reticulography[13] have been used to reveal the senses of MPs, it is extremely difficult to resolve the sign of an individual closed-core TSD, due to its significantly weaker strain field (and hence smaller

contrast feature size) compared with MPs. For section topography, the ultra fine slit has to be applied at exactly the dislocation core. For TSDs, this is possible but extremely difficult practically and certainly not suitable for the mapping of TSD sense over large crystal areas. For reticulography, the mesh size must be at least smaller than 20 μm (the image size of the TSDs). At this scale, it is difficult to discern the necessary detail to determine the sense of twist of the mesh image since we are approaching the resolution limit of the x-ray film. On as-grown surfaces, the sense of TSDs can be revealed by the sense of rotation of the associated growth spirals, as observed by, for example, atomic force microscopy. Such mapping is not possible for polished wafers, although destructive H-etching could, in principle, be applied to reveal the spirals. Recently, Okunev *et al.* reported the determination of sign of 1***c*** screw dislocation in 6*H*-SiC using x-ray topography based on the Borrman effect.[180] However, first, likewise in section topography, an ultra fine slit is needed; second, crystals with extremely low dislocation densities are required [crystals grown by the physical vapor transport (PVT) are not applicable]. Until now, no study has reported obtaining the sense information of closed-core TSDs from large crystal areas in a simple, non-destructive and reliable way. In this chapter, grazing-incidence SWBXT images have been recorded allowing the sense of the TSDs in 4*H*-SiC to be revealed, based on ray-tracing simulations. "Small Bragg angle" back-reflection topography was used to confirm the sense assignment. Complete agreement between the results of both techniques demonstrates that both can be used to reveal the sense of closed-core TSDs unambiguously.

8.3. Experimental

Grazing-incidence SWBXT images using pyramidal plane reflections were recorded from Si-faces of the specimens at an x-ray incident angle of 2^{o}. (0008) back-reflection images using a 32^{o} Bragg angle were recorded from the same region. The ray-tracing method was used to simulate the grazing-incidence topographic images of closed-core TSDs, with plate type surface relaxation effects taken into account. The point of view is from behind the x-ray film. The projection of the reflection vector on the plate is pointing downwards throughout our discussion.

8.4. Results and discussion

Figure 67 shows a highly-enlarged (11-28) grazing-incidence SWBXT image, containing closed-core TSDs with Burgers vector 1***c*** (indicated by arrows). It is assumed that the TSDs are well enough spaced that the interactions between their strain fields can be ignored. This assumption is reasonable since the topograph was recorded from a specimen with a very low density of dislocations (TSD: $\sim 2\times10^{3}/cm^{2}$, BPD: $\sim 2.56 \times 10^{3}/cm^{2}$). An individual TSD appears as a white, roughly elliptical shaped feature, with an asymmetric perimeter of dark contrast, which is greatly enhanced on one side or other of the **g**-vector. The long dimension is approximately 20 μm. Clearly, the TSDs visible can be divided into two groups, according to the position of the enhanced perimeter contrast relative to the **g**-vector (each type is indicated by an arrow with one of two orientations). One example for each kind is marked by "L" and "R" in Figure 67. The labeled pair is quite close and forms an opposite sign TSD pair. The enhanced perimeter

contrast is located to the right side of the white contrast for the TSD "L," and to the left side for the TSD "R." All the other TSDs have similar configurations, with the enhanced perimeter contrast being located either to the right or left of the white contrast. According to fundamental dislocation theory, screw dislocations can exist with one of two signs (left-handed or right-handed), so that the two configurations observed most probably correspond to these two signs, although it remains uncertain which is left-handed and which is right-handed.

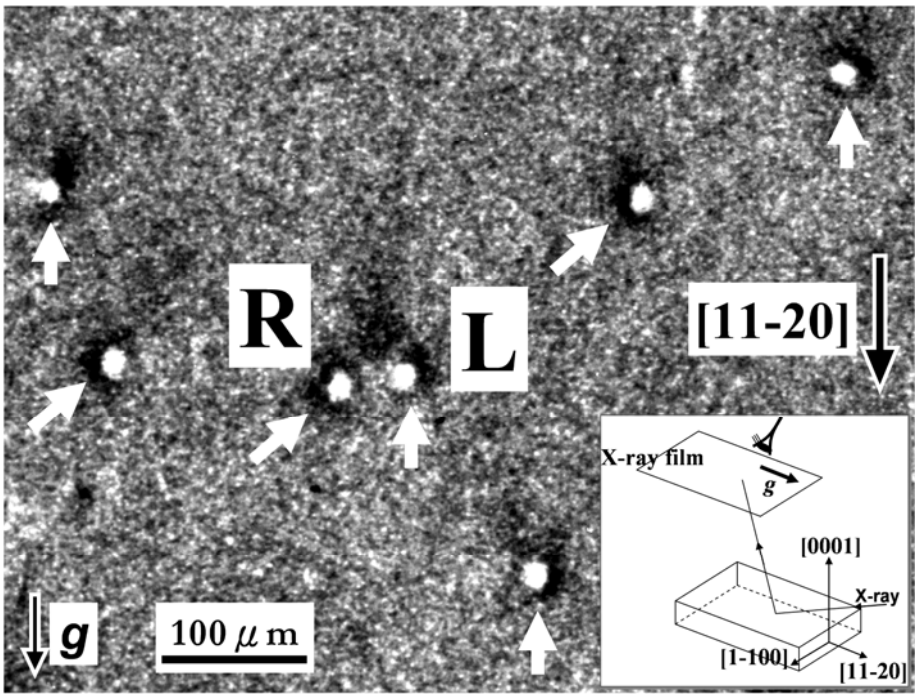

Figure 67. A highly enlarged (11-28) grazing-incidence SWBXT image showing many closed-core 1***c*** TSDs. The enhanced perimeter contrast stays at either the right hand side ("L") or the left hand side ("R") of the white contrast.

In order to determine the sense of the TSDs, the ray-tracing method has been used to simulate the grazing-incidence topographic images of closed-core TSDs. Such modeling has already been carried out to simulate the images of MPs in back-reflection and grazing-incidence topography. [13,48] Threading edge dislocations of various Burgers vectors have been observed and simulated by Kamata *et al*. [181] For MPs, sense determination has been reported, based on the orientation of the roughly elliptically shaped white contrast features; i.e., whether they were canted clockwise or counterclockwise from the orientation of the **g**-vector.[13] However, using the orientation of the elliptical feature to determine sense becomes more ambiguous for TSDs for two reasons. First, the feature size is smaller making it more difficult to discern the inclination. Second, both the eccentricity of the roughly elliptical white contrast feature plus its inclination change as the line direction deviates with respect to the *c*-axis (TSD line directions often tend to adopt slight inclination angles to the *c*-axis, unlike MPs, which tend to align along *c*-axis due to the much larger line energy). Simulated grazing-incidence x-ray topographic images of 1***c*** TSDs using the ray-tracing method, taking into account surface relaxation effects, are shown in Figure 68. Figure 68(a) and (b)

correspond to left-handed and right-handed 1***c*** TSDs, respectively, simulated at a specimen-film distance of 15 cm, where the viewpoint is from behind the x-ray film (see inset on Figure 67). They appear as asymmetric, roughly elliptical white features with perimeters of dark contrast which thicken along one side and at both ends. Such asymmetrical contrast results from surface relaxation effects, which lead to in-plane (*c*-plane) displacements in addition to those along the TSD line direction. For TSDs with line directions slightly inclined to the *c*-axis, both the eccentricity and the inclination angle of the roughly elliptical features change slightly but the enhancement of perimeter contrast along one side persists, acting as an indicator of sign.

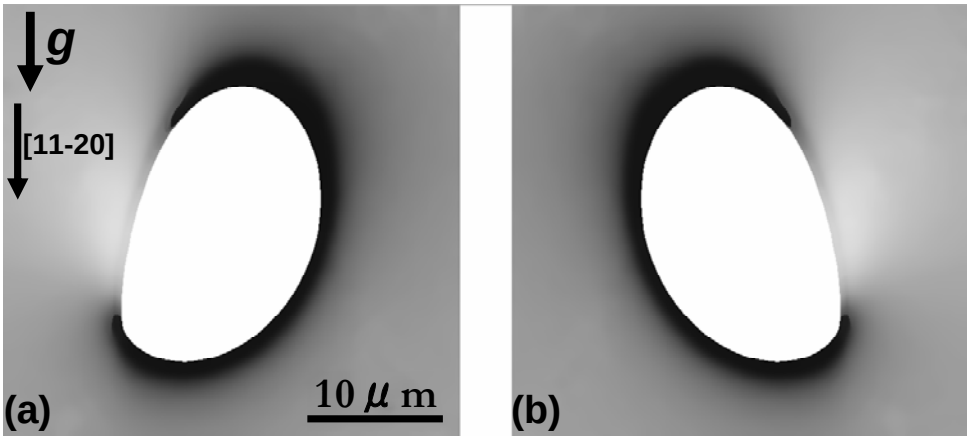

Figure 68. Simulated (11-28) grazing-incidence x-ray topographic images of a left-handed (a) and a right-handed (b) 1***c*** TSDs at specimen-plate distance of 15 cm.

In order to confirm such sense determination of 1*c* TSDs using grazing-incidence SWBXT, "small Bragg angle" back-reflection SWBXT using the basal plane reflection [Bragg angle of 32^{o}, see schematics in Figure 69(a)] was carried out on the same region of the crystal. As reported by Huang,[48] transmission SWBXT of cross-sectional samples can also be used to unambiguously determine the sense of MPs in SiC. Comparison of simulated and observed images recorded in such geometry shows that MPs appear as double-contrast columns, which are mutually shifted both vertically (parallel to *c*) and laterally (in the ***c***-plane) due to the helical lattice plane configuration surrounding the hollow-core of the MP. The sense of the MP can be readily obtained from the sense of the vertical shift of the double contrast columns. In the "small Bragg angle" back-reflection geometry, the x-rays penetrate quite deep into the crystal and the TSD again appears as bimodal contrast features via a similar mechanism to that in the transmission mode; both are using basal plane reflection, albeit in different geometry. In "small Bragg angle" back-reflection geometry, a downward mutual shift of the left-hand column indicates a left-handed TSD while a downward shift of the right-hand indicates right-handed, as schematically illustrated in Figure 69(a). Vectors $\vec{n}_1$ and $\vec{n}_2$ are the plane normals at either side of the TSD core. Simulated images of left-handed and right-handed TSDs using the ray-tracing method, with x-ray absorption being considered, are shown in Figure 69(b). Figure 69(c) is the "small Bragg angle" back-reflection SWBXT image of the 1***c*** TSD pair "L" and "R" discussed in Figure 67. The gradual attenuation of the bimodal contrast intensity is due to the x-ray absorption, and the slight tilt between the

two bimodal images from the direction parallel to the **g**-vector (which is vertical) is due to the inclination of the TSDs to the *c*-axis. The downward shift of the left-hand column of the bimodal image of TSD "L" indicated a left-handed sign, while the downward shift of the right-hand column "R" indicates right-handed. This is consistent with our observations from grazing-incidence SWBXT, based on ray-tracing simulations. Such opposite-sign pairs of TSDs may have nucleated at an inclusion, as proposed by Dudley et al.[11] Thus, revealing the sense of TSDs can provide critical information regarding their formation mechanism. Many other 1*c* TSDs have also been examined and their senses revealed using the position of the enhanced side perimeter contrast on the white contrast features observed on grazing-incidence SWBXT images. The results are fully consistent with those from the sense of the mutual shift in the bimodal contrast features observed on "small Bragg angle" back-reflection SWBXT images (see Figure 70). Notice that some of the TSD images overlap with each other in Figure 70(b), making the sense difficult to discern in "small Bragg angle" back-reflection SWBXT; however, they can be easily revealed from the grazing-incidence SWBXT images [see R' and L' in Figure 70(a)].

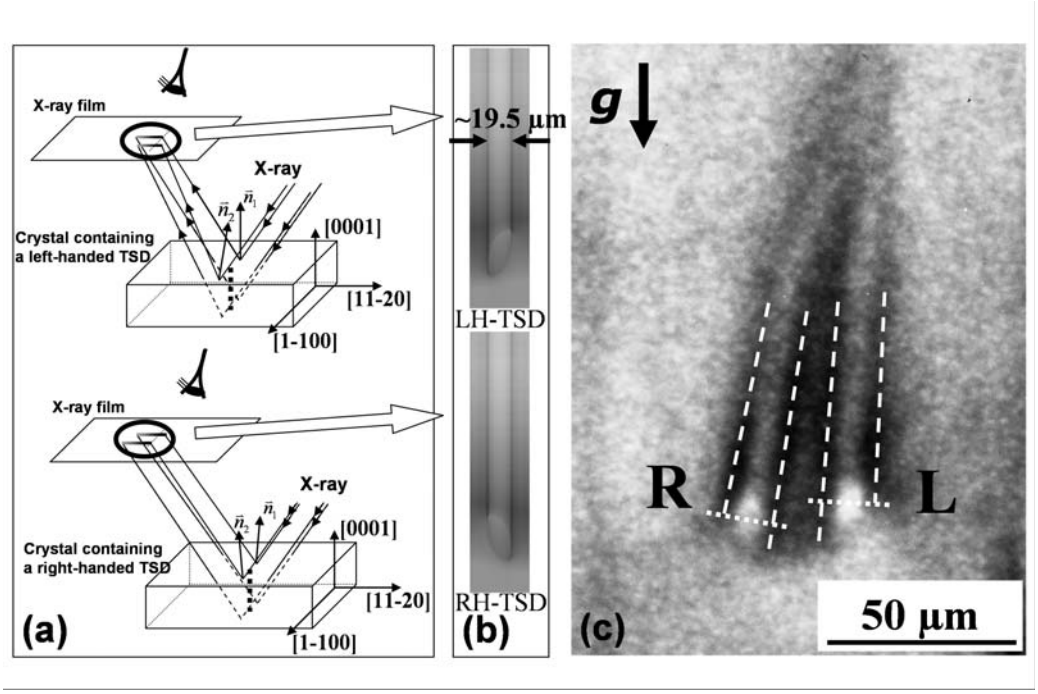

Figure 69. (a) Schematics showing the mutual shift of the bimodal contrast for a left-handed TSD (upper) and a right-handed TSD (bottom) in "small Bragg angle" back-reflection SWBXT; (b) Simulated images by ray-tracing method; (c) the image of the 1***c*** TSD pair "L" and "R" in Fig. 1.

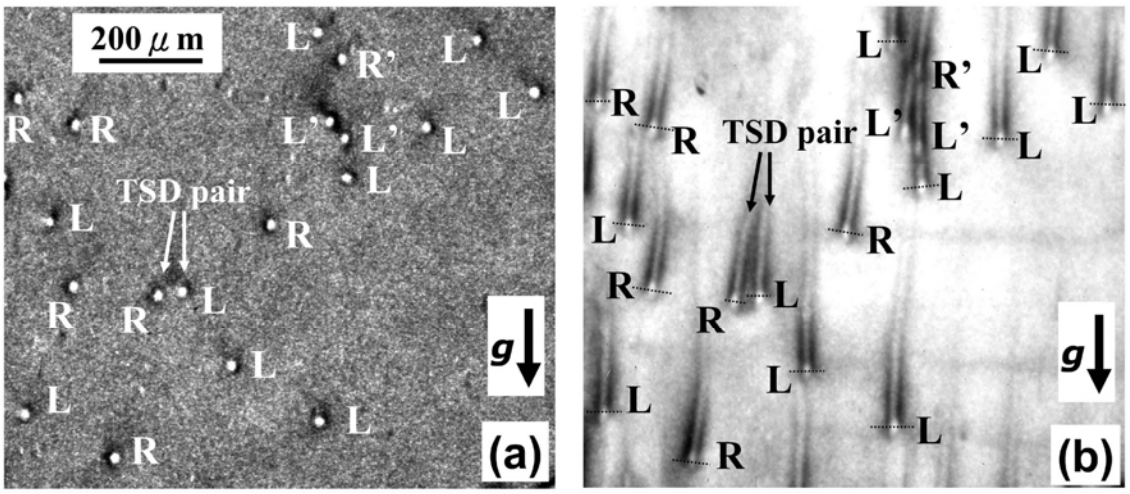

Figure 70. Comparison of sense determination of 1***c*** TSDs by grazing-incidence SWBXT (a) and "small Bragg angle" back-reflection SWBXT (b). The results are fully consistent with each other. Opposite-sign TSD pairs are observed, probably due to inclusions.

8.5. Conclusion

In summary, closed-core threading screw dislocations in 4*H*-SiC appear on grazing-incidence synchrotron white beam x-ray topographic images using pyramidal plane reflections as roughly elliptically shaped white features, with an asymmetric perimeter of dark contrast which is greatly enhanced on one side or other of the **g**-vector. Ray-tracing simulation indicates that the sense of the threading screw dislocations can be revealed according to the position of the dark contrast enhancement: if it is to the left side of the white contrast, this indicates a right-handed threading screw dislocation, and to the right indicates a left-handed threading screw dislocation. "Small Bragg angle" back-reflection synchrotron white beam x-ray topography has been applied to validate our argument. Complete agreement between the results from grazing-incidence synchrotron white beam x-ray topography and "small Bragg angle" back-reflection synchrotron white beam x-ray topography proves that either method provides a simple, non-destructive and unambiguous way to reveal the sense of closed-core threading screw dislocations in 4*H*-SiC. Similar results are expected in 6*H*-SiC.

9. Grazing-incidence x-ray topographic studies of threading edge dislocations in *4H*-SiC

9.1. Outline

Threading edge dislocations were studied by synchrotron x-ray topography using grazing-incidence geometry. Six types of threading edge dislocation images were observed in (11-28) grazing-incidence x-ray topographs. The topographic images of threading edge dislocations with six different Burgers vectors have been simulated using the ray-tracing method. The simulated results can subsequently be used to determine the Burgers vectors of threading edge dislocations from a single grazing-incidence topograph. Further verification was carried out by an additional equivalent (11-28) reflection and a dislocation half loop comprising two threading edge dislocation segments and a basal plane dislocation segment. The threading edge dislocation arrays are tending to orient along the direction perpendicular to their Burgers vectors, which is <1-100> direction, to minimize the total strain energy.

9.2. Introduction

The threading edge dislocations (TEDs) have been observed to be one of the major components of the LAGBs and they play critical roles in the defect structures in SiC, e.g., they act as barrier for the gliding BPDs if the spacing between adjacent TEDs is less than a critical value.[182] However, the TEDs have not been studied in detail. For example, the Burgers vectors of the TEDs cannot be revealed in a simple and unambiguous way in SiC wafers and their behaviors in LAGBs are still obscure yet. Four types of TEDs have been observed in XRT in previous studies.[183,184] However, our preliminary studies have shown that there are six types of TED images existing.[185] The detailed simulation process will also be given and complete Burgers vector analysis of TED will be discussed in this chapter.

9.3. Experimental and simulation

A 5 μm thick epilayer was deposited on 8^{o} off-cut commercial SiC wafers using chemical vapor deposition (CVD). The ray-tracing method was used to simulate the grazing-incidence topographic images of the TEDs. We are giving the detailed process used in simulating the images of TEDs by ray-tracing principle below.

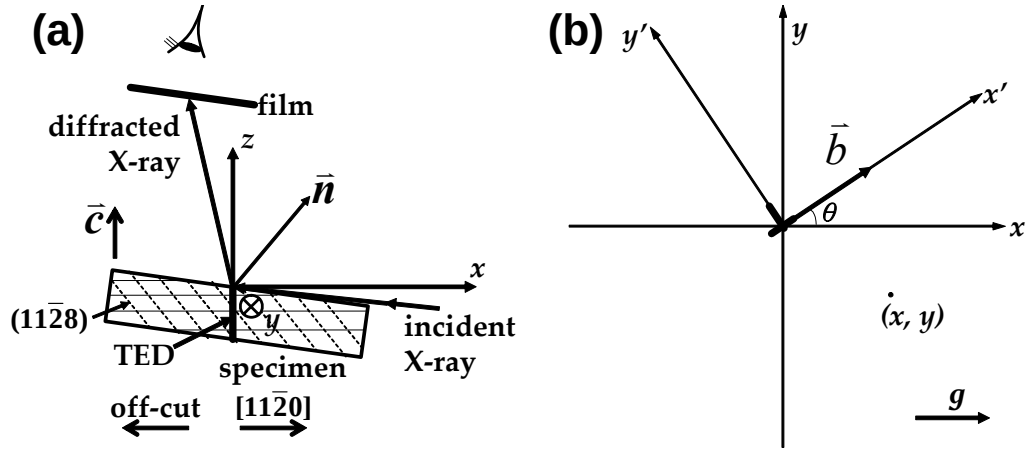

Figure 71. (a) Geometry used in the grazing-incidence x-ray topography. (b) Coordinate system used in obtaining the displacement field of the TED.

Figure 71(a) illustrates the geometry used in the simulation. The incident x-ray is at 2^o to the sample surface and (11-28) reflection is recorded. The point of view is from behind the X-ray film. Coordinate system is set so that the dislocation line of the TED is along *z*-axis and *x*-axis is parallel to the projection of reflection vector on the *xy* plane. Figure 71(b) is the view of the dislocation by looking anti-parallel to the *z*-axis from above the sample. The Burgers vector is at angle θ to the *x*-axis. A new coordinate system *x'y'z* is set in such way that the *x'*-axis is parallel to the Burgers vector direction and *y'*-axis is pointing toward the side where the extra half plane associated with the TED is (*z*-axis is kept same). First we need to obtain the displacement field associated with the TED in *xyz* coordinate system. Assuming a point on the sample surface (*xyz*), its coordinate (*x'y'z*) in *x'y'z* coordinate system is given by:

$x'=x\cos\theta+y\sin\theta$

$y'=-x\sin\theta+y\cos\theta$

$z'=z,$

where θ is the angle between *x'*-axis and *x*-axis. According to fundamental dislocation theory,[186] the displacements associated with the TED at (*x,y,*z) along *x'*-axis and *y'*-axis, respectively, are given by:

$$u_{x'}(x,y)=\frac{b}{2\pi}\left\{\tan^{-1}\frac{-x\sin\theta+y\cos\theta}{x\cos\theta+y\sin\theta}+\frac{(x\cos\theta+y\sin\theta)(-x\sin\theta+y\cos\theta)}{2(1-\nu)\left[(x\cos\theta+y\sin\theta)^2+(-x\sin\theta+y\cos\theta)^2\right]}\right\},$$

$$u_{y'}(x,y)=-\frac{b}{2\pi}\left\{\frac{1-2\nu}{4(1-\nu)}\ln\left[(x\cos\theta+y\sin\theta)^2+(-x\sin\theta+y\cos\theta)^2\right]+\frac{(x\cos\theta+y\sin\theta)^2-(-x\sin\theta+y\cos\theta)^2}{4(1-\nu)\left[(x\cos\theta+y\sin\theta)^2+(-x\sin\theta+y\cos\theta)^2\right]}\right\},$$

where ν is the Poisson's ratio. Thus displacement field in (*xyz*) coordination system is thus given by:

$u_x(x,y)=u_{x'}(x,y)\cos\theta-u_{y'}(x,y)\sin\theta$

$u_y(x,y)=u_{x'}(x,y)\sin\theta+u_{y'}(x,y)\cos\theta.$

Once the displacement field is obtained, the plane normal at each small area on the sample surface after distortion can therefore be calculated by equation $\boldsymbol{g'=g-\nabla(g\cdot u)}$, where $\boldsymbol{g'}$ is the plane normal of the reflection plane after lattice distortion coming from the TED, $\boldsymbol{g}$ is the plane normal of the reflection plane before distortion (without the TED) and $\boldsymbol{u}$ is the displacement vector. Diffracted x-ray beams from each divided small areas

on the sample surface is assumed to have the same intensity and their directions can be determined from the plane normals at each small area. The penetration of x-ray beam below the sample surface can be neglected in our discussion due to two reasons: 1) the penetration depth in our geometry is small (~2 μm); 2) the effect of considering penetration of x-ray is equivalent to a shift of the dislocation image on the x-ray film, which is negligible due to the projection effect.

9.4. Results and discussion

Figure 72 shows a typical optical micrograph of an 8° off-cut *4H*-SiC after KOH etching. Several types of etch pits are observed, according to their geometrical configuration. The large hexagonal black etch pits and the small hexagonal etch pits are associated with the closed-core TSDs and TEDs, respectively. The etch pits from the TSDs are larger than the ones from TEDs because of the stronger strain field associated with the TSDs due to larger magnitude of Burgers vectors ($|b_{TSD}|$=10.05 Å and $|b_{TED}|$=3.08 Å in *4H*-SiC). The etch pits of TSDs and TEDs deviates slightly from symmetrical hexagonal shape due to the off-cut surface. Besides the etch pits from the TSDs and TEDs, another type of oval etch pits is visible as well in the image (as marked by triangles) and they are associated with the BPDs, which are in the basal plane and intersect the sample surface. The etch pits associated with the same type of dislocations appear as the same configuration, regardless of their Burgers vectors. Therefore, although the KOH etching reveals the intersection of the dislocations with the crystal surface, the detailed character of the dislocations, such as the dislocation sense and the direction of Burgers vectors, remains unknown.

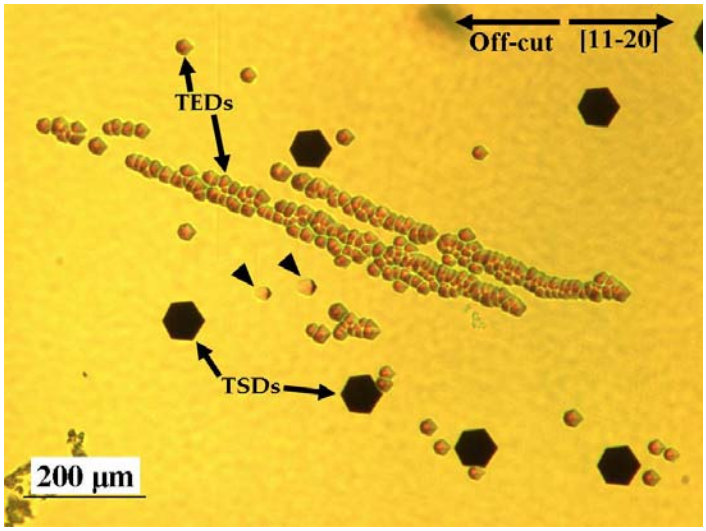

Figure 72. KOH etch patter of an 8° off-cut *4H*-SiC substrate. The large hexagonal black etch pits and the small hexagonal etch pits are associated with the closed-core TSDs and TEDs, respectively. Etch pits deviate from symmetrical hexagon due to off-cut. The TEDs are aligned along preferred direction, which is one of the <1-100> directions.

Previous studies by XRT have successfully revealed the handedness of TSDs by using asymmetric reflections (see Chapter 8). In order to study the detailed character of the TEDs, (11-28) asymmetric reflections were used for the TEDs as well. Figure 73(a) is a (11-28) topograph recorded from a *4H*-SiC wafer. The large roughly white circles are images of TSDs, as marked in the figure. Other than the TSDs, smaller images are also seen, corresponding to the TEDs with various Burgers vectors. They appear as two dark

arcs, either separated by a white spot or canted to one side or the other of the g-vector. By carefully examining the images of the TEDs in more than 50 topographs recorded, six different configurations of TEDs were observed and their highly magnified images are shown in Figs. 76(b) – 76(g). It can be seen that they appear as two dark arcs canted to one side or the other of the g-vector and these two dark arcs are either shifted vertically with each other [(b) and (c)], or separated by a white contrast [(d) – (g)]. The image (d) can be distinguished from (e) in that the white contrast in (d) is slightly smaller than the one in (e) and the two dark arcs in (e) are canted more with respect to the g-vector (vertical in the figure) than the ones in (d). Similar configurations are observed in (f) and (g), albeit the dark arcs are canted in an opposite way with respect to the g-vector. It has been well known that in *4H*-SiC each Si-C bilayer is closed-packed and there are six types of TEDs with six different Burgers vectors. The TED images observed in Figure 73 probably correspond to these six types of TEDs. However, which is which remains unknown.

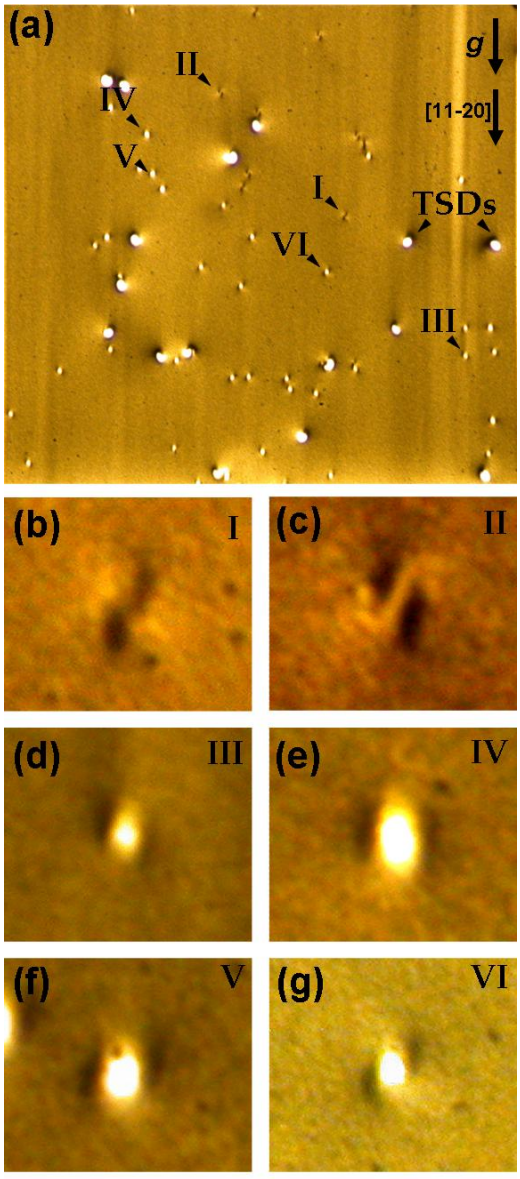

Figure 73. (a) (11-28) topograph showing various images of TEDs. (b) – (g): six different types of images of TEDs observed in the topographs, probably corresponding to the six types of TEDs.

The topographic images of the six types of TEDs have been simulated by ray-tracing method and they are shown in Figure 74. The schematics of six types TEDs is illustrated on the top of the figure, according to the extra atomic half planes associated with them. They appear as two dark arcs canted to one side or the other of the g-vector and these two dark arcs are either shifted vertically [(a) and (b)] or separated by an area of white contrast [(c) – (f)]. Their Burgers vectors are at 60^o, 120^o, 180^o, 240^o, 300^o and 0^o counterclockwise to the g-vector on the x-ray films for (a) – (f), respectively. The image dimensions of the TEDs in the direction perpendicular to the reflection vector range between 7 – 12 μm, at specimen-to-film distance of 10 cm.

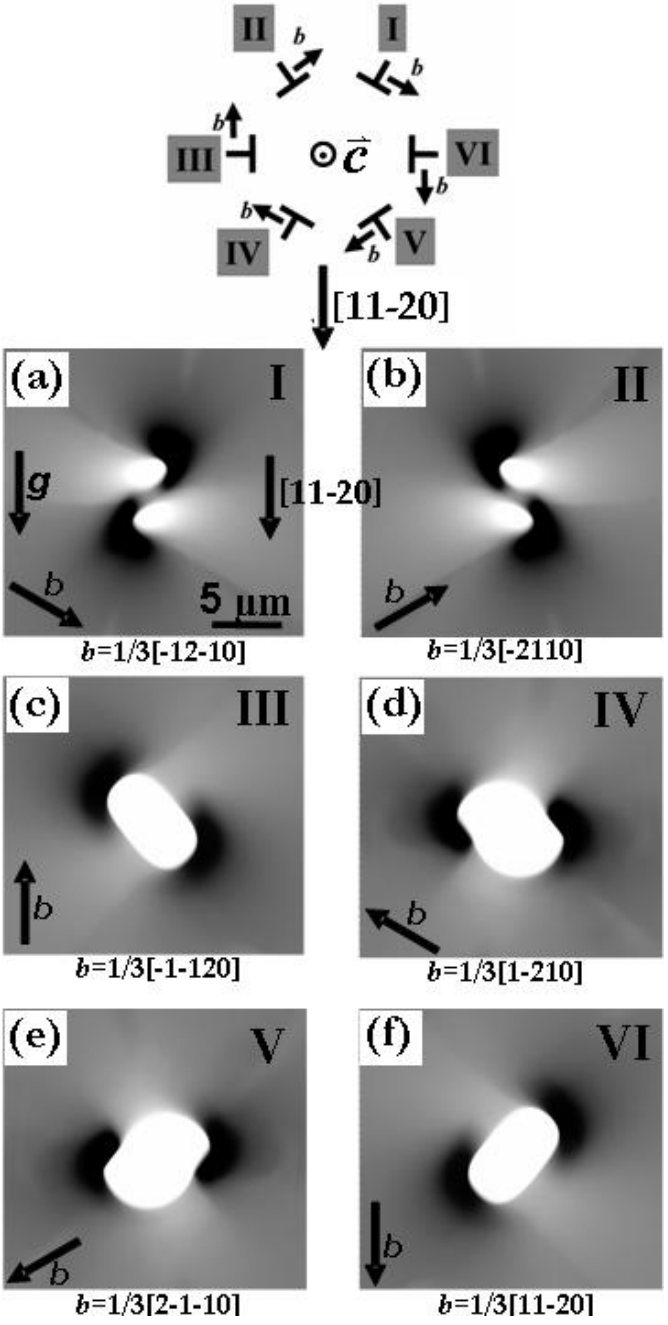

Figure 74. Simulated (11-28) grazing-incidence XRT images of TEDs with six different Burgers vectors [(a) – (f)]. Top: Six types of TEDs are illustrated according to the position of their extra atomic half planes associated with them.

By comparing the simulated images in Figure 74 and the observation in Figure 73, one-to-one correspondence can be seen. Therefore, the Burgers vectors of the TEDs can be revealed from a single reflection (11-28) grazing-incidence x-ray topograph, based on their topographic contrast. The image size and the dimension of the white contrast in (d) and (e) are larger and the two dark arcs are canted more with respect to the g-vector than in (c) and (f), respectively. In order to confirm our determination, an additional grazing-incidence topograph using an equivalent {11-28} reflection can be recorded. Figure 75 shows the topographs recorded using two equivalent {11-28} reflections and the projections of their reflection vectors are at 60^{o} with each other (indicated in the topographs). Three types of TEDs are observed in the (11-28) topograph (a) and marked by II, III and IV. By comparing their images with the simulation, one can notice that the Burgers vector of TED II can be unambiguously determined (see inset for the matched simulation and Burgers vector) and it is at 120^{o} counterclockwise to the projection of the reflection vector on the film. The simulated images are shown in the insets for comparison and the Burgers vectors can thus be determined. The TED III and IV can be further confirmed by an additional grazing-incidence topograph recorded using (-12-18) reflection [Figure 75(b)]. It should be noted that in Figure 75(b), the angle of view has to be such that **g**-vector is pointing downward (the simulated images have to be re-oriented as well). From such angle of view, the Burgers vectors of TEDs III in Figure 75(b) can be unambiguously determined (see the inset simulation for comparison) and its Burgers vector is at 120^{o} counterclockwise to the g-vector in the geometry. Similarly, the Burgers vector of TED IV can be unambiguously determined as well: it is at 240^{o} counterclockwise to the g-vector in Figure 75(a). These results are completely consistent with the ones from Figure 75(a). Note that the dark arcs of TED II in (b) are canted in an opposite way with respect to the g-vector, compared with in (a), which is expected according to simulation.

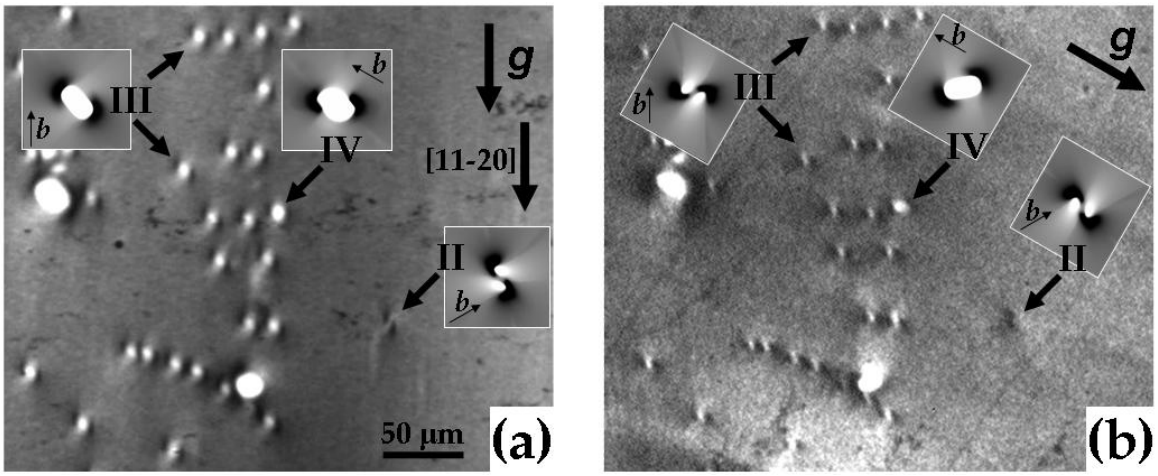

Figure 75. Two grazing-incidence topographs taken using equivalent {11-28} reflections. (a) (11-28); (b) (-12-18).

The determination of Burgers vectors of TEDs can be further verified by the observation of a BPD converted into TED segments at both ends. Figure 76 shows one of the examples and it is actually a dislocation half loop with a BPD segment connecting the

two TED segments intersecting the sample surface. The two TED segments appear as different configurations and by comparing their images with the simulation we can easily determine their Burgers vectors, as indicated in the insets. Their Burgers vectors are anti-parallel with each other since in the simulation we assume that the line direction is always pointing out of the paper. This is not against the conservation of Burgers vectors, since their Burgers vectors are the same if we assume the line direction is going from one TED segment to the other within the half loop (If so, the line directions of the two TEDs are anti-parallel). The extra atomic half planes associated with the TED segments are indicated in the figure. Many other similar examples have been examined as well and they all confirmed our determination of the Burgers vectors of TEDs.

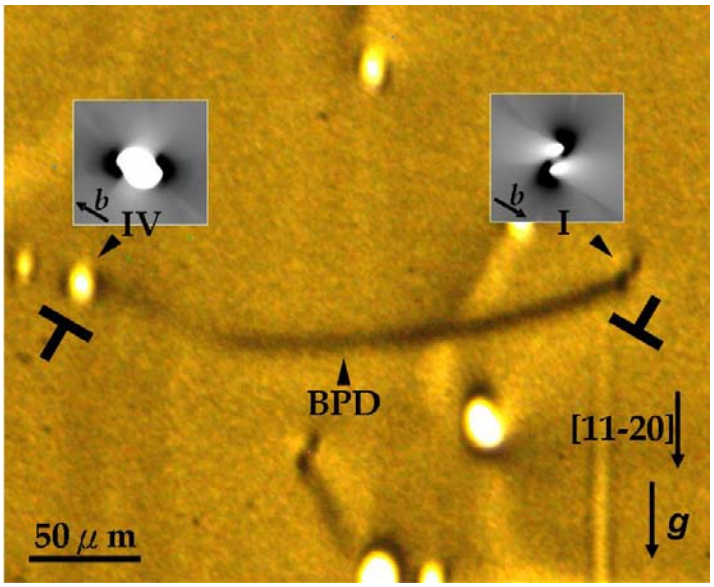

Figure 76. (11-28) grazing-incidence x-ray topograph showing a BPD, which is converted into TEDs at both ends.

The TEDs are often observed to aggregate into arrays, oriented at certain directions and one example can been seen in the KOH etch pattern in Figure 72. The TED arrays are parallel to [01-10] direction. Large amount of observations in synchrotron x-ray topographs also indicate that the TED arrays prefer to be oriented along <1-100> and one of the examples is shown in Figure 77. A few TED arrays can be observed and they are oriented along one of the <1-100> directions. Based on the simulated images of TEDs in the previous studies, one can unambiguously determine the Burger vectors of the TEDs in the arrays. Five TED arrays, comprising three different types of TEDs corresponding to type II, IV and V in Figure 74, are marked in the figure and one can find out that their Burgers vectors are perpendicular to the arrays. This is consistent with the fundamental dislocation theory that the edge-oriented dislocations are tending to align perpendicular to their Burgers vector direction to minimize the total strain energy.[187]

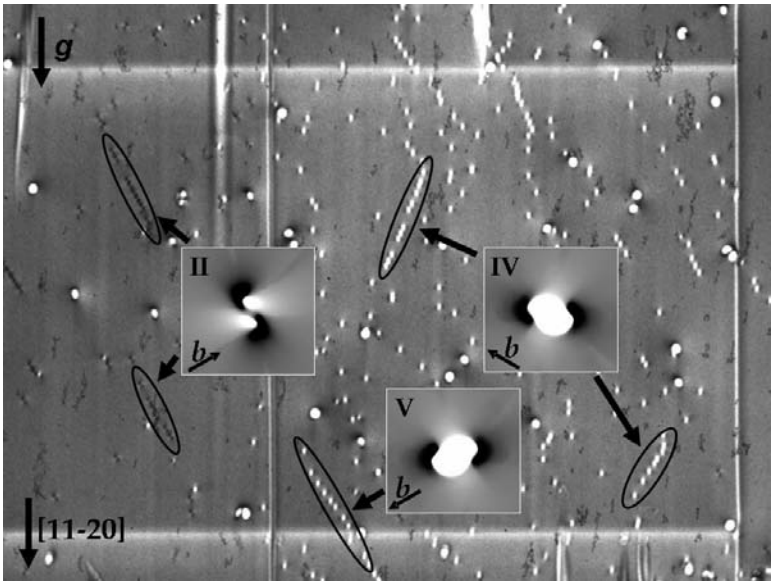

Figure 77. (11-28) grazing-incidence x-ray topograph showing the TED arrays. Their Burgers vectors are perpendicular to the direction of the TED array.

9.5. Conclusion

In summary, six types of x-ray topographic images of threading edge dislocations were observed and their Burgers vectors can be determined from a single grazing-incidence x-ray topograph, based on the simulation using ray-tracing method. Their Burgers vectors can be further verified by an additional equivalent (11-28) reflection or a dislocation half loop containing two threading edge dislocation segments. The threading edge dislocation arrays are tending to orient along <1-100> directions and the Burgers vectors of the threading edge dislocations comprising them are perpendicular to the arrays, which is expected for minimizing the total strain energy.

10. On the Susceptibility of Basal Plane Dislocations to the Recombination Enhanced Dislocation Glide in *4H* Silicon Carbide

10.1. Outline

The susceptibility of basal plane dislocations to the recombination enhanced dislocation glide was studied in 4*H* silicon carbide bipolar devices. The susceptibility of the basal plane dislocations can be straightforward determined based on its character. Full susceptibility map has been proposed. Basal plane dislocations with extra half planes extending toward silicon-face and Burgers vector more than 30^{o} with respect to its line direction are most detrimental, as both partial dislocations are mobile under forward bias. Screw-oriented basal plane dislocations dissociate into one mobile and one immobile partial dislocation. Experimental proof has been presented.

10.2. Introduction

Dissociation of basal plane dislocations (BPDs) into mobile silicon-core (Si-core) partial dislocations and subsequent advancement of these partial dislocations under forward bias pose a big challenge on the lifetime of silicon carbide (SiC) based bipolar devices,[188] since the expansion of Shockley stacking faults (SFs) associated with the advancement of Si-core partials causes the forward voltage drop. Such expansion of basal SFs is activated by the electron-hole recombination enhanced dislocation glide (REDG) process[189-191] and the driving force has been attributed to the thermodynamic stability of cubic SiC.[192] Si-core partial dislocations are found to be mobile while carbon-core (C-core) partials are stationary. This is due to the electron-hole recombination, reducing the activation enthalpy of Si-core partial dislocations by ~2.2 eV.[193] Although the influence of the SFs on degradation of SiC-based bipolar devices and their behaviors have been studied by many researchers,[194-197] the susceptibility of BPDs on the REDG process remains obscure. In this chapter, the susceptibility of basal plane dislocations to the REDG process was studied in 4*H* SiC bipolar devices. Full susceptibility map has been proposed.

10.3. Experimental

The 4*H*-SiC substrates used in this study were commercially available wafers grown by the physical vapor transport (PVT) technique with an 8° off-cut angle in the [11-20] direction. The epitaxial layer structure is typical for 10 kV PiN diodes. It consists of a 16 μm n^+ buffer layer, 2×10^{18} cm^{-3}, and a 115 μm n^- layer, 2×10^{14} cm^{-3}, capped by a 2 μm p^+ layer, 8×10^{18} cm^{-3}. Contact to the p^+ layer is formed by depositing aluminum and patterning a grid structure. The device was electrically stressed in the range from 1-14 A/cm^2 and synchrotron x-ray topographs were recorded following the forward bias stressing. The imaging was carried out at the Stony Brook Synchrotron Topography Station, Beamline X-19C, at the National Synchrotron Light Source at Brookhaven National Laboratory, and Beamline XOR-33BM, at the Advanced Photon Source at Argonne National Laboratory, using Ilford L4 nucleate plates at a specimen-to-film distance between 10 and 13 cm.

10.4. Results and discussion

It has been established that the Burgers vectors of the BPDs in SiC are 1/3<11-20> and two extra (11-20) half planes are associated with an edge-oriented BPD, as the magnitude of its Burgers vector is twice the *d*-spacing of (11-20) plane.[198] The BPD is energetically favorable to be dissociated into two Shockley partial dislocations with a SF area in between and the equilibrium separation *d* of the two Shockley partial dislocations is given by $d=Gb^2/4\pi\gamma$, where *G* is the shear modulus, *b* is the magnitude of Burgers vector of Shockley partial dislocation and γ is the energy of the SF. This equilibrium separation is ~330 Å for 4*H*-SiC, assuming the SF energy is 14.7 mJ/m^2.[199] Experimental observations indicate that the Shockley partials dissociated from the BPD can be either mobile or stationary under forward bias. Large amount of experimental and theoretical studies indicate that the Si-core partial is mobile via REDG process, while C-core partial is immobile.[193,200,201] Now the issue of the susceptibility of the BPDs to REDG process arises.

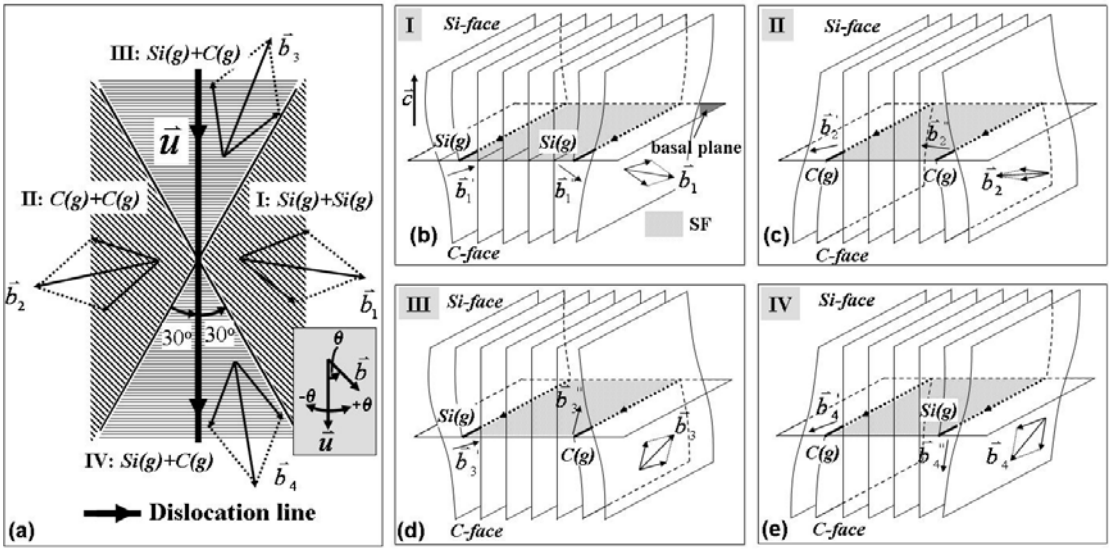

Figure 78. Schematics showing Shockley partial dislocations of different core structures dissociated from a perfect BPD. (a) Four regions defined, according to the direction of Burgers vector with respect to the line direction of the dislocation, assuming Si-face is facing up; (b) Region I: $30^o<\theta<150^o$, the BPD is dissociated into two Si-core partials; (c) $210^o<\theta<330^o$, the BPD is dissociated into two C-core partials; (d) $-30^o<\theta<30^o$, one Si-core and one C-core; (e) $150^o<\theta<210^o$, one Si-core and one C-core. θ is defined in the inset of (a).

The dislocation character of a BPD is determined by the angle between its line direction and the Burgers vector. Figure 78 illustrates the various cases when a perfect BPD is dissociated into Shockley partial dislocations. The angle θ is defined as following: it is the counterclockwise angle from the line direction to the Burgers vector direction (clockwise angles are negative), see the inset of Figure 78(a). In region "I", in which $30^o<\theta<150^o$, the extra half plane(s) associated with the BPD extend toward the Si-face (assuming the Si-face is facing the reader), determined by the right-hand rule $\boldsymbol{u}\times\boldsymbol{b}$. If

$30^o<\theta<150^o$, when the BPD with Burgers vector $\boldsymbol{b_1}$ is dissociated into two partial dislocations of Burgers vectors $\boldsymbol{b_1}'$ and $\boldsymbol{b_1}''$ [Figure 78(b)], the angles between $\boldsymbol{b_1}'/\boldsymbol{b_1}''$ and their line directions (assuming the same line direction as the BPD) will be in the range (0^o, 180^o). The extra half planes associated with the two partials can be subsequently determined again by right-hand rule $\boldsymbol{u}\times\boldsymbol{b_1}'$ and $\boldsymbol{u}\times\boldsymbol{b_1}''$: both are extending toward the Si-face. Since the Shockley partials in *4H*-SiC are glide set dislocations, both partials are Si-core. Under this circumstance, the SF will expand toward both directions, as both partials are mobile. Similar mechanism can be applied for regions II, III and IV: in region II [Figure 78(c)], both dissociated partials are C-core and neither of them advances; while for regions III [Figure 78(d)] and IV [Figure 78(e)], a Si-core and a C-core partial are formed and the SF expands as the Si-core partial advances. Notice that if the Burgers vector of the BPD is at $30^o/150^o/210^o/330^o$ to its line direction, it is dissociated into a screw-oriented and a C-core or Si-core partial. Therefore, comprehensive understanding of the susceptibility of the BPD on the REDG process can be obtained based on our discussion.

X-ray topography has been employed to verify the argument. EL observation[202] indicates that a straight long BPD was dissociated into two partials and one of them advanced, expanding the SF. Figure 79 shows the x-ray topographs [(a)-(e)] and schematic configuration after the advancement of the mobile partial. During the advancement of the partial, it interacted with a few TSDs and the configuration is obtained, as illustrated in the schematics [Figure 79(g)]. The interaction process between advancing partial and TSDs can be referred to Ref. 195. The bounding partials are clearly observed in (11-20) transmission topograph [Figure 79(a)] and the SF area is out of contrast since $\boldsymbol{g}\cdot\boldsymbol{R}$ is equal to an integer. The SF is bounded by a horizontal partial segment P1, which is at the initial position of the straight BPD, and a segment P2, whose configuration is obtained after its advancement and interaction with threading dislocations under REDG process. The dislocation segment U is not related to the SF discussed here. The SF is clearly seen in Figure 79(b) and a few other SFs are also observed. Segment P2 disappears in (2-1-10) transmission topograph [Figure 79(c)], indicating a Burgers vector of 1/3(0-110) or 1/3(01-10) and segment P1 disappears in (1-210) transmission topograph [Figure 79(d)], indicating a Burgers vector of 1/3(-1010) or 1/3(10-10). The dislocation sense of the partials can be revealed from back-reflection topograph [Figure 79(e)], in which the extra half planes associated with the partials can be determined. The detailed discussion has been reported by Chen *et al*.[202] Assume the line direction of P1 is pointing leftward, the Burgers vectors of segments P1 and P2 are 1/3(-1010) and 1/3(0-110), respectively, as indicated in Figure 79(f). The Burgers vector $\boldsymbol{b}$ of the original BPD can be subsequently determined to be 1/3(-1-120), as indicated in Figure 79(f). Therefore, the original BPD is screw-oriented ($\theta=0^o$) and it is dissociated into a C-core and a Si-core partials. This is consistent with our prediction and corresponds to the case in region IV of Figure 78, in which θ is between -30^o and 30^o.

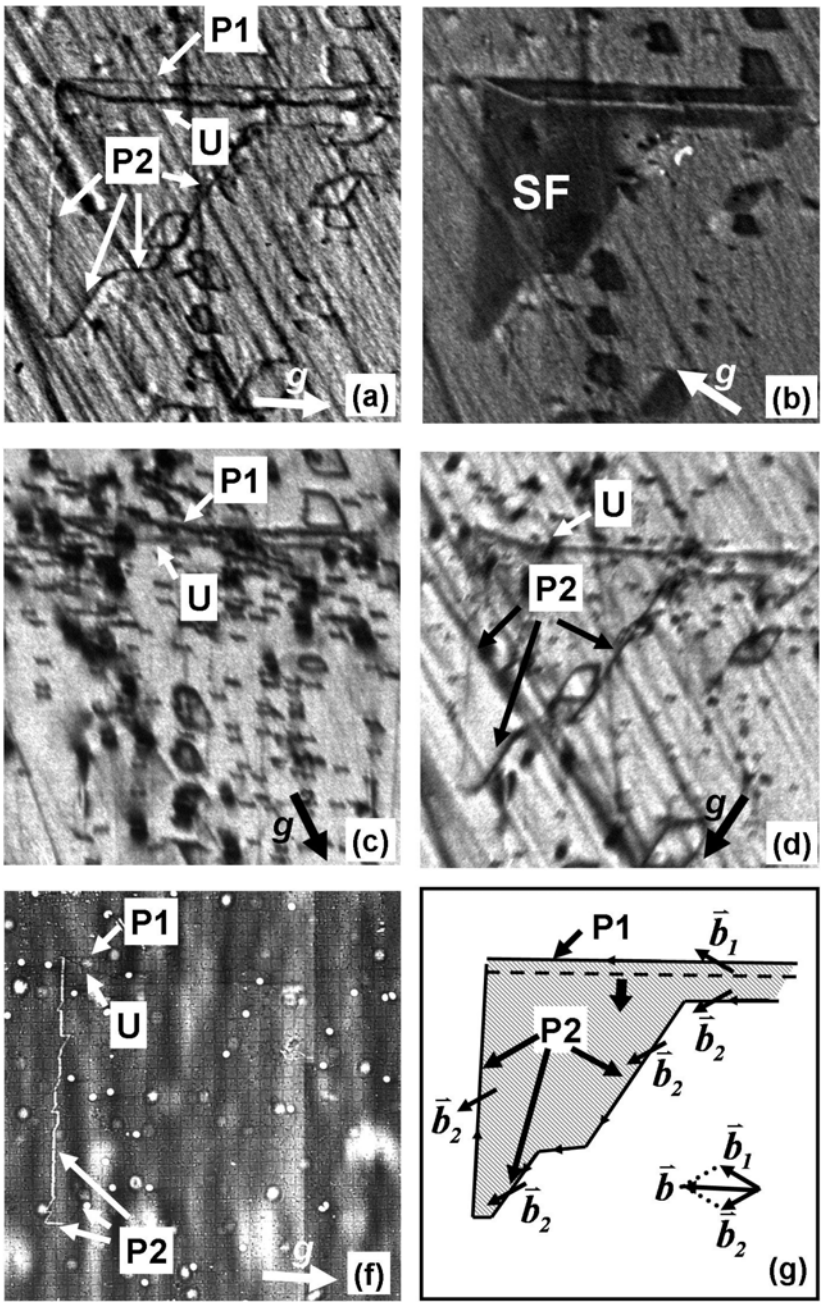

Figure 79. REDG activated SF after forward bias from a screw-oriented BPD. (a) (11-20) transmission topograph showing the partials (P1 and P2) bounding the SF. The SF area is out of contrast since $\boldsymbol{g \cdot R}$ is equal to an integer; (b) (-1010) transmission topograph showing the SF; (c) P2 is out of contrast in (2-1-10) transmission topograph, indicating its Burgers vector of 1/3(0-110); (d) P1 is out of contrast in (1-210) transmission topograph, indicating its Burgers vector of 1/3(-1010); (e) (0008) back-reflection topograph. The sign of P1 and P2 can be determined; (f) schematics showing the SF configuration. The SF is obtained via expansion of Si-core partial toward the bottom edge of the view (see the dashed line) and interaction with TSDs. The Burgers vector of each partial segment is labeled; the Burgers vector $\boldsymbol{b}$ of the original BPD can be obtained and it is screw-oriented.

As discussed in Figure 78, a perfect BPD is dissociated into two Si-core partials if the Burgers vector falls in region I. In such situation the SF will expand toward both directions since both partials are mobile under forward biasing. Observations of the expansion of both partials have been reported from an array of dislocation half loop.[203] Such dislocation half loops containing two threading edge dislocations and short basal plane segments are observed near the substrate/epilayer interface in CVD grown epilayers.[204] The basal plane segment is between 0.5-8 μm in length[204] and it is expected to be nearly straight, considering the low thermal stress during CVD growth (at a shear stress of 10^5 Pa, the equilibrium diameter is ~1200 μm, which is much larger than the dimension of the basal plane segment). According to the nucleation mechanism of the dislocation half loop array proposed by Zhang,[205] the basal plane segment has Burgers vector antiparallel to the off-cut directions, with extra atomic half plane extending toward the Si-face, which corresponds to the case in region I (see Figure 78). Therefore, two mobile Si-core partial dislocations are expected and it is consistent with the observation in EL.

10.5. Conclusion

In summary, the susceptibility of the basal plane dislocations to recombination enhanced dislocation glide process is determined by the counterclockwise angle θ from the line direction to its Burgers vector. Full susceptibility map has been proposed. The basal plane dislocations with $30^o<\theta<150^o$ are most detrimental, as both partials will advance under forward bias. If $-30^o<\theta<30^o$ or $150^o<\theta<210^o$, only one partial advances. Both partials are immobile if $210^o<\theta<330^o$. Experimental observations were discussed, which are consistent with our argument.

11. Direction determination of core structures of Shockley PDs in SiC

11.1. Outline

Core structures of electron-hole recombination activated partial dislocations in 4*H* silicon carbide bipolar devices have been studied using synchrotron x-ray topography and electroluminescence. The mobile Shockley partial dislocations bounding the stacking faults appear as white stripes while the immobile partial dislocations appear as narrow dark lines in x-ray topography using basal plane reflection. Such variation of contrast of partial dislocations is attributed to the defocusing/focusing of diffracted x-rays by the convex/concave lattice planes resulted by the edge component of the partial dislocations. Simulation results prove the argument. The core structure can be readily determined.

11.2. Introduction

Although the density of threading dislocations can be reduced via repeated *a*-face growth by two to three orders,[206] the forward voltage drop under forward biasing in bipolar devices, due to the expansion of basal stacking faults (SFs) caused by the advancement of Shockley partial dislocations, poses a big challenge on the lifetime of SiC-based bipolar devices. Such expansion of basal SFs is activated by the electron-hole recombination enhanced dislocation glide (REDG) process[207-210] and the driving force could be attributed to the thermodynamic stability of cubic SiC.[192] First-principles calculation indicates that the reconstructions along the dislocation lines can be electrically active by giving rise to energy states in the forbidden band gap.[211] Both types of partial dislocations [carbon-core (C-core) and silicon-core (Si-core)] can be mobile under different circumstances: e.g., Si-core partial is highly mobile under forward bias, while C-core partial is more mobile at high temperatures.[212] The more mobile C-core at high temperatures is due to its lower glide activation energy.[212] However, the highly mobile Si-core partial under forward biasing is owing to the REDG process and the activation enthalpy for its motion is subsequently reduced by more than 2 eV.[213] Thus, it is of great importance to understand the chemical structures of partial dislocations so as to study their influence on energy states in the band gap. S. Ha and X. J. Ning have employed transmission electron microscopy to determine the core structure of partial dislocations in SiC.[214,215] However, difficulties in sample preparation pose drawbacks in determining the core structures of partial dislocations using transmission electron microscopy. Synchrotron x-ray topography stands out due to its capability of nondestructive analysis and much less rigid sample preparation process, enabling complete analysis of defects, e.g., line direction, Burgers vector, and even dislocation sense. [13,14,56] In this letter we employ x-ray topography to directly reveal the core structures of the Shockley partial dislocations bounding the REDG activated SFs in *4H*-SiC bipolar devices. This method was found to be capable of revealing the core structure of Shockley partial dislocation unambiguously and it can in principle facilitate the determination the characters of Shockley partial dislocations in any binary compound semiconductor materials directly and nondestructively.

11.3. Experimental

The epitaxial layer structure consists of a 16 μm n^+ buffer layer, $2x10^{18}$ cm^{-3}, and a 115 μm n^- layer, $2x10^{14}$ cm^{-3}, capped by a 2 μm p^+ layer, $8x10^{18}$ cm^{-3}. Contact to the p^+ layer is formed by depositing aluminum and patterning a grid structure. This method has been shown to be just as effective as using fully processed PiN diodes for the purpose of electroluminescence (EL) imaging dislocations.[216] The EL imaging was carried out at 1 A/cm^2 and electrical stressing was in the range from 1-14 A/cm^2. Images were collected in the wavelength range from 600 to 1000 nm using a sensitive setup that is described elsewhere.[217] Back-reflection topographs were recorded following the forward bias stressing. The specimen was then thinned down from the substrate side to ~140 μm for transmission topograph. The ray-tracing method was used to simulate the topographic images of partial dislocations in back-reflection x-ray topography. Detailed simulation process can be referred to Ref.13.

11.4. Results and discussion

It has been established that the advancement of Shockley partial dislocation is activated by the REDG process and the basal stacking fault expands as the leading Shockley partial advances. *In situ* EL has been used to study the expansion process in our study. Sequential EL images were excerpted from a large number of images, see Figure 80(a)-(c). Figure 80(d)-(f) are the corresponding schematics showing the configurations of SF in Figure 80(a)-(c), respectively. In Figure 80(a), a long BPD, A_1B_1, and some bright dots are observed. The bright dots are threading dislocations (either edge or screw) and they can be distinguished by x-ray topograph (not shown). Some of the TSDs are marked in Figure 80. This BPD was propagated from the substrate into the epilayer during chemical vapor deposition (CVD) growth via the step-controlled growth, along the step-flow direction. The screw character of this BPD has been determined by Burgers vector analysis after thinning down,[218] which is consistent with the report from Jacobson *et al*.[219] During the electrical stressing, the screw-oriented BPD is dissociated into two partials and one of them advances toward the bottom side of the view, trailing behind a Shockley-type stacking fault on the basal plane. It occurs only in n- layer where the advancement of leading Shockley partial is activated by the electron-hole recombination process. When the advancing partial dislocation interacts with a TSD, it is split into two dislocation segments, normally advancing at different velocity, separated by the pinning point at the TSD core. The interaction between the advancing partials and the TSDs is not discussed here, though detailed interaction process can be referred to Chapter 6. The splitting of partial dislocation by the TSD can be observed in Figure 80(b) [dislocation configuration in Figure 80(b) is schematically shown in Figure 80(e)] and the two split mobile segments E_2F_2 and G_2H_2 continue to advance (toward the bottom, as marked by arrows). A partial dislocation segment D_2E_2, lying along its Peierls valley direction, is expected to be deposited as E_2F_2 advances (not visible in EL) in order to maintain the continuity of the dislocation. The configuration in Figure 80(c) is observed after further expansion of SF and the corresponding configuration is illustrated in Figure 80(f). Since the electron–hole recombination only occurs in the n^- layer, the motion of the mobile partial dislocation will terminate at the p^+/n^- interface where a segment of "60°" partial

dislocation is deposited near the p^+/n^- interface during the process [see A_2H_2 in Figure 80(b) or A_3I_3 in Figure 80(c)]. They are expected to appear as zigzag configuration in a fine scale, with each segment lying along its Peierls valley direction.

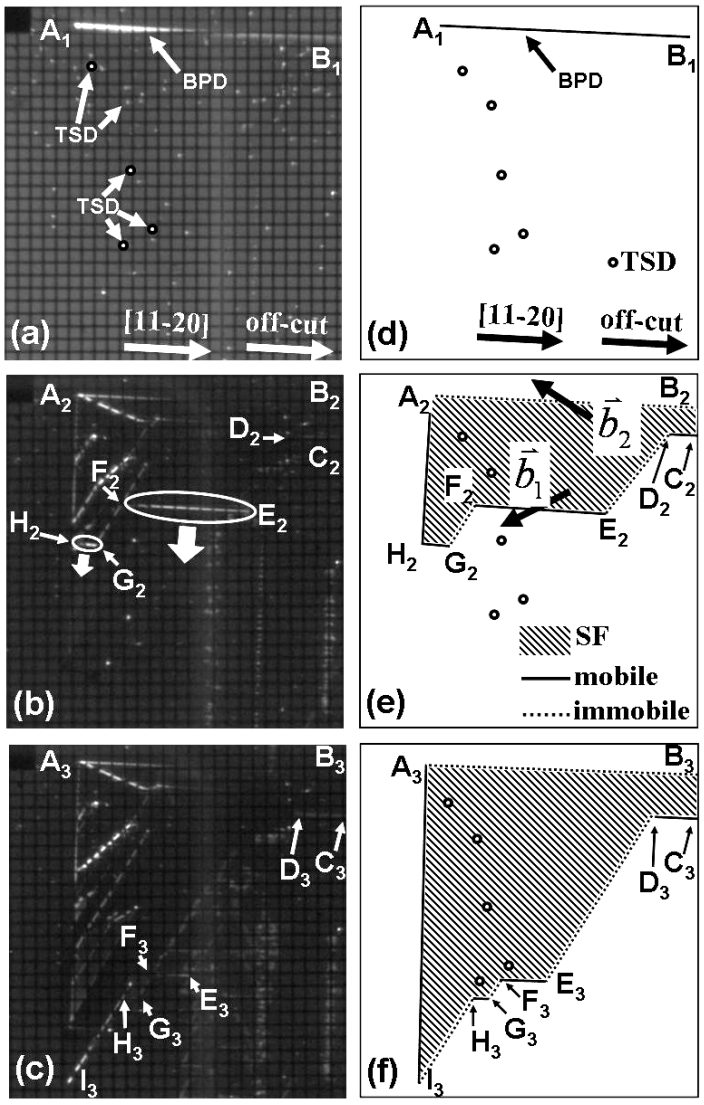

Figure 80. (a) A BPD and several TSDs are observed in EL image before electrical stressing; (b) The leading Shockley partial dissociated from the BPD advances, expanding the SF and interacts with TSDs; (c) Further expansion of SF; (d)-(f) Schematic diagrams showing the configurations in (a)-(c), respectively.

After first electrical stressing, the sample was then low-temperature annealed (~500°C) for 72 hours and electrically stressed under the same condition again. Back-reflection x-ray topography was subsequently recorded after second stressing. Previous observations from EL indicate that low temperature annealing is just a reverse process of the expansion of Shockley SF.[220] Therefore, the topograph recorded after second electrical stressing process can be considered as an image taken *in situ* during the first electrical stressing. Figure 81(a) shows the topograph recorded from the same device cell as in Figure 80, using (0008) reflection. The small square shaped features observed throughout Figure 81(a) are associated with the device pattern. The features indicated by the letters "PC" are artifacts produced by phase contrast associated with defects on the beamline x-ray windows (contrast which arises due to the coherence of the incident x-ray

beam). Figure 81(b) is the (-1011) transmission topograph of the same area after thinning down and a 3-D schematics is shown in Figure 81(c), based on topography and EL. Four partial dislocations bounding the SF are visible in the Figure 81(a) (marked by "D1", "D2", "F1" and "F2") and the SF area itself is out of contrast since $\boldsymbol{g \cdot R}$ is equal to an integer (zero). The circular white dots in the topograph correspond to elementary TSDs with Burgers vector 1*c*. The complete configuration of the SF can be seen in transmission topograph in Figure 81(b), in which the dark contrast area corresponds the SF (some small-area SFs are also seen). The configuration of the SF is achieved via a process discussed in Figure 80. The dislocation segment "U" is unrelated to the SF discussed here and it shows as a white line in Figure 81(b). The status of the SF on the topograph is between Figure 80(b) and (c) and the configuration in Figure 80(c) is expected with further advancement of partial segments D2 to the p^+/n^- interface ["D1" corresponds to A_3I_3 in Figure 80(c)]. Since the partial dislocation "D1" has not completely reached the interface, it appears as zigzag configuration at certain positions on the topograph. The straight segment on "D1" is also expected to appear as zigzag at a very fine scale, with each segment lying along its Peierls valley direction. Due to the limited penetration depth of x-ray, only part of bounding partial dislocations is visible on the topograph and the invisible segments can be visualized from the SF configuration observed in Figure 81(b). The topograph shows that the contrast from the partial dislocations bounding the SF appears in one of two possible configurations: either as a narrow dark line or as a white stripe with diffuse narrow bands of dark contrast running along its edges. The dark contrast bands lying alongside the white stripe can be more clearly seen in an example under higher magnification, as shown in the inset of Figure 81(a). The roughly vertical partial dislocation "D1" and the short horizontal segment "D2" at the bottom end of the vertical segment appear as white stripe configuration while the partial dislocations "F1" and "F2" appear as narrow dark lines.

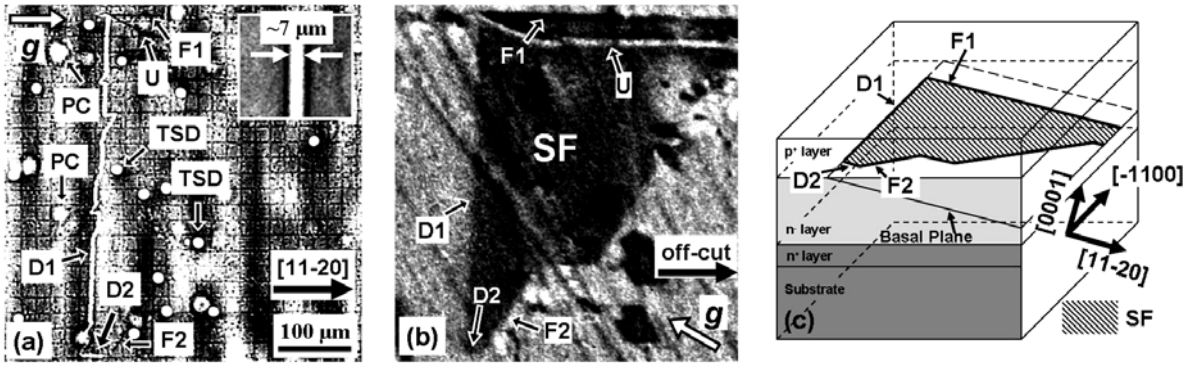

Figure 81. (a) Back-reflection topograph showing partial dislocations bounding a SF (SF area is out of contrast). Inset shows the highly magnified image of the white strip feature, with diffuse narrow bands of dark contrast running along its edges. (b) (-1011) transmission topograph showing the complete configuration of the SF. (c) Three-dimensional schematics showing the structure of the device and configuration of the SF.

Based on observation of images of MPs in SiC, Dudley *et al.* found that in the low absorption case, the direct dislocation image comprises a dominant orientation contrast contribution arising from the overlap and separation of the inhomogeneously diffracted x-

rays with continuously varying directions.[221] Such orientation contrast has been first used in simulating the topographic images of MPs in back-reflection geometry, enabling their dislocation character to be elucidated.[56] Chen *et al.* also has employed such orientation contrast mechanism to successfully simulate the TSD/MP images in grazing-incidence geometry and revealed their dislocation senses (Chapter 7 and Chapter 8). These studies indicate that orientation contrast rather than extinction contrast is the dominant determinant of the contrast of TSDs on reflection topographs. Furthermore, Huang *et al.* recently explained the contrast variation of two types of BPDs observed in SiC back-reflection topograph based on this orientation contrast mechanism.[29] Thus, it is reasonable to apply this mechanism to the observations of partial dislocations in back-reflection geometry, as portrayed schematically in Figure 82. As we know, the partial dislocations usually are composed of 30^o or 90^o segments lying along their Peierls valley directions. The 90^o segment is moving much faster[222] and it vanishes, leaving only 30^o segments remaining. In our case, segments "D2", "F1" and "F2" are 30^o dislocations, while "D1" is approximately a 60^o segment (since it has terminated its motion upon arrival at the n^-/p^+ interface where the electron-hole recombination goes to zero). Because the partial dislocations are not of pure screw character they have edge components which have extra atomic half planes associated with them. Although the straight segment of "D1" observed in Figure 81(a) is expected to appear as zigzag configuration (each segment is lying along its Peierls valley direction) in a very fine scale, the overall effect would be equivalent to imaging a 60^o dislocation x-ray topography. The screw component does not contribute to the topographic contrast since both $\boldsymbol{g}\cdot\boldsymbol{b}_s$ and $\boldsymbol{g}\cdot\boldsymbol{b}_s\times\boldsymbol{l}$ are equal to zero (here $\boldsymbol{g}$ is the reflection vector, $\boldsymbol{b}_s$ is the Burgers vector of screw component and $\boldsymbol{l}$ is the line direction of the dislocation). Thus the contrast is exclusively arisen from the edge component of the partial dislocation. In the case shown in Figure 82(a) where the extra half plane extends toward the bottom face of the crystal, the basal planes appear as a concave configuration near the dislocation core. This distortion of the basal planes tends to focus the x-ray beam, giving rise to the overlap of diffracted x-rays on the film. In contrast, when the extra half plane associated with the partial dislocation extends toward the upper face of the crystal [Figure 82(b)], it causes a convex distortion of the basal planes, giving rise to a defocusing or separation of diffracted x-rays on the film. The intensity distribution is illustrated in Figure 82 for both cases. Notice here that the defocused x-rays in Figure 82(b) overlap along the sides of the white stripe, producing double dark contrast bands. The ray-tracing method has been employed to simulate the images of a 60^o dislocation with extra half plane extending toward the x-ray reflection surface [see the simulated image in Figure 82(a)] and a 30^o dislocation with extra half plane extending in the opposite direction [see the simulated image in Figure 82(b)]. The simulated image in Figure 82(a) appears as a narrow dark line while the one in Figure 82(b) shows as a white stripe (~7.5 μm in width) with defocused x-rays overlapping beside it, giving rise to double dark contrast bands. These dark bands along the sides of the white stripe can be seen more clearly in the inset of Figure 81(a) which shows a magnified image of the boxed region. Detailed examination shows that the simulated images show very good correspondence with the recorded images, in both contrast and dimension. The width of "D1" in its zigzag portion varies due to the variation of dislocation character (the magnitude of the edge component of the Burgers vector varies with the line direction). It should be noticed here that the straight partial dislocation

segment “D2”, which is lying strictly along its Peierls valley direction, also appear as white stripe in x-ray topography. Its image is also consistent with simulated image based on ray-tracing, in both contrast and dimension. It is narrower than the “straight” segment on “D1”, since “D2” is a 30^{o} dislocation (less edge component). Therefore, the simulation validates our argument that the topographic contrast results from the concave or convex shaped lattice planes near the dislocation core caused by the displacement field associated with the edge segment of the partial dislocations, giving rise to focusing or defocusing of x-ray beams.

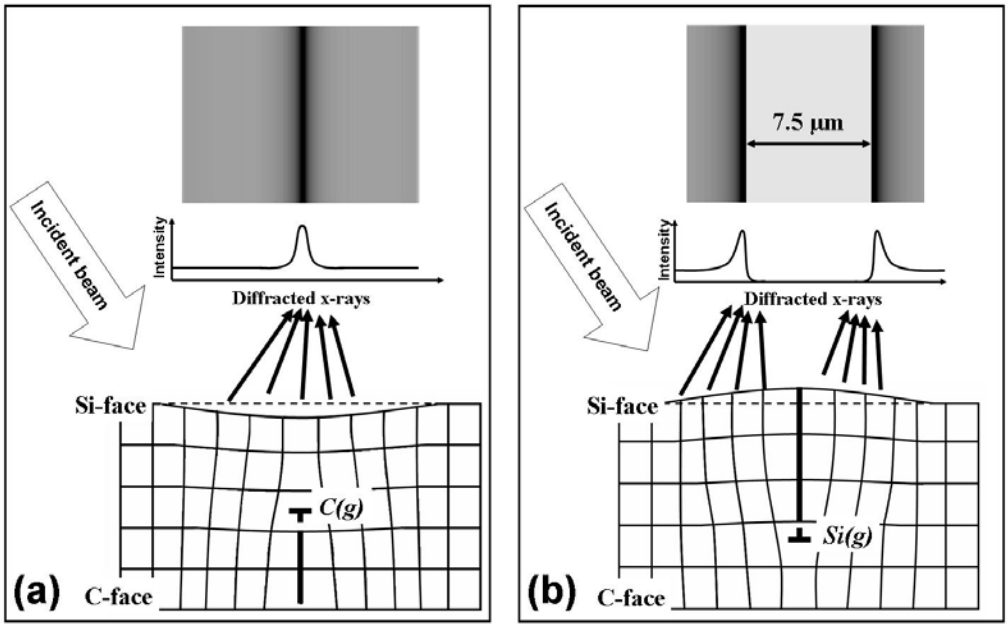

Figure 82. Focusing (a) and defocusing (b) of x-ray beams by the concave and convex basal planes, caused by the displacement field associated with the edge component of the partial dislocations, giving rise to the dislocation image of narrow dark line or white stripe.

Obtaining the configuration of the extra half planes associated with the partial dislocations enables us to reveal their core structures straightway. It has been established that the Shockley partials in SiC are glide set dislocations and if the extra half plane is extending toward the C-face, the corresponding Shockley partial is a C-core dislocation, while the converse is a Si-core dislocation. Since the device structure is fabricated on the Si-face of a 4*H*-SiC substrate in our case, the partial dislocation, which causes the focusing of x-rays, corresponds to a C-core partial [Figure 82(a)], while the partial dislocation, giving rise to the defocusing of x-rays, is Si-core [Figure 82(b)]. Therefore, the core structure of the partial dislocations in Figure 81(a) can be subsequently determined: “D1” and “D2” are Si-core dislocations, while “F1” and “F2” are C-core. This is consistent with previous report that the mobile partials are Si-core and immobile ones are C-core.[214]

11.5. Conclusion

In summary, the partial dislocations bounding stacking faults in *4H*-SiC bipolar device have been studied using synchrotron x-ray topography and electroluminescence. The mobile partials appear as white stripes and the immobile C-core partials show as narrow dark lines in x-ray topography using basal plane reflection. Such contrast variation has been ascribed to the focusing or defocusing of diffracted x-ray beams, due to the concave or convex basal planes caused by the displacement field associated with the edge segment of the partial dislocation. The core structure can be subsequently revealed by the contrast variation and it is consistent with previous report that mobile partial is Si-core while immobile partial is C-core. This will facilitate the direct and nondestructive determination of core structures of Shockley partial dislocations in any binary compound semiconductor materials.

12. Structure and formation mechanism of Frank fault in *4H*-SiC Epilayers

12.1. Outline

Structure of Frank faults nucleated in chemical vapor deposition grown 4*H* silicon carbide epilayers have been studied by synchrotron x-ray topography. The Frank fault is bounded by two Frank partial dislocations lying roughly along the step-flow direction. The bounding Frank partials have identical Burgers vectors ½[0001] and the fault vector is also ½[0001]. The formation mechanism of such Frank fault can be the conversion of elementary threading screw dislocations via the overgrowth of the vicinal steps on top of screw dislocation spirals.

12.2. Introduction

The defects nucleated in the chemical vapor deposition (CVD) grown epilayers are causing severe issues, degrading the device performance. For instance, the carrot defects increase reverse leakage current of 4*H*-SiC Schottky and *p-n* junction diodes.[223] Moreover, the forward voltage drop under forward biasing in bipolar devices, due to the expansion of basal stacking faults (SFs) resulted from the advancement of Shockley partial dislocations, poses a big challenge on the lifetime of the bipolar devices. Recently, Tsuchida *et al.* observed the disappearance of elementary threading screw dislocations (TSDs) after epitaxial growth and they predicted that the TSD existing in the substrate has been converted into Frank-type SF near the substrate/epilayer interface.[224] However, the structure of such Frank-type SFs and their formation mechanism remain obscure. The Frank-type SFs is expected to affect the device performance negatively, since thin layers of *3C*-SiC are introduced. Studies of the structure of Frank-type SFs in 4*H*-SiC epilayers will shed light on the formation mechanism and facilitate designing strategies to reduce or eliminate them during epitaxial growth. In this letter, the structures of Frank-type SFs were studied using synchrotron x-ray topography and their formation mechanism was proposed.

12.3. Experimental

The epitaxial layer was grown by chemical vapor deposition (CVD) on 8^{o} off-cut commercial SiC wafer. After CVD growth, the specimen was thinned down to ~120 μm and polished from the substrate side using diamond lapping films. Synchrotron x-ray topographs were subsequently recorded.

12.4. Results and discussion

Figure 83 shows a monochromatic synchrotron reflection topograph, recorded from a 100 micron thick epilayer from which the substrate was removed by polishing, showing several examples (labeled by F1 – F6) of what appear to be pairs of linear defects running approximately parallel to the off-cut direction and diverging away from each other towards the down step direction. The white circular dots are the images of

closed-core TSDs. Some phase contrasts resulted from the x-ray window are marked by "PC" [see Figure 83(b) and 1(d)]. Two kinds of configurations are seen: F3 appears as single linear features with dagger shaped end with enhanced and diffuse dark contrast at two edges close to the epilayer surface; while F2 and F5 comprise double linear features with the separation gradually increased toward the down step direction and the individual linear features appear as similar configuration to the first kind, albeit narrower. The enhanced dark contrast at the right end of the linear features can be either on the top [see Figure 83(b)] or at the bottom edge [see Figure 83(c)] of the white contrast. Figure 83(d) is an enlarged image from the right end of F2, showing the separation of the double linear features. The density of such defects in our sample is 58/cm^2. It has been well documented that carrot is a commonly observed extended defect nucleated during epitaxial growth and a trench appears at the intersection of carrot defect with the as-grown epilayer surface due to the presence of a prismatic SF. However, no surface roughness was observed for F1, F2, F3 and F5 under optical microscope. Therefore, they are carrot defects. Defect F4 corresponds to a carrot defect with trench-like surface roughness and F6 is a basal plane dislocation existing in the epilayer.

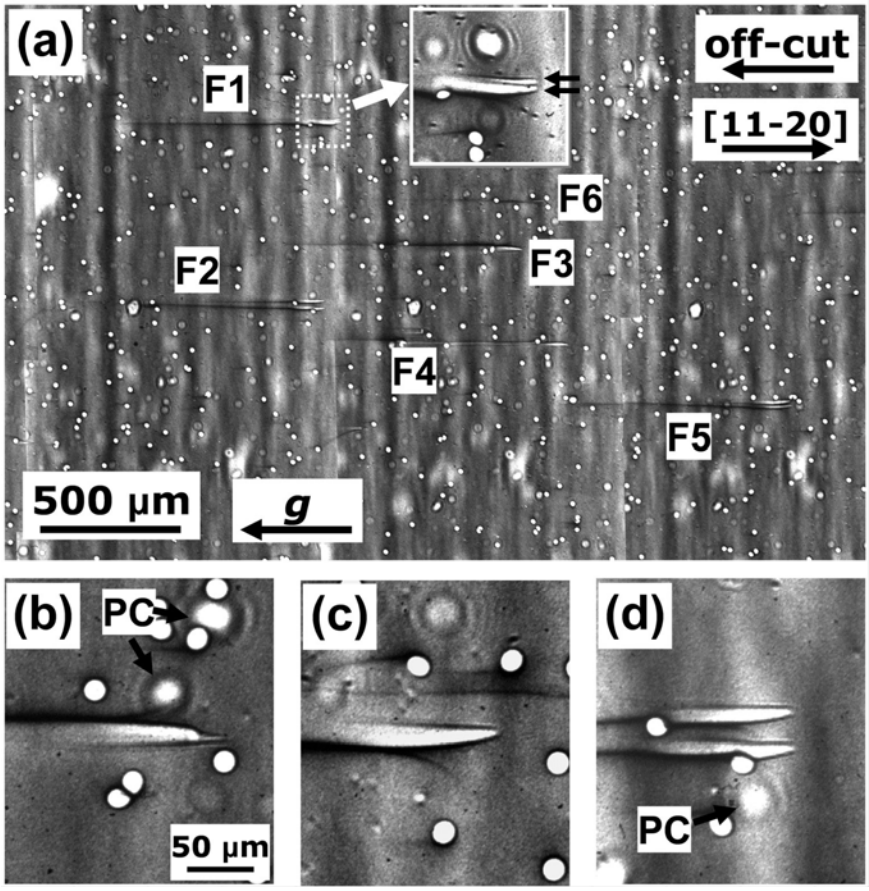

Figure 83. (a) (0008) back-reflection x-ray topograph of a specimen with CVD grown epilayer. (b) - (d): enlarged images showing the contrast of the end of the defect close to the epilayer surface. (b): enhanced dark contrast at the top edge of the white contrast; (c) enhanced dark contrast at the bottom edge; (d): separated double-line image. Six extended defects (F1-F6) are observed, parallel to the off-cut direction.

As we mentioned earlier, each individual linear features in the double-line images of F2 and F5 appear as similar contrast to the ones of F1 and F3, albeit narrower. This is probably because the two dislocations in F1 and F3 are close with each other and the images of individual dislocations cannot be resolved in x-ray topography. This can be deduced from the inset of Figure 83(a): under higher magnification, the right end of F1 appears as two separate dislocations which are close together. In order to study the detailed structure of such defects, a specimen containing two well-separated linear defects has been chosen for transmission x-ray topography. The specimen was thinned down and polished from the substrate side. A series of SWBXT images recorded in transmission from this diverging pair is shown in Figure 84. Projected length calculations carried out for several different diffraction geometries indicate that this pair of defects lie on the basal plane and diverge from nucleation points located close to the substrate/epilayer interface. The straight diagonal lines in Figure 84are polishing marks and the circular dark lines in the middle of the images are the contrast from the edge of the device pattern. On Figure 84(a) and (b), stacking fault contrast can be observed between the two diverging lines establishing that we have some kind of stacking fault bounded by two partial dislocations. In all the {11-20} [Figure 84(d)-(f)] and {10-10} [Figure 84(g)-(i)] reflections, the bounding partial dislocations are in contrast while the SF area is out of contrast. As we know, Shockley-type SFs are often formed in SiC bipolar devices after electric stressing, via electron-hole recombination enhanced dislocation glide process. Now the question whether they are Shockley-type SF arises.

In order to determine quantitatively the structure of the SF, the contrast variation of SF and bounding partial dislocations in x-ray topography using various reflections has been summarized in Table 7. As shown in Table 7, if this fault had Shockley character, the fault would be visible on all {1-100} type reflections, and the two partials would have different extinction behavior (each would show weak contrast on a single {11-20} type reflection). However, the fault is invisible on Figure 84(g)-(i), and one of the partials is visible on all three {11-20} reflections [Figure 84(d)-(f)], with the other being visible on two out of the three [Figure 84(e)-(f)]. This rules out the possibility of a Shockley fault bounded by two Shockley partials. Another possibility is a Frank fault bounded by two Frank partials. The Frank-type SF area is expected to be out of contrast in all six {11-20} and {1-100} reflections. By examining the topographs in Figure 84, one can notice that the SF area is out of contrast in all the six {11-20} and {1-100} reflections, which agrees with the situation of Frank-type SF. On the other hand, the bounding partials do not disappear in any of the reflections, except that a short segment of the upper one is out of contrast in Figure 84(d), where its dislocation line is straight and perpendicular to the **g**-vector. This is also consistent with the case of Frank-type SF. Therefore, the SF in Figure 84 can be a Frank-type SF bounded by two Frank partial dislocations with Burgers vectors along [0001], based on the contrast variation of not only SF area, but also the bounding partials. However, the magnitude of the Frank partials still remains unknown, since a Burgers vector of ¼[0001] or [0001] would fulfill the same contrast variation. The fault vector cannot be [0001] since the SF area is in contrast ($\boldsymbol{g}\cdot\boldsymbol{R}\neq$integer) in (0-111) and (-1011) reflections [Figure 84(a) and (b)]. Figure 84(c) shows a (-13-22) transmission topograph where the SF area is out of contrast: this implies that the fault vector $\boldsymbol{R}$ has to

be ½[0001], since $\boldsymbol{R}$=¼[0001] does not satisfy $\boldsymbol{g}\cdot\boldsymbol{R}$=integer. Thus, the fault vector and the Burgers vectors of the bounding partials have been determined to be ½[0001], whose magnitude is half of the unit cell magnitude along ***c***-direction. However, if the fault has an in-plane component imparted to it by the surface intersection of a faulted Shockley it is possible that the extinction behavior is consistent with this possibility also (see Table 7).

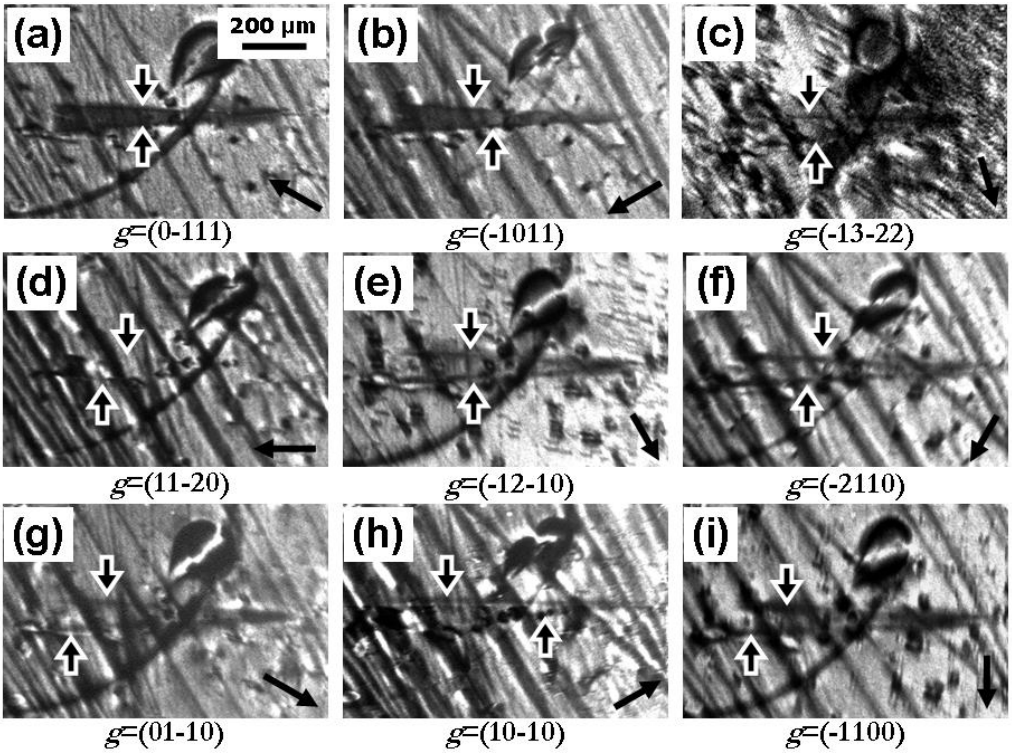

Figure 84. Transmission topographs of a Frank-type SF. (a) *g*=(0-111); (b) *g*= (-1011); (c) *g*= (-13-22); (d) *g*= (11-20); (e) *g*= (-12-10); (f) *g*= (-2110); (g) *g*= (01-10); (h) *g*= (10-10); (i) *g*= (-1100). The projections of **g**-vector on the films are indicated at the bottom right corner of each image. The images of the two dislocations bounding the SF are marked by arrows, which are in contrast in all images, except that a short segment of the upper dislocation disappears in (d). SF area is in contrast in (a) and (b) and out of contrast in the rest ones.

Table 7. Burgers vector analysis of the Frank fault. $\boldsymbol{b}_1$ and $\boldsymbol{b}_2$ are the Burgers vectors of the bounding partials and $\boldsymbol{R}$ is the fault vector. $\boldsymbol{g}\cdot\boldsymbol{R}$ and $\boldsymbol{g}\cdot\boldsymbol{b}$ are calculated for the stacking fault and the dislocations, respectively.

Fault type	$\boldsymbol{g}$	[11-20]	[1-210]	[-2110]	[1-100]	[10-10]	[01-10]
Shockley ($\boldsymbol{b}_1$=⅓[01-10], $\boldsymbol{b}_2$=⅓[10-10], $\boldsymbol{R}$=⅓[01-10])	$\boldsymbol{b}_1$	≠0	≠0	0	≠0	≠0	≠0
	$\boldsymbol{b}_2$	≠0	0	≠0	≠0	≠0	≠0
	Fault	1	-1	0	-⅓	⅓	⅔
Frank ($\boldsymbol{b}_1$=½[0001], $\boldsymbol{b}_2$=½[0001], $\boldsymbol{R}$=½[0001])	$\boldsymbol{b}_1/\boldsymbol{b}_2$	≠0	≠0	≠0	≠0	≠0	≠0
	Fault	0	0	0	0	0	0
Shockley-Frank ($\boldsymbol{b}_1$=1/6 [2-203], $\boldsymbol{b}_2$=1/6 [0-223], $\boldsymbol{R}$=1/6 [2-203])	$\boldsymbol{b}_1$	0	≠0	≠0	≠0	≠0	≠0
	$\boldsymbol{b}_2$	≠0	≠0	≠0	≠0	≠0	≠0
	Fault	0	1	-1	⅔	⅓	-⅓

Based on the aforementioned observations, these defects appear similar to the ones Tsuchida *et al.* recently observed in CVD grown epilayers. They observed the disappearance or appearance of a TSD simultaneously with a basal defect after CVD epitaxial growth and they predicted that the basal defect is a Frank-type SF.[224] In the SF discussed in Figure 84, no TSD was observed at the end of the defect image and it is expected to be converted from a TSD during the CVD growth. The conversion process can be explained by the overgrowth of vicinal steps on top of the TSD spiral and it is schematically illustrated in Figure 85. Initially the polished substrate surface comprises vicinal steps (VS) and spiral steps (SS) associated with TSDs. Atomic force microscopic studies indicate that the spiral in *4H*-SiC comprises steps with the height of *½c*, due to the different bonding configuration and subsequently different advancing velocity between "AB" steps and "CB" steps (assuming the stacking sequence is "ABCB" for 4*H*-SiC).[225] Therefore, in the step-controlled CVD, the growth is expected to be achieved via the advancement of *½c* vicinal and spiral steps, as illustrated in Figure 85(a). At the initial stage of growth, vicinal steps "VS I" and "VS II", as well as spiral steps "SS I" and "SS II", advance toward the down step direction. They may advance at different velocity [indicated by arrows of different sizes in Figure 85(b)], depending upon their bonding configuration. As growth continues, the vicinal steps continue toward the step-flow direction, while spiral steps start winding around the TSD core [Figure 85(c)]. The vicinal step "VS I" will arrive at the TSD core and it can possibly overgrow the spiral steps "SS I" and "SS II" [Figure 85(d)]. The spiral steps "SS I" and "SS II" are buried under the vicinal step "VS I", forming two Frank partial dislocations with Burgers vectors ***½c*** (note that there are two extra half basal planes associated with each Frank partial)**.** The area between the two Frank partial dislocations is a Frank-type SF, with fault vector same as the Burgers vectors of bounding partials. These Frank partials are growth dislocations, propagating toward the step flow direction as growth continues. The two Frank partials are tending to separate during the growth process due to the repulsive force between them.[226] The 3-D configuration of a converted TSD into two Frank partials with a SF in between can be schematically seen in Figure 85(e). The Burgers vector is

conserved as the sum of the Burgers vectors of the two Frank partials is equal to the one of the TSD.

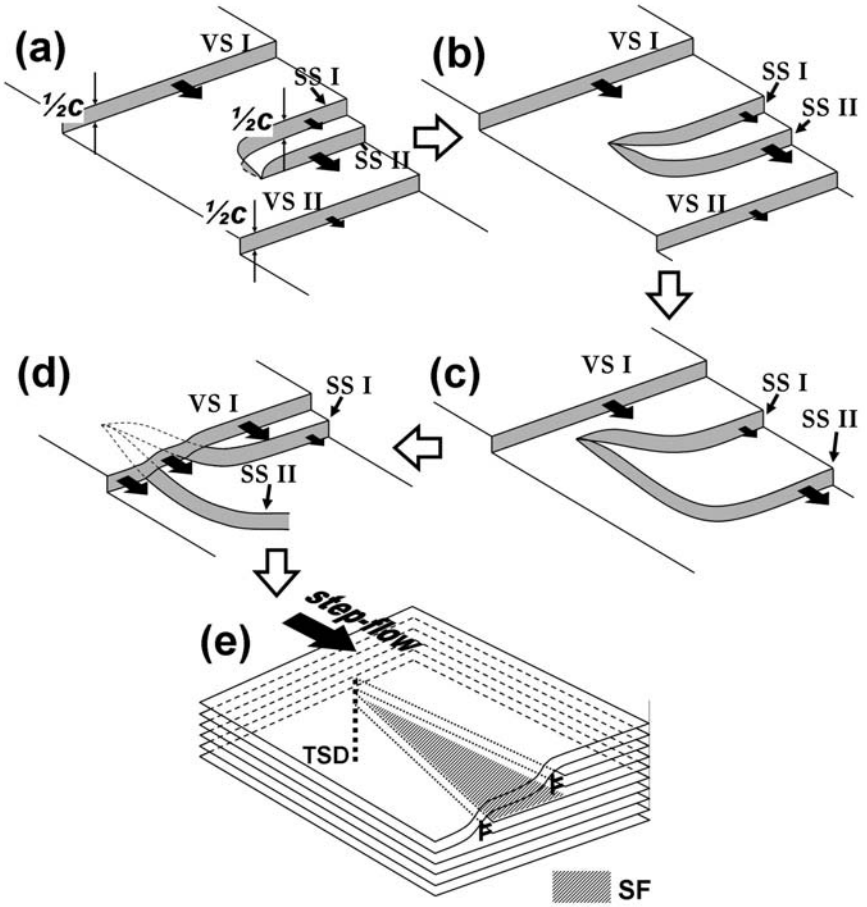

Figure 85. Formation mechanism of Frank-type SF via conversion of TSD [(a)-(d)]. (e) 3D lattice configuration of a TSD converted Frank-type SF.

12.5. Conclusion

In summary, Frank-type basal SFs nucleated in step-controlled chemical vapor deposition growth have been studied by synchrotron x-ray topography. They are bounded by two Frank partial dislocations with Burgers vectors ½[0001] and their fault vectors are the same as the bounding partials. They can be nucleated via the overgrowth of vicinal steps on top of threading screw dislocation spirals. Such mechanism can be potentially used to significantly reduce the density of threading screw dislocations or even eliminate them in SiC by converting them into Frank partial dislocations.

13. Stress/strain Mapping Analysis vis Ray Tracing (SMART)

13.1. Outline

We propose a novel method, SMART, to non-destructively and non-invasively map the complete stress tensor as a function of three dimensional position in any single crystal or large grain polycrystal. This method uses the technique of x-ray topography in combination with a fine-scale mesh/grating/reticule, otherwise referred to as synchrotron white beam x-ray reticulography (SWBXR)[227], followed by detailed image analysis and calculation enabling determination of all stress components.

13.2. Principle of SMART

The basic principle of SMART is that there exists a relationship between the stress state in a crystal and the local lattice plane orientation and that this relationship can be exploited in order to determine the full strain tensor as a function of position inside the crystal. Subsequently, the crystal's elastic constants can be utilized to convert the strain values into stresses. Local lattice plane orientation can be accurately mapped using ray tracing enabled by applying the non-destructive and non-invasive technique of SWBXR. The results of such measurements carried out using three independent x-ray reflections can be input into the mathematical relationship between the strain tensor and the local lattice plane orientation allowing calculation of the complete strain tensor as a function of lateral position in the crystal. This is the essence of SMART. Measurements carried out using various grazing incidence angles can, in addition, provide a depth profile of the stresses enabling 3D stress maps to be generated.

13.3. Experimental Fundamentals of SMART

Local plane orientation is mapped using SWBXR which involves the use of a high precision, fine scale, x-ray absorbing mesh/reticule placed between the diffracting specimen and the detector (x-ray film) or in the path of the incident beam. This mesh will split the diffracted beams into an array of microbeams (Figure 86). The orientation differences between the strained crystal elements reflecting individual microbeams are converted to angular dispersal of diffracted microbeams which in turn are manifested as displacements from the normal unstrained positions on the detector (x-ray film). Thus, the resulting x-ray topograph, recorded through the mesh, will give a map of misorientation vectors over the area of sample imaged. Small elastic distortions of nearly perfect crystals that cause misorientations <1 arcsec can be measured using appropriate fine-scale meshes.

The lateral spatial resolution of the stress maps will be limited by the size of the smallest feature on the grating used in the SWBXR. Ultimately this cannot be lower than the spatial resolution of the best detectors (high resolution x-ray film) which is currently on the order of a micron. This translates into a strain resolution of around 10^{-5} (i.e. smallest detectable strain), which corresponds to a typical stress resolution (i.e. smallest detectable stress) of 1 MPa. The stress resolution can be improved by increasing the

specimen-to-detector distance although this is at the expense of spatial resolution. Therefore a compromise has to be made regarding the specimen-detector distance.

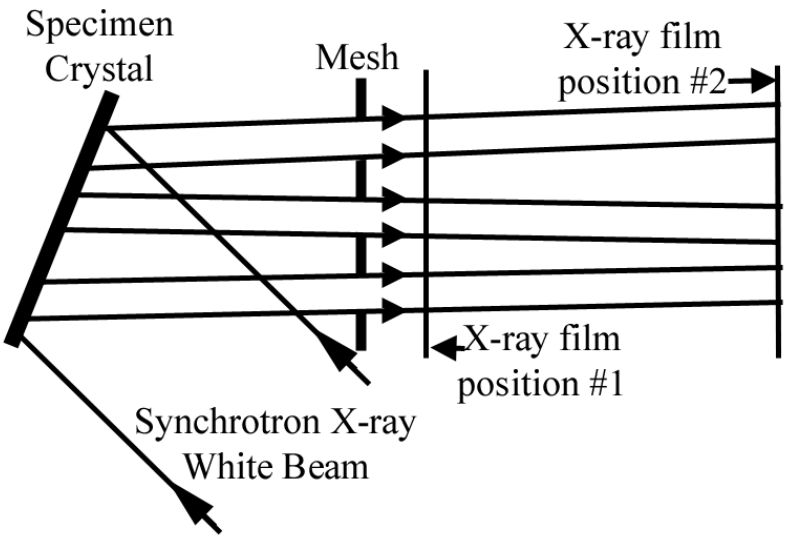

Figure 86. Schematic for synchrotron white beam x-ray reticulography (SWBXR) measurements The above measurement method is described using the synchrotron white beam. A similar experimental setup can also be used for measurement using a laboratory x-ray source (for example sealed tube or rotating anode) with appropriate collimating tubes. While the measurement and mapping procedures remain the same, the resolution accessible by this setup will be lower than the corresponding synchrotron setup.

13.4. Theoretical Basis for SMART

The mathematical relationship between local lattice plane normal and local stress tensor provides the theoretical basis for SMART. This provides the analysis methodology which enables the determination of the full stress tensor as a function of 3D position in the crystal. Initially, the strain tensor components are determined and the stress tensor components (Figure 87) are subsequently obtained through the relationship:

$$\sigma_{ij} = c_{ijkl}\varepsilon_{kl}$$

where c_{ijkl} is the stiffness matrix for the material of the specimen.

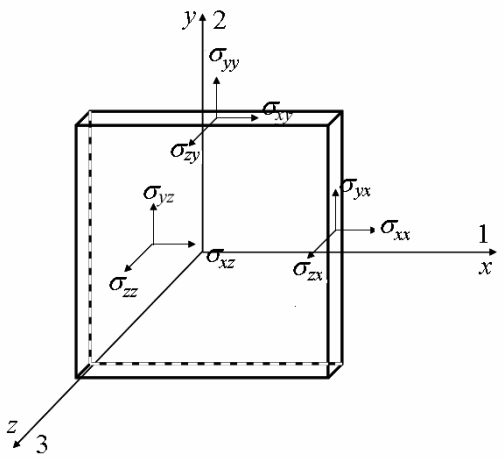

Figure 87. Stress components for the crystalline specimen.

A schematic illustrating the geometry involved in the measurement of the strain tensor using SMART is shown in Figure 88(a). As demonstrated in Figure 88(b), the lattice plane normals are shifted due to strains. We can write a general equation for this shift:

$$\vec{n}(x,y,z) = \vec{n}^0(x,y,z) - \nabla\left[\vec{n}^0(x,y,z)\cdot\vec{u}(x,y,z)\right], \tag{47}$$

where $\vec{n}(x,y,z) = n_x\vec{i} + n_y\vec{j} + n_z\vec{k}$: plane normal at ***(x,y,z)*** before distortion

$\vec{n}^0(x,y,z) = n_x^0\vec{i} + n_y^0\vec{j} + n_z^0\vec{k}$: plane normal at ***(x,y,z)*** after distortion

$\vec{u}(x,y,z) = u_x\vec{i} + u_y\vec{j} + u_z\vec{k}$: displacement vector at ***(x,y,z)***

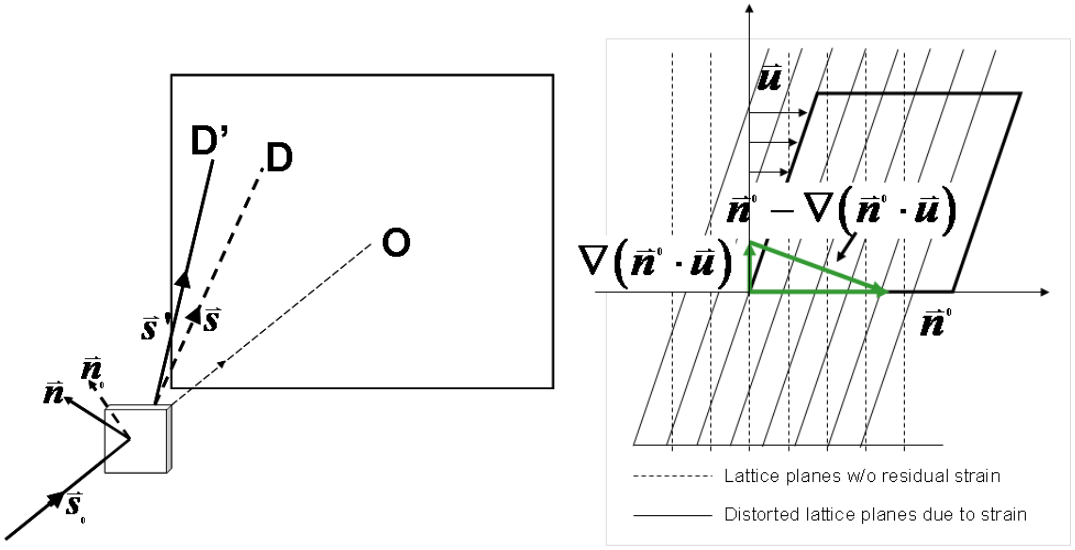

(a) (b)

Figure 88. (a) Schematic for general strain measurement; (b) Shift in plane normals due to strain. (**D** and **D'** are the diffraction spot locations for unstrained and strained conditions, respectively; $\vec{s}_0$, $\vec{s}$ and $\vec{s}'$ are unit vectors along incident beam, unstrained diffracted beam and strained diffracted beam directions, respectively. $\vec{n}^0$ and $\vec{n}$ are the plane normals before and after distortion respectively while $\vec{u}$ is the distortion vector.

Physically, $\vec{n}^0$ is the plane normal without strain and $\vec{n}$ the plane normal after deformation. $\nabla\left(\vec{n}^0 \cdot \vec{u}\right)$ is a vector pointing in the direction of the greatest rate of increase of $\vec{n}^0 \cdot \vec{u}$ and its magnitude is the greatest rate of change of $\vec{n}^0 \cdot \vec{u}$. $\vec{n}^0 - \nabla\left(\vec{n}^0 \cdot \vec{u}\right)$ is the vector perpendicular to the plane after deformation, which is the plane normal.

Equation (47) can be split into three components:

$$\begin{aligned}
n_x &= n_x^0 - \left(n_x^0 \frac{\partial u_x}{\partial x} + n_y^0 \frac{\partial u_y}{\partial x} + n_z^0 \frac{\partial u_z}{\partial x} \right) \\
n_y &= n_y^0 - \left(n_x^0 \frac{\partial u_x}{\partial y} + n_y^0 \frac{\partial u_y}{\partial y} + n_z^0 \frac{\partial u_z}{\partial y} \right) \\
n_z &= n_z^0 - \left(n_x^0 \frac{\partial u_x}{\partial z} + n_y^0 \frac{\partial u_y}{\partial z} + n_z^0 \frac{\partial u_z}{\partial z} \right).
\end{aligned} \tag{48}$$

If we select three different diffraction spots, we can write a similar set of equations for each of these leading to the following nine equations.

$$\begin{aligned}
n_{1x} &= n_{1x}^0 - \left(n_{1x}^0 \frac{\partial u_x}{\partial x} + n_{1y}^0 \frac{\partial u_y}{\partial x} + n_{1z}^0 \frac{\partial u_z}{\partial x} \right) \\
n_{1y} &= n_{1y}^0 - \left(n_{1x}^0 \frac{\partial u_x}{\partial y} + n_{1y}^0 \frac{\partial u_y}{\partial y} + n_{1z}^0 \frac{\partial u_z}{\partial y} \right) \\
n_{1z} &= n_{1z}^0 - \left(n_{1x}^0 \frac{\partial u_x}{\partial z} + n_{1y}^0 \frac{\partial u_y}{\partial z} + n_{1z}^0 \frac{\partial u_z}{\partial z} \right) \\
n_{2x} &= n_{2x}^0 - \left(n_{2x}^0 \frac{\partial u_x}{\partial x} + n_{2y}^0 \frac{\partial u_y}{\partial x} + n_{2z}^0 \frac{\partial u_z}{\partial x} \right) \\
n_{2y} &= n_{2y}^0 - \left(n_{2x}^0 \frac{\partial u_x}{\partial y} + n_{2y}^0 \frac{\partial u_y}{\partial y} + n_{2z}^0 \frac{\partial u_z}{\partial y} \right) \\
n_{2z} &= n_{2z}^0 - \left(n_{2x}^0 \frac{\partial u_x}{\partial z} + n_{2y}^0 \frac{\partial u_y}{\partial z} + n_{2z}^0 \frac{\partial u_z}{\partial z} \right) \\
n_{3x} &= n_{3x}^0 - \left(n_{3x}^0 \frac{\partial u_x}{\partial x} + n_{3y}^0 \frac{\partial u_y}{\partial x} + n_{3z}^0 \frac{\partial u_z}{\partial x} \right) \\
n_{3y} &= n_{3y}^0 - \left(n_{3x}^0 \frac{\partial u_x}{\partial y} + n_{3y}^0 \frac{\partial u_y}{\partial y} + n_{3z}^0 \frac{\partial u_z}{\partial y} \right) \\
n_{3z} &= n_{3z}^0 - \left(n_{3x}^0 \frac{\partial u_x}{\partial z} + n_{3y}^0 \frac{\partial u_y}{\partial z} + n_{3z}^0 \frac{\partial u_z}{\partial z} \right)
\end{aligned} \tag{49}$$

$n_{1x}, n_{1y}, n_{1z}, n_{2x}, n_{2y}, n_{2z}, n_{3x}, n_{3y}, n_{3z}$ are obtained from the measurements on the three diffraction spots. It should be noted that the stress mainly influences the orientation of the plane normal and the variation of its length is negligible.

Solving the nine equations, we obtain the nine distortional components $\frac{\partial u_x}{\partial x}, \frac{\partial u_x}{\partial y}, \frac{\partial u_x}{\partial z}, \frac{\partial u_y}{\partial x}, \frac{\partial u_y}{\partial y}, \frac{\partial u_y}{\partial z}, \frac{\partial u_z}{\partial x}, \frac{\partial u_z}{\partial y}, \frac{\partial u_z}{\partial z}$ from which the strains and rotations can be calculated. The rotation tensor, ω_{ij}, and the pure strain tensor, ε_{ij}, can be derived from the distortion tensor components using the following equations:

$$\omega_{ij} = \frac{1}{2}\left(\frac{\partial u_i}{\partial j} - \frac{\partial u_j}{\partial i}\right) \tag{50}$$

$$\varepsilon_{ij} = \frac{1}{2}\left(\frac{\partial u_i}{\partial j} + \frac{\partial u_j}{\partial i}\right), \text{ where } \boldsymbol{i, j} = \boldsymbol{x, y} \text{ or } \boldsymbol{z}. \tag{51}$$

Subsequently, the strains can be converted to stresses using the crystal's elastic constants.

13.5. Example of Application of SMART: Mapping of Stress around micropipes in silicon carbide

Micropipes (MPs) are hollow-core screw dislocations with giant Burgers vectors along the *c*-axis (usually >30 Å). Dislocations of this kind, with their large and extensive stress fields, provide ideal examples to demonstrate our stress mapping technique. Using SWBXR in the back-reflection geometry with a 50 μm copper mesh placed on the surface of the crystal, we obtain an x-ray reticulograph [see Figure 89(a)]. Figure 89(b) shows the theoretical shear stress distribution, σ_{xz} (z is along *c*-axis of SiC and x is in *c*-plane), around a MP. By applying our stress mapping technique to the x-ray reticulograph, the resultant map of the stress tensor, σ_{xz}, obtained is shown in Figure 90(a). In spite of the low resolution, this map shows good agreement with the theoretical stress map. Figure 90(b) shows a simulation of what might be expected using a 9 μm periodicity grating. These maps clearly demonstrate the veracity of our mapping technique.

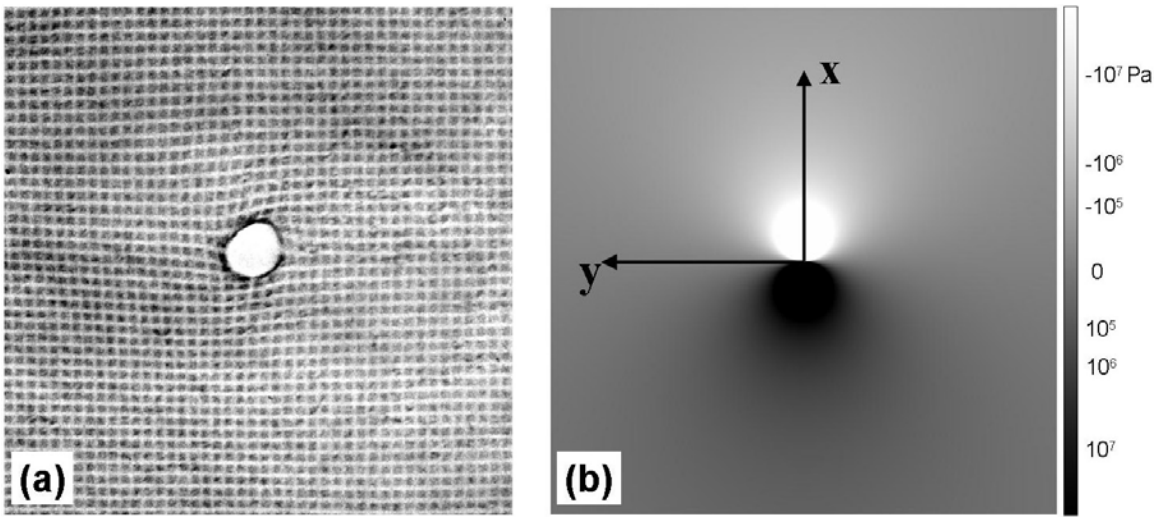

Figure 89. (a) Back-reflection reticulograph of a MP (mesh spacing: 50 μm); (b) Theoretical map of the stress tensor component σ_{xz} around the MP.

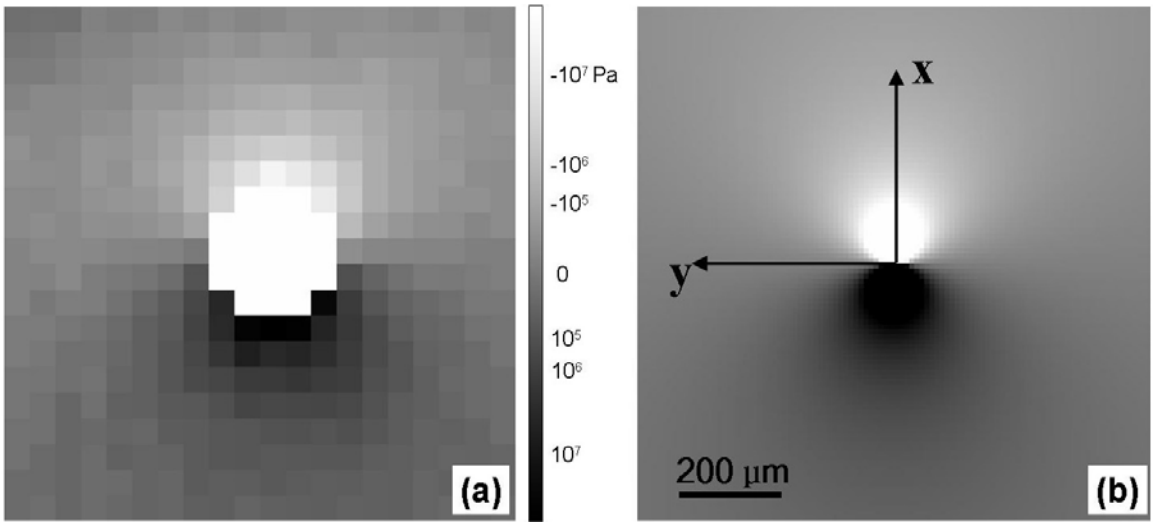

Figure 90. (a) Map of the stress tensor component σ_{xz} obtained experimentally using a 50 μm mesh around a MP; (b) Simulated map of the shear stress component, σ_{xz} using a 9 μm mesh.

13.6. Conclusion

A new technique, strain/stress mapping analysis via ray tracing (SMART), has been invented, based on ray-tracing principle. The 2D mapping for the nine components in the strain/stress tensor can be subsequently calculated based on three diffraction spots and the transmitted radiograph. As an example, the strain field of a micropipe has been calculated and good agreement has been obtained between the results from SMART and the fundamental dislocation theory.

14. Conclusions

Defect structures in SiC bulk crystals, epilayers and devices have been studied using synchrotron x-ray topography as well as other characterization techniques.

I) Epilayers with mirror-like surface could be grown at growth rate up to 10 μm/hr. Thermodynamic process studies indicate that $SiCl_2$ is the dominant Si carrier at all temperatures and C_2H_2 is the dominant C carrier at temperatures above ~1800K. *3C*-SiC is the thermodynamically stable phase up to 1700^{o}C. Rocking curve became narrower after chemical vapor deposition growth on off-oriented substrate due to the conversion of basal plane dislocations into threading edge dislocations. 2D dimensional growth mechanism dominates at high growth rates, forming island features and *3C* inclusions were observed in epilayers grown hexagonal substrate by reciprocal space mapping.

II) The interactions between the basal plane dislocations and threading dislocations as well as the formation mechanisms of low angle grain boundaries) have been studied. The threading screw dislocations act as effective pinning points for the BPDs, while the threading edge dislocations do not. Threading edge dislocation walls act as obstacles for the glide of basal plane dislocations and aggregation of basal plane dislocations is observed. Interactions between the distributions of BPDs can induce the formation of low angle grain boundaries. Two cases were observed: (1) where edge type basal plane dislocations of opposite sign are observed to aggregate together to form basal plane tilt boundaries and (2) where similar aggregation occurs against pre-existing prismatic tilt boundaries thereby contributing some basal plane tilt to the boundaries.

III) The interaction between the Shockley partial dislocations and threading dislocations in SiC bipolar devices has been studied. The advancing Shockley partial dislocations are able to cut through threading edge dislocations without generating any trailing dislocation segments. However, when the advancing Shockley partial dislocation encounters a threading screw dislocation, a prismatic stacking fault is generated via the cross-slip and annihilation of partial dislocation dipole. This configuration is sessile and precludes the formation of double stacking faults which would be even more detrimental to device performance than the single stacking faults.

IV) The dislocation sense of micropipes has been studied. The ray-tracing method has been applied into the simulation of grazing-incidence synchrotron white beam x-ray topographic images of micropipes. The features are canted to one or other side of the reflection vector, depending on the handedness of the micropipe. The different image orientations of the left-handed and right-handed micropipes provide a simple, non-destructive and reliable way to reveal their senses. Back-reflection reticulography verified our results.

V) The handedness of closed-core threading screw dislocations has been studied. Ray-tracing simulation indicates that the sense of the threading screw dislocations can be revealed according to the position of the dark contrast enhancement in their x-ray topographic images. “Small Bragg angle” back-reflection synchrotron white beam x-ray

topography has been applied to validate our argument. Complete agreement between the results from grazing-incidence synchrotron white beam x-ray topography and "small Bragg angle" back-reflection synchrotron white beam x-ray topography proves that either method provides a simple, non-destructive and unambiguous way to reveal the sense of closed-core threading screw dislocations.

VI) X-ray topographic images of threading edge dislocations have been studied. Six types were observed and their Burgers vectors can be determined from a single {11-28} grazing-incidence x-ray topograph, based on the simulation using ray-tracing method. Their Burgers vectors can be further verified by an additional equivalent {11-28} reflection or a dislocation half loop containing two threading edge dislocation segments. The threading edge dislocation arrays are tending to orient along <1-100> directions and the Burgers vectors of the threading edge dislocations comprising them are perpendicular to the arrays, which is expected for minimizing the total strain energy.

VII) The core-structure of Shockley partial dislocations has been studied. The contrast variation in x-ray topography between mobile and immobile partial dislocations has been ascribed to the focusing or defocusing of diffracted x-ray beams, due to the concave or convex basal planes caused by the displacement field associated with the edge segment of the partial dislocation. The core structure can be subsequently revealed by the contrast variation and it is consistent with previous report that mobile partial is Si-core while immobile partial is C-core. This method can in principle be used in any binary compound semiconductors to determine the core-structure of Shockley partial dislocations.

VIII) The susceptibility of basal plane dislocations to the recombination enhanced dislocation glide process has been studied. The susceptibility of the basal plane dislocations to recombination enhanced dislocation glide process is determined by the counterclockwise angle θ from the line direction to its Burgers vector. The basal plane dislocations with $30^o<\theta<150^o$ are most detrimental, as both partials are mobile and will advance under forward bias. If $-30^o<\theta<30^o$ or $150^o<\theta<210^o$, only one partial advances. Both partials are immobile if $210^o<\theta<330^o$. Experimental observations confirmed our argument.

IX) Frank-type stacking faults in chemical vapor deposition grown epilayers have been studied. They are bounded by two Frank partial dislocations with Burgers vectors ½[0001] and the fault vectors are the same as the Burgers vectors of bounding partials. They are nucleated via the overgrowth of vicinal steps on top of threading screw dislocation spirals. This mechanism provides a potential way to significantly reduce the threading screw dislocation density in SiC.

X) A new technique, strain/stress mapping analysis via ray tracing (SMART), has been invented, based on ray-tracing principle. The 2D mapping for the nine components in the strain/stress tensor can be subsequently calculated based on three diffraction spots and the transmitted radiograph. As an example, the strain field of a micropipe has been calculated and good agreement has been obtained between the results from SMART and the fundamental dislocation theory.

15. Future work

The nucleation mechanisms of the various types of dislocation in SiC still remain obscure. For example, no adequate explanation exists for the nucleation of individual threading screw dislocations, although opposite-sign screw or micropipe pairs can be nucleated at inclusions. Frank partial dislocations, which are associated with extra atomic half planes, are expected to play critical roles in the nucleation of micropipes and closed-core threading screw dislocations. However, threading screw dislocations have not been observed in other materials with similar lattice constants, e.g., sapphire and lithium niobate. It is therefore of great importance to study the nucleation of threading screw dislocations in depth.

We have shown in Chapter 12 that the closed-core threading screw dislocations can be converted into Frank partial dislocations during chemical vapor deposition on vicinal substrates. This provides a potential way to significantly reduce the density of threading screw dislocations. Detailed studies on the growth parameters controlling the conversion process are of great importance.

Threading edge dislocations, which exist at densities which can be one-order of magnitude higher than elementary threading screw dislocations in silicon carbide, have not yet been afforded enough attention. The influence of threading edge dislocations on device performance has not been reported and the nucleation mechanism of individual threading edge dislocations is still unknown. Although some of the threading edge dislocations could be converted from the basal plane dislocations during epitaxial growth, most of them are inherited from the substrates. The individual threading edge dislocations are nucleated during the bulk growth and no detailed studies have been done regarding their nucleation mechanism.

Epi-growth is the basis for device fabrication. Many epilayer defects are still not fully understood, although some of them, such as carrots, can be prevented by modifying the chemical vapor deposition process. For example, dislocation half loops and double basal plane dislocations in the epilayers need to be further investigated.

Ray-tracing simulation based on the orientation contrast mechanism has been successfully used in our studies and excellent correspondence between simulation and experimental observation has been obtained. However, the reason why the orientation contrast dominates in x-ray topographs of silicon carbide needs to be clarified. The relationship between the orientation contrast and extinction contrast in x-ray topography needs to be well clarified.

References

[1] L. S. Ramsdell, American Mineralogist **32**, 64 (1947)
[2] W. F. Knippenberg, Philips Res. Rept. **18**, 161 (1963)
[3] F. C. Frank, Phil. Mag. **42,** 1014 (1951)
[4] H. Jagodzinski, Acta Cryst. **7,** 300 (1954)
[5] G. Augustine, H. M. Hobgood, V. Balakrishna et al., Phys. Stat. Sol. (b) **202**, 137 (1997)
[6] Yu.M. Tairov and V.F. Tsvetkov, *J. Crystal Growth* **43,** 209 (1978)
[7] D. Chaussende, P. J. Wellmann, and M. Pons, J. Phys. D: Appl. Phys. **40**, 6150 (2007)
[8] R. W. Olesinski and G. J. Abbaschian, Bull. Alloy Phase Diagrams **5**, 486 (1984)
[9] H. Klapper, Mater. Chem. Phys. **66**, 101 (2000)
[10] W. Vetter and M. Dudley, J. Mater. Res. **15**, 1649 (2000)
[11] M. Dudley, X. R. Huang, W. Huang, A. Powell, S. Wang, P. Neudeck and M. Skowronski, Appl. Phys. Lett. **75**, 784 (1999)
[12] M. Dudley *et al*, Nuovo Cemento **19**, 153 (1997)
[13] Y. Chen, G. Dhanaraj, M. Dudley, E. Sanchez, and M. F. MacMillan, Appl. Phys. Lett. **91**, 071917 (2007)
[14] Y. Chen and M. Dudley, Appl. Phys. Lett. **91**, 141918 (2007)
[15] M. Dudley and X. R. Huang, Mater. Sci. Forum **338**, 431 (2000)
[16] T. A. Kuhr, E. K. Sanchez, M. Skowronski, W. Vetter, and M. Dudley, J. Appl. Phys. **89**, 4625 (2001)
[17] Y. Chen, X. R. Huang, H. Chen, and M. Dudley (to be published)
[18] J. Bai, X. Huang, M. Dudley, *et al*, J. Appl. Phys. **98**, 063510 (2005)
[19] H. Tsuchida, I. Kamata, and M. Nagano, J. Cryst. Growth **306**, 254 (2007)
[20] I. Kamata, M. Nagano, H. Tsuchida, Y. Chen, and M. Dudley, Mater. Sci. Forum (in press)
[21] G. Dhanaraj, Y. Chen, H. Chen, W. M. Vetter, H. Zhang, and M. Dudley, Mater. Soc. Res. Symp. Proc. **911**, B05-27 (2006)
[22] H. Chen, G. Wang, Y. Chen, and M. Dudley, **Mater. Res. Soc. Symp. Proc. 911,** 163 (2006)
[23] T. Ohno, H. Yamaguchi, S. Kuroda, K. Kojima, T. Suzuki and K. Arai, J. Cryst. Growth **260**, 209 (2004)
[24] M. Zhang *et al*, Mater. Sci. Forum **457-460**, 371 (2004)
[25] S. P. Timoshenko and J. N. Goodier, in "*Theory of Elasticity*", McGraw-Hill, 3rd Ed., 1970 p. 437
[26] K. Maeda, M. Sato, A. Kubo and S. Takeuchi, J. Appl. Phys. **54**, 161 (1983)
[27] M. Skowronski *et al*, J. Appl. Phys. **92,** 4699 (2002)
[28] Y. Chen, M. Dudley, K. X. Liu, and R. E. Stahlbush, Appl. Phys. Lett. **91**, 171930 (2007)
[29] X. R. Huang, D. R. Black, A. T. Macrander, J. Maj, Y. Chen, and M. Dudley, Appl. Phys. Lett. **91**, 231903 (2007)
[30] Y. Chen and M. Dudley (to be published)
[31] Y. Chen, X. R. Huang, N. Zhang and M. Dudley, (unpublished)
[32] K. Koga, Y. Fujikawa, Y. Ueda and T. Yamaguchi, Springer Proc. Phys. **71**, 96 (1992)
[33] H. Chen, B. Raghothamachar, W. Vetter, M. Dudley, Y. Wang, and B. Skromme, Mater. Res. Soc. Symp. Proc. **911**, B05-24 (2006)

[34] Y. Chen, G. Dhanaraj, W. Vetter, R. Ma, and M. Dudley, Mater. Sci. Forum **556-557,** 231 (2007)
[35] P.G. Neudeck and J.A. Powell, IEEE Electron Device Lett. **15,** 63 (1994)
[36] P. G. Neudeck, W. Huang, and M. Dudley, Solid-State Electron. **42,** 2157 (1998)
[37] Y. Chen, G. Dhanaraj, M. Dudley, H. Zhang, R. Ma, Y. Shishkin, and S. Saddow, Mater. Res. Soc. Symp. Proc. **911,** B09-04 (2006)
[38] Y. Chen, M. Dudley, K. X. Liu, and R. E. Stahlbush, Mater. Res. Soc. Symp. Proc. Spring, **0994,** F12-03 (2007)
[39] A. Authier, in "*Dynamical Theory of X-ray Diffraction*", Oxford University Press, 2001 pp. 46
[40] D. K. Bowen and B. K. Tanner, in "*High Resolution X-Ray Diffractometry and Topography*", Taylor & Francis, 1998 pp. 74
[41] A. Authier, in "*Dynamical Theory of X-ray Diffraction*", Oxford University Press, 2001 pp. 104-106
[42] B. D. Cullity, in "*Elements of X-ray Diffraction*", Addison-Wesley Publishing Company, Inc., 1977 pp. 120
[43] W. M. Vetter and M. Dudley, J. Appl. Cryst. **31**, 820 (1998)
[44] A. Authier, in "*Dynamical Theory of X-ray Diffraction*", Oxford University Press, 2001 pp. 85
[45] D. K. Bowen and B. K. Tanner, in "*High Resolution X-Ray Diffractometry and Topography*", Taylor & Francis, 1998 pp. 225
[46] D. K. Bowen and B. K. Tanner, in "*High Resolution X-Ray Diffractometry and Topography*", Taylor & Francis, 1998 pp. 173
[47] A. Authier, in "*Dynamical Theory of X-ray Diffraction*", Oxford University Press, 2001 pp. 16-20
[48] X. R. Huang, M. Dudley, W. M. Vetter, W. Huang, W. Si, and C. H. Carter, Jr., J. Appl. Cryst. **32**, 516 (1999)
[49] Y. Chen, M. Dudley *et al.*, (unpublished)
[50] A. Authier, in "*Dynamical Theory of X-ray Diffraction*", Oxford University Press, 2001 pp. 23-25
[51] J. P. Hirth and J. Lothe, in "*Theory of Dislocations*", 2nd Ed., John Wiley & Sons Publication, New York, 1982, pp. 60
[52] J. P. Hirth and J. Lothe, in "*Theory of Dislocations*", 2nd Ed., John Wiley & Sons Publication, New York, 1982, pp. 78
[53] J. D. Eshelby and A. N. Stroh, Phil. Mag. **42,** 1401 (1951)
[54] H. Tsuchida, I. Kamata and M. Nagano, J. Cryst. Growth **306**, 254 (2007)
[55] E. H. Yoffe, Phil. Mag. **6**, 1147 (1961)
[56] X. R. Huang, M. Dudley, W. M. Vetter, W. Huang, S. Wang and C. H. Carter, Jr. Appl. Phys. Lett. **74,** 353 (1999)
[57] D. K. Bowen and B. K. Tanner, in "*High Resolution X-Ray Diffractometry and Topography*", Taylor & Francis, 1998 pp. 189
[58] Par A. Authier, J. Physique **27**, 57 (1966)
[59] G. Dhanaraj, M. Dudley, R. H. Ma, H. Zhang and V. Prasad, Review of Scientific Instruments **75**, 2843 (2004)

[60] G. Dhanaraj, F. Liu, M. Dudley, H. Zhang and V. Prasad, Mater. Res. Soc. Symp. Proc. **815**, J5.31.1 (2004)
[61] R. H. Ma, H. Zhang, V. Prasad and M. Dudley, Cryst. Growth Design **2**, 213 (2002)
[62] M. C. Luo, J. M. Li and Q. M. Wang et al., J. Cryst. Growth **249**, 1 (2003)
[63] H. Kim and D. Choi, J. Am. Ceram. Soc. **82,** 331 (1999)
[64] Y. M. Lu and I. C. Leu, Surf. Coat. Tech. **124**, 262 (2000)
[65] A. Figueras, S. Garelik and J. Santiso et al., Mater. Sci. Eng. B **11**, 83 (1992)
[66] G. D. Papasouliotis and S. V. Sotirchos, J. Mater. Res. **14**, 3397 (1999)
[67] H. Kim and D. Choi, Thin Solid Films **312**, 195 (1998)
[68] I. M. Kostjuhin and S. V. Sotirchos, Ind. Eng. Chem. Res. **40**, 2586 (2001)
[69] T. Kaneko, H. Sone and N. Mitakawa et al., Jpn. J. Appl. Phys. **38**, 2089 (1999)
[70] W. V. Munch and U. Ruhnau, J. Cryst. Growth **158**, 491 (1996)
[71] Y. Chen, K. Matsumoto, and Y. Nishio et al., Mater. Sci. Eng. B **61-62**, 579 (1999)
[72] H. Sone, T. Kaneko and N. Miyakawa, J. Cryst. Growth **219**, 245 (2000)
[73] J. M. Bluet, J. Camassel and L. A. Falkovsky, Diamond and Related Mater. **6**, 1385 (1997)
[74] A. Leycuras, Diamond and Related Mater. **6**, 1857 (1997)
[75] K. –W. Lee, K. –S. Yu and Y. Kim, J. Cryst. Growth **179**, 153 (1997)
[76] Y. Ishida, T. Takahashi and H. Okumura et al., Jpn. J. Appl. Phys. **36**, 6633 (1997)
[77] K. Yagi and H. Nagasawa, J. Cryst. Growth **174**, 653 (1997)
[78] J. –H. Boo, S. –B. Lee and K. –S. Yu et al., Surf. and Coat Tech. **131**, 147 (2000)
[79] C. Wang and D. Tsai, Mater. Chem. Phys. **63**, 196 (2000)
[80] K. Teker, C. Jacob and J. Chung et al., Thin Solid Films **371**, 53 (2000)
[81] M. Kitabatake, Thin Solid Films **369**, 257 (2000)
[82] Z. Zhang, W. Zhao and X. Wang et al., Mater. Sci. Eng. B **75**, 177 (2000)
[83] J. –H. Boo, D. –C. Kim and S. –B. Lee et al., J. Vac. Sci. Tech. B **21**, 1870 (2003)
[84] M. J. Hernandez, G. Ferro and T. Chassagne et al., J. Cryst. Growth **253**, 95 (2003)
[85] Y. Narita, T. Inubushi and K. Yasui et al., Appl. Surf. Sci. **212-213**, 730 (2003)
[86] Y. Narita, T. Inubushi and M. Harashima et al., Appl. Surf. Sci. **216**, 575 (2003)
[87] J. D. Hwang, Y. K. Fang and Y. J. Song et al., Thin Solid Films **272**, 4 (1996)
[88] C. H. Wu, C. Jacob and X. J. Ning et al., J. Cryst. Growth **158**, 480 (1996)
[89] J. Hwang, Y. Fang and Y. Song et al., Jpn. J. Appl. Phys. **34**, 1447 (1995)
[90] A. D. Johnson, J. Perrin and J. A. Mucha et al., J. Phys. Chem. **97**, 12937 (1993)
[91] Y. Ohshita, J. Cryst. Growth **147**, 111 (1995)
[92] Y. Hattori, T. Suzuki and T. Murata et al., J. Cryst. Growth **115**, 607 (1991)
[93] Y. H. Mo, Md. Shajahan and K. S. Lee, Doamond and Related Mater. **11**, 1703 (2002)
[94] T. Shimizu, Y. Ishikawa and N. Shibata, Jpn. J. Appl. Phys. **39**, L617 (2000)
[95] Y. Hirabayashi, S. Karasawa and K. Kobayashi, J. Cryst. Growth **128**, 369 (1993)
[96] R. Beccard, D. Schmitz and E. G. Woelk et al., Mater. Sci. Eng. B **61-62**, 314 (1999)
[97] T. Kimoto, T. Hirao and S. Nakazawa et al., J. Cryst. Growth **249**, 208 (2003)
[98] I. Kamata, H. Tsuchida and T. Jikimoto et al., Jpn. J. Appl. Phys. **41**, L1137 (2002)
[99] D. Chaussende, G. Ferro and Y. Monteil, J. Cryst. Growth **234**, 63 (2002)
[100] M. Mynbaeva, S. E. Saddow, and G. Melnychuk *et al.*, Appl. Phys. Lett. **78**, 117 (2001)
[101] V. V. Zelenin, M. L. Korogodskii and A. A. Lebedev, Semiconductors **35**, 1172 (2001)

[102] S. Tamura, K. Fujihira and T. Kimoto et al., Jpn. J. Appl. Phys. **40**, L319 (2001)
[103] H. Behner and R. Rupp, App. Surf. Sci. **99**, 27 (1996)
[104] O. Kordina, C. Hallin and A. Henry et al., Phys. Stat. Sol. (b) **202**, 321 (1997)
[105] C. Hallin, I. G. Ivanov and T. Egilsson et al., J. Cryst. Growth **183**, 163 (1998)
[106] J. Zhang, A. Ellison and A. Henry et al., Mater. Sci. Eng. B **61-62**, 151 (1999)
[107] S. Nakamura, T. Kimoto and H. Matsunami, Jpn. J. Appl. Phys. **42**, L846 (2003)
[108] Y. Chen, T. Kimoto and Y. Takeuchi et al., J. Cryst. Growth **254**, 115 (2003)
[109] A. O. Konstantinov, C. Hallin and O. Kordina et al., J. Appl. Phys. **80**, 5704 (1996)
[110] K. Kojima, T. Suzuki and S. Kuroda et al., Jpn. J. Appl. Phys. **42**, L637 (2003)
[111] T. Kimoto, S. Tamura and Y. Chen et al., Jpn. J. Appl. Phys. **40**, L374 (2001)
[112] R. Rupp, A. Wiedenhofer and P. Friedrichs et al., Mater. Sci. Forum **264-268**, 89 (1998)
[113] O. Kordina, C. Hallin and A. Ellison et al., Appl. Phys. Lett. **69**, 1456 (1996)
[114] H. Tsuchida, I. Kamata and T. Jikimoto et al., J. Cryst. Growth **237-239**, 1206 (2002)
[115] J. Nishio, M. Hasegawa and K. Kojima et al., J. Cryst. Growth **258**, 113 (2003)
[116] E. Neyret, L. Di Cioccio and J. M. Bluet et al., Mater. Sci. Eng. B **80**, 332 (2001)
[117] S. E. Saddow, M. S. Mazzola and S. V. Rendakova et al., Mater. Sci. Eng. B **61-62**, 158 (1999)
[118] S. Karlsson, N. Nordell and F. Spadafora et al., Mater. Sci. Eng. B **61-62**, 143 (1999)
[119] R. Rupp, Y. N. Makarov and H. Behner et al., Phys. Stat. Sol. (b) **202**, 281 (1997)
[120] V. V. Zelenin, A. A. Lebedev and S. M. Starobinets et al., Mater. Sci. Eng. B **46**, 300 (1997)
[121] R. Rupp, A. Wiedenhofer and D. Stephani, Mater. Sci. Eng. B **61-62**, 125 (1999)
[122] M. S. Saidov, Kh. A. Shamuratov and M. A. Kadyrov, J. Cryst. Growth **87**, 519 (1988)
[123] S. Karmann, C. Haberstroh and F. Engelbrecht et al., Phys. B **185**, 75 (1993)
[124] G. Bramberg and M. Koniger, Solid-State Electron. **15**, 285 (1972)
[125] S. E. Saddow, T. E. Schattner and J. Brown et al., J. Electron. Mater. **30**, 228 (2001)
[126] B. Reznik, D. Gerthsen and W. Zhang et al., J. Euro. Ceram. Soc. **23**, 1499 (2003)
[127] A. Ellison, J. Zhang and J. Peterson et al., Mater. Sci. Eng. B **61-62**, 113 (1999)
[128] R. Wang, I. B. Bhat and T. P. Chow, J. Appl. Phys. **92**, 7587 (2002)
[129] J. Zhang, A. Ellison and O. Danielsson et al., J. Cryst. Growth **241**, 421 (2002)
[130] A. Ellison, J. Zhang and A. Henry et al., J. Cryst. Growth **236**, 225 (2002)
[131] J. Zhang, U. Forsberg and M. Isacson et al., J. Cryst. Growth **241**, 431 (2002)
[132] S. Nigam, H. J. Chung and A. Y. Polyakov et al., J. Cryst. Growth **284**, 112 (2005)
[133] J. A. Powell, D. J. Larkin and L. G. Matus et al., Appl. Phys. Lett. **56**, 1442 (1990)
[134] A. Henry, I. G. Ivanov and T. Egilsson et al., Diamond and Related Materials **6**, 1289 (1997)
[135] A. Ellison, J. Zhang and J. Peterson et al., Material Science and Engineering B **61-62**, 113 (1999)
[136] S. Nakazawa, T. Kimoto and K. Hashimoto et al., J. Cryst. Growth **237-239** 1213 (2002)
[137] J. K. Jeong, H. J. Na and J. Choi et al., J. Cryst. Growth **210**, 629 (2000)
[138] A. A. Burk Jr., M. J. O'Loughlin and H. D. Nordby Jr., J. Cryst. Growth **200**, 458 (1999)
[139] T. Kimoto, A. Itoh and H. Matsunami, Phys. Stat. Sol. (b) **202**, 247 (1997)

[140] I. Regiani and M. F. De Souza, Surf. Coat. Tech. **162**, 131 (2003)
[141] D. Dietrich, H. Podlesak and G. Marx et al., Fresenius J. Anal. Chem. **361**, 568 (1998)
[142] R. Brutsch, Thin Solid Films **126**, 313 (1985)
[143] N. Kuroda, K. Shibahara, W. Yoo, S. Nishino and H. Matsunami, Extended Abstract 34th Spring Meeting of Japan Society of Applied Physics and Related Societies, Tokyo, March, 1987, 28p-ZC-2,3
[144] K. Shibahara, N. Kuroda, S. Nishino and H. Matsunami, Jpn. J. Appl. Phys. **26**, L1815 (1987)
[145]. A. I. Kingon, L. J. Lutz, P. Liaw and R. F. Davis, J. Am. Ceram. Soc. **66,** 558 (1983)
[146]. G. S. Fischman and W. T. Petuskey, J. Am. Ceram. Soc. **68,** 185 (1985)
[147] S. Nigam, H. J. Chung, A. Y. Polyakov, M. A. Fanton, B. E. Weiland, D. W. Snyder and M. Skowronski, J. Cryst. Growth **284**, 112 (2005)
[148] T. Ohno, H. Yamaguchi, S. Kuroda, K. Kojima, T. Suzuki and K. Arai, J. Cryst. Growth **260**, 209 (2004)
[149] S. Ha, P. Mieszkowski, M. Skowronski and L. B. Rowland, J. Cryst. Growth **244**, 257 (2002)
[150] R. -H. Ma, H. Zhang, S. Ha and M. Skowronski, J. Cryst. Growth **252**, 523 (2003)
[151] F. C. Frank, Acta. Cryst. **4**, 497 (1951)
[152] M. Zhang, H. M. Hobgood and P. Pirouz, Mater. Sci. Forum **457-460**, 371 (2004)
[153] M. Zhang, H. M. Hobgood and P. Pirouz: Mater. Sci. Forum **457-460**, 371 (2004)
[154] D. Hull and D. J. Bacon, in "*Introduction to Dislocations*", (Butterworth Heinemann, 4th Edition, Oxford, UK pp.191)
[155] S. Ha, M. Skowronski, W. M. Vetter and M. Dudley, J. Appl. Phys. **92**, 778 (2002)
[156] A. Galekas, J. Linnros and P. Pirouz, Appl. Phys. Lett. **81**, 883 (2002)
[157] S. Ha, M. Benamara, M. Skowronski and H. Lendinmann, Appl. Phys. Lett. **83**, 4957 (2003)
[158] R. E. Stahlbush, M. Fatemi, J. B. Fedison, S. D. Arthur, L. B. Rowland and S. Wang, J. Elec. Mater. **31**, 370 (2002)
[159] M. Skowronski, J. Q. Liu, W. M. Vetter, M. Dudley, C. Hallin and H. Lendenmann, J. Appl. Phys. **92,** 4699 (2002)
[160] The core structure can be verified by using right-hand rule to determine the position of the extra half plane associated with the PD: assuming the line direction of the Shockley PD loop bounding the SF is clockwise, one can determine that the extra half planes for segments AB, CD and EF lie on the same side of the dislocation line (above the plane of the pictures) therefore they have the same core structure. On the contrary, the extra half planes of segment BC and DE lie underneath the plane of the pictures indicating opposite core structure.
[161] M. Zhang, H. M. Hobgood and P. Pirouz, Mater. Sci. Forum **457-460,** 371 (2004)
[162] P. Pirouz, J. L. Demenet and M. H. Hong, Phil. Mag. A **81,** 1207 (2001)
[163] T. Rasmussen, T. Vegge, T. Leffers, O. B. Pedersen and K. W. Jacobsen, Phil. Mag. A **80,** 1273 (2000)
[164] U. Essmann and H. Mughrabi, Phil. Mag. A **40,** 731 (1979)
[165] J. P. Hirth and J. Lothe, in "*Theory of Dislocations*", 2nd Ed., John Wiley & Sons Publication, New York, 1982, pp. 160

[166] B. J. Skromme, K. C. Palle, M. K. Mikhov, H. Meidia, S. Mahajan, X. R. Huang, W. M. Vetter, M. Dudley, K. Moore, S. Smith and T. Gehoski, Mat. Res. Soc. Symp. Proc. **742,** K3.4.1 (2003)
[167] P. Pirouz, M. Zhang, A. Galeckas and J. Linnros, Mater. Sci. Forum **815,** J6.1.1 (2004)
[168] P. G. Neudeck, W. Huang and M. Dudley, Solid-State Electron. **42,** 2157 (1998)
[169] K. Koga, Y. Fujikawa, Y. Ueda and T. Yamaguchi, Springer Proc. Phys. **71**, 96 (1992)
[170] A. R. Lang and A. P. W. Makepeace, J. Phys. D: Appl. Phys. **32,** A97 (1999)
[171] J. P. Hirth and J. Lothe, in "*Theory of Dislocations*", 2nd Ed., John Wiley & Sons Publication, New York, 1982, pp. 60
[172] J. D. Eshelby, and A. N. Stroh, Phil. Mag. **42,** 1401 (1951)
[173] A. R. Lang and A. P. W. Makepeace, J. Phys. D: Appl. Phys. **32,** A97 (1999)
[174] M. Dudley, X. Huang and W. M. Vetter, J. Phys. D: Appl. Phys. **36,** A30 (2003)
[175] Y. Chen, M. Dudley, E. K. Sanchez, and M. F. MacMillan, J. Electron. Mater. 2007 (in press)
[176] A. R. Verma, Nature **167,** 939 (1951).
[177] S. Amelinckx, Nature **167,** 939 (1951).
[178] P. G. Neudeck, W. Huang and M. Dudley, Solid-State Electron. **42,** 2157 (1998)
[179] Y. Chen, M. Dudley, K. X. Liu, and R. E. Stahlbush, Mater. Res. Soc. Symp. Proc. **0994,** 0994-F12-03 (2007).
[180] A. O. Okunev, L. N. Danil'chuk, and V. A. Tkal', Phys. Solid State **48,** 2084 (2006)
[181] I. Kamata, H. Tsuchida, W. M. Vetter, and M. Dudley, J. Mater. Res. **22,** 845 (2007).
[182] Y. Chen, H. Chen, N. Zhang, M. Dudley, and R. Ma, Mater. Res. Soc. Symp. Proc. **955**, 0955-I07-50 (2007)
[183] I. Kamata, H. Tsuchida, W. M. Vetter, and M. Dudley, J. Mater. Res. **22**, 845 (2007)
[184] I. Kamata, H. Tsuchida, W. M. Vetter, and M. Dudley, Mater. Res. Soc. Symp. Proc. **911,** 0911-B05-11 (2006)
[185] I. Kamata, M. Nagano, H. Tsuchida, Y. Chen, and M. Dudley, Mater. Sci. Forum (in press)
[186] J. P. Hirth and J. Lothe, in "*Theory of Dislocations*", 2nd ed., Wiley, New York, 1982, p. 78.
[187] D. Hull and D. J. Bacon, in "*Introduction to Dislocations*", 4th ed., Butterworth-Heinemann, Oxford, 2002, p. 158.
[188] H. Lendenmann, F. Dahlquist, N. Johansson, R. Soderholm, P. A. Nilsson, J. P. Bergman, and P. Skytt, Mater. Sci. Forum **353-356**, 727 (2001)
[189] A. Galeckas, J. Linnros, and P. Pirouz, Appl. Phys. Lett. **81**, 883 (2002)
[190] J. D. Weeks, J. C. Tully, and L. C. Kimerling, Phys. Rev. B **12,** 3286 (1975).
[191] H. Sumi, Phys. Rev. B 29, 4616 (1984).
[192] S. Ha, M. Skowronski, J. J. Sumakeris, M. J. Paisley, and M. K. Das, Phys. Rev. Lett. **92,** 175504 (2004)
[193] A. Galeckas, J. Linnros, and P. Pirouz, Phys. Rev. Lett. **96,** 025502 (2006)
[194] M. Skowronski and S. Ha, J. Appl. Phys. **99,** 011101 (2006)
[195] Y. Chen, M. Dudley, K. X. Liu, and R. E. Stahlbush, Appl. Phys. Lett. **90,** 171930 (2007)
[196] J. D. Caldwell, R. E. Stahlbush, K. D. Hobart, O. J. Glembocki, and K. X. Liu, Appl. Phys. Lett. **90,** 143519 (2007)

[197] S. Ha, K. Hu, and M. Skowronski, Appl. Phys. Lett. **84,** 5267 (2004)
[198] A. Seeger, in "*Dislocations and Mechanical Properties of Crystals*", Editors: J. C. Fisher, W. G. Johnson, R. Thomson, and T. Vreeland, Jr., John Wiley & Sons Publication, New York, 1956, pp. 252
[199] M. H. Hong, A. V. Samant, and P. Pirouz, Phil. Mag. A **80,** 919 (2000)
[200] S. Ha, M. Benamara, M. Skowronski, and H. Lendenmann, Appl. Phys. Lett. **83,** 4957 (2003)
[201] M. E. Twigg, R. E. Stahlbush, M. Fatemi, S. D. Arthur, J. B. Fedison, J. B. Tucker, and S. Wang, Appl. Phys. Lett. **82,** 2410 (2003)
[202] Y. Chen, N. Zhang, M. Dudley, J. D. Caldwell, K. X. Liu, and R. E. Stahlbush, J. Electron. Mater. 2007 (in press)
[203] K. X. Liu, R. E. Stahlbush, S. I . Maximenko, and J. D. Caldwell, Appl. Phys. Lett. **90,** 153503 (2007)
[204] S. Ha, H. J. Chung, N. T. Nuhfer, and M. Skowronski, J. Cryst. Growth **262,** 130 (2004)
[205] X. Zhang, M. Skowronski, K. X. Liu, R. E. Stahlbush, J. J. Sumakeris, M. J. Paisley and M. J. O'Loughlin, J. Appl. Phys. **102**, 093520 (2007)
[206] D. Nakamura, I. Gunjishima, S. Yamaguchi, T. Ito, A. Okamoto, H. Kondo, S. Onda, and K. Takatori, Nature **430,** 1009 (2004)
[207] H. Lendenmann, F. Dahlquist, N. Johansson, R. Soderholm, P. A. Nilsson, J. P. Bergman, and P. Skytt, Mater. Sci. Forum **353-356**, 727 (2001)
[208] A. Galeckas, J. Linnros, and P. Pirouz, Appl. Phys. Lett. **81**, 883 (2002)
[209] J. D. Weeks, J. C. Tully, and L. C. Kimerling, Phys. Rev. B **12,** 3286 (1975).
[210] H. Sumi, Phys. Rev. B **29**, 4616 (1984).
[211] G. Savini, M. I. Heggie, and S. Oberg, Farad. Disc. **134,** 353 (2007)
[212] A. T. Blumenau, C. J. Fall, R. Jones, S. Oberg, T. Frauenheim, and P. R. Briddon, Phys. Rev. B **68,** 174108 (2003)
[213] A. Galeckas, J. Linnros, and P. Pirouz, Phys. Rev. Lett. **96,** 025502 (2006)
[214] S. Ha, M. Benamara, M. Skowronski, and H. Lendenmann, Appl. Phys. Lett. **83**, 4957 (2003)
[215] X. J. Ning and P. Pirouz, J. Mater. Res. **11,** 884 (1996)
[216] K. X. Liu, R. E. Stahlbush, K. B. Hobart, and J. J. Sumakeris, Mater. Sci. Forum **527-529,** 387 (2006)
[217] R. E. Stahlbush, M. Fatemi, J. B. Fedison, S. D. Arthur, L. B. Rowland, and S. Wang, J. Elec. Mater. **31**, 370 ((2002)
[218] Y. Chen and M. Dudley (to be published)
[219] H. Jacobson, J. Birch, R. Yakimova, M. Syvajarvi, J. P. Bergman, A. Ellison, T. Tuomi, and E. Janzen, J. Appl. Phys. **91,** 6354 (2002)
[220] J. D. Caldwell, R. E. Stahlbush, K. D. Hobart, O. J. Glembocki, and K. X. Liu, Appl. Phys. Lett. **90,** 143519 (2007)
[221] M. Dudley, X. R. Huang, and W. Huang, J. Phys. D: Appl. Phys. **32,** A139 (1999)
[222] P. Pirouz, M. Zhang, A. Galeckas, and J. Linnros, Mater. Sci. Forum **815,** J6.1.1 (2004)
[223] Q. Wahab, A. Ellison, A. Henry, E. Janzén, C. Hallin, J. Di Persio and R. Martinez, Appl. Phys. Lett. **76**, 2725 (2000)
[224] H. Tsuchida, I. Kamata, and M. Nagano, J. Cryst. Growth **306,** 254 (2007)

[225] J. A. Powell, P. G. Neudeck, A. J. Trunek, G. M. Beheim, L. G. Matus, R. W. Hoffman, and L. J. Keys, Appl. Phys. Lett. **77,** 1449 (2000)
[226] See equation (4.36), D. Hull and D. J. Bacon, in "Introduction to Dislocations", 4th Ed., Butterworth-Heinemann, Oxford, 2001, pp. 76
[227] A. R. Lang, A. P. W. Makepeace, Synchrotron x-ray reticulography: principles and applications, J. Phys. D – Appl. Phys., 32(10A), A97-A103 (1999).

Appendix I --- Mathematica® code of (11-28) simulation of a 1*c* TSD with surface relaxation

```
{μ, γ, ν} = {193×10^9, 0.94, 0.18}
{d, m, t} = {150000, 1, 215};
b = 0.001005 m;
resolution = 0.1;
(*****d: film-specimen distance in z-axis, m: Burgers vector of the MP (mc)
   t: half of wafer thickness, for surface relaxation
  resolution: the resolution of the final image, in μm
  μ,γ, ν: shear modulus, surface energy (not necessarily needed), Poisson's coefficient *****)

r_x = Cos[190 °];
r_y = 0;
r_z = Sin[190 °];
(*****unit vector of incident beam*****)

g0x = Cos[π/2 - ArcTan[10.05/(8×1.54)]];
g0y = 0;
g0z = Sin[π/2 - ArcTan[10.05/(8×1.54)]];
(*g0*)

(*The center of the film*)
g0x' =
  1/g0z (g0z r_x - ((g0x)^2 g0z r_x) / ((g0x)^2 + (g0y)^2 + (g0z)^2) - (g0x g0y g0z r_y) / ((g0x)^2 + (g0y)^2 + (g0z)^2) -
    g0x r_z + ((g0x)^3 r_z) / ((g0x)^2 + (g0y)^2 + (g0z)^2) + (g0x (g0y)^2 r_z) / ((g0x)^2 + (g0y)^2 + (g0z)^2) +
    1/(2 ((g0x)^2 + (g0y)^2 + (g0z)^2))
     (g0x √((2 g0x g0z r_x + 2 g0y g0z r_y - 2 (g0x)^2 r_z - 2 (g0y)^2 r_z)^2 -
          4 ((g0x)^2 + (g0y)^2 + (g0z)^2) (-(g0z)^2 + (g0z)^2 r_x^2 + (g0z)^2 r_y^2 - 2 g0x g0z r_x r_z -
            2 g0y g0z r_y r_z + (g0x)^2 r_z^2 + (g0y)^2 r_z^2))));
g0y' =
  1/g0z (-(g0x g0y g0z r_x) / ((g0x)^2 + (g0y)^2 + (g0z)^2) + g0z r_y - ((g0y)^2 g0z r_y) / ((g0x)^2 + (g0y)^2 + (g0z)^2) -
    g0y r_z + ((g0x)^2 g0y r_z) / ((g0x)^2 + (g0y)^2 + (g0z)^2) + ((g0y)^3 r_z) / ((g0x)^2 + (g0y)^2 + (g0z)^2) +
    1/(2 ((g0x)^2 + (g0y)^2 + (g0z)^2))
     (g0y √((2 g0x g0z r_x + 2 g0y g0z r_y - 2 (g0x)^2 r_z - 2 (g0y)^2 r_z)^2 -
          4 ((g0x)^2 + (g0y)^2 + (g0z)^2) (-(g0z)^2 + (g0z)^2 r_x^2 + (g0z)^2 r_y^2 - 2 g0x g0z r_x r_z -
            2 g0y g0z r_y r_z + (g0x)^2 r_z^2 + (g0y)^2 r_z^2))));
g0z' = 1/(2 ((g0x)^2 + (g0y)^2 + (g0z)^2))
   (-2 g0x g0z r_x - 2 g0y g0z r_y + 2 (g0x)^2 r_z + 2 (g0y)^2 r_z +
    √((2 g0x g0z r_x + 2 g0y g0z r_y - 2 (g0x)^2 r_z - 2 (g0y)^2 r_z)^2 -
      4 ((g0x)^2 + (g0y)^2 + (g0z)^2) (-(g0z)^2 + (g0z)^2 r_x^2 + (g0z)^2 r_y^2 - 2 g0x g0z r_x r_z - 2 g0y g0z r_y r_z +
        (g0x)^2 r_z^2 + (g0y)^2 r_z^2)));
xco0 = -((d + t Sec[8 °]) g0x') / (Tan[8 °] g0x' - g0z');
yco0 = -((d + t Sec[8 °]) g0y') / (Tan[8 °] g0x' - g0z');
zco0 = -((d + t Sec[8 °]) g0z') / (Tan[8 °] g0x' - g0z');
(*The center of the film (xco0, yco0, zco0)*)

intenmatrrow = {0};
Do[intenmatrrow = Prepend[intenmatrrow, 0], {i, 1, 499}];
intenmatr = Append[{intenmatrrow}, intenmatrrow];
Do[intenmatr = Append[intenmatr, intenmatrrow], {i, 1, 498}];
(*****define a 500 x500 matrix (intenmatr) which records the reflected beam intensity*****)

Do[ (*If[√(10^-12 ((x0)^2+(y0)^2)) ≥ (μ (10.05×10^-10 m)^2) / (8 π^2 γ), *)
 z0 = x0 Tan[8 °];
```

$$
\begin{aligned}
n_x = {} & g0x + \frac{b\, g0z\, y0}{2\pi\, x0^2 \left(1 + \frac{y0^2}{x0^2}\right)} - \\
& \frac{1}{\sqrt{x0^2 + y0^2}} \\
& \left(g0y\, x0 \right. \\
& \left(-\frac{1}{2\pi} \left(b \left(-\frac{x0\sqrt{x0^2 + y0^2}}{\sqrt{x0^2 + y0^2 + z0^2}\left(-z0 + \sqrt{x0^2 + y0^2 + z0^2}\right)^2} + \frac{x0}{\sqrt{x0^2 + y0^2}\left(-z0 + \sqrt{x0^2 + y0^2 + z0^2}\right)} + \right. \right. \right. \\
& \left. \left. \left(x0\sqrt{x0^2 + y0^2} \right) \Big/ \left(\sqrt{x0^2 + y0^2 + (2t + z0)^2}\left(2t + z0 + \sqrt{x0^2 + y0^2 + (2t + z0)^2}\right)^2 \right) - \right. \right. \\
& \left. \left. x0 \Big/ \left(\sqrt{x0^2 + y0^2}\left(2t + z0 + \sqrt{x0^2 + y0^2 + (2t + z0)^2}\right) \right) \right) \right) + \\
& \frac{1}{2\pi} \left(b \left(-\left(x0\sqrt{x0^2 + y0^2} \right) \Big/ \left(\sqrt{x0^2 + y0^2 + (2t - z0)^2}\left(2t + \sqrt{x0^2 + y0^2 + (2t - z0)^2} - z0\right)^2 \right) + \right. \right. \\
& \left. x0 \Big/ \left(\sqrt{x0^2 + y0^2}\left(2t + \sqrt{x0^2 + y0^2 + (2t - z0)^2} - z0\right) \right) + \right. \\
& \left. \left(x0\sqrt{x0^2 + y0^2} \right) \Big/ \left(\sqrt{x0^2 + y0^2 + (4t + z0)^2}\left(4t + z0 + \sqrt{x0^2 + y0^2 + (4t + z0)^2}\right)^2 \right) - \right. \\
& \left. \left. x0 \Big/ \left(\sqrt{x0^2 + y0^2}\left(4t + z0 + \sqrt{x0^2 + y0^2 + (4t + z0)^2}\right) \right) \right) \right) - \\
& \frac{1}{2\pi} \left(b \left(-\left(x0\sqrt{x0^2 + y0^2} \right) \Big/ \left(\sqrt{x0^2 + y0^2 + (4t - z0)^2}\left(4t + \sqrt{x0^2 + y0^2 + (4t - z0)^2} - z0\right)^2 \right) + \right. \right. \\
& \left. x0 \Big/ \left(\sqrt{x0^2 + y0^2}\left(4t + \sqrt{x0^2 + y0^2 + (4t - z0)^2} - z0\right) \right) + \right. \\
& \left. \left(x0\sqrt{x0^2 + y0^2} \right) \Big/ \left(\sqrt{x0^2 + y0^2 + (6t + z0)^2}\left(6t + z0 + \sqrt{x0^2 + y0^2 + (6t + z0)^2}\right)^2 \right) - \right. \\
& \left. \left. x0 \Big/ \left(\sqrt{x0^2 + y0^2}\left(6t + z0 + \sqrt{x0^2 + y0^2 + (6t + z0)^2}\right) \right) \right) \right) \Bigg) + \\
& \frac{1}{\sqrt{x0^2 + y0^2}} \\
& \left(g0x\, y0 \right. \\
& \left(-\frac{1}{2\pi} \left(b \left(-\frac{x0\sqrt{x0^2 + y0^2}}{\sqrt{x0^2 + y0^2 + z0^2}\left(-z0 + \sqrt{x0^2 + y0^2 + z0^2}\right)^2} + \frac{x0}{\sqrt{x0^2 + y0^2}\left(-z0 + \sqrt{x0^2 + y0^2 + z0^2}\right)} + \right. \right. \right. \\
& \left. \left. \left(x0\sqrt{x0^2 + y0^2} \right) \Big/ \left(\sqrt{x0^2 + y0^2 + (2t + z0)^2}\left(2t + z0 + \sqrt{x0^2 + y0^2 + (2t + z0)^2}\right)^2 \right) - \right. \right. \\
& \left. \left. x0 \Big/ \left(\sqrt{x0^2 + y0^2}\left(2t + z0 + \sqrt{x0^2 + y0^2 + (2t + z0)^2}\right) \right) \right) \right) + \\
& \frac{1}{2\pi} \\
& \left(b \left(-\left(x0\sqrt{x0^2 + y0^2} \right) \Big/ \left(\sqrt{x0^2 + y0^2 + (2t - z0)^2}\left(2t + \sqrt{x0^2 + y0^2 + (2t - z0)^2} - z0\right)^2 \right) + \right. \right. \\
& \left. x0 \Big/ \left(\sqrt{x0^2 + y0^2}\left(2t + \sqrt{x0^2 + y0^2 + (2t - z0)^2} - z0\right) \right) + \right. \\
& \left. \left(x0\sqrt{x0^2 + y0^2} \right) \Big/ \left(\sqrt{x0^2 + y0^2 + (4t + z0)^2}\left(4t + z0 + \sqrt{x0^2 + y0^2 + (4t + z0)^2}\right)^2 \right) - \right. \\
& \left. \left. x0 \Big/ \left(\sqrt{x0^2 + y0^2}\left(4t + z0 + \sqrt{x0^2 + y0^2 + (4t + z0)^2}\right) \right) \right) \right) - \\
& \frac{1}{2\pi} \\
& \left(b \left(-\left(x0\sqrt{x0^2 + y0^2} \right) \Big/ \left(\sqrt{x0^2 + y0^2 + (4t - z0)^2}\left(4t + \sqrt{x0^2 + y0^2 + (4t - z0)^2} - z0\right)^2 \right) + \right. \right. \\
& \left. x0 \Big/ \left(\sqrt{x0^2 + y0^2}\left(4t + \sqrt{x0^2 + y0^2 + (4t - z0)^2} - z0\right) \right) + \right. \\
& \left. \left(x0\sqrt{x0^2 + y0^2} \right) \Big/ \left(\sqrt{x0^2 + y0^2 + (6t + z0)^2}\left(6t + z0 + \sqrt{x0^2 + y0^2 + (6t + z0)^2}\right)^2 \right) - \right. \\
& \left. \left. x0 \Big/ \left(\sqrt{x0^2 + y0^2}\left(6t + z0 + \sqrt{x0^2 + y0^2 + (6t + z0)^2}\right) \right) \right) \right) \Bigg) +
\end{aligned}
$$

$$\frac{1}{(x0^2+y0^2)^{3/2}}\left(g0y\,x0^2\left(-\frac{b\left(\frac{\sqrt{x0^2+y0^2}}{-z0+\sqrt{x0^2+y0^2+z0^2}}-\frac{\sqrt{x0^2+y0^2}}{2t+z0+\sqrt{x0^2+y0^2+(2t+z0)^2}}\right)}{2\pi}+\right.\right.$$

$$\frac{1}{2\pi}\left(b\left(\frac{\sqrt{x0^2+y0^2}}{2t+\sqrt{x0^2+y0^2+(2t-z0)^2}-z0}-\frac{\sqrt{x0^2+y0^2}}{4t+z0+\sqrt{x0^2+y0^2+(4t+z0)^2}}\right)\right)-$$

$$\left.\left.\frac{1}{2\pi}\left(b\left(\frac{\sqrt{x0^2+y0^2}}{4t+\sqrt{x0^2+y0^2+(4t-z0)^2}-z0}-\frac{\sqrt{x0^2+y0^2}}{6t+z0+\sqrt{x0^2+y0^2+(6t+z0)^2}}\right)\right)\right)-$$

$$\frac{1}{(x0^2+y0^2)^{3/2}}\left(g0x\,x0\,y0\left(-\frac{b\left(\frac{\sqrt{x0^2+y0^2}}{-z0+\sqrt{x0^2+y0^2+z0^2}}-\frac{\sqrt{x0^2+y0^2}}{2t+z0+\sqrt{x0^2+y0^2+(2t+z0)^2}}\right)}{2\pi}+\right.\right.$$

$$\frac{1}{2\pi}\left(b\left(\frac{\sqrt{x0^2+y0^2}}{2t+\sqrt{x0^2+y0^2+(2t-z0)^2}-z0}-\frac{\sqrt{x0^2+y0^2}}{4t+z0+\sqrt{x0^2+y0^2+(4t+z0)^2}}\right)\right)-$$

$$\left.\left.\frac{1}{2\pi}\left(b\left(\frac{\sqrt{x0^2+y0^2}}{4t+\sqrt{x0^2+y0^2+(4t-z0)^2}-z0}-\frac{\sqrt{x0^2+y0^2}}{6t+z0+\sqrt{x0^2+y0^2+(6t+z0)^2}}\right)\right)\right)-$$

$$\frac{1}{\sqrt{x0^2+y0^2}}\left(g0y\left(-\frac{b\left(\frac{\sqrt{x0^2+y0^2}}{-z0+\sqrt{x0^2+y0^2+z0^2}}-\frac{\sqrt{x0^2+y0^2}}{2t+z0+\sqrt{x0^2+y0^2+(2t+z0)^2}}\right)}{2\pi}+\right.\right.$$

$$\frac{1}{2\pi}\left(b\left(\frac{\sqrt{x0^2+y0^2}}{2t+\sqrt{x0^2+y0^2+(2t-z0)^2}-z0}-\frac{\sqrt{x0^2+y0^2}}{4t+z0+\sqrt{x0^2+y0^2+(4t+z0)^2}}\right)\right)-$$

$$\left.\left.\frac{1}{2\pi}\left(b\left(\frac{\sqrt{x0^2+y0^2}}{4t+\sqrt{x0^2+y0^2+(4t-z0)^2}-z0}-\frac{\sqrt{x0^2+y0^2}}{6t+z0+\sqrt{x0^2+y0^2+(6t+z0)^2}}\right)\right)\right);$$

(** nx *****)**

$$n_y = g0y-\frac{b\,g0z}{2\pi\,x0\left(1+\frac{y0^2}{x0^2}\right)}-$$

$$\frac{1}{\sqrt{x0^2+y0^2}}\left(g0y\,x0\left(-\frac{1}{2\pi}\left(b\left(-\frac{y0\sqrt{x0^2+y0^2}}{\sqrt{x0^2+y0^2+z0^2}\left(-z0+\sqrt{x0^2+y0^2+z0^2}\right)^2}+\frac{y0}{\sqrt{x0^2+y0^2}\left(-z0+\sqrt{x0^2+y0^2+z0^2}\right)}+\right.\right.\right.\right.$$

$$\left(y0\sqrt{x0^2+y0^2}\right)\Big/\left(\sqrt{x0^2+y0^2+(2t+z0)^2}\left(2t+z0+\sqrt{x0^2+y0^2+(2t+z0)^2}\right)^2\right)-$$

$$\left.\left.\left.\left.y0\Big/\left(\sqrt{x0^2+y0^2}\left(2t+z0+\sqrt{x0^2+y0^2+(2t+z0)^2}\right)\right)\right)\right)\right)+$$

$$\frac{1}{2\pi}\left(b\left(-\left(y0\sqrt{x0^2+y0^2}\right)\Big/\left(\sqrt{x0^2+y0^2+(2t-z0)^2}\left(2t+\sqrt{x0^2+y0^2+(2t-z0)^2}-z0\right)^2\right)+\right.\right.$$
$$y0\Big/\left(\sqrt{x0^2+y0^2}\left(2t+\sqrt{x0^2+y0^2+(2t-z0)^2}-z0\right)\right)+$$
$$\left(y0\sqrt{x0^2+y0^2}\right)\Big/\left(\sqrt{x0^2+y0^2+(4t+z0)^2}\left(4t+z0+\sqrt{x0^2+y0^2+(4t+z0)^2}\right)^2\right)-$$
$$\left.\left.y0\Big/\left(\sqrt{x0^2+y0^2}\left(4t+z0+\sqrt{x0^2+y0^2+(4t+z0)^2}\right)\right)\right)\right)-$$
$$\frac{1}{2\pi}\left(b\left(-\left(y0\sqrt{x0^2+y0^2}\right)\Big/\left(\sqrt{x0^2+y0^2+(4t-z0)^2}\left(4t+\sqrt{x0^2+y0^2+(4t-z0)^2}-z0\right)^2\right)+\right.\right.$$
$$y0\Big/\left(\sqrt{x0^2+y0^2}\left(4t+\sqrt{x0^2+y0^2+(4t-z0)^2}-z0\right)\right)+$$
$$\left(y0\sqrt{x0^2+y0^2}\right)\Big/\left(\sqrt{x0^2+y0^2+(6t+z0)^2}\left(6t+z0+\sqrt{x0^2+y0^2+(6t+z0)^2}\right)^2\right)-$$
$$\left.\left.y0\Big/\left(\sqrt{x0^2+y0^2}\left(6t+z0+\sqrt{x0^2+y0^2+(6t+z0)^2}\right)\right)\right)\right)\Big)+$$
$$\frac{1}{\sqrt{x0^2+y0^2}}\left(g0x\,y0\left(-\frac{1}{2\pi}\left(b\left(-\frac{y0\sqrt{x0^2+y0^2}}{\sqrt{x0^2+y0^2+z0^2}\left(-z0+\sqrt{x0^2+y0^2+z0^2}\right)^2}+\frac{y0}{\sqrt{x0^2+y0^2}\left(-z0+\sqrt{x0^2+y0^2+z0^2}\right)}+\right.\right.\right.\right.$$
$$\left(y0\sqrt{x0^2+y0^2}\right)\Big/\left(\sqrt{x0^2+y0^2+(2t+z0)^2}\left(2t+z0+\sqrt{x0^2+y0^2+(2t+z0)^2}\right)^2\right)-$$
$$\left.\left.\left.\left.y0\Big/\left(\sqrt{x0^2+y0^2}\left(2t+z0+\sqrt{x0^2+y0^2+(2t+z0)^2}\right)\right)\right)\right)\right)+$$
$$\frac{1}{2\pi}\left(b\left(-\left(y0\sqrt{x0^2+y0^2}\right)\Big/\left(\sqrt{x0^2+y0^2+(2t-z0)^2}\left(2t+\sqrt{x0^2+y0^2+(2t-z0)^2}-z0\right)^2\right)+\right.\right.$$
$$y0\Big/\left(\sqrt{x0^2+y0^2}\left(2t+\sqrt{x0^2+y0^2+(2t-z0)^2}-z0\right)\right)+$$
$$\left(y0\sqrt{x0^2+y0^2}\right)\Big/\left(\sqrt{x0^2+y0^2+(4t+z0)^2}\left(4t+z0+\sqrt{x0^2+y0^2+(4t+z0)^2}\right)^2\right)-$$
$$\left.\left.y0\Big/\left(\sqrt{x0^2+y0^2}\left(4t+z0+\sqrt{x0^2+y0^2+(4t+z0)^2}\right)\right)\right)\right)-$$
$$\frac{1}{2\pi}\left(b\left(-\left(y0\sqrt{x0^2+y0^2}\right)\Big/\left(\sqrt{x0^2+y0^2+(4t-z0)^2}\left(4t+\sqrt{x0^2+y0^2+(4t-z0)^2}-z0\right)^2\right)+\right.\right.$$
$$y0\Big/\left(\sqrt{x0^2+y0^2}\left(4t+\sqrt{x0^2+y0^2+(4t-z0)^2}-z0\right)\right)+$$
$$\left(y0\sqrt{x0^2+y0^2}\right)\Big/\left(\sqrt{x0^2+y0^2+(6t+z0)^2}\left(6t+z0+\sqrt{x0^2+y0^2+(6t+z0)^2}\right)^2\right)-$$
$$\left.\left.\left.y0\Big/\left(\sqrt{x0^2+y0^2}\left(6t+z0+\sqrt{x0^2+y0^2+(6t+z0)^2}\right)\right)\right)\right)\right)+$$

$$\frac{1}{(x0^2+y0^2)^{3/2}}\left(g0y\,x0\,y0\left(-\frac{b\left(\frac{\sqrt{x0^2+y0^2}}{-z0+\sqrt{x0^2+y0^2+z0^2}}-\frac{\sqrt{x0^2+y0^2}}{2t+z0+\sqrt{x0^2+y0^2+(2t+z0)^2}}\right)}{2\pi}+\frac{1}{2\pi}\left(b\left(\frac{\sqrt{x0^2+y0^2}}{2t+\sqrt{x0^2+y0^2+(2t-z0)^2}-z0}-\frac{\sqrt{x0^2+y0^2}}{4t+z0+\sqrt{x0^2+y0^2+(4t+z0)^2}}\right)\right)-\frac{1}{2\pi}\left(b\left(\frac{\sqrt{x0^2+y0^2}}{4t+\sqrt{x0^2+y0^2+(4t-z0)^2}-z0}-\frac{\sqrt{x0^2+y0^2}}{6t+z0+\sqrt{x0^2+y0^2+(6t+z0)^2}}\right)\right)\right)-\right.$$

$$\frac{1}{(x0^2+y0^2)^{3/2}}\left(g0x\,y0^2\left(-\frac{b\left(\frac{\sqrt{x0^2+y0^2}}{-z0+\sqrt{x0^2+y0^2+z0^2}}-\frac{\sqrt{x0^2+y0^2}}{2t+z0+\sqrt{x0^2+y0^2+(2t+z0)^2}}\right)}{2\pi}+\frac{1}{2\pi}\left(b\left(\frac{\sqrt{x0^2+y0^2}}{2t+\sqrt{x0^2+y0^2+(2t-z0)^2}-z0}-\frac{\sqrt{x0^2+y0^2}}{4t+z0+\sqrt{x0^2+y0^2+(4t+z0)^2}}\right)\right)-\frac{1}{2\pi}\left(b\left(\frac{\sqrt{x0^2+y0^2}}{4t+\sqrt{x0^2+y0^2+(4t-z0)^2}-z0}-\frac{\sqrt{x0^2+y0^2}}{6t+z0+\sqrt{x0^2+y0^2+(6t+z0)^2}}\right)\right)\right)+\right.$$

$$\frac{1}{\sqrt{x0^2+y0^2}}\left(g0x\left(-\frac{b\left(\frac{\sqrt{x0^2+y0^2}}{-z0+\sqrt{x0^2+y0^2+z0^2}}-\frac{\sqrt{x0^2+y0^2}}{2t+z0+\sqrt{x0^2+y0^2+(2t+z0)^2}}\right)}{2\pi}+\frac{1}{2\pi}\left(b\left(\frac{\sqrt{x0^2+y0^2}}{2t+\sqrt{x0^2+y0^2+(2t-z0)^2}-z0}-\frac{\sqrt{x0^2+y0^2}}{4t+z0+\sqrt{x0^2+y0^2+(4t+z0)^2}}\right)\right)-\frac{1}{2\pi}\left(b\left(\frac{\sqrt{x0^2+y0^2}}{4t+\sqrt{x0^2+y0^2+(4t-z0)^2}-z0}-\frac{\sqrt{x0^2+y0^2}}{6t+z0+\sqrt{x0^2+y0^2+(6t+z0)^2}}\right)\right)\right);\right.$$

(**** ny *****)

$$
\begin{aligned}
n_z = {} & g0z - \frac{1}{\sqrt{x0^2+y0^2}} \left(g0y\, x0 \left(-\frac{1}{2\pi} \left(b \left(-\frac{\sqrt{x0^2+y0^2}\left(-1+\frac{z0}{\sqrt{x0^2+y0^2+z0^2}}\right)}{\left(-z0+\sqrt{x0^2+y0^2+z0^2}\right)^2} + \frac{\sqrt{x0^2+y0^2}\left(1+\frac{2t+z0}{\sqrt{x0^2+y0^2+(2t+z0)^2}}\right)}{\left(2t+z0+\sqrt{x0^2+y0^2+(2t+z0)^2}\right)^2} \right) \right) + \right. \right. \\
& \frac{1}{2\pi} \left(b \left(-\frac{\sqrt{x0^2+y0^2}\left(-1-\frac{2t-z0}{\sqrt{x0^2+y0^2+(2t-z0)^2}}\right)}{\left(2t+\sqrt{x0^2+y0^2+(2t-z0)^2}-z0\right)^2} + \frac{\sqrt{x0^2+y0^2}\left(1+\frac{4t+z0}{\sqrt{x0^2+y0^2+(4t+z0)^2}}\right)}{\left(4t+z0+\sqrt{x0^2+y0^2+(4t+z0)^2}\right)^2} \right) \right) - \\
& \left. \left. \frac{1}{2\pi} \left(b \left(-\frac{\sqrt{x0^2+y0^2}\left(-1-\frac{4t-z0}{\sqrt{x0^2+y0^2+(4t-z0)^2}}\right)}{\left(4t+\sqrt{x0^2+y0^2+(4t-z0)^2}-z0\right)^2} + \frac{\sqrt{x0^2+y0^2}\left(1+\frac{6t+z0}{\sqrt{x0^2+y0^2+(6t+z0)^2}}\right)}{\left(6t+z0+\sqrt{x0^2+y0^2+(6t+z0)^2}\right)^2} \right) \right) \right) + \\
& \frac{1}{\sqrt{x0^2+y0^2}} \left(g0x\, y0 \left(-\frac{1}{2\pi} \left(b \left(-\frac{\sqrt{x0^2+y0^2}\left(-1+\frac{z0}{\sqrt{x0^2+y0^2+z0^2}}\right)}{\left(-z0+\sqrt{x0^2+y0^2+z0^2}\right)^2} + \frac{\sqrt{x0^2+y0^2}\left(1+\frac{2t+z0}{\sqrt{x0^2+y0^2+(2t+z0)^2}}\right)}{\left(2t+z0+\sqrt{x0^2+y0^2+(2t+z0)^2}\right)^2} \right) \right) + \right. \right. \\
& \frac{1}{2\pi} \left(b \left(-\frac{\sqrt{x0^2+y0^2}\left(-1-\frac{2t-z0}{\sqrt{x0^2+y0^2+(2t-z0)^2}}\right)}{\left(2t+\sqrt{x0^2+y0^2+(2t-z0)^2}-z0\right)^2} + \frac{\sqrt{x0^2+y0^2}\left(1+\frac{4t+z0}{\sqrt{x0^2+y0^2+(4t+z0)^2}}\right)}{\left(4t+z0+\sqrt{x0^2+y0^2+(4t+z0)^2}\right)^2} \right) \right) - \\
& \left. \left. \frac{1}{2\pi} \left(b \left(-\frac{\sqrt{x0^2+y0^2}\left(-1-\frac{4t-z0}{\sqrt{x0^2+y0^2+(4t-z0)^2}}\right)}{\left(4t+\sqrt{x0^2+y0^2+(4t-z0)^2}-z0\right)^2} + \frac{\sqrt{x0^2+y0^2}\left(1+\frac{6t+z0}{\sqrt{x0^2+y0^2+(6t+z0)^2}}\right)}{\left(6t+z0+\sqrt{x0^2+y0^2+(6t+z0)^2}\right)^2} \right) \right) \right);
\end{aligned}
$$

```
(*****plane normal at (x0,y0,z0);
u0[x0_, y0_, z0_]=-b/(2π) ( sqrt(x0^2+y0^2)/(t-(z0+t)+sqrt((t-(z0+t))^2+(x0^2+y0^2))) - sqrt(x0^2+y0^2)/(t+(z0+t)+sqrt((t+(z0+t))^2+(x0^2+y0^2))) );
Do[
 u0[x0, y0, z0]=
  u0[x0, y0, z0]+
   (-1)^n
    (-b/(2π) ((sqrt(x0^2+y0^2))/((2n+1) t-(z0+t)+sqrt(((2n+1) t-(z0+t))^2+(x0^2+y0^2))) -
        (sqrt(x0^2+y0^2))/((2n+1) t+(z0+t)+sqrt(((2n+1) t+(z0+t))^2+(x0^2+y0^2)))), {n,1,10}];
ux[x0_, y0_, z0_]=u0[x0, y0, z0] (-y0/sqrt(x0^2+y0^2));
uy[x0_, y0_, z0_]=u0[x0, y0, z0] (x0/sqrt(x0^2+y0^2));
uz[x0_, y0_, z0_]=b/(2π) ArcTan[y0/x0];
g0u[x0_, y0_, z0_]=g0x ux[x0, y0, z0]+g0y uy[x0, y0, z0]+g0z uz[x0, y0, z0];
nx[x0_, y0_, z0_]=g0x-D[g0u[x0, y0, z0], x0];
ny[x0_, y0_, z0_]=g0y-D[g0u[x0, y0, z0], y0];
nz[x0_, y0_, z0_]=g0z-D[g0u[x0, y0, z0], z0];
nx[x0, y0, z0]
 ny[x0, y0, z0]
 nz[x0, y0, z0]
*****)

rx' =
 1/nz (nz rx - (nx^2 nz rx)/(nx^2+ny^2+nz^2) - (nx ny nz ry)/(nx^2+ny^2+nz^2) - nx rz + (nx^3 rz)/(nx^2+ny^2+nz^2) +
    (nx ny^2 rz)/(nx^2+ny^2+nz^2) +
    1/(2 (nx^2+ny^2+nz^2))
     (nx
       sqrt((2 nx nz rx + 2 ny nz ry - 2 nx^2 rz - 2 ny^2 rz)^2 -
          4 (nx^2+ny^2+nz^2) (-nz^2 + nz^2 rx^2 + nz^2 ry^2 - 2 nx nz rx rz - 2 ny nz ry rz + nx^2 rz^2 + ny^2 rz^2))));
ry' =
 1/nz (-(nx ny nz rx)/(nx^2+ny^2+nz^2) + nz ry - (ny^2 nz ry)/(nx^2+ny^2+nz^2) - ny rz + (nx^2 ny rz)/(nx^2+ny^2+nz^2) +
    (ny^3 rz)/(nx^2+ny^2+nz^2) +
    1/(2 (nx^2+ny^2+nz^2))
     (ny
       sqrt((2 nx nz rx + 2 ny nz ry - 2 nx^2 rz - 2 ny^2 rz)^2 -
          4 (nx^2+ny^2+nz^2) (-nz^2 + nz^2 rx^2 + nz^2 ry^2 - 2 nx nz rx rz - 2 ny nz ry rz + nx^2 rz^2 + ny^2 rz^2))));
rz' =
 1/(2 (nx^2+ny^2+nz^2))
  (-2 nx nz rx - 2 ny nz ry + 2 nx^2 rz + 2 ny^2 rz +
    sqrt((2 nx nz rx + 2 ny nz ry - 2 nx^2 rz - 2 ny^2 rz)^2 -
       4 (nx^2+ny^2+nz^2) (-nz^2 + nz^2 rx^2 + nz^2 ry^2 - 2 nx nz rx rz - 2 ny nz ry rz + nx^2 rz^2 + ny^2 rz^2)));
(*****unit vector of outcoming beam*****)
```

```
xco = -(d rx' - z0 rx' + t Sec[8 °] rx' + x0 rz') / (Tan[8 °] rx' - rz');
xco >>> result_x.txt;
yco = -(y0 Tan[8 °] rx' - d ry' + z0 ry' - t Sec[8 °] ry' - x0 Tan[8 °] ry' - y0 rz') / (-Tan[8 °] rx' + rz');
yco >>> result_y.txt;
(*****Write coordinates into files*****)

If[IntegerPart[-(xco - xco0) / Cos[8 °] × 1/resolution] ≥ -249 && IntegerPart[-(xco - xco0) / Cos[8 °] × 1/resolution] ≤ 250 &&
  IntegerPart[-(yco - yco0) × 1/resolution] ≥ -249 && IntegerPart[-(yco - yco0) × 1/resolution] ≤ 250,
 intenmatr = ReplacePart[intenmatr,
   Extract[intenmatr, {IntegerPart[-(xco - xco0) / Cos[8 °] × 1 / resolution] + 250,
      IntegerPart[-(yco - yco0) × 1 / resolution] + 250}] + 1,
   {IntegerPart[-(xco - xco0) / Cos[8 °] × 1 / resolution] + 250,
    IntegerPart[-(yco - yco0) × 1 / resolution] + 250}]],
(*****write intensity into intenmatr*****)

{x0, -25.0125, 25.0125, 0.025},
{y0, -25.0125, 25.0125, 0.025}]
```

```
ListDensityPlot[intenmatr, Mesh → False]
```